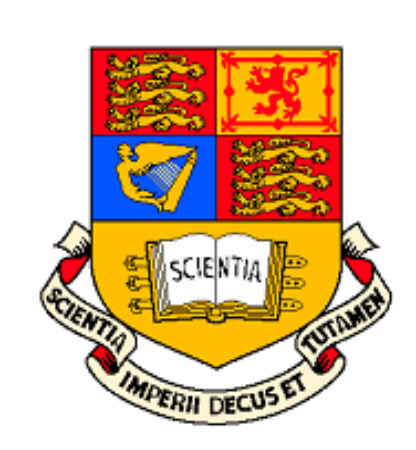


Chemical Biology Centre
Department of Chemistry
Imperial College London
University of London

Multi-Dimensional Fluorescence Microscopy for Förster Resonance Energy Transfer Studies of Cell Signaling

David M. Grant

Thesis submitted in partial fulfilment of the requirements for the degree of Doctor of Philosophy of the University of London

2008

Abstract

This thesis discusses the development of novel multi-dimensional fluorescence microscopy, particularly fluorescence lifetime imaging (FLIM) technology, and its application to imaging Förster Resonance Energy Transfer (FRET) events in live cells. Particular emphasis is placed on imaging activation of Ras family GTP-ases and binding to their effectors, including Phospholipase C Epsilon (PLCε).

The early part of the thesis discusses FLIM-FRET experiments performed using a standard confocal microscope with time correlated single photon counting (TCSPC) to image interactions between PLCε and Ras. These early experiments suggested a weak interaction but this mode of imaging was too slow to capture dynamics of Ras activation in live cells.

The long acquisition times required by the TCSPC microscope prompted the development of a high speed FLIM microscope using wide-field time-gated imaging, which was combined with a Nipkow disc confocal scan head to achieve optical sectioning. This system was characterised and its performance compared with commercially available TCSPC FLIM microscopes, demonstrating the enhancement in imaging speed for comparable accuracy of lifetime determination. This new microscope was subsequently applied to study the activation of the H-Ras oncogene in live cells following EGF stimulation.

The latter part of the thesis discusses the development of a second novel microscope system for multiplexed FRET studies – using both FLIM and spectral ratiometric imaging to monitor two different FRET pairs expressed within a single live cell. A CFP-YFP cameleon FRET biosensor was used to probe calcium signals in cells expressing different PLC isoforms and this was complemented by several novel Ras activation sensors that were designed using fluorescent proteins in the red end of the visible spectrum. Calibration experiments were carried out to determine the optimal fluorophores and filter sets for imaging multiplexed biosensors and the potential for imaging dynamics of calcium flux and Ras activation within the same cell were investigated.

Author declaration

The work in this thesis is solely that of the author, with the following exceptions:

- Software for FLIM data acquisition and the analysis of FLIM data was co-written by Dr. C. Dunsby, Dr. I. Munro and Dr. C. B. Talbot.
- Software for co-registration of images for spectral ratiometric imaging was written by S. Kumar.
- Characterisation of the signal to noise characteristics of the gated optical intensifier was done in collaboration with Dr. J. McGinty and was based on a method developed earlier by Dr. J McGinty and Dr. J. Requejo-Isidro. Rapid lifetime analysis for high speed optically sectioned lifetime imaging was performed in collaboration with Dr. J. McGinty.
- Spectroscopic measurements of FRET between Enhanced Green Fluorescent Protein EGFP and Red Fluorescent Protein in solution were done in collaboration with H. Manning.
- Fluorescent constructs used throughout were engineered by Dr. T. Bunney and Dr. W. Zhang at the Institute of Cancer Research, London.
- Multiplexed FRET experiments were done in collaboration with Dr. E. McGhee.

Acknowledgements

I would like to begin by thanking my supervisors Professor Paul French, Dr. Matilda Katan and Dr. Mark Neil for giving me the opportunity to work on this project and for all the help and advice they have given me throughout, especially in always finding time to discuss any ideas or questions I might have.

At Imperial, I would like to acknowledge the many lecturers, post-docs and students who have made the group a great place to do a PhD - thank you to Dan, Chris, Jose, Peter, James, Cliff, Richard, Pieter, Gordon, Valerie, Ewan, Ian, Khadija, Dylan, Sunil, Egidijus, Vincent, Bosanta, Hugh, Tom and Stephane. Special thanks must go to Peter for showing me the ins and outs of the confocal microscope and to James for his help in characterising the optical intensifier. Further thanks go to Cliff, Ian and Sunil for all their help with the software and a big thank you to Ewan for all his help with things FRET related. This thesis could also not have been completed without the skill and dedication of the Optomechanical Instrumentation Facility - a big thank you to Martin Kehoe, Martin Dowman, Simon, James and Paul for all the work they have done on my behalf.

At the Institute of Cancer Research, I would like to express my gratitude to Dr. Tom Bunney and Dr. Wei Zhang for cloning the many different constructs used throughout the project, and for explaining all manner of things biological. I'd also like to thank Dr. Neil Jones for answering my main questions on cell biology, and everyone else in the lab whose input was always greatly valued - thank you to Rhona, Prabs, Mandy, Katy, Isaac, Alessia, Natalia and Michelle. Further thanks must go to Dr. Hugh Paterson for his help with the microscopy at the Institute and for teaching me how to microinject cells, and to Dr. Anna Peyker for many helpful discussions regarding FRET.

Finally, one last big thank you to all those outside of work, particularly my family - Mum, Dad, Ben, Simon and Michelle, for all their continued support and encouragement.

Funding for this project was provided by an Engineering and Physical Sciences Research Council (EPSRC) studentship via the Chemical Biology Centre (CBC).

Table of contents

Acknowledgements……. 4

List of figures…….. 10

List of tables…… 15

Chapter 1: Thesis Overview……..... 16

Chapter 2: Introduction to Fluorescence Microscopy……. 19

2.0. Chapter overview…… 19

2.1. Fluorescence…… 19

2.2. Properties of Fluorescence…….. 20

2.2.1. Quantum yield and absorption coefficient…….. 20

2.2.2. Fluorescence absorption and emission spectra……... 21

2.2.3. Fluorescence lifetime…….. 22

2.2.4. Photobleaching and photostability…….. 23

2.3. Types of fluorophore……... 24

2.3.1. Fluorescent dyes……. 24

2.3.2. Green fluorescent protein (GFP)…… 25

2.3.3. Quantum dots..... 27

2.3.4. Endogenous fluorophores (autofluorescence)..... 28

2.4. Fluorescence microscopy…… 29

2.5. Wide-field fluorescence microscopy…….. 29

2.6. Optically sectioned fluorescence microscopy……. 30

2.6.1. Confocal microscopy…….. 30

2.6.2. Multiphoton microscopy……. 31

2.6.3. Other optical sectioning techniques…… 32

2.7. Fluorescence imaging techniques……... 33

2.7.1. Intensity imaging…… 33

2.7.2. Spectral imaging and ratiometric imaging…….. 34

2.7.3. Fluorescence anisotropy / polarisation resolved imaging..... 35

2.7.4. Fluorescence lifetime imaging…… 35
2.8. Instrumentation for fluorescence lifetime imaging……. 35
2.8.1. Time correlated single photon counting……. 36
2.8.2. Wide-field time domain fluorescence lifetime imaging……. 38
2.8.3. Wide-field frequency domain fluorescence lifetime imaging 40
2.9. Conclusion…….. 41

Chapter 3: Förster Resonance Energy Transfer…….. 42

3.0. Chapter overview…… 42
3.1. Förster Resonance Energy Transfer (FRET)…….. 42
3.1.1. Theory of non-radiative energy transfer……. 42
3.2. Use of FRET in biology…….. 45
3.2.1. Intramolecular FRET: Imaging conformational changes…... 45
3.2.2. Intermolecular FRET: Imaging protein-protein interactions.. 47
3.3. Imaging FRET in the microscope……... 47
3.3.1. Intensity based measurements…..……... 47
3.3.2. Spectral ratiometric measurements……. 48
3.3.3. Fluorescence lifetime measurements…….. 49
3.3.4. Polarisation resolved measurements……... 51
3.4. Choice of fluorophores for FRET……... 52
3.5. Experimental study of FRET between different FRET pairs…….. 54
3.5.1. Measurements in bulk solution……... 56
3.5.2. Measurements of immobilised proteins on beads……... 57
3.5.3. Discussion of measured FRET efficiencies…… 59
3.6. Conclusion…….. 60

Chapter 4: Materials and methods…….. 61

4.0. Cell culture…….. 61
4.1. Fluorescent constructs……. 61
4.2. MaxiPrep procedure…… 62
4.3. Cell transfection……..... 64

4.4. Cell microinjection…….. 64
4.5. SDS PAGE and Western blotting……... 64
4.6. EGF stimulation…….. 65
4.7. Fixing cells…….. 66
4.8. Labeling of beads with fluorescent constructs…… 66

Chapter 5: FLIM-FRET studies of Phospholipase C Epsilon interactions with Ras GTP-ases……. 67

5.0. Chapter overview…… 67
5.1. Ras family proteins……. 67
5.1.1. GTP-binding nature of Ras……. 67
5.1.2. Signaling via Ras: Upstream signaling and Ras activation… 69
5.1.3. Signaling via Ras: Downstream Ras effectors……... 70
5.2. Phospholipase C Epsilon: A novel Ras effector……. 72
5.2.1. Mechanism for Ras interactions with PLCε……... 73
5.3. Imaging interactions between Ras and PLCε…….. 74
5.3.1. FLIM-FRET studies of Ras and rPLCε-EGFP……... 75
5.3.2. Studies of over-expressed Ras and PLCε……... 78
5.3.3. Studies of RA2 domain interaction with Ras……. 80
5.3.4. Comparison of interactions with Raf Ras binding domain…. 82
5.4. Summary……. 84

Chapter 6: High speed optically sectioned FLIM to image FRET in live cells…….. 86

6.0. Chapter overview…… 86
6.1. Motivation for this work……. 86
6.2. Considerations for high speed FLIM…….. 87
6.3. Wide-field Fluorescence Lifetime Imaging…… 87
6.4. Implementing optical sectioning in wide-field microscopy…… 88
6.5. High power supercontinuum sources for FLIM…….. 89
6.6. Set up for high speed Nipkow disc FLIM microscope……... 91

6.7. Preliminary FLIM experiments……... 93
6.8. Comparison of wide-field system with confocal TCSPC……... 94
6.9. Noise characterisation of wide-field detector……. 96
6.9.1. Measurements of LED flux on detector……. 98
6.9.2. Signal to Noise Ratio measurements…….. 100
6.9.3. Calculating SNR as a function of photon number…….. 102
6.9.4. Comparison of wide-field time gating and TCSPC: Simulations……. 104
6.10. Application to imaging Ras activation in live cells…….. 106
6.11. Application to high throughput screening……. 108
6.12. Summary……... 110

Chapter 7: Multiplexed FRET for imaging dual FRET sensors…. 111

7.0. Chapter overview…… 111
7.1. Motivation for multiplexed FRET experiments…….. 111
7.1.1. Basis for investigating PLCε activity by multiplexed FRET 112
7.2. Imaging calcium flux in cells…….. 114
7.2.1. Choice of FRET sensors for imaging calcium…… 115
7.3. Preliminary studies: Cameleon imaging with PLCs……... 116
7.3.1. Image analysis…… 117
7.3.2. Results of dual view calcium imaging…… 118
7.4. Extension to multiplexed FRET…….. 119
7.4.1. FRET Sensors for imaging Ras activity in live cells…….. 120
7.5. Choice of second FRET pair for the Ras sensor……. 122
7.5.1. Considerations for fluorophore……... 122
7.5.2. Choice of donor for the second FRET pair……. 123
7.5.3. Choice of acceptor for the second FRET pair…… 125
7.6. Imaging the second FRET pair……... 125
7.6.1. FLIM analysis of mOrange-Raichu-Cherry……... 127
7.7. Effects of spectral bleed-through on measured lifetimes…… 130
7.8. Increasing the spectral bandwidth for multiplexing…… 131
7.9. Comparing spectral bleed-through of mPlum with mCherry…….. 133

7.10. Imaging mOrange-Raichu-mPlum…… 135
7.11. Use of separately labelled constructs…… 136
7.12. TagRFP: An alternative donor for the second pair……... 137
7.12.1. Investigating FRET between TagRFP and mPlum……... 138
7.13. Experimental set-up for multiplexed FRET…….. 140
7.14. Results of multiplexing……. 142
7.15. Conclusions……... 144

Chapter 8: Conclusions…… 146

8.0. Chapter overview…… 146
8.1. Results summary and discussion……. 146
8.2. Future directions……. 148

Publications and conference presentations arising from this work……. 150
References……... 153

List of figures

Figure 2.0 Jablonski diagram showing electron transitions between quantum states in a molecule.

Figure 2.1 Example absorption and emission spectra for a fluorescent species. The Stokes shift defines the shift in wavelengths between the excitation and emission, relating to the energy lost by the electron through internal conversion.

Figure 2.2 Chemical structure of chemical dyes commonly used in fluorescence microscopy. Systems of conjugated carbon bonds are evident throughout.

Figure 2.3 Left: Aequorea Victoria jellyfish: Right: Ribbon model of GFP structure. The protein has a barrel-like structure composed of 11 Beta sheets, through the centre of which runs an alpha-helix. The chromophore region of the molecule is contained inside the Beta-barrel, as shown here in orange.

Figure 2.4 Chromophore maturation within GFP. For clarity, the alkyl groups of serine 65 and tyrosine 66 are shaded in grey and pink respectively (the third alkyl group, in glycine 67 constitutes a single hydrogen atom, hence is not shown). The yellow shaded areas show the two atoms involved in nucleophilic attack which leads to the formation of the imidazole ring shown on the right.

Figure 2.5 Wide-field fluorescence microscope. The sample is illuminated by an incoherent light source and the ensuing fluorescence imaged on to a wide-field detector. Use of a suitable dichroic and emission filter allows one to separate the excitation light from fluorescence with high signal to noise.

Figure 2.6 Principle of the confocal microscope: The sample is illuminated by a point source and fluorescence imaged onto a point detector (blue rays). An aperture placed in front of the detector excludes light from planes outside of focus reaching the detector (red rays), thus by scanning the beam across the sample one can build up an image of a single plane.

Figure 2.7 Jablonski diagrams for single photon and two-photon excitation. In the latter, two photons combine in a single absorption event, provided the incident photon flux is high enough.

Figure 2.8 Spectral imaging. By measuring the intensity of fluorescence emission in different spectral channels, one can discriminate the signal from fluorophores with different emission spectra.

Figure 2.9 Instrumental components for time correlated single photon counting (TCSPC) FLIM. The arrival times of individual photons are measured with respect to the excitation pulse and the resultant histogram used to extract the fluorescence decay and lifetime.

Figure 2.10 Time-gated detection of fluorescence decays. By varying the delay between the excitation pulse signal and the gate on the intensifier, one is able to collect intensity images at different times during the fluorescence decay. This series of images can then be used to compute the lifetime for each pixel in the image series.

Figure 2.11 Gated optical intensifier (GOI). This figure shows the 3 main components - the photocathode, microchannel plate (MCP) and phosphor screen.

Figure 2.12 Principle of frequency domain lifetime analysis. An intensity modulated light source is used to excite the sample, and the lifetime calculated by measuring the phase shift or change in modulation depth of the fluorescence intensity.

Figure 3.0 The overlap integral J(λ) in Förster's equation defines the extent of overlap between the donor emission spectrum and the acceptor absorption spectrum.

Figure 3.1 FRET efficiency as a function of donor-acceptor separation R for an arbitrary value of $R_{O.}$

Figure 3.2 Intramolecular FRET. Labelling a protein or molecule with both donor and acceptor allows one to image protein activation or ligand binding by reading out FRET between the two fluorophores.

Figure 3.3 Intermolecular FRET. Labelling of separate species with donor and acceptor allows one to image their interactions by reading out the FRET signal between the two fluorophores.

Figure 3.4 Spectral ratiometric FRET analysis: FRET can be detected by a relative increase in

fluorescence at longer wavelengths, due to sensitised emission from the acceptor.
Figure 3.5 Fluorescence lifetime decays in the presence of (red) and absence of FRET (green). If FRET occurs, the donor fluorescence is quenched and the molecule on average spends less time in the excited state. This means that proportionally more photons are emitted at earlier time points.
Figure 3.6 Imaging Homo-FRET by polarisation anisotropy. Secondary excitation of acceptors by FRET results in an increase in the depolarisation of fluorescence, when the sample is excited by a polarised light source.
Figure 3.7 FlAsH technology for labelling proteins (Figure courtesy of *Invitrogen*).
Figure 3.8 Spectral overlap between the EGFP emission spectrum and the absorption spectra of the three prospective FRET acceptors mOrange, mRFP and mCherry.
Figure 3.9 Temporal decay profiles for EGFP and each of the 3 donor/acceptor pairs EGFP-mRFP, EGFP-mOrange and EGFP-mCherry.
Figure 3.10 Labelling of S-Agarose beads with purified protein FRET constructs.
Figure 3.11 Top - FLIM images of beads labelled with EGFP, EGFP-mRFP and EGFP-mCherry (Scale bar = 50 μm) Bottom - Fluorescence lifetime histograms for the images shown.
Figure 5.0 Regulation of GTP-ase activation by GEFs and GAPs. GEFs facilitate the transition from a GDP bound state to a GTP-bound state in which the GTP-ase is able to engage with effectors and so propagate downstream signals. GAPs, meanwhile return the protein to an inactive form by helping speed the protein's hydrolysis of GTP back to GDP.
Figure 5.1 Ras is activated in response to signals from outside the cell. Activation of tyrosine receptor kinases by signal ligands initiates the Grb-2-Sos pathway, leading to Ras activation at the plasma membrane.
Figure 5.2 Key Ras effectors and downstream signal pathways.
Figure 5.3 Signaling via Phospholipase C (PLC) In response to agonist stimulation of cell surface receptors, PLC is recruited to the membrane where it catalyses hydrolysis of PIP_2, resulting in the soluble product IP_3 and membrane bound diacylglycerol DAG. IP_3 in turn promotes release of Ca^{2+} from intracellular stores through binding to the IP_3 receptor in the endoplasmic reticulum.
Figure 5.4 Domain structure of Phospholipase C family members PLCβ, PLCγ, PLCδ, and PLCε. The X-Y catalytic domain is conserved across all members, as are the C2 and EF domains. PLCε (bottom) possesses an additional 2 Ras association (RA) domains at the C terminus, while the CDC25 domain at the N terminus has been implicated in GEF signaling to small GTP-ases.
Figure 5.5 Truncated PLCε fusion protein (rPLCε-EGFP).
Figure 5.6 Western blots of mRFP-labelled small Ras GTP-ases (left) and rPLCε-EGFP (right), using whole cell lysates from transfected COS cells.
Figure 5.7 Localisation of rPLCε-EGFP in COS cells (top row) and MDCK cells (bottom row). In a small number of cells, rPLCε-EGFP was seen to translocate to the membrane in response to EGF stimulation. The left hand panel shows serum starved cells prior to stimulation. The 4 images in the right hand panel were acquired 10 - 30 mins post EGF stimulation. Scale bar = 15 μm.
Figure 5.8 FLIM images of MDCK cells expressing rPLCε-EGFP and H-Ras-mRFP. The top row in each panel shows localisation images of rPLCε-EGFP (green) and H-Ras-mRFP (red). The bottom row in each panel shows the fluorescence lifetime map (left) and a merged image of lifetime with donor intensity (right). In both cases, the colorbar bounds are 2000 ps (blue) to 3000 ps (red). Scale bars = 20 μm.
Figure 5.9 FLIM images of MDCK cells expressing rPLCε-EGFP and K-Ras-mRFP. The top row in each panel shows localisation images of rPLCε-EGFP (green) and K-Ras-mRFP (red). The bottom row in each panel shows the fluorescence lifetime map (left) and a merged image of lifetime with donor intensity (right). In both cases, the colorbar bounds are 2000 ps (blue) to 3000 ps (red). Scale bars = 20 μm.
Figure 5.10 FLIM images of MDCK cells expressing rPLCε-EGFP and N-Ras-mRFP. The top row in each panel shows localisation images of rPLCε-EGFP (green) and N-Ras-mRFP (red). The bottom row in each panel shows the fluorescence lifetime map (left) and a merged image of lifetime with donor intensity (right). In both cases, the colorbar bounds are 2000 ps (blue) to 3000 ps (red). Scale bars = 20 μm.
Figure 5.11 FLIM images of MDCK cells expressing rPLCε-EGFP and K-Ras-mRFP. From

left: Intensity image of rPLCε-EGFP localisation, with membrane translocation particularly evident. Second from left: Fluorescence lifetime map (continuous color-scale). Third from left: Fluorescence lifetime map (binary color-scale, to emphasise the shorter lifetime seen at the cell membrane). Fourth from left: Intensity image merged with FLIM map (continuous color-scale). Scale bar = 10 μm.

Figure 5.12 FLIM images of MDCK cells overexpressing rPLCε-EGFP and K-Ras-mRFP. The top row in each panel shows localisation images of rPLCε-EGFP (green) and K-Ras-mRFP (red). The bottom row in each panel shows the fluorescence lifetime map (left) and a merged image of lifetime with donor intensity (right). The colorbar bounds are 2000 ps (blue) to 3000 ps (red). EGF was not used to treat the cells in either data set. Scale bars = 20 μm.

Figure 5.13 FLIM images of MDCK cells overexpressing rPLCε-EGFP and H-Ras-mRFP. The top row in each panel shows localisation images of rPLCε-EGFP (green) and H-Ras-mRFP (red). The bottom row in each panel shows the fluorescence lifetime map (left) and a merged image of lifetime with donor intensity (right). The colorbar bounds are 2000 ps (blue) to 3000 ps (red). EGF was not used to treat the cells in either data set. Scale bars = 20 μm.

Figure 5.14 FLIM images of MDCK cells expressing PLCε(RA2)-EGFP and H-Ras-mRFP. The top row in each panel shows localisation images of PLCε(RA2)-EGFP (green) and H-Ras-mRFP (red). The bottom row in each panel shows the fluorescence lifetime map (left) and a merged image of lifetime with donor intensity (right). The colorbar bounds are 2100 ps (blue) to 3000 ps (red). Scale bars = 20 μm.

Figure 5.15 FLIM images of PLCε(RA2)-EGFP in COS cells coexpressing H-Ras-mRFP. Top left: Intensity image, top right: Fluorescence lifetime (discrete lifetime scale), bottom left (continuous lifetime scale), bottom right: lifetime merged with intensity image. Scale bars = 10 μm.

Figure 5.16 FLIM images of MDCK cells expressing Raf-RBD-EGFP and H-Ras-mRFP. The top row in each panel shows localisation images of Raf-RBD-EGFP (green) and H-Ras-mRFP (red). The bottom row in each panel shows the fluorescence lifetime map (left) and a merged image of lifetime with donor intensity (right). The colorbar bounds are 2100 ps (blue) to 3000 ps (red). Scale bars = 20 μm.

Figure 5.17 Fluorescence lifetime images of Raf-RBD-EGFP in MDCK cells coexpressing H-Ras-mRFP. Top left: Intensity image, top right: Fluorescence lifetime (discrete lifetime scale), bottom left (continuous lifetime scale), bottom right: lifetime merged with intensity image. Scale bars = 10 μm.

Figure 5.18 Fluorescence lifetime histograms of Raf-RBD-EGFP (left) and PLCε(RA2)-EGFP (right) in COS cells expressing H-Ras-mRFP. Both pairs of constructs showed a fall in lifetime at the membrane compared to the cytoplasmic fraction, although this shift was smaller in the case of PLCε(RA2)-EGFP.

Figure 6.0 Instrumentation for wide-field time-gated fluorescence lifetime imaging.

Figure 6.1 The Yokogawa CSU10 microscope series uses an array of microlenses to focus light through each hole in the Nipkow disc. This increases the transmission of excitation light through the disc whilst keeping the spacing between pinholes large enough the preserve the optical sectioning effect.

Figure 6.2 Optical set up for wide-field optically sectioning FLIM microscope.

Figure 6.3 Schematic of Yokogawa CSU10 scan head, microscope and CCD camera. (The GOI, which for FLIM measurements is placed between the CSU10 and CCD, is not shown in this figure).

Figure 6.4 Excitation light path in Yokogawa CSU10 scan head.

Figure 6.5 Fluorescence light path in the Yokogawa CSU10 scan head.

Figure 6.6 Sectioned image stack through a COS 7 cell expressing H-Ras-mRFP and Raf-RBD-EGFP, displaying FRET at the plasma membrane following stimulation by epidermal growth factor EGF. Each image was recorded in 5s, with a 120s total acquisition time.

Figure 6.7 Representative images of EGFP expressing cells captured on the Nipkow disc microscope (left column) and confocal system (right column) with different acquisition times. Note that the noise is far more prevalent in the images of cells obtained on the TCSPC. The white pixels seen here are those where an erroneous lifetime has been calculated while lies beyond the bounds of the color scale.

Figure 6.8 Plots of the mean fluorescence lifetime and standard deviation measured from cells expressing EGFP using confocal TCSPC, and time-gated Nipkow disc microscopy. The mean lifetime recorded on the Nipkow disc is constant across the range of acquisition times, even with as short an acquisition time as 1s. In contrast, on the confocal TCSPC system an artefact is seen for acquisition times below 10s, owing to the reduced number of photons detected. This shortage of fluorescence photons is further highlighted in the plot of standard deviation, where the increased width of the lifetime distribution is evident across the full range of acquisition times.
Figure 6.9 Optical set-up for characterising the intensifier noise. A CW LED was focussed onto a diffuser wheel and then collimated to fill the aperture of the photocathode. The total flux incident on the GOI was adjusted by use of different ND filters placed before the detector.
Figure 6.10 a) Acquired intensity image at 850 V, 1 ms integration time with a 0.0076% transmission filter. Figures b and c show the same image thresholded at 200DN and 250DN, respectively.
Figure 6.11 Mean photon count as a function of integration time, for ND 0.0076% transmission.
Figure 6.12 Intercept of fitted function for different threshold values, at ND 0.0076% transmission.
Figure 6.13 Variation in standard deviation squared with digital number, at different gain settings.
Figure 6.14 Standard deviation measured for different gain settings.
Figure 6.15 Signal to noise ratio SNR as a function of digital number for different gain settings.
Figure 6.16 k values for different MCP gain settings.
Figure 6.17 Signal to noise ratio as a function of detected photons for different MCP gain settings. Inset: An expanded region of the graph for lower numbers of detected photons.
Figure 6.18 Accuracy in lifetime as a function of acquisition time for three cases: i) confocal time correlated single photon counting with a count rate of 106s-1; ii) confocal time correlated single photon counting with a count rate of 105s-1; iii) the Nipkow disc system, assuming a flux per pixel equal to that calculated from cells expressing EGFP. Note that lines drawn here do not take into account the effects of image smoothing, hence the slight increase in error compared to Figure 5.8.
Figure 6.19 Time lapse fluorescence lifetime imaging of Raf-RBD-EGFP interacting with H-Ras-mRFP at the cell membrane in MDCK cells. Within 30 seconds of adding EGF, a shortening of the EGFP donor lifetime was observed at the cell membranes, indicating activation of H-Ras-mRFP. The maximum shift in lifetime was seen at 10 mins, after which the lifetimes began to rise, indicating a transient activation profile. Left column: Donor fluorescence lifetime (continuous scale); middle column: donor fluorescence lifetime (binary scale, thresholded at 2400 ps); right column: merged fluorescence lifetime with intensity; bottom: H-Ras-mRFP localization.
Figure 6.20 a) Mercury lamp images of live MDCK cells expressing either EGFP or a tandem construct of EGFP-mRFP. The fluorescence in the red channel shows only this cell expresses both fluorophores. b) Fluorescence lifetime images of the same field of view, captured at frame rates of 1 Hz (top row), 5 Hz (middle row) and 10 Hz (bottom row). Also shown are the lifetime histograms for each image. Lifetimes were measured using a two gate RLD method. The shorter lifetime in the cell expressing both fluorophores is evident even when imaging at 10 Hz.
Figure 7.0 Schematic of the Dual View Imager from Optical Insights. The Dual View can be used to spectrally resolve fluorescence from the sample into two channels, imaged onto the same CCD chip.
Figure 7.1 Dual channel image of COS cells expressing the YCAM 3.6 sensor.
Figure 7.2 Flow chart for batch analysis of dual view time-lapse sequence images.
Figure 7.3 Time-lapse sequence of ratiometric FRET images of cells expressing full length (untagged) PLCε and YCAM 3.6, stimulated with EGF. Immediately after stimulation, a large calcium flux was seen to occur in the perinuclear region of the cell, as seen here from the increased ratio of the Venus / ECFP channel intensities, which gradually subsided over the course of 5 minutes.
Figure 7.4 Variation in Venus/ECFP intensity ratio for live COS cells coexpressing YCAM 3.6 and the three PLC isoforms, or YCAM 3.6 alone, when stimulated with EGF.

Figure 7.5 FRET probes for sensing Ras activation. Left: The Raichu intramolecular FRET sensor designed by Miyawaki *et al*. Right: An intermolecular FRET sensor consisting of separately labelled Ras and Raf constructs. (Note that the domain labelled Raf here refers only to the Ras binding domain of Raf Kinase and not the full length protein).
Figure 7.6 Absorption and emission spectra of visible fluorescent proteins.
Figure 7.7 Absorption and emission spectra for ECFP/Venus and mOrange/mCherry FRET pairs. The absorption spectra have been normalised to the respective absorption coefficient of each fluorophore and the emission spectra normalised to their respective quantum yields. The vertical lines in the absorption spectra indicate possible choices for the excitation wavelength. The shaded regions in the emission spectra are suggested filters for dual channel intensity measurements.
Figure 7.8 Fluorescence lifetime images of mOrange (top row) and mOrange-Raichu-mCherry (bottom row) in COS cells stimulated by EGF. Images on the right are the lifetime maps merged with the intensity image. Inset: Illustration of the mOrange-Raichu-mCherry probe.
Figure 7.9 Absorption and emission spectra of Venus, mOrange and mCherry, with the spectral bands used in Filter set 1 (left column) and set 2 (right column) shown in the shaded regions. The dotted lines indicate the dichroic cut-off wavelength in the two cases.
Figure 7.10 Fluorescence intensity and lifetime images of mOrange-Raichu-mCherry expressed in MDCK cells, imaged using the two filter sets F1 (top row) and F2 (bottom row).
Figure 7.11 Lifetime histograms for the images in Figure 7.10 above.
Figure 7.12 Box plot showing the distribution of mean lifetimes in the mOrange spectral channel, when imaging cells expressing different combinations of mOrange, YCAM and mCherry with the two filter sets F1 and F2.
Figure 7.13 Absorption and emission spectra of Venus, mOrange and mPlum with the spectral bands used to excite and detect shown in the shaded regions. The dotted lines indicate the dichroic cut-off.
Figure 7.14 Box plot showing distributions of mean lifetime in cells expressing different combinations of mOrange, YCAM and mPlum.
Figure 7.15 Fluorescence lifetime images of mOrange and mOrange-Raichu-mPlum in COS cells. Top row: FLIM map and intensity merged image of mOrange. Middle and bottom rows: FLIM maps and intensity merged images of mOrange-Raichu-mPlum fixed after different periods of stimulation by EGF.
Figure 7.16 Fluorescence lifetime histograms from cells expressing mOrange, and mOrange-Raichu-mPlum stimulated for different periods with EGF.
Figure 7.17 Absorption spectra and emission spectra for TagRFP, YCAM and mPlum. Shaded areas indicate filters used to excite and detect TagRFP fluorescence.
Figure 7.18 Box plot showing distributions of mean lifetime in cells expressing different combinations of TagRFP, YCAM and mPlum.
Figure 7.19 Top: Fluorescence lifetime images of TagRFP-Raf-RBD in COS cells coexpressing H-Ras-mPlum, after 10 mins EGF stimulation. Bottom: Lifetime histograms for regions in the above images, from a region in the cytosol and the plasma membrane. The lifetime shift at the membrane is evidence of FRET between TagRFP-Raf-RBD and H-Ras-mPlum.
Figure 7.20 Top: Final probe selection for multiplexed FRET: An ECFP/Venus YCAM 3.6 cameleon and TagRFP-Raf-RBD/H-Ras-mPlum intermolecular FRET pair for sensing Ras activation at the membrane. Bottom: Full absorption and emission spectra showing excitation wavelengths and spectral detection channels for multiplexed imaging.
Figure 7.21 Instrumental set up for multiplexed FRET.
Figure 7.22 Multiplexed FRET imaging of cells expressing the two FRET sensors and full length PLCε. Top: Ratiometric images of YCAM acquired using the Dual-View at intervals before and after stimulation (numbers above indicate time in seconds after cell stimulation with EGF). Middle: FLIM images and merged intensity images of TagRFP in the same cells, at the time points shown above. Bottom: Graphs of ECFP and Venus intensity from a region in the cytosol, and TagRFP lifetime from a region in the cell membrane.

List of tables

Table 3.0 Advantages and disadvantages of different fluorophores for FRET applications.
Table 3.1 Molar absorption coefficients and predicted R_O values for the three FRET acceptors.
Table 5.0 Mammalian small GTP-ases
Table 6.0 Calculated photon flux for different ND filter combinations.
Table 7.0 Pros and cons of different calcium imaging methods
Table 7.1 Advantages and disadvantages of intramolecular (Raichu) sensors and intermolecular FRET probes for imaging Ras activity.
Table 7.2 Advantages and disadvantages of prospective donors for second FRET pair in multiplexed FRET.
Table 7.3 Pass bands for two filter sets used to image mOrange-Raichu-mCherry.
Table 7.4 Spectral properties of far-red emitting fluorescent proteins.

Chapter 1: Thesis overview

In recent years, the measurement of Förster Resonant Energy Transfer (FRET) - the non-radiative transfer of energy from an excited state molecule to a neighbouring molecule spaced at close proximity - has become an increasingly popular tool for *in vivo* studies of cell function and behaviour. FRET is a particularly important spectroscopic technique since it can be used to quantify molecular separation at the scale of nanometers. When implemented in the microscope, FRET provides a valuable means for studying interactions between proteins and other species which together form the basis of cell signal networks.

The growing use of FRET microscopy can be attributed to several factors. The development of novel laser sources, detectors and filters have made spectroscopic imaging techniques such as fluorescence lifetime imaging (FLIM) and spectral ratiometric imaging more widespread and have helped to enhance the sensitivity and reliability of FRET measurements. Techniques such as confocal and multiphoton microscopy have also played a role, helping to make measurements of fluorescence intensities more robust through elimination of out of focus light. Most importantly, perhaps, has been the explosion in novel fluorescent probes and methods for using them to label different cellular species. Together, these advances have opened up new possibilities for labelling of species with suitable tags for FRET.

The goal of this thesis has been to expand the amount of information that can be acquired from FRET studies of cell behaviour. This has involved developing novel tools and instrumentation for imaging FRET in live cells. The biological utility of these instruments has been illustrated by applying them to monitor the activity of Ras small GTP-ases and associated signaling components in live cells. Ras proteins lie at the intersection of a number of key signal pathways linked to cell growth, division and survival and the information obtained from such studies is therefore highly important for understanding the regulation of different biological processes, particularly deregulation in cancer. The following paragraphs provide a brief outline of each chapter in this thesis.

Chapter 2 outlines the basic concepts of fluorescence and fluorescence microscopy. The properties which characterise a fluorescence signal are discussed, including emission intensity, absorption and emission spectra, fluorescence lifetime and fluorescence polarisation. The different types of fluorescence microscope are presented with a discussion of how spectroscopic techniques, including spectrally resolved imaging and fluorescence

lifetime imaging can be implemented in such systems. The instrumentation for fluorescence lifetime imaging, including time correlated single photon counting (TCSPC) and wide-field time-gated and frequency domain imaging, are also discussed.

Chapter 3 introduces FRET as a process in which a fluorophore can transfer energy non-radiatively to a neighbouring chromophore through long range coupling of the two species' transition dipole moments. The dependence of energy transfer efficiency on the distance separation of the two species is discussed and used to explain the utility of FRET for probing intermolecular distances. Different methods for imaging FRET are presented – these include ratiometric imaging, fluorescence lifetime imaging (FLIM) and polarisation resolved imaging. The typical fluorophores and labelling strategies used in FRET microscopy are also reviewed. The chapter concludes with the results of experiments comparing the extent of energy transfer between different pairs of fluorescent proteins when covalently linked by a short peptide sequence.

Chapter 4 outlines methods used for preparation of biological samples throughout this thesis.

In Chapter 5, the role of Ras family proteins in cell signal pathways is discussed, with particular emphasis placed on the novel downstream effector, Phospholipase C Epsilon (PLCε). Interactions between these proteins are studied using time correlated single photon counting FLIM-FRET measurements of fluorescently labelled Ras and PLCε in cells fixed prior to and after EGF stimulation. The results of these experiments are also compared with those using another well documented Ras effector, Raf Kinase.

Chapter 6 discusses the design and characterisation of a wide-field, optically sectioned FLIM microscope, used to address some of the speed limitations imposed by time correlated single photon counting techniques. By combining a wide-field time-gated FLIM acquisition strategy with a spinning Nipkow disc microscope and high power supercontinuum source, it is possible to acquire optically sectioned FLIM images comparable to those of confocal microscopes using time correlated single photon counting, at much shorter integration times. This is verified experimentally by comparing the signal to noise ratio in images of fluorescently labelled cells acquired using both approaches and through use of simulations, which model the noise characteristics of each detector and their respective photon acquisition rate. The improved speed of the wide-field microscope allowed us to study the dynamics of Ras activation in live MDCK cells, and the possible application of this system to high throughput screening assays is also discussed.

In Chapter 7, we discuss the design and implementation of a second wide-field microscope, capable of monitoring resonant energy transfer between two, spectrally distinct pairs of fluorophores. Design considerations for the microscope and the probes are presented, with particular emphasis on the choice of fluorophores used. Using this system, we are able to demonstrate multiplexed imaging of calcium flux and Ras activation in single live COS cells following EGF stimulation. The potential of this approach for reporting on multiple aspects of cell signaling networks is discussed.

Chapter 8 summarises the key results and findings of this thesis, followed by discussion of possible future directions for this work. This is followed by a list of journal publications and conference presentations generated by this project. A bibliography of references is provided at the end.

Chapter 2: Introduction to Fluorescence Microscopy

2.0. Chapter overview

This chapter introduces some of the core concepts in fluorescence and its implementation in microscopy. The different modes of fluorescence imaging, including spectrally resolved, polarisation resolved and time resolved imaging are discussed, together with a review of fluorescence microscopes commonly used in biology. The chapter also provides an introduction to different varieties of fluorophores for labelling cellular species and the relative merits of each.

2.1. Fluorescence

Fluorescence is a physical process whereby a material or medium will absorb a photon of light, and after a brief interval (typically nanoseconds) reemit a photon, at a slightly longer wavelength. The absorption and emission of light in this way is caused by the transition of electrons between different energy levels within the molecule [1]. This is most easily explained by reference to the Jablonski diagram (Figure 2.0).

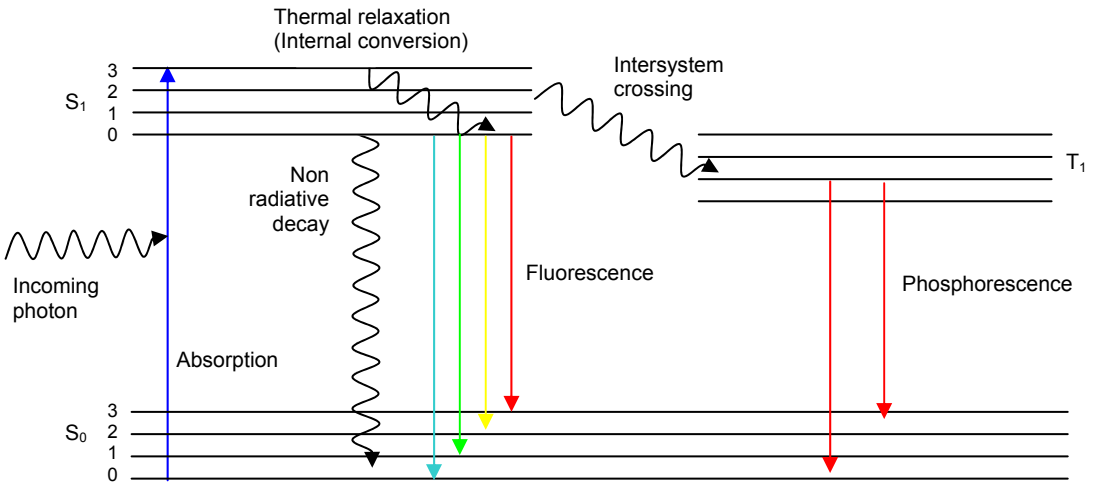


Figure 2.0: Jablonski diagram showing electron transitions between quantum states in a molecule.

The Jablonski diagram shows the different energy states an electron may occupy within an atom or molecule. S_O is the ground state, whilst S_1 is the first excited singlet state and T_1 the first excited triplet state. Within each state there exist additional rotational and vibrational

modes of freedom, giving rise to a band like structure with a continuum of energy levels. Following absorption of an incident photon, an electron may be promoted from the ground state S_O to the upper energy state S_1. Once in the upper energy band, the electron will rapidly dissipate its energy and fall to the lowest energy level in that band, a process known as internal conversion. Typically, this will occur over a time scale of 10^{-12}s. The electron may then relinquish its remaining energy through one of several processes. In fluorescence, the electron returns to the ground state via the radiative emission of a photon. The energy lost through internal conversion is reflected in the longer wavelength of the emission, an effect known as the Stokes shift. Alternatively, the electron may decay non-radiatively by some form of quenching mechanism - for example through collisions with other molecules in the environment. A third possibility is that of intersystem crossing, in which the electron will undergo a change in spin orientation and populate the triplet state T_1. In order to return to the ground state, the electron must revert to its original spin configuration. The slow rate of spin conversion means that radiative emission from the triplet state (phosphorescence) is delayed by many orders of magnitude relative to fluorescence, and may ensue for several seconds after the initial excitation pulse.

2.2. Properties of Fluorescence

A fluorescent species can be characterised by one of several parameters. These include its quantum yield, absorption coefficient, absorption (excitation) and emission spectra and fluorescence lifetime. Each one of these is dependent on the configuration of electronic energy levels within the molecule. A fluorophore's interaction with its environment may lead to perturbations in the electronic configuration – this will in turn be reflected by a change in one or more of its fluorescent properties. Fluorescence measurements can therefore be used not only to discriminate between separate species of fluorophore, but also to report on their local environment. We shall now look at these properties in more detail.

2.2.1. Quantum yield and absorption coefficient

The quantum yield defines the number of photons emitted by the fluorophore as a fraction of those absorbed when excited to a higher energy state. It therefore indicates how probable spontaneous emission is, compared against other non-radiative decay routes. This can be written as shown in Equation 2.0:

$$\eta = \frac{k_R}{k_{NR} + k_R} \qquad \text{(Equation 2.0)}$$

where k_R and k_{NR} are the radiative and non-radiative rates of energy loss, respectively.

The absorption coefficient measures the number of photons absorbed as a fraction of those which are incident on the fluorophore. Its value can be derived from the Beer-Lambert Law, which determines the fall in intensity as light passes through a medium containing the absorbing species:

$$I = I_O \, exp - \left[\varepsilon \, b \, c \right] \qquad \text{(Equation 2.1)}$$

Here, I_O is the initial light intensity, ε is the molar absorption coefficient (measured in units of $Mol^{-1}cm^{-1}$) and b and c are the distance travelled in the medium and concentration of the absorbing species, respectively.

For fluorophores, the product of the absorption coefficient and quantum yield can be used to define a quantity called "brightness." For most types of imaging it is preferable to have as high a brightness as possible in order to maximise signal to noise ratio (SNR).

2.2.2. Fluorescence absorption and emission spectra

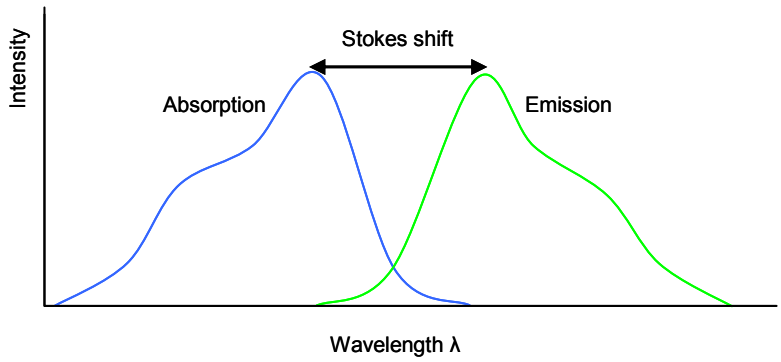


Figure 2.1: Example absorption and emission spectra for a fluorescent species. The Stokes shift defines the shift in wavelengths between the excitation and emission, relating to the energy lost by the electron through internal conversion .

A fluorophore's absorption and emission spectra are two of its most characteristic features. Together, they define the range of wavelengths over which the fluorophore will absorb and radiate light (Figure 2.1). The origins of these spectra can be understood when we consider

that each of the states S_0, S_1, T_1 has an associated number of vibrational levels, giving rise to a range of possible energy transitions. At room temperature, Boltzmann statistics predict that the population of any one electronic state will tend to reside in the lowest vibrational mode of that state. Thus, the absorption spectrum can be considered as the probability distribution for transitions between the lowest energy level in the ground state and different vibrational levels in the excited state. The emission spectrum, conversely, reflects the probability of transitions between the lowest energy level in the excited state and different vibrational levels in the ground state. Two important points emerge from this: first, since emission always occurs from the lowest energy level in the excited state, the shape of the emission spectrum is independent of excitation wavelength. Secondly, since the spacing of vibrational energy levels is the same in both S_O and S_1, the probability of transition from a vibrational level in S_O to S_1 is equivalent for the reverse transition occurring. This has the result that the emission spectrum tends to mirror the absorption spectrum (although there are some exceptions to this rule).

2.2.3. Fluorescence lifetime

The fluorescence lifetime is defined as the average amount of time a molecule will remain in an excited state once it has absorbed an incident photon. If we consider a system containing a single fluorescent species that is excited by a pulse of light, the number of molecules that remain in the upper energy band will fall exponentially with time. The measured intensity of the fluorescence emission will hence follow a relationship of the form:

$$I(t) = I_O \exp\left[\frac{-t}{\tau}\right] \qquad \text{(Equation 2.2)}$$

Like the quantum yield, the fluorescence lifetime is determined by the relative rates of decay by radiative and non- radiative processes:

$$\tau = \frac{1}{k_{NR} + k_R} \qquad \text{(Equation 2.3)}$$

In practice, many samples will exhibit lifetime decays with multiple components. The different components might reflect the presence of more than one fluorescent species, or alternatively, differences in microenvironment of individual fluorophores. In such cases, a single exponential decay model may produce an erroneous fit to the data. The general solution is to fit a multiexponential decay model, in which the fluorescence signal is assumed to be a linear sum of single exponential decays with varying amplitudes (Equation 2.4).

$$I(t) = \sum_{i}^{N} \alpha_i \exp\left(\frac{-t}{\tau_i}\right) \qquad \text{(Equation 2.4)}$$

Assuming one can accurately determine the parameters τ_i and α_i, one can obtain a greater insight into the relative populations of different species and their environments. This has often been applied to FRET analysis of lifetime data, discussed in more detail in Chapter 3.

2.2.4. Photobleaching and photostability

A fluorophore's photostability relates to its ability to maintain its brightness when subjected to prolonged illumination by a light source. In general, any fluorescent species undergoing illumination will display a decrease in fluorescence intensity over time. This decrease results from irreversible degradation of the fluorophore into a non-emitting species, a process known as photobleaching. The photophysical mechanisms underlying this process are still not fully understood, and are believed to differ depending on the type of illumination used (pulsed or continuous wave, single photon or multiphoton, etc). One of the most likely mechanisms, at least in the case of single photon excitation, relates to reactions of the fluorophore with excited singlet state oxygen species. The latter may themselves be produced following the (non-radiative) transfer of energy from a fluorophore's excited (T_1) triplet state to the ground triplet state of oxygen (O_2) [2]. Other mechanisms also include the absorption of photons from an excited singlet (S_1) or triplet (T_1) state [3].

The rate at which photobleaching occurs is highly dependent on the illumination power. For most fluorophores, the rate of photobleaching increases linearly with laser power, up until a certain threshold. At higher excitation powers, the rate becomes non-linear, resulting in overall fewer photons being collected than would be the case if the laser power were reduced and a longer acquisition used [4] The compromise between efficient excitation and higher rates of photobleaching have important implications for high speed imaging, particularly in regard to live cell microscopy, discussed in Chapter 6.

It should be stressed that a fluorophore's photostability is not an absolute quantity; rather, it can only be defined in relation to other fluorophores' behaviour under the same conditions of illumination. It is therefore more usual to talk about a fluorophore's *relative photostability*. Although not an intrinsic property of a fluorophore in the same way as lifetime, quantum yield or emission spectrum, the relative photostability is nonetheless a very important consideration when choosing between different fluorophores.

2.3. Types of fluorophore

In theory, the term fluorophore can be applied to any molecule that will undergo radiative decay from an excited singlet state. In view of this, the number of naturally occurring fluorophores can be said to be quite vast. Nonetheless, in the large majority of these species, the energy gap between ground and excited state levels is large, limiting excitation and detection to the deep UV. Such species therefore have limited use in microscopy.

In certain molecules, sharing of electrons between individual atoms can result in a lowering of energy levels between ground and excited states, with the result that electron transitions occur within the visible region of the spectrum. (This follows directly from the particle in a box model in quantum mechanics, which predicts that the energy level spacing is inversely related to the size of the confined region). An example of this can be found in organic molecules containing systems of conjugated carbon bonds, where overlap between pi-orbitals of individual carbon atoms allows the electrons to become delocalised throughout. Most of the fluorophores we shall discuss will be based on this principle.

2.3.1. Fluorescent dyes

The origins of this class of fluorophore date back to the turn of the 19th century and the birth of histology. It was around this time that xanthene, the forerunner of many of today's most widely used histological dyes, was first synthesised. This compound, in common with those that have come after it is based upon a heterocyclic carbon ring system, composed of multiple conjugated double carbon bonds. The chemical structures for three of the most commonly used dyes in fluorescence microscopy are shown in Figure 2.2.

Targeting of organic dyes to specific proteins within the cell became possible in 1942 with the advent of immunofluorescence labelling. This method, first developed by Coons [5], enables a dye molecule to be conjugated to a specific antibody. Following permeabilisation of the membrane with a suitable detergent, the dye labelled antibody can be introduced into a cell where it will bind to its target protein, thus the fluorescence from the dye can be used to localise and contrast different proteins.

A number of dyes have also been developed to report on the local cellular environment, through changes in their intensity or emission spectra. Examples of these include the

membrane probe laurdan, used to report on lipid order in membranes [6], and calcium sensitive dyes Fura-2 and Indo-1 [7].

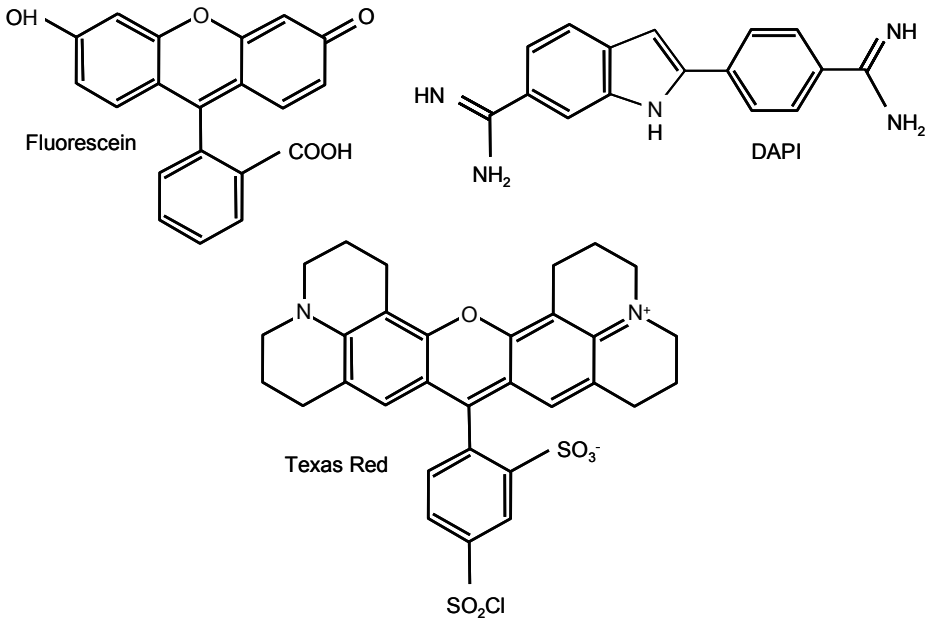


Figure 2.2: Chemical structure of chemical dyes commonly used in fluorescence microscopy. Systems of conjugated carbon bonds are evident throughout.

2.3.2. Green fluorescent protein (GFP)

The introduction of genetically expressible fluorophores, originating with green fluorescent protein (GFP) [8], has marked something of a revolution in fluorescence microscopy. These fluorophores have the immense advantage that they can be directly appended to other proteins' gene sequences. Once transfected into cells, the GFP moiety is transcribed along with the target protein, serving to highlight its localisation when fluorescence is imaged in the microscope. GFPs therefore provide unrivalled specificity for labelling different proteins. It is also possible to set up stable cell lines expressing a fluorescently labelled protein of interest.

The gene encoding GFP was first isolated and sequenced by Prasher [9] from the marine jellyfish species *Aequorea Victoria*. This was in turn used by Chalfie to purify the protein in bacteria [10]. In 1996, the molecular structure of GFP was published independently by two groups in *Science* and *Nature Biotechnology* respectively (Figure 2.3) [11, 12].

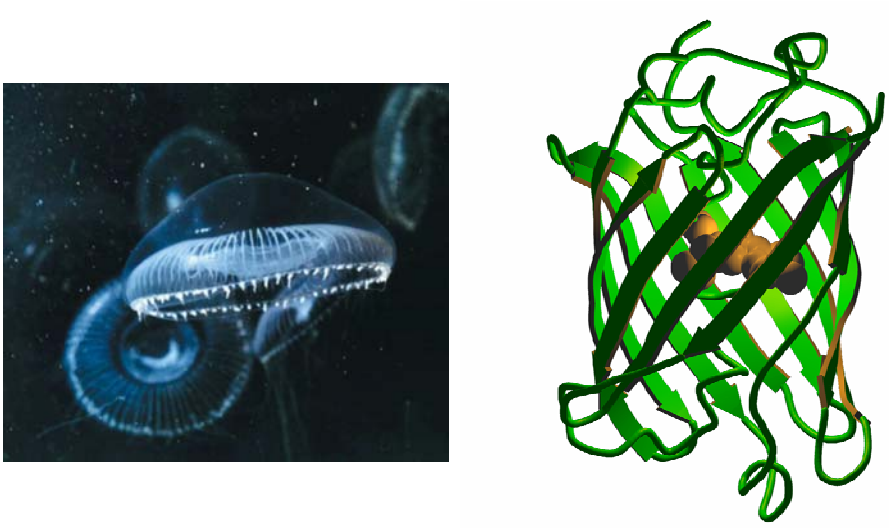


Figure 2.3: Left: Aequorea Victoria jellyfish: Right: Ribbon model of GFP structure. The protein has a barrel-like structure composed of 11 Beta sheets, through the centre of which runs an alpha-helix. The chromophore region of the molecule is contained inside the Beta-barrel, as shown here in orange.

Like the synthetic dyes above, GFP obtains its fluorescent properties from a system of delocalised charge, formed through sharing of electrons between amino acid residues within the tertiary structure of the protein. In the original GFP, a three residue system is involved, consisting of the three residues Serine 65, Tyrosine 66 and Glycine 67 [13]. Maturation of the chromophore occurs following nucleophilic attack on the carboxyl atom of serine 65 by the amide nitrogen in glycine 67, resulting in the formation of the imidazole ring shown in Figure 2.4. A further oxidation step is required to extend the region of electron delocalisation from the imidazole ring to the phenyl group of tyrosine 66, thus creating the fluorophore's absorption dipole.

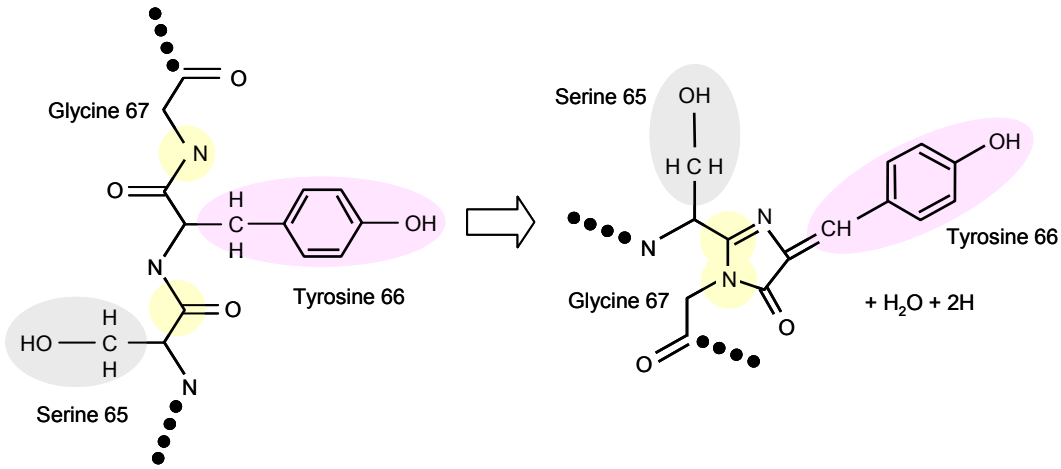


Figure 2.4: Chromophore maturation within GFP. For clarity, the alkyl groups of serine 65 and tyrosine 66 are shaded in grey and pink respectively (the third alkyl group, in glycine 67 constitutes a single hydrogen atom, hence is not shown). The yellow shaded areas show the two atoms involved in nucleophilic attack which leads to the formation of the imidazole ring shown on the right.

Since GFP was first cloned and expressed in mammalian cells, research has focussed on improving its fluorescence properties. In this respect, the work of R. Tsien and colleagues has been of particular significance. In addition to identifying the crystal sequence, this group was amongst the first to engineer new variants of GFP by mutation of specific amino acids within the chromophore region of the molecule [14, 15]. In 1995, the group published findings that substitution of the serine residue at position 65 of the primary amino acid sequence with Threonine resulted in a mutant with enhanced quantum yield and an absorption peak at 490 nm. A subsequent mutation of phenylalanine at position 64 to lysine resulted in a variant with better folding efficiency, which has come to be known as *enhanced* GFP (EGFP) [16]. Somewhat fortuitously, this protein's absorption peak coincided almost precisely with the 488 nm line of an Argon gas laser, whilst its emission, peaking at 507 nm coincided well with existing filter sets for fluorescein, thereby greatly facilitating its uptake as a probe in microscopy. In addition, the group were able to develop different spectral variants, most notably the cyan and yellow varieties ECFP and EYFP [17-19].

The isolation of a second, red emitting fluorescent protein from *Anthozoa* sea coral in 1999 marked a further milestone by expanding the range of available colours to longer wavelengths [20]. Mutagenesis performed on both this and GFP have since given rise to a large family of different colour fluorescent proteins [21, 22]. In addition to spectral diversity, it has also been possible to engineer mutants with enhanced fluorescent properties, including greater brightness [23, 24], photostability [25, 26] and pH resistance [27]. Elsewhere, proteins have been developed with specific features such as larger Stokes shifts [28] or different fluorescent lifetimes [29]. Other variants have also been reported that display interesting effects of photochromism [30] and photoactivation [31, 32], the latter having interesting applications in super-resolution microscopy [33, 34].

2.3.3. Quantum dots

Quantum dots are a relatively new addition to the spectrum of fluorophores available for biology. Formed from small nanocrystals of semiconductor materials, they are able to emit fluorescence through the recombination of electron-hole pairs created following absorption of incident light [35]. One particularly interesting feature of these fluorophores is the relationship between size and emission wavelength – one can tune the emission spectrum simply by changing the radius of the sphere. Quantum dots also have the advantage that they possess broad absorption spectra but narrow emission spectra, making it is possible to image multiple different colours when exciting the sample at a single wavelength.

Although quantum dots offer several attractive features, their uptake in fluorescence imaging has been held back by difficulties encountered when trying to target these fluorophores to specific sites or species within the cell. The approach most often used is to coat the outside of the sphere with a polymeric film and conjugate this to a series of biomolecules which will preferentially bind to the species of interest [36]. This can, however, result in a large and somewhat cumbersome molecule that may still only bind with limited specificity. Other concerns arise over the possibly toxic effects of cadmium compounds being released inside cells, although recent developments have seen the use of other, non-toxic materials being employed.

2.3.4. Endogenous fluorophores (autofluorescence)

The final class of fluorophores we shall discuss pertains to those naturally expressed within the system under study. The signal emitted from these species is known collectively as autofluorescence. Amongst the different sources of autofluorescence are the aromatic ring structures found in the amino acids tryptophan, phenylalanine and tyrosine, as well as larger proteins such as keratins and porphyrins, and the molecules nicotinamide adenine dinucleotide (NADH) and flavin adenine dinucleotide (FAD). Generally, these fluorophores do not contain the extensive regions of delocalisation found in dyes or visible fluorescent proteins and are only accessible by excitation in the UV and blue regions of the spectrum.

Imaging of autofluorescence signals is a highly active area of research, particularly in understanding cell metabolism [37, 38]. Nonetheless, for many experiments, auto-fluorescence may simply constitute a large (unwanted) background signal to the fluorescent species under study. This is true for example when imaging other, exogenous species, such as dyes or GFPs, particularly if short (<430 nm) excitation wavelengths are used.

2.4. Fluorescence Microscopy

It is clear that fluorescence can provide highly specific information on molecules and their surrounding environment. By implementing fluorescence measurements in a microscope, one can also observe the fluorophore's localisation. The combination of spatial and spectroscopic information afforded in such an approach is of particular value for biology, where one wishes to understand protein and molecular function within the structure of an intact cell or organism. Here, we look at some of the underlying principles of this technique.

2.5. Wide-field fluorescence microscopy

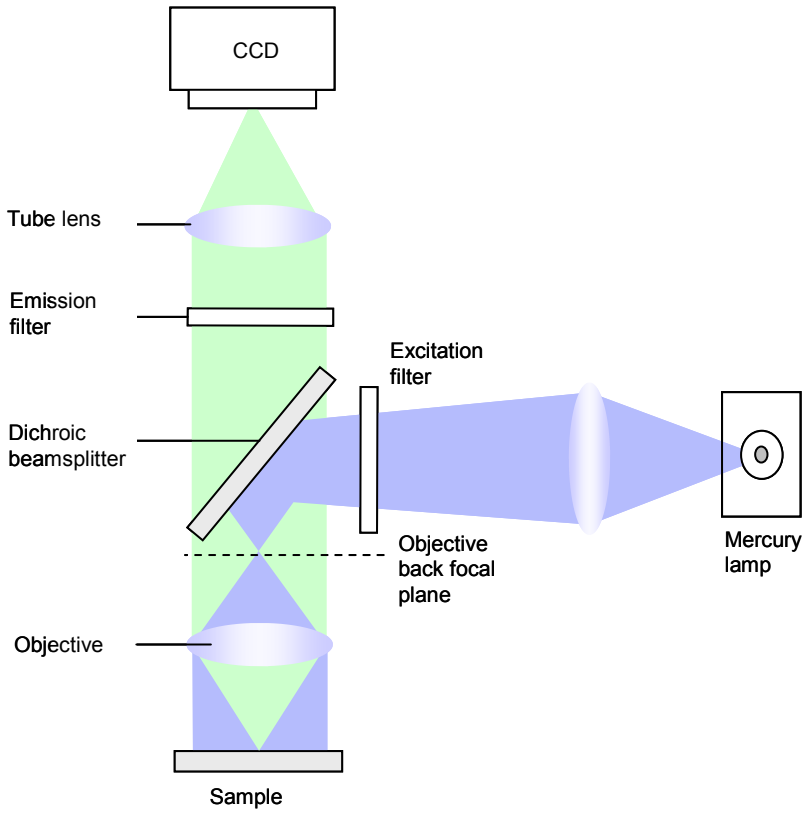


Figure 2.5: Wide-field fluorescence microscope. The sample is illuminated by an incoherent light source and the ensuing fluorescence imaged on to a wide-field detector. Use of a suitable dichroic and emission filter allows one to separate the excitation light from fluorescence with high signal to noise.

The simplest configuration of fluorescence microscope - the standard wide-field or epi-fluorescence microscope - is shown in Figure 2.5. An incoherent light source, traditionally a mercury or xenon arc-lamp is used to illuminate the sample (more modern microscopes may also use LEDs or laser illumination, with the spatial coherence of the laser beam destroyed

by passing the beam through a rotating diffuser wheel or a multimode fibre that is continuously agitated). A filter is used to select the wavelength band for excitation of the specific fluorophore. The filtered light is reflected by a dichroic mirror and focussed into the back aperture of the microscope (the method of Köhler illumination), thus ensuring uniform illumination in the sample plane. The ensuing fluorescence is imaged back through the objective where, owing to the longer wavelength from the Stokes shift, it is transmitted through the dichroic mirror. This is then imaged by the tube lens onto a wide-field detector such as a CCD camera. An additional emission filter is placed in the fluorescence path after the dichroic mirror to reject any scattered light and increase the signal to noise.

2.6. Optically sectioned fluorescence microscopy

In a conventional wide-field microscope, light detected on the camera emanates from all planes irradiated by the excitation source. The presence of light from outside of focus can produce glare in the image, which degrades the image quality and reduces spatial resolution. Optical sectioning confers the ability to discriminate against this background light and to acquire depth-resolved images of individual planes throughout the sample. This is of prime concern for quantitative imaging if one is to avoid spurious data from out of focus glare. Using an optically sectioning instrument, one is much better able to delineate different subcellular compartments within cells and so localise signaling events to these regions with greater accuracy. A further advantage is the ability to obtain stacks of images from different sample planes and so render 3 dimensional images of cells and tissue.

2.6.1. Confocal microscopy

The confocal microscope, originally described by Minsky [39] is the most common form of optically sectioning microscope. The principle of this microscope is shown in Figure 2.6. Here, a point source, most commonly a laser, is used to illuminate the sample. The beam is expanded to fill the back aperture of the objective, so that a diffraction limited spot is formed at the sample plane. Light from fluorophores excited in the focal volume is imaged back through the objective and onto a point detector, in front of which is placed a pinhole or aperture. The pinhole prevents light from planes outside of focus from reaching the detector, so that only fluorescence from the focal plane is collected.

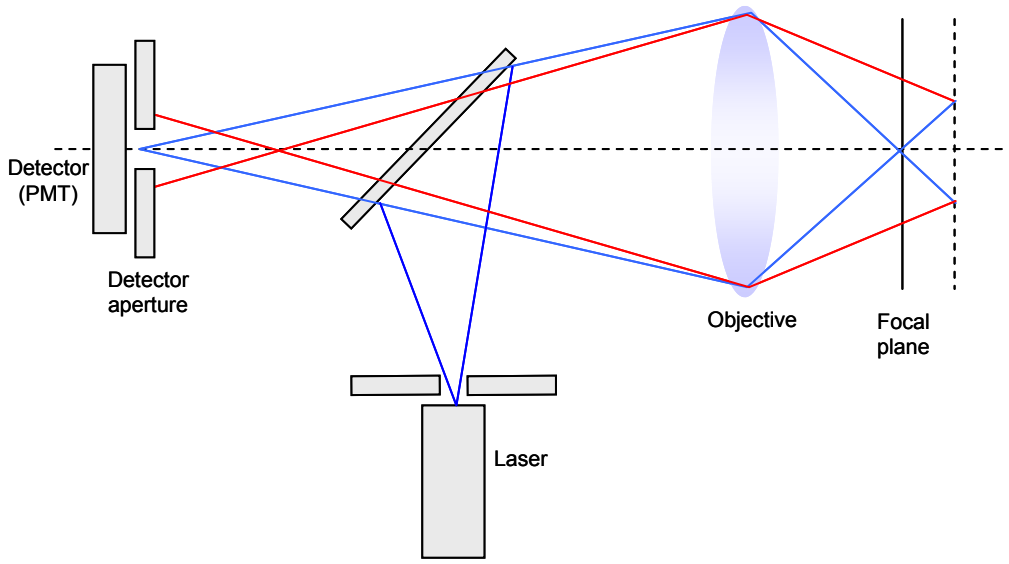


Figure 2.6: Principle of the confocal microscope: The sample is illuminated by a point source and fluorescence imaged onto a point detector (blue rays). An aperture placed in front of the detector excludes light from planes outside of focus reaching the detector (red rays). By scanning the beam across the sample one can build up an image of a single plane.

Since this is a point illumination / detection method, it is necessary to scan the sample in order to build up an image. Older microscopes achieved this by stage scanning, whilst more modern microscopes employ galvonometric mirrors that are used to scan the laser beam [40]. The intensities measured at each point are registered as current signals on the detector and compiled together with their scan coordinates to form an image. By shifting the focus of the objective, one can acquire an image of a different plane in the sample. Where multiple planes are imaged, the resultant stack can be rendered into a single 3D image [41].

2.6.2. Multiphoton microscopy

Multiphoton microscopy is an alternative means for achieving optically sectioned fluorescence images. This technique is based on simultaneous absorption of two photons, each one with energy half of that of the transition gap between ground and excited states in the fluorophore [42] (Figure 2.7).

The efficiency of multiphoton absorption scales non-linearly with the photon flux incident on the fluorophore. Thus, where one focuses light through an objective, the rate of two-photon absorption at focus will be significantly higher than elsewhere throughout the focal volume. Efficient excitation will therefore only occur in this plane, with the result that any detected fluorescence must emanate from this one plane alone and is intrinsically sectioned.

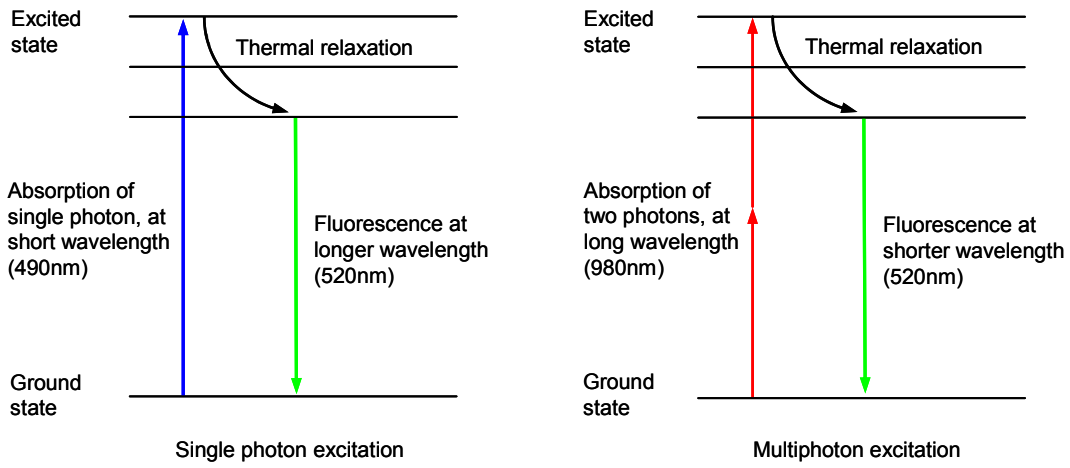


Figure 2.7: Jablonski diagrams for single photon and two-photon excitation. In the latter, two photons combine in a single absorption event, provided the incident photon flux is high enough.

For efficient multiphoton excitation one requires a light source capable of producing the desired flux at the sample, but with average power levels appropriate for biological samples. This is usually achieved by taking advantage of the high peak powers produced by an ultrafast (femtosecond) pulsed laser, and combining this with a high NA objective. As with the confocal microscope, the single point excitation again requires that the beam is scanned across the sample to build up an image.

2.6.3. Other optical sectioning techniques

Due to the need for scanning, confocal and multiphoton microscopes generally require longer acquisition times than wide-field microscopes. This can be an issue in samples with high motility, where motion artefacts can occur if the sample moves during the course of individual frame acquisitions. To offset this problem, several imaging methods have been developed which maintain the benefits of optical sectioning without sacrificing imaging speed. The first of these, Nipkow disc or spinning disc microscopy involves exciting the sample at multiple spots in parallel. This is achieved by first expanding the excitation source and passing it through a disc containing an array of pinholes, to form multiple beams which probe different points on the sample [43, 44]. The fluorescence from each point is imaged back through the same pinhole. One can conceive of this as a series of confocal microscopes acting in parallel. As the disc rotates, the beams' positions change, so that during the course of a single rotation the entire area of the sample is swept out.

High speed optically sectioned microscopy can also be achieved in line scanning microscopes, in which a line of illumination is used to scan the sample, rather than a single

spot, and the fluorescence imaged back through a slit to a detector [45]. This parallel pixel acquisition allows one to scan the sample at much higher frame rates, although the axial resolution is slightly compromised owing to the extended size of the slit.

A similar concept to the Nipkow disc has also been applied to multiphoton excitation. Here, the excitation beam is again split into multiple beams that can scan the sample area within a much smaller space of time. The fluorescence can be imaged either onto a wide-field detector [46], or as has recently been demonstrated, onto an array of PMTs [47]. The need for a sufficiently high intensity at each focus for efficient multiphoton excitation limits the number of separate beams to below that available in the Nipkow disc microscope. This method does, however, offer the advantage of non-descanned detection in which the fluorescence can be imaged directly onto the detector without the need for any pinholes.

In addition to these scanning techniques, several other methods have been developed which enable the possibility of optical sectioning in a wide-field set up. These methods generally rely on image reconstruction following collection of a sequence of wide-field images. In structured illumination microscopy, the sample is illuminated through a grid to provide a spatial modulation of the image. Translating the grid enables the user to collect a series of images with a phase shift in the modulation, the higher frequency components of which are resolvable only within the focal plane. The use of a suitable computer algorithm then allows one to recover the signal from the plane containing this modulation, and so reject the light from outside of focus [48, 49]. Deconvolution, an alternative wide-field method, involves the acquisition of an entire image stack, which is then post processed and deconvolved with a pre-measured 3D point spread function to return a series of depth resolved images through the sample [50].

2.7. Fluorescence imaging techniques

2.7.1. Intensity imaging

The simplest and most commonly used technique in fluorescence microscopy is intensity imaging, in which the absolute number of photons emitted from each point on the sample is recorded on the detector in order to build up a map of fluorophore concentration. More sophisticated techniques, including single molecule imaging, rely on the sensitivity of fluorescence intensity measurements to report on the localisation of individual molecules,

which when imaged at high frame rates can be used to observe the diffusion rates and trajectories of these molecules throughout the cell [51, 52].

2.7.2. Spectral imaging and ratiometric imaging

In spectral imaging, the fluorescence is separated into different emission wavelength bands, either by a dispersive mechanism such as a prism, or use of multiple emission filters. By measuring the intensity of light in different channels, it is possible to study the colocalisation of different fluorescent species whose emission spectra are distinct from one another (Figure 2.8). This technique has become increasingly popular in biology due to the ever-increasing number of different colour fluorescent probes and new methods for labelling them to specific proteins or organelles [53].

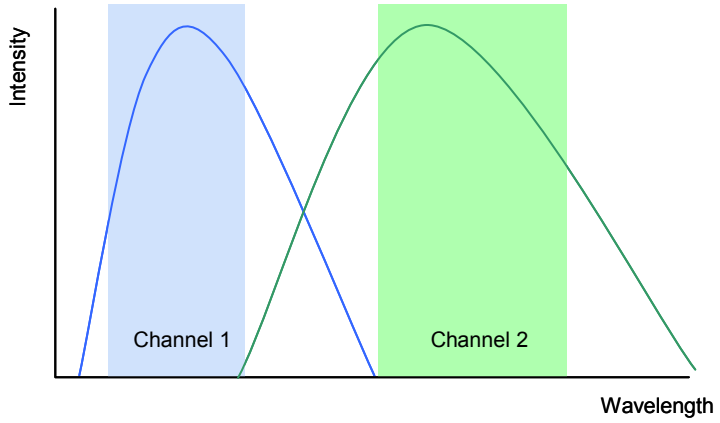


Figure 2.8: Spectral imaging. By measuring the intensity of fluorescence emission in different spectral channels, one can discriminate the signal from fluorophores with different emission spectra.

An extension of spectral imaging is ratiometric imaging, in which the signal detected in different emission channels is ratioed to provide quantitative measurements of a fluorescent probe's activity. This is particularly useful when studying probes that display environmental contrast i.e. changes in emission spectra due to the surrounding environment (examples might be ion concentration [54], membrane voltage potential [55], or membrane lipid order [56]). Spectral imaging can also be used to 'unmix' fluorescence signals emanating from different species with similar or overlapping emission spectra [57, 58]. This can be further extended to hyperspectral imaging in which the entire emission spectrum is recorded for every pixel in the image, with accompanying increase in sensitivity to spectral changes [59, 60].

2.7.3. Fluorescence anisotropy / polarisation resolved imaging

The polarisation of fluorescence emission provides a further parameter for imaging a fluorophore's environment [1]. When polarised light is used to illuminate a sample, only those molecules whose absorption dipoles have a component aligned with the incident field will be excited to a higher energy state. During the excited state lifetime, the emission dipole may shift to a different orientation, either through the molecule's natural rotation, or its interaction with other molecules in the environment. The intensity of fluorescence resolved parallel ($I_{\parallel}$) and perpendicular ($I_{\perp}$) to the excitation polarisation can be used to define the anisotropy parameter *r*:

$$r = \frac{I_{\parallel} - I_{\perp}}{I_{\parallel} + 2 I_{\perp}} \qquad \text{(Equation 2.5)}$$

The anisotropy parameter can provide information on dipole orientation and the rotational dynamics of the molecule [61]. In addition, anisotropy measurements can report on other effects such as FRET [62], which act to depolarise the emission through subsequent interaction with other molecule dipoles during the course of the excited state lifetime.

2.7.4. Fluorescence lifetime imaging

As mentioned in section 2.2.3, measurements of a fluorophore's mean excited state lifetime can reveal a significant amount of information, not only on the type of fluorophore under consideration but also its interactions with its environment. This might include quenching mechanisms, changes in solvent polarity or ion concentration. A key area of interest in the technique is its application to FRET experiments, for which lifetime measurements can often provide a more robust solution than other, spectrally resolved techniques.

2.8. Instrumentation for fluorescence lifetime imaging

Measurements of fluorescence lifetime can be separated into two categories: time domain and frequency domain. In the time domain, the sample is excited by a short laser pulse, and the intensity of the fluorescence sampled at intervals thereafter in order to recover the fluorescence decay profile. In the frequency domain, the sample is excited by an intensity modulated light source, resulting in a fluorescence emission which is similarly modulated. The lifetime is then computed from the relative phase shift or change in modulation depth

between these two waveforms. The main methods for measuring fluorescence lifetimes, and their implementation in microscopy are discussed in more detail below.

2.8.1. Time correlated single photon counting

In the past decade, time correlated single photon counting (TCSPC) has become the pre-eminent technique for fluorescence lifetime imaging [63]. This is a time domain method that measures the arrival times of individual fluorescence photons following pulsed excitation of the sample. The arrival times are then stored in memory and used to build up a histogram that reflects the fluorescence decay. As a point detection technique, TCSPC is readily implemented in point scanning microscopes such as confocal and multiphoton systems.

The principle of time correlated single photon counting can be understood with reference to Figure 2.9 below. The sample is first excited by a pulse from a mode-locked laser. The excitation pulse is also registered on a photodetector located inside the laser cavity or in the light path before the microscope. The signal from the photodetector is used to trigger the time to amplitude converter (TAC) - an electronic component that functions as a delay timer. In response to the trigger signal, the TAC begins charging a capacitor, building a voltage ramp that increases linearly with time. This continues until a fluorescence photon is detected by the photomultiplier tube in the microscope's emission channel. At this point, a second signal is sent to the TAC, causing it to stop and discharge an electronic pulse whose amplitude is proportional to the time between the excitation pulse and the fluorescence emission. The voltage is sampled by an analogue-to-digital-converter (ADC), which converts it into a time delay and then stores this in a memory file. The process is repeated over the course of many hundreds of photons, during which time a histogram of arrival times is built up. The histogram can then be used to determine the fluorescence lifetime.

As a technique, time correlated single photon counting offers a number of important advantages. These include the high spatial resolution afforded by the confocal microscope, the signal / noise benefits of single photon detection which allows the noise to be accurately modelled when fitting the decays and a high photon economy, since all the photons detected contribute to the measurement. The main drawback to this approach is its speed. This can be understood when one considers that in order to maintain accuracy, it is important that no more than one fluorescence photon be detected for each laser excitation pulse. Following the detection of a photon, there is a characteristic dead time in which the TAC discharges and resets itself to zero. Any additional photons arriving during this time are not recorded and so

do not contribute to the lifetime histogram. Thus, in the event that multiple photons are emitted during each period, only the first one to arrive will be detected, while the information encoded in the later arrival of the additional photons will be lost. This has the effect of biasing the measured lifetimes to shorter values, an effect known as "pulse pile up." To ensure this does not happen, the maximum count rate must be kept below a fraction of the laser repetition rate.

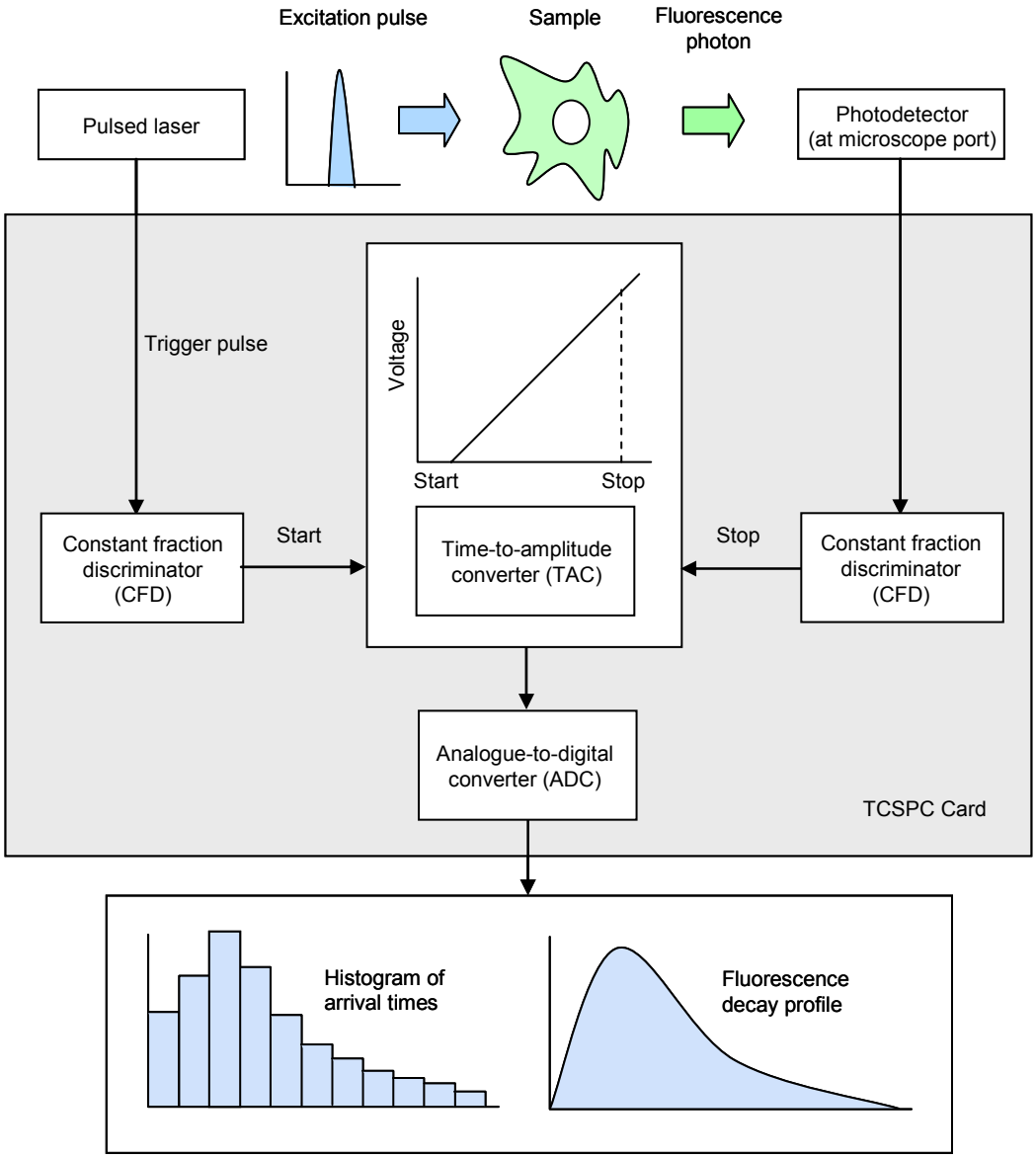


Figure 2.9: Instrumental components for time correlated single photon counting (TCSPC) FLIM. The arrival times of individual photons are measured with respect to the excitation pulse and the resultant histogram used to extract the fluorescence decay and lifetime.

In order to extract the lifetime for each pixel in the image, the number of photons in each temporal window can be fit to an exponential decay model, as described in section 2.2.3.

This is typically done by using a non-linear least squares analysis, in which one varies the lifetime and intensity parameters in order to minimise the goodness of fit parameter χ^2 (Equation 2.6):

$$\chi^2 = \sum_{i=1}^{N} \frac{(y_i - f(x_i))^2}{\sigma_{yi}^2} \qquad \text{(Equation 2.6)}$$

Here, i defines the temporal window under consideration, y_i is the number of photons detected in that window, σ_{yi} is the standard deviation on the measured number of photons (for single photon counting the square root of the photon number) and $f(x)$ is the form of the function used to model the decay.

2.8.2. Wide-field time domain fluorescence lifetime imaging

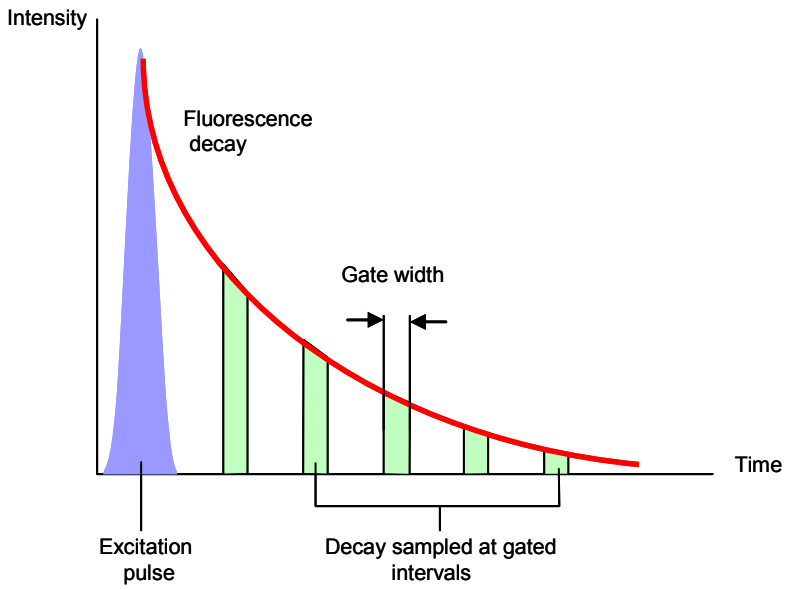


Figure 2.10: Time-gated detection of fluorescence decays. By varying the delay between the excitation pulse signal and the gate on the intensifier, one is able to collect intensity images at different times during the fluorescence decay. This series of images can then be used to compute the lifetime for each pixel in the image series.

Fluorescence lifetime imaging can also be implemented in wide-field microscopy. In the time domain, the lifetime in each pixel is resolved by collecting images of the fluorescence intensity at different points during the fluorescence decay. This is usually achieved by placing an image intensifier in front of the camera to act as a form of shutter [64 - 66].

The period in which the intensifier gain is on defines a gate – a period in which fluorescence photons arriving at the intensifier are amplified and the ensuing signal exposed on the

camera. Photons which arrive outside of this period are not amplified and are effectively shuttered. By introducing a delay between the trigger signal and the intensifier, it is possible to shift the position of the gate in time, allowing one to collect a series of intensity images from different points in the fluorescence decay (Figure 2.10). The lifetimes can then be calculated by fitting each pixel in the image series to an exponential decay, using the same least squares analysis described above in section 2.8.1.

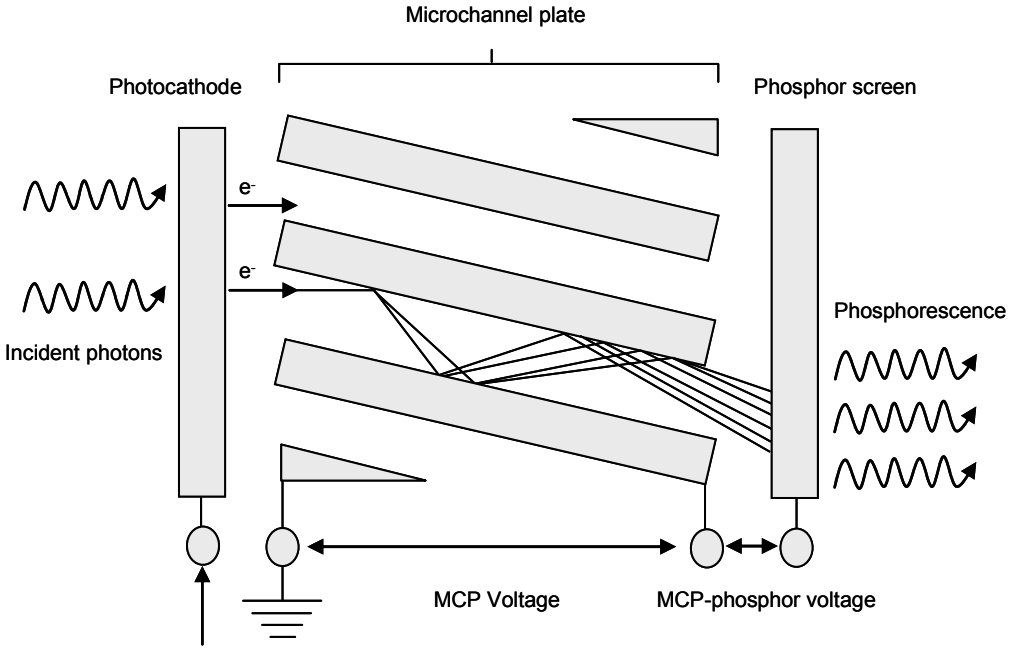


Figure 2.11: Gated optical intensifier (GOI). This figure shows the 3 main components - the photocathode, microchannel plate (MCP) and phosphor screen.

Figure 2.11 shows the main components of the image intensifier. On arrival at the photocathode, photons emitted from the sample undergo photoconversion to electrons. In response to the synchronisation pulse from the laser, a negative voltage is applied to the photocathode causing electrons to accelerate to the front of the MCP. The microchannel plate itself comprises an array of small (~10 μm) diameter glass tubes, the inner surfaces of which are coated in an electron emission film. A potential difference is applied across the MCP which in turn accelerates the electrons through the microchannels towards the phosphor screen. During this time the electronic signal is amplified by collisional excitation of secondary electrons from the walls of each channel. This amplified electron signal is converted back to an optical signal following collisions of the electrons with the phosphor screen. The ensuing phosphorescence can then be imaged by relay lens onto the camera.

Gating is produced by controlling the voltage applied to the photocathode. Only when this voltage is applied will electrons be accelerated to the MCP and so result in emission of

phosphorescence, which will then be imaged onto the CCD. The potential difference across the MCP is usually adjusted at the start of the FLIM acquisition so that the signal in the first time gate fills the dynamic range of the CCD over the course of the camera's integration time. This then remains constant throughout the rest of the measurement.

2.8.3. Wide-field frequency domain fluorescence lifetime imaging

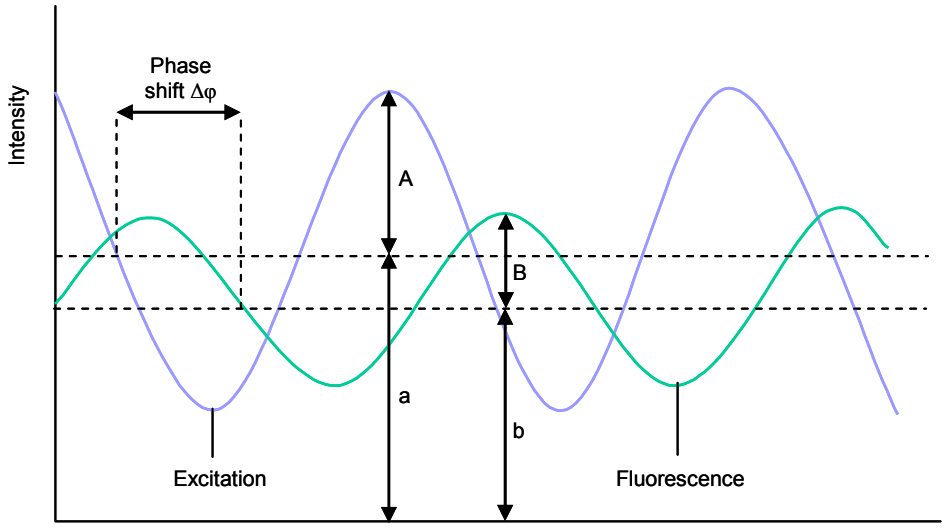


Figure 2.12: Principle of frequency domain lifetime analysis. An intensity modulated light source is used to excite the sample, and the lifetime calculated by measuring the phase shift or change in modulation depth of the fluorescence intensity.

A similar set up to that described in 2.8.2 can be used in the frequency domain. In this case the laser source is not pulsed but modulated sinusoidally (typically modulation frequencies are in the MHz range). This results in a fluorescence signal which is modulated at the same frequency, but with a relative phase shift owing to the delay between excitation and fluorescence emission (Figure 2.12). The phase shift is recovered by modulating the intensifier gain at the source frequency, and varying the phase separation between the two. A series of images is collected at different phase separations, and the relative intensity in each image used to reconstruct the fluorescence waveform. Both the phase shift and change in modulation depth can be used to calculate the lifetimes, in accordance with Equation 2.7 [67, 68].

$$\tau_{\varphi} = \frac{\tan(\Delta\varphi)}{\omega} \qquad \tau_{m} = \sqrt{\frac{1-m^2}{m^2\omega^2}} \qquad m = \frac{B.a}{A.b} \qquad \text{(Equation 2.7)}$$

where τ_{φ} and τ_{m} are the lifetimes recovered from measurement of the phase shift and change in modulation depth, respectively and ω is the frequency of the source modulation.

2.9. Conclusion

This chapter has introduced the core concepts of fluorescence and its application in microscopy. As a technique, fluorescence microscopy offers many advantages including the ability to label and detect specific molecular species and to report on differences in the local fluorophore environment. From a biological standpoint, the development of new fluorophores, together with high resolution imaging techniques (confocal, multiphoton) have made fluorescence a particularly powerful means for reporting on cell events and function.

In what follows, we discuss some of the more advanced uses of this technique, in particular, its application to Förster Resonance Energy Transfer, and how this can be used to disseminate interactions between proteins at the molecular scale.

Chapter 3: Förster Resonance Energy Transfer (FRET)

3.0. Chapter overview

This chapter introduces Förster Resonance Energy Transfer as a means for probing protein interactions and conformational changes in cells. The conditions under which FRET will occur are discussed, as are the different methods for its detection. Examples are given of different fluorescent labelling strategies for FRET measurements. Finally, results are shown from experiments comparing the FRET efficiencies of different pairs of fluorescent proteins.

3.1. Förster Resonance Energy Transfer (FRET)

Förster Resonance Energy Transfer (FRET) describes the non-radiative transfer of energy from the excited state of a fluorophore to a second, spatially colocalised chromophore. These two species are referred to as the donor and acceptor, respectively. Energy transfer occurs through long range coupling of the donor's emission dipole with the absorption dipole of the acceptor. For FRET to take place, the following conditions must be satisfied [69]:

- The donor emission spectrum must overlap the acceptor absorption spectrum.
- The transition dipoles of the donor and acceptor must be orientated favourably with one another (energy transfer will not occur if they are orthogonal to one another).
- The two species must lie within close enough proximity of one another.

In what follows, we provide an outline of the theory behind this form of energy transfer, and its application to microscopy.

3.1.1. Theory of non-radiative energy transfer

The original theory of non-resonant energy transfer dates back to 1927, in the work of Jean Baptiste Perrin [70]. Perrin was hoping to explain the curious observation that the fluorescence emission from fluorophores in solution became highly depolarised with respect to the excitation, once the concentration of fluorophores exceeded a certain value. This effect was seen to occur when the mean separation between molecules fell below 10 nm. Since this distance was larger than both the molecular diameter and the distance a molecule might diffuse during its excited state lifetime, the depolarised light signal could not be explained by

collisions between molecules. Rotational effects too could be ruled out, as the same observation was made in highly viscous solutions in which the molecules would have limited rotational mobility. Therefore, some alternative mechanism must be responsible.

Perrin reasoned that the excited molecules (whose dipole transition moments were aligned parallel with the excitation source polarisation) might be transferring their excited state energy to other molecules whose transition dipoles had a greater perpendicular component relative to the incident field. The observed fluorescence would then emanate from these secondary excited molecules, hence the depolarised emission. Perrin went on to conjecture that this transfer of energy could occur through the long range coupling of the molecules' electron dipole moments - a simple analogy would be the mechanical exchange of energy between two coupled pendulums.

Although Perrin's theory could explain the origin of the fluorescence depolarisation, it predicted the effect would occur at much lower concentrations than that seen experimentally, with energy transfer occurring across distances of several hundred nanometers. In 1948, Theodore Förster published a refined theory that could be used to make more accurate predictions [71]. The key result of Förster's work was an expression for the rate of non-radiative energy transfer k_{FRET}:

$$k_{FRET} = \frac{1}{\tau_D}\left(\frac{R_O}{R}\right)^6 \qquad \text{(Equation 3.0)}$$

where τ_D is the fluorescence lifetime of the donor in the absence of FRET, R is the donor-acceptor separation and R_O is the distance at which the efficiency of energy transfer is 50% (the distance at which half the donor excited state energy is transferred to the acceptor):

$$R_O^6 = c_O \kappa^2 J n^{-4} \eta \qquad \text{(Equation 3.1)}$$

Here, c_O is a constant, which takes into account the respective size of the donor and acceptor dipole moments and κ^2 is an orientation factor, which describes the relative alignment between the two. The constant η is the donor quantum yield and n is the refractive index of the medium. J is a parameter that defines the extent of overlap between the donor emission spectrum and the acceptor absorption spectrum:

$$J = 10^{17} \int q_{d,\lambda}\, \varepsilon_{d,\lambda}\, \lambda^4\, d\lambda \qquad \text{(Equation 3.2)}$$

where $q_{d,\lambda}$ and $\varepsilon_{d,\lambda}$ are the normalised donor emission and acceptor absorption spectra, respectively. This can be seen understood with reference to Figure 3.0 below.

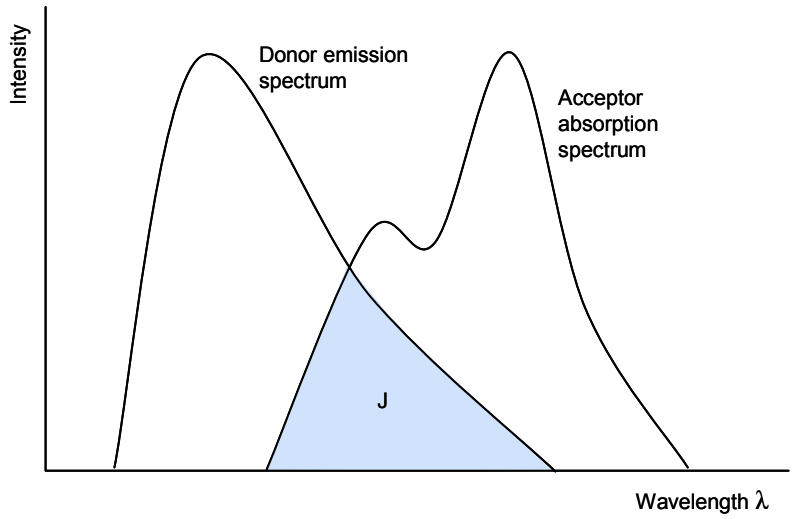


Figure 3.0: The overlap integral J(λ) in Förster's equation defines the extent of overlap between the donor emission spectrum and the acceptor absorption spectrum.

Using the equation for the rate of energy transfer, Förster was able to write down an expression for the FRET efficiency *E,* defined as:

$$E\,(\%) = \frac{\textit{Number of quanta transferred from donor to acceptor}}{\textit{Number of quanta absorbed by donor}} \qquad \text{(Equation 3.3)}$$

This can be related to the rates of decay from the excited states by the different processes:

$$E = \frac{k_{FRET}}{k_{FRET} + k_R + k_{NR}} \qquad \text{(Equation 3.4)}$$

Note that here, k_{NR} relates to non-radiative processes other than resonant energy transfer. Recalling Equation 2.3, which relates the donor fluorescence lifetime to the rates of decay by radiative and non-radiative processes k_R and k_{NR}, we can express the efficiency thus:

$$E = \frac{k_{FRET}}{k_{FRET} + \frac{1}{\tau_D}} = \frac{\frac{1}{\tau_D}\left(\frac{R_O}{R}\right)^6}{\frac{1}{\tau_D}\left(\frac{R_O}{R}\right)^6 + \frac{1}{\tau_D}} = \frac{R_O{}^6}{R_O{}^6 + R^6} \qquad \text{(Equation 3.5)}$$

Figure 3.1 below shows how the efficiency varies with the donor – acceptor separation for an arbitrary value of R_O:

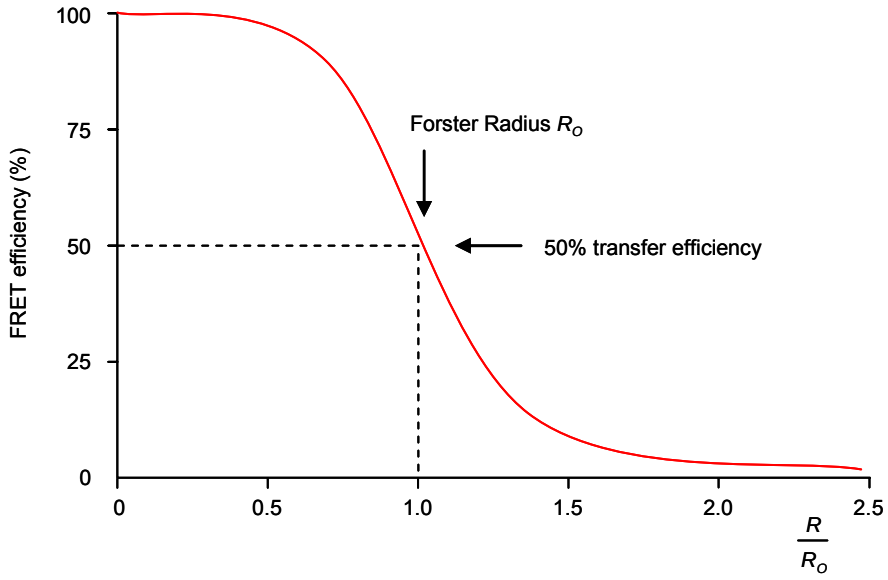


Figure 3.1: FRET efficiency as a function of donor-acceptor separation R for an arbitrary value of R_O

One can see from Figure 3.1 above that there is a sharp drop in FRET efficiency as R approaches and exceeds R_O. This distance dependence is key to understanding the utility of FRET for mapping molecular interactions in cells. By labelling two proteins with a compatible donor and acceptor pair, and detecting FRET between them, one can deduce their proximity to within a few nanometers. FRET therefore allows one to study the spatial colocalisation of species on a scale far smaller than that which can be resolved by the microscope alone.

3.2. Use of FRET in biology

The information afforded by FRET measurements is particularly valuable to biology since it is one of the only methods by which molecular interactions can be verified in the context of a live cell. This is generally applied in one of two ways: intermolecular FRET or intramolecular FRET.

3.2.1. Intramolecular FRET: Imaging conformational changes

In intramolecular FRET experiments the donor and acceptor species are located on the same molecule. The molecule itself may be a large protein, in which case changes in tertiary structure associated with protein phosphorylation / dephosphorylation may shift the relative orientation and / or distance separation of the donor and acceptor, causing a rise or fall in

FRET efficiency. Thus, one can correlate changes in FRET efficiency with these conformational changes. This principle is shown in Figure 3.2.

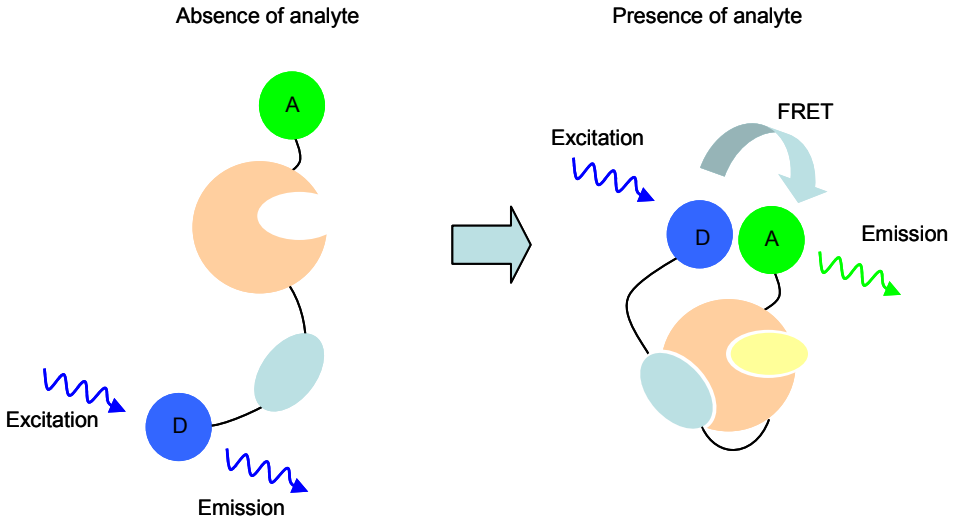


Figure 3.2: Intramolecular FRET. Labelling a protein or molecule with both donor and acceptor allows one to image protein activation or ligand binding by reading out FRET between the two fluorophores.

In order to optimise the dynamic range in the FRET signal between different conformational states, it can be useful to place the probes at strategic points in the molecule, where the relative separation is likely to increase to the greatest extent during a conformational change. This has to be balanced against the need to avoid disrupting the protein's innate folding mechanism, which could be highly sensitive to insertions, especially where enzyme function is concerned. For this reason, it is usually the case that the donor and acceptor are placed at opposite ends of the protein. Although this may limit the dynamic range, it is usually the best approach to preserve the protein's function.

Aside from measuring changes in conformation, intramolecular FRET has also been used to monitor a variety of cellular processes through use of specifically designed FRET probes. Such probes, or biosensors, are formed from two or more sub-domains of larger proteins that are known to bind to one another with high affinity. The most prolific of these are the calcium sensors, developed from a calmodulin calcium binding domain and the myosin light chain kinase, which are linked to the fluorophores CFP and YFP [72]. On binding to calcium, the calmodulin domain will bind to myosin kinase, bringing the CFP and YFP probes within shorter distance of one another, and producing a high degree of sensitised emission. Such calcium probes have been through several generations of evolution, the most recent of which (YCAM 3.6) is now commercially available from *Invitrogen.* The number of

probes based on this principle continues to expand, being used to report on, amongst other things, small GTP-ase activity, membrane voltage, and the cleavage of various membrane phospholipids [73-77].

3.2.2. Intermolecular FRET: Imaging protein-protein interactions

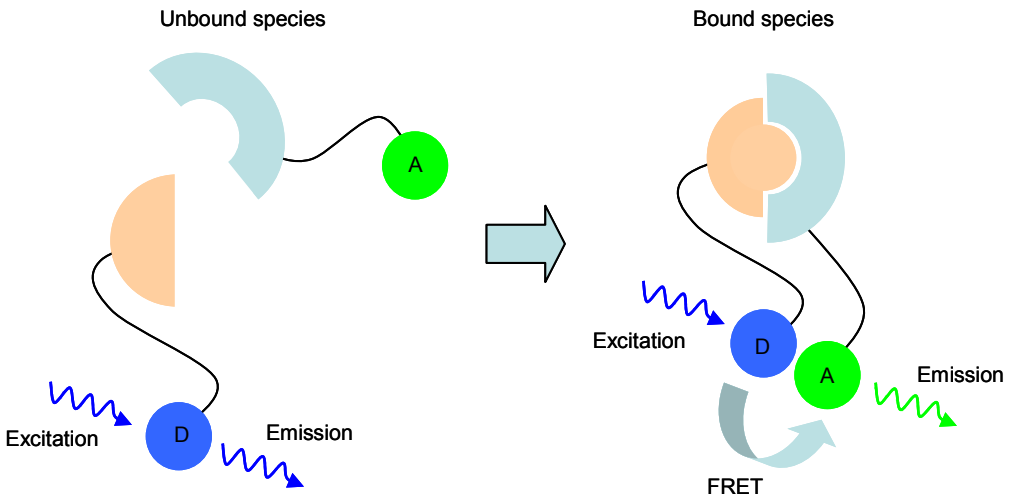


Figure 3.3: Intermolecular FRET. Labelling of separate species with donor and acceptor allows one to image their interactions by reading out the FRET signal between the two fluorophores.

Intermolecular FRET refers to measurements where the donor and acceptor are used to label different molecules. Examples of where this approach might be used include monitoring protein-protein interactions [78-80], or binding of an enzyme to a substrate [81] (Figure 3.3).

3.3. Imaging FRET in the microscope

3.3.1. Intensity based measurements

Changes in donor fluorescence intensity provide the simplest measure of FRET. The transfer of excited state energy from the donor to the acceptor results in a fall in overall donor emission, which can be quantified. This is usually achieved by comparing images of cells expressing the donor and acceptor prior to and after photobleaching of the acceptor [82]. The FRET efficiency at any pixel can then be calculated thus:

$$E = 1 - \frac{F_{DA}}{F_D} \qquad \text{(Equation 3.6)}$$

where F_{DA} and F_D are the donor fluorescence prior to and after photobleaching the acceptor. Since this method requires an extended period of illumination in order to bleach the acceptor, it is usually confined to fixed cells.

3.3.2. Spectral ratiometric measurements

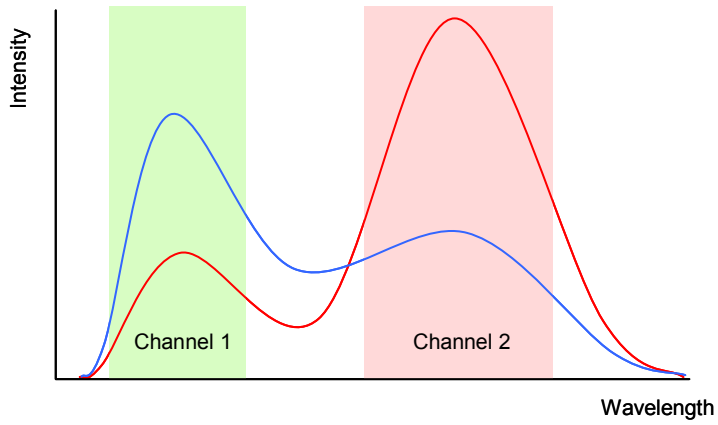


Figure 3.4: Spectral ratiometric FRET analysis: FRET can be detected by a relative increase in fluorescence at longer wavelengths (red spectrum), due to sensitised emission from the acceptor.

Spectral ratiometric imaging is an alternative method for imaging FRET. In addition to quenching of the donor's fluorescence emission, FRET will also result in an increased fluorescence signal at longer wavelengths, following the radiative (sensitised) emission of acceptors excited during the energy transfer process (Figure 3.4). By measuring the acceptor and donor emission intensities in two spectrally resolved wavelength channels and ratioing them, one can detect changes in the emission signature if and when FRET occurs.

Although more robust than measurements of donor fluorescence intensity alone, ratiometric imaging can be complicated by various sources of cross-talk or spectral 'bleed-through'. These include the detection of donor fluorescence in the second (acceptor) wavelength channel and acceptor fluorescence emanating from direct excitation at the donor wavelength. If the spectral overlap between donor emission and acceptor emission is particularly large, acceptor fluorescence may also be detected in the donor channel. Together, these constitute a noise background above which it may be difficult to distinguish genuine changes in emission ratio arising from FRET. Several algorithms have been proposed for quantifying the extent of cross-talk in any given experiment, and then subtracting this from the final FRET signal [83-86]. This can make the analysis somewhat more involved, and necessitates performing calibration experiments with samples of donor or acceptor alone beforehand.

A further caveat to this approach is that it is mainly restricted to studies of intramolecular FRET, in which the local stoichiometries of donor and acceptor are certain to be equal. In the case of intermolecular FRET, where the local concentration of donors and acceptors will vary on a pixel-pixel basis, it can be very hard to distinguish changes in emission ratio due to FRET, from simple diffusion of donors and acceptors into or out of the focal volume.

3.3.3. Fluorescence lifetime measurements

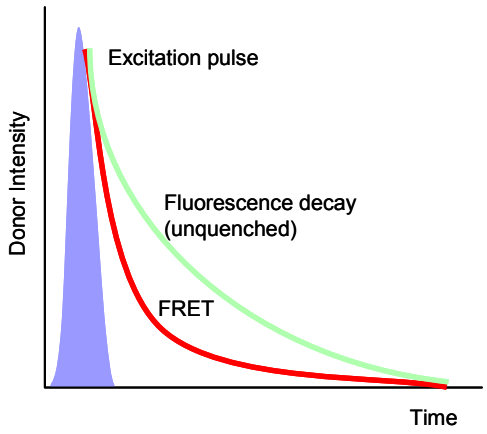


Figure 3.5: Fluorescence lifetime decays in the presence (red) and absence (green) of FRET. If FRET occurs, the donor fluorescence is quenched and the molecule on average spends less time in the excited state. This means that proportionally more photons are emitted at earlier time points.

In fluorescence lifetime imaging (FLIM-FRET), energy transfer can be detected through an apparent shortening of the donor's fluorescence lifetime. Non-radiative energy transfer provides an additional path of relaxation back to the donor's ground state, hence the donor will, on average, spend less time in an excited state if and when FRET occurs (Figure 3.5). The change in fluorescence lifetime resulting from FRET can be obtained from Equation 3.7:

$$\tau_D = \frac{1}{k_R + k_{NR}} \qquad \tau_{DA} = \frac{1}{k_{FRET} + k_R + k_{NR}} \qquad \text{(Equation 3.7)}$$

where τ_D is the fluorescence lifetime of the donor in the absence of the acceptor (c.f. Equation 2.3) and τ_{DA} is the lifetime in the presence of FRET. One can see from this that the additional rate constant k_{FRET} in the denominator will be reflected in a smaller value of τ_{DA} compared to $\tau_{D.}$

From Equation 3.4, it follows that the FRET efficiency can be written:

$$E = 1 - \frac{\tau_{DA}}{\tau_D} \qquad \text{(Equation 3.8)}$$

Fluorescence lifetime imaging is arguably the most robust method for imaging FRET. Unlike intensity based approaches such as those discussed above, the fluorescence lifetime is largely independent of concentration. Lifetime measurements are therefore not complicated by issues of different donor and acceptor stoichiometries [87]. Thus, FLIM-FRET can be applied to both intra- and intermolecular FRET studies. Since only the donor fluorescence is measured, artefacts arising from donor bleed-through or direct acceptor excitation are no longer an issue (although the latter may still diminish the actual FRET signal by pre-populating the excited state of the acceptors).

This technique is also the most quantitative method of imaging FRET. In ensemble measurements where one is imaging a population of donor and acceptors (as opposed to single molecule imaging), one measures FRET as a shift in the equilibrium between the populations of bound and unbound species. The measured FRET signal, which may be the lifetime decay or ratio of intensities in different spectral channels, is therefore a product of the rate of energy transfer between individual donor/acceptor pairs and the proportion of donor and acceptor labelled species that are in complex at any one time. Temporally resolved measurements can in theory uncouple these two factors by assigning them different parameters in a bi-exponential model of the fluorescence decay (Equation 3.9).

$$I(t) = \underbrace{\alpha_1 \exp\left[\frac{-t}{\tau_1}\right]}_{\text{Bound species}} + \underbrace{\alpha_2 \exp\left[\frac{-t}{\tau_2}\right]}_{\text{Unbound species}} \qquad \text{(Equation 3.9)}$$

In the above equation, the pre-exponential factors α_1 and α_2 represent the fractional number of bound and unbound species for the pixel in question, whilst the two values τ_1 and τ_2 are the lifetimes of the fluorophore in the presence and absence of the acceptor, respectively (the same as τ_{DA} and τ_D in Equation 3.8). These can be used to derive the FRET efficiency (and hence distance separation) for an individual donor/acceptor undergoing FRET [88].

In practice, it is very difficult to obtain a sufficiently high photon count in each pixel for independent fitting of bi-exponential decays. It is therefore increasingly common to use techniques for *global analysis* [89, 90]. This approach assumes the lifetimes for the two components are constant across the image, and only the relative fractions of each component vary. The two lifetimes can be obtained by spatially binning all pixels in the image into one, providing a high enough photon count for bi-exponential analysis. The lifetime values to emerge from this may then used to globally fit the pre-exponential factors across the image, building up a map of the populations of bound and unbound species. Examples of where this

approach has been used include quantifying the spatial activity of protein-tyrosine phosphatase PTP1B [91] and monitoring the proportion of phosphorylated ErbB1 receptors in live cells [92].

3.3.4. Polarisation resolved measurements

As was seen earlier in our discussion of J. Perrin's work on the subject, FRET can also be detected through a fall in the polarisation anisotropy of the fluorescence emission. This effect occurs because acceptors whose transition dipoles do not have components aligned with the excitation may undergo resonant energy transfer from donors whose dipoles are more favourably aligned (Figure 3.6).

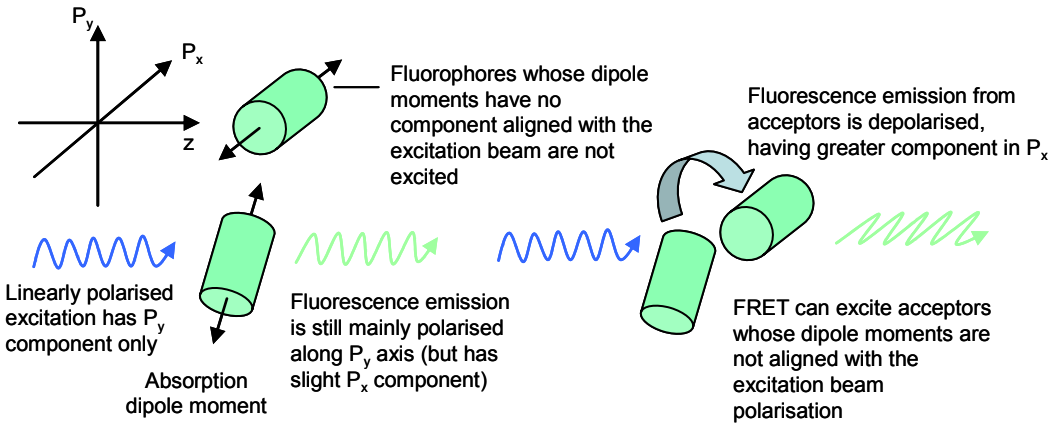


Figure 3.6: Imaging Homo-FRET by polarisation anisotropy. Secondary excitation of acceptors by FRET results in an increase in the depolarisation of fluorescence, when the sample is excited by a polarised light source.

An interesting feature of this approach is that it is not necessary to use spectrally distinct fluorophores – it is equally applicable to studies of Homo-FRET i.e. the transfer of energy from a donor fluorophore to an equivalent acceptor fluorophore. In this case, the measured fluorescence will stem from molecules directly excited by the laser (donors) and those which have been excited following energy transfer (acceptors). Assuming the molecules have a long rotational correlation time, emission from the donors will remain polarised in the same approximate direction as the excitation. Fluorescence from acceptors meanwhile is likely to be more depolarised. It follows that FRET between closely packed molecules can be detected by a fall in the overall anisotropy of the emission. This method is particularly useful for studying the clustering and oligomerisation of proteins each labelled with the same fluorescent species [93, 94].

Although polarisation imaging is a versatile technique, it is important not to underestimate the technical issues involved. Experiments may be difficult to implement on commercial microscopes where the polarization properties of internal components aren't always known. Perhaps more challenging is to calibrate for the differences in flexibility of linkers used to bind fluorophores to their target protein, since different linkers may affect the fluorophore's freedom to rotate to greater or lesser extent [95].

3.4. Choice of fluorophores for FRET

In theory, almost any pair of fluorophores that offers sufficient brightness and spectral overlap between the donor emission and acceptor can be used for FRET. For cellular imaging, however, the choice is restricted to those which can be targeted to a specific protein or cellular species. This is by no means trivial given the huge number of different molecules found within a single cell.

GFPs and RFPs have, by virtue of the ease with which they can be used to label different proteins, become the favoured type of fluorophore for live cell FRET [96]. This said, they do pose one or two limitations. The location of the chromophore within the Beta-barrel of the protein limits the distance of closest approach between any two GFP chromophores to the sum of the two barrel radii – in the range of 4 nm. This is of the order of R_O for a typical GFP/RFP pair, thus there is an upper limit to the maximum FRET that can occur between these species (~50%). Other issues include the position of the GFP moiety. Owing to their size and the need to avoid disrupting the innate folding of the target protein, GFPs are for the most part fused to the N or C terminus of the protein. This may give rise to false negative readouts for proteins that do actually bind to one another, since the fluorescent labels may still be separated by a sizeable distance.

Organic dyes, although not having the same labelling specificity as genetically expressed fluorophores, do offer other advantages from a FRET perspective. Being small molecules, they arguably pose less disruption to the molecule under investigation. In addition, there is no restriction on how close the donor and acceptor chromophores can approach one another, meaning higher FRET efficiencies are possible. In light of this, work has focussed on developing technology for introducing dyes non-intrusively into the cells, and targeting them to specific proteins, without the need for an intermediary antibody. One example of this is the FlAsH technology pioneered by R. Tsien's lab [97]. FlAsH, (fluorescein-arsenical-hairpin) is a cell permeable fluorescein derivative that by itself is non-fluorescent. This

molecule has a high affinity for tetracysteine motifs - short series of amino acids containing two or more pairs of cysteine residues. Upon binding to the tetracysteine motif, the molecule adopts a different electronic configuration resulting in an enhanced fluorescence (Figure 3.7) Fluorescence will therefore only emanate from the probe when bound to the protein.

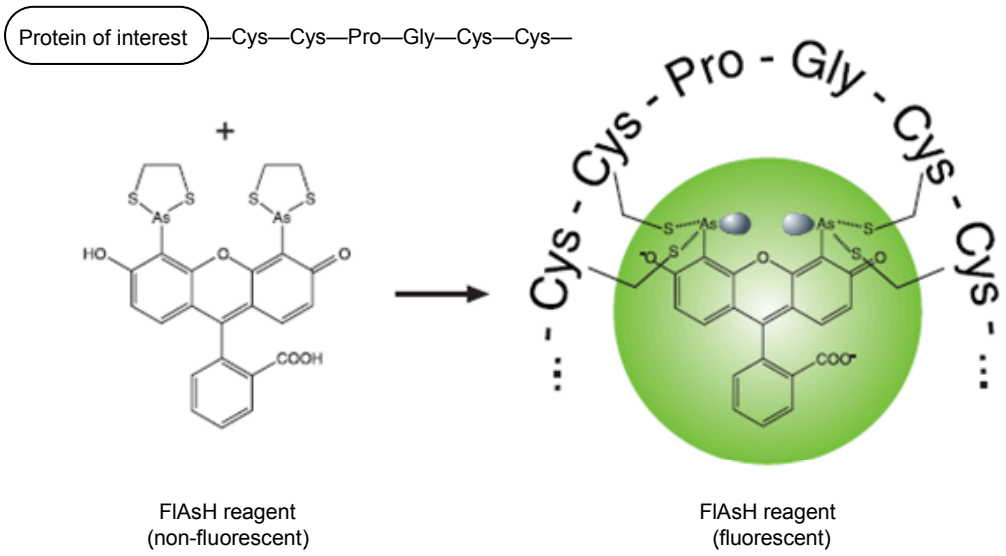


Figure 3.7: FlAsH technology for labelling proteins (Figure courtesy of Invitrogen).

The tetracysteine motif can be introduced into gene sequences using the same steps used to construct GFP fusions. Being much smaller than GFP, the tetracysteine motif can be positioned at numerous locations along the protein's length without so significantly disrupting its function. The modified gene is then transfected into a cell population where it will be expressed. The cells are incubated with the dye which will diffuse through the membrane and bind to the tetracysteine tag. Any remaining dye is then removed by successive washes in buffer solution. The result is a donor or acceptor positioned at a unique site on the protein, permitting a close interaction with a partner fluorophore and resultant high FRET efficiency. This approach has been used on a number of occasions, for example in studies of G-protein coupled receptor signaling [98] and dimerisation of endothelin receptors [99].

Whilst these results are impressive, issues with this technique still remain. It is not uncommon to experience a high background signal from residual dye molecules binding to cysteine rich regions of endogenous proteins. Cysteine residues themselves are reactive and can lead to disruption of the protein's function through formation of disulphide bridges. This can have negative consequences for preserving the innate function of the protein.

Quantum dots, whilst having been demonstrated as having good potential as FRET donors [100, 101] have so far mainly been used for intramolecular FRET probes, where it is not necessary to target the fluorophore to a specific cellular protein. Some of the key advantages and disadvantages of the different fluorophores / labelling strategies are listed in Table 3.0.

Fluorophore	Advantages	Disadvantages
Synthetic dyes	• Small, no limit to how close FRET partner can approach • Can be used to label endogenous species by immunostaining with antibodies • Large number of colours	• Difficult to use in live cells, immunostaining only possible in fixed cells • Low specificity for target proteins
GFPs	• Easily expressed in cells, highly suitable to live cell microscopy • Maximum specificity for labelling proteins • Large number of colours	• Large size – may exceed size of target protein • In majority of cases, can only be positioned at N or C terminal of protein • Distance of closest approach limited by Beta-Barrel
ReAsh / FlAsH	• Small, no limit to how close FRET partner can approach • Can be targeted to specific sites in protein • Multiple sites in protein can be labelled	• High fluorescence background can result from non-specific binding to endogenous species • Tetracysteine motifs may affect protein folding • Limited number of colours
Quantum dots	• High photostability and long fluorescence lifetime makes suitable FRET donors	• Poor targeting specificity • Large size – may exceed size of target protein

Table 3.0: Advantages and disadvantages of different fluorophores for FRET applications.

3.5. Experimental study of FRET between different FRET pairs

The choice of which type of fluorophore will of course depend on the nature of the experiment. It is fair to say, however, that for most applications GFPs offer a significant advantage through their ease of implementation. As a prelude to the work described later in this thesis, we introduce some initial experiments that were carried out to evaluate the performance of different pairs of fluorescent proteins as FRET pairs.

At the time when the work in this thesis was begun, the majority of live cell FRET experiments reported in the literature had utilised the donor-acceptor pair ECFP / EYFP (or their spectral equivalents Cerulean / Venus / Citrine etc). Although brighter and more

photostable than most CFPs, EGFP's use as a donor had up until this point been limited by the absence of a suitable long wavelength acceptor. The only red fluorescent protein available at this time, DsRed, was somewhat problematic owing to its long maturation process (which includes an intermediate green emitting state), as well as issues regarding tetramerisation. This issue was resolved in 2005 following the introduction of the DsRed derivative mRFP [102]. Additional red protein derivatives, such as monomeric cherry (mCherry) and monomeric orange (mOrange) [21] which were developed shortly afterwards, opened up further opportunities for exploiting the benefits of EGFP as a FRET donor.

To evaluate the potential of these new red acceptors for FRET experiments, fusion constructs consisting of EGFP linked by a 6 amino acid chain to mOrange, mCherry or mRFP were cloned and then expressed in E-coli, after which the fluorescence lifetime of EGFP in the purified proteins was measured and compared to EGFP alone. The length of the linker was chosen to ensure the two fluorophores would be within the requisite distance for FRET to occur. Since, on average, each of the acceptors would have the same distance separation / orientation relative to the EGFP donor, any difference in FRET between the pairs should reflect innate differences in the fluorophores' ability to act as acceptors for EGFP.

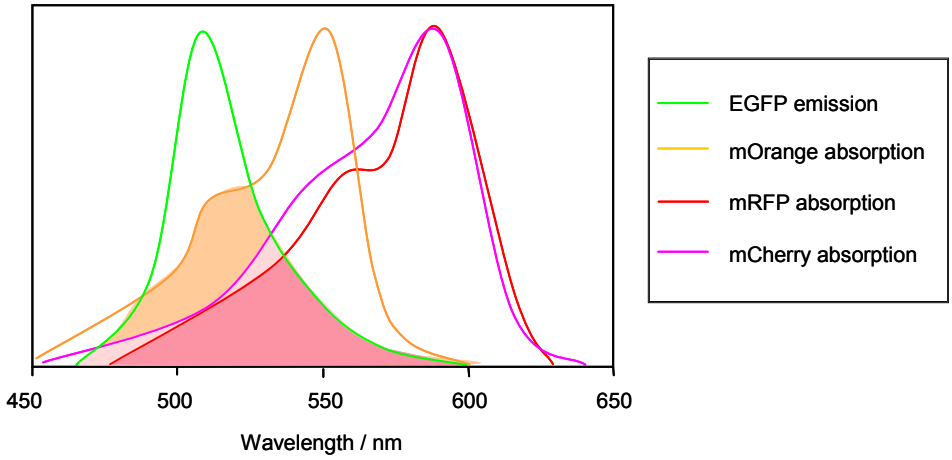


Figure 3.8: Spectral overlap between the EGFP emission spectrum and the absorption spectra of the three prospective FRET acceptors mOrange, mRFP and mCherry.

Figure 3.8 shows the spectral overlap $J(\lambda)$ for EGFP and each of these three acceptors. Table 3.1 shows the molar extinction coefficients for the three red fluorophores, and their predicted R_O value, calculated using the online feature at the Nikon website: www.microscopyu.com.

	mOrange	mRFP	mCherry
Molar absorption coefficient / $M^{-1}cm^{-1}$	71,000	50,000	72,000
Predicted R_O for EGFP donor / nm	5.5	5.0	5.2

Table 3.1: Molar absorption coefficients and predicted R_O values for the three FRET acceptors.

From Table 3.1 we see that the expected R_O values for the two red proteins are approximately equal, with mOrange having a slightly higher value owing to the greater extent of spectral overlap with the EGFP emission spectrum. The lower value of R_O for mRFP compared to mCherry arises from a smaller absorption coefficient. On this basis, one would predict that mRFP and mCherry would have similar FRET efficiencies when used as acceptors for EGFP, while FRET between EGFP and mOrange would be slightly enhanced.

3.5.1. Measurements of FRET in bulk solution

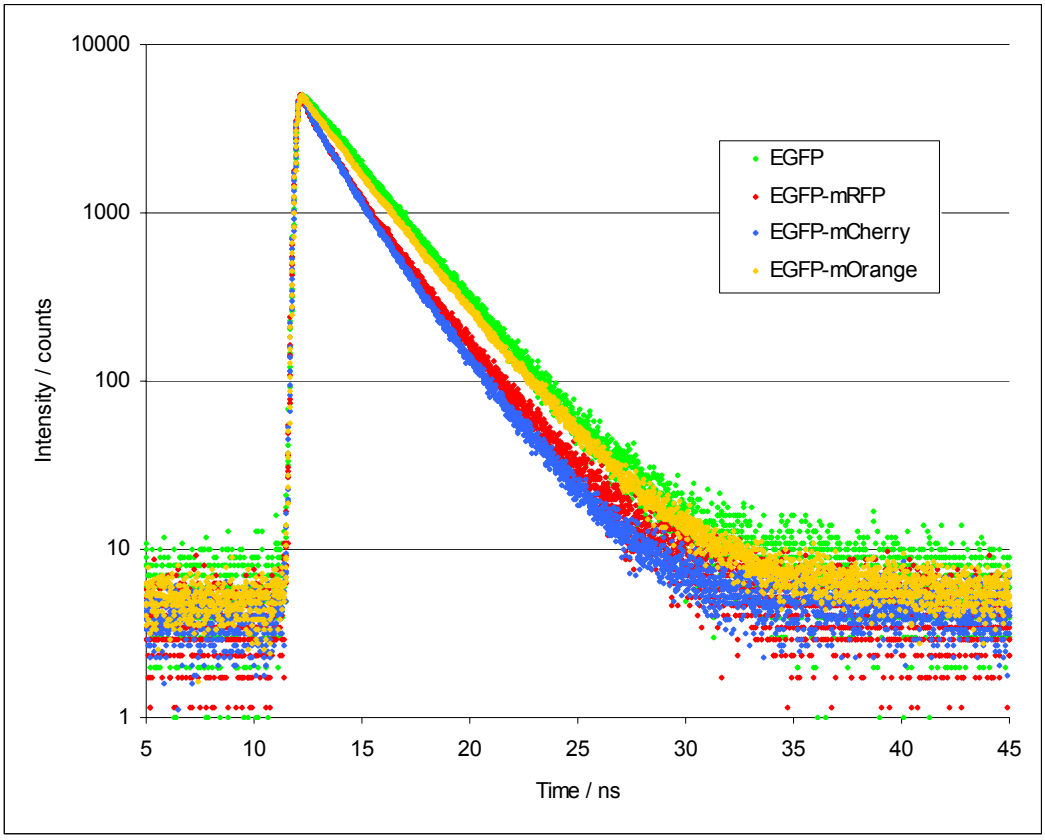


Figure 3.9: Temporal decay profiles for EGFP and each of the 3 donor/acceptor pairs EGFP-mRFP, EGFP-mOrange and EGFP-mCherry.

To validate the above hypothesis, the purified proteins were placed in a cuvette and lifetime decays measured using a novel, multispectral lifetime fluorometer developed by H. Manning

and colleagues at Imperial College London. This probe uses a time correlated single photon counting module (SPC-830, *Becker & Hickl GmBh*) to resolve lifetime decays across 16 spectral windows. For the purposes of these experiments, the fluorescence signal in channels spanning the EGFP emission spectrum were binned into a single decay and compared for the different constructs. Representative decays for the different combinations are shown in Figure 3.9. From this, we can see that EGFP has, to strong approximation, a monoexponential decay profile. Of the 3 FRET pairs looked at, EGFP-mCherry has the greatest deviation from the EGFP decay, followed by EGFP-mRFP. This is in keeping with the predicted values of R_o. Surprisingly, the temporal decay profile for EGFP-mOrange is almost identical to EGFP alone, suggesting FRET between these species is minimal.

3.5.2. Measurements of immobilised proteins on beads

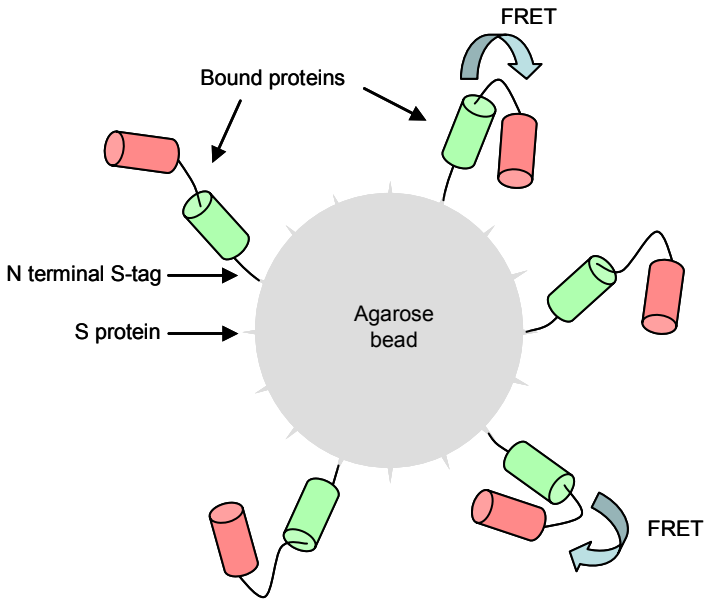


Figure 3.10: Labelling of S-Agarose beads with purified protein FRET constructs.

In the cuvette experiments discussed above, FRET would arise primarily from interactions between bound donors and acceptors, but there also existed the possibility of intermolecular FRET between different pairs of molecules. To exclude this signal, we sought to immobilise the proteins on a substrate such that individual donors would only have interactions with the acceptor they were linked to. The purified proteins, by virtue of the vector they were expressed in (pTriEx4 – *Novagen*) also encode an N terminal His-tag and S-tag sequence. The latter is a 15 amino acid sequence that binds with high affinity to the 103 amino acid S-protein, the two both being derived from the same RNase protein. By incubating the purified protein with S-protein coated agarose beads (*Novagen*), we were able to immobilise protein

on the surface of the beads (Figure 3.10). These could then be imaged under the microscope. (See Chapter 4 for details of the steps used in labelling the beads).

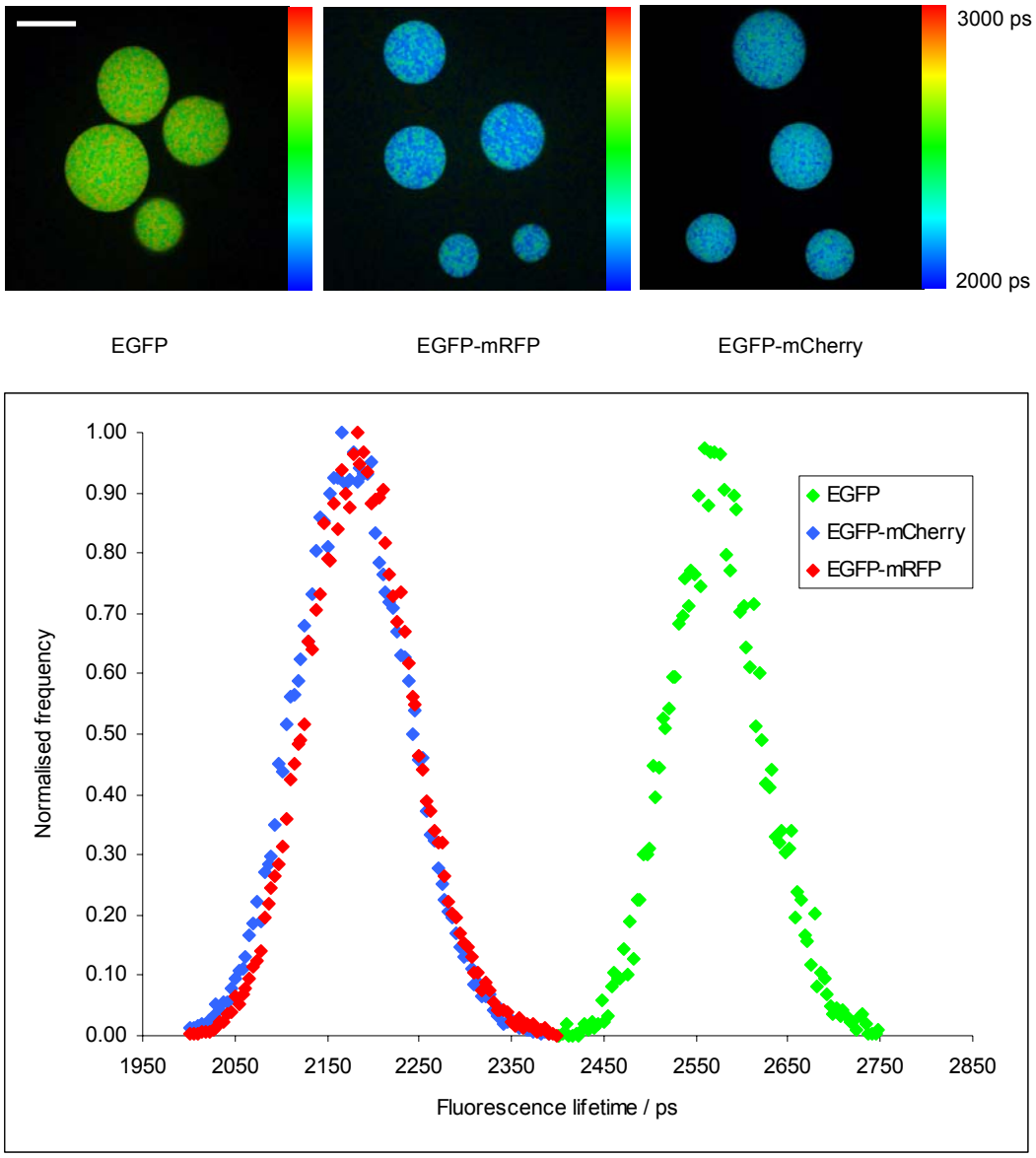


Figure 3.11: Top - FLIM images of beads labelled with EGFP, EGFP-mRFP and EGFP-mCherry (Scale bar = 50 µm) Bottom - Fluorescence lifetime histograms for the images shown.

Beads labelled with the different proteins were imaged on a Leica-SP5 confocal microscope with excitation provided by a pulsed Ti:Sapphire laser (Tsunami, *Spectraphysics*) tuned to 960 nm. Before coupling the laser into microscope, the wavelength was frequency doubled by focussing through a BBO crystal to provide an output wavelength of 480 nm. Fluorescence was collected through a 525/50 nm emission filter. EGFP lifetimes were measured using an SPC-830 time correlated single photon counting module (*Becker-Hickl Gmbh*) that was synchronised with the scan coordinates of the microscope to provide lifetime

data for each pixel in the final image. Figure 3.11 shows representative images of beads labelled with EGFP, EGFP-mRFP and EGFP-mCherry, together with lifetime histograms for the same images. Note that the data for EGFP-mOrange is not shown, since the decays measured here were indistinguishable from EGFP alone.

The figures above concur with the data obtained in bulk solution, and indicate a significant degree of FRET between EGFP-mRFP and EGFP-mCherry. The lifetime histogram for EGFP and mOrange is not shown owing to the minimal shift from that of EGFP alone.

3.5.3. Discussion of measured FRET efficiencies

The data in sections 3.5.1 and 3.5.2 are a useful indicator of the shift in mean lifetime one can expect to obtain when using fluorescent protein FRET pairs. Although it is unlikely one would encounter scenarios in which the donor and acceptor were in much closer proximity, it would be unwise to construe these as being close to the maximum FRET efficiencies possible for these fluorophores. To do so would be to neglect the issue of favourable alignment of transition dipoles, and one should not rule out the possibility that a different orientation between the two fluorophores might lead to higher FRET efficiencies.

One interesting observation in these experiments has been the small FRET signal seen for the EGFP-mOrange FRET pair. In the time since this work was carried out, several other groups have published work along similar lines, using fused constructs of GFP variants to determine optimal pairings for FRET. In 2008, van der Krogt *et al* published an extensive survey of FRET pair efficiencies, which found similar results to those above, including an unexpectedly poor performance of mOrange (although the lifetime shift was larger than that reported here) [103]. This result is puzzling because in theory these two proteins possess all the necessary criteria for FRET to occur and mOrange has been shown to function successfully as an acceptor for the UV excited EGFP mutant T-Sapphire [104]. In the aforementioned paper by van Der Krogt *et al*, the lack of FRET between EGFP and mOrange was ascribed to incomplete maturation of mOrange, however, this seems unlikely given that bright orange fluorescence was clearly visible when exciting this protein at longer wavelengths. The possibility that the acceptor excited state might be saturated by absorption at 480 nm was also ruled out by tuning the laser to shorter wavelengths, at which point there was still no change in the measured lifetime. A possible explanation is that during folding the mOrange and EGFP dipoles had become orientated at a particularly unfavourable angle for FRET to occur. To determine this for certain would necessitate engineering new

constructs, however, given the limited returns on this, it was decided not to pursue this line of enquiry, but instead focus on mRFP or mCherry in future experiments.

3.6: Conclusion

In this chapter, we have introduced Förster Resonance Energy Transfer and its application to imaging molecular interactions within cells. The different methods for imaging FRET in the microscope have been discussed, with emphasis being placed on the advantages of fluorescence lifetime imaging (FLIM). Some experimental data has also been presented comparing the performance of different pairs of fluorescent proteins for FRET.

The next chapter discusses methods for preparation of biological samples used throughout this thesis. In Chapter 5, the key signaling components studied in this thesis, namely Ras family GTP-ases and the novel Ras effector Phospholipase C Epsilon (PLCε) will be introduced. These proteins and the interactions between them will form the basis for the main focus of this thesis - development of novel microscopy tools and instrumentation for using FRET to report on live cell signaling events.

Chapter 4: Materials and methods

4.0. Cell culture

COS 7 and MDCK cells were grown in 75 cm^2 tissue culture flasks, in 15 ml Dulbecco's modified Eagle Medium (DMEM) with 10% added foetal bovine serum (FBS) and 2.5 mM added L-glutamine. Flasks were stored in a 37.4 ^{O}C incubator, at 5% CO_2 concentration.

For microscopy, cells were plated out onto 3 cm diameter, glass bottom microscopy dishes (*MatTek*^{TM}). Prior to seeding, cells were removed from flasks using 2 ml trypsin/versine and suspended in 10 ml DMEM solution. Cells were then centrifuged for 5 minutes at 1200rpm, and the medium aspirated to remove any remaining trypsin. The cell pellet was resuspended in 10 fresh medium and cell densities determined by haemocytometry. Cells were plated out at approximately 2.0 x 10^5 cells / dish. Cells were incubated for 24 hours prior to transfection.

4.1. Fluorescent constructs

Enhanced Green Fluorescent Protein (EGFP) was expressed in live cells using the pEGFP-C1 vector (*Clontech*). Constructs expressing human Ras were prepared in the pTriEx4 vector (*Novagen*) and incorporated the full-length open reading frame (ORF) fused at the N-terminus to the ORFs of fluorescent proteins mOrange, mRFP, mCherry or mPlum. The fluorescent tag was separated from the Ras protein by a linker incorporating the sequence GGSGGS. Tandem constructs of EGFP-mRFP, EGFP-mOrange and EGFP-mCherry were prepared in the pTriEx4 vector, and also contained the GGSGGS sequence as a linker between the two fluorophores. Standard splicing PCR was used to generate fused expression constructs. In brief, the ORFs of fluorescent proteins and Ras were amplified with an overlapping region consisting of a glycine-glycine-serine-glycine-glycine-serine linker (in the final expressed construct). The two gel purified PCR products were mixed and a second PCR initiated with oligos allowing amplification of a fused construct and allowing cloning into pTriEx4 by Ligation Independent Cloning (LIC). The fused PCR product was gel purified and cloned into pTriEx4 following the manufacturers protocol. Cloned constructs were sequence verified and expression of correct fusion proteins confirmed by Western blotting.

Generation of rPLCε-EGFP: The ORF of rat PLCε amino acids 1258-2225 was cloned in the pTriEx4 vector (*Novagen*) as previously described [105]. The ORF of EGFP was amplified by PCR from the EGFP vector (*Clontech*) using primers encoding for *AflII* restriction sites at both ends. The PCR product was ligated by standard methods into the *AflII* site downstream of the RA2 domain of rPLCε.

The Raf-RBD-EGFP construct was constructed in the pEGFP-C1 vector and comprised amino acids 51-200 of human Raf-RBD from C-Raf Kinase, separated from EGFP by the same GGSGGS sequence. The Raf-RBD-TagRFP construct was later generated from this. The coding sequence of EGFP in Raf-RBD-EGFP was substituted by the full-length open reading frame (ORF) of TagRFP by excision and re-ligation from pTagRFP-C vector (*Evrogen*, Moscow, Russia) using *Age I* and *BspE I* restriction sites. Cloned constructs were sequence verified and expression of correct fusion proteins confirmed by Western blotting.

For cloning of novel Raichu constructs mOrange-Raichu-mCherry and mOrange-Raichu-mPlum, the original DNA sequence from CFP-Raichu-YFP [180] was amplified by PCR, followed by transfer into the pCR4Blunt topo vector (*Invitrogen*). The YFP fluorophore was deleted by mutagenesis PCR, and mOrange inserted in its place using the *XhoI* restriction site. The mCherry and mPlum DNA sequences were inserted at the *NotI* site, after the Raf-RBD DNA sequence. Each of these steps was designed to maintain the exact amino acids linker sequences present in the original CFP-Raichu-YFP construct.

4.2. MaxiPrep procedure

All constructs were amplified in E-Coli bacteria to obtain stocks for multiple experiments. A standard in house protocol was used.

Approximately 50 µl of bacterial cells was added to 0.5 µg plasmid DNA and left on ice for 30 minutes. The mixture was then submerged in a heat bath at 42^{O}C for 2 minutes, before returning it to ice for a further 20 minutes. The mixture was then incubated for 1 hour at 37 ^{O}C with 0.5 ml L-Broth.

After incubating, 200 µl of the mixture was pipetted onto the surface of an Agar plate with specific antibiotics. The plate was left to incubate overnight at 37^{O}C.

The following day a single bacterial colony was removed from the Agar plate and transferred to a flask containing 500 ml L-Broth with added antibiotics (ampicillin and kanamycin were used at final concentration 50 $\mu g ml^{-1}$). The flask was again left overnight to incubate at 37 ^{O}C.

After 24 hours, bacteria were reclaimed from the L-Broth solution by centrifuging at 4000 rpm for 10 minutes and removing the supernatant. The bacterial pellet was resuspended in 18.5 ml Alkaline Lysis Buffer Solution I, before adding 18.5 ml Alkaline Lysis Buffer solution II to precipitate out genomic DNA. The mixture was centrifuged at 4000 rpm for 10 minutes at $4^{O}C$, and the supernatant then filtered through a cheesecloth into a second centrifuge tube. A volume of propan-2-ol was then added equal to 0.7 times the volume of the collected supernatant.

The solution was centrifuged again for 15 minutes at 4000 rpm and the supernatant removed. The pellet was redissolved in 1.5 ml TE Buffer pH 8.0. An equal volume of 5 M LiCl solution was added to the tube to precipitate out RNA. The tube was centrifuged at 4000 rpm for 10 minutes and the supernatant poured into a fresh falcon tube. To this was added 5 µl RNAse A (*Qiagen*) at 100 $mg ml^{-1}$, and the solution incubated at 37 ^{O}C for a further 15 minutes. The contents were then added to an equal volume of solution of 13% PEG 8000 (*Promega*) and 1.6M NaCl and transferred to a microfuge tube. This was left on ice for 50 minutes.

The tube was centrifuged at 14000 rpm for 5 minutes, and the pellet separated from the supernatant. The pellet was resuspended in 200 µl TE Buffer pH 8.0 and a further 200 µl of Phenol / Chloroform (*Sigma*) was added. The mixture was vortexed for 30 seconds and then centrifuged for 5 minutes at 14000 rpm.

On removing the tube from the centrifuge, the upper phase was pipetted into a new microfuge tube. DNA was precipitated by adding 20 µl of 0.1 M sodium acetate and 400 µl 100% ethanol. The DNA was reclaimed by centrifuging at 14000 rpm for 2 minutes at 4 ^{O}C and removing the supernatant. The DNA pellet was redissolved in 100 µl TE Buffer pH 8.0 and the concentration determined by UV absorption spectrophotometry.

4.3. Cell transfection

Cells were transiently transfected with fluorescent constructs using a standard Lipofectamine transfection protocol obtained from *Invitrogen*. Approximately 1.5 µg of plasmid DNA was added with 4 µl PLUS^{TM} reagent to 96 µl of serum free Optimem (*Gibco*®) in a sterile tube. The mixture was then allowed to incubate for 15 minutes, during which time cells were washed in serum free Optimem. Following this, a second mixture containing 90 µl serum free Optimem and 10 LipofectAMINE reagent was added to the tube, and the whole incubated for a further 15 minutes. A further 0.8 ml serum free Optimem was then added to the transfection mix, and the whole overlaid onto the cells. Cells were incubated for 3 hours at 37 ^{O}C in 5% CO_2. After 3 hours, the transfection mix was aspirated and replaced with 2 ml DMEM with 10% added FBS. Cells were then incubated overnight at 37^{O}C.

4.4. Cell microinjection

For microinjection, plasmids were diluted to concentrations between 5-30 µgml^{-1}, and centrifuged at 14000 rpm for 10 mins to remove debris. Needles were pulled on an in-house pulling tower, using 10 cm borosilicate glass capillaries (*Harvard Apparatus*, part no. 30-0044) and back filled with 5 µl DNA. Microinjection was performed on a Zeiss phase contrast microscope fitted with piezoelectric micropipette control, using a x40 objective lens.

4.5. SDS PAGE and Western blotting

All constructs used for imaging experiments were checked for size and degradation products in COS cells using SDS PAGE followed by Western Blotting. Thirty six hours post transfection, cells were harvested in standard lysis buffer (25 mM Tris buffer pH 7.5, 1 mM EDTA, 0.1% Triton, 1 mM DTT with added protease inhibitors [*Roche*]) in 100 µl ependorf tubes. Following sonication (10 µm amplitude), tubes were left on a rotating wheel for 15 mins 4 ^{O}C, after which they were centrifuged at 14000 rpm for 10 mins to remove membrane and insoluble components.

The clear supernatant was assayed for protein concentration using a standard Bradford assay: 1 µl of protein was added to 1 ml of 5-fold diluted Bradford reagent (*BioRad*) in a cuvette, and the absorbance at 595 nm quantified in a spectrophotometer. Protein concentrations were then determined by reference to a BSA standard curve.

Resolving gels, composed of 6-12% acrylamide, 0.2-0.5% bisacrylamide, 375 nM Tris buffer pH 8.8, 0.1% SDS, 0.04% TEMED and 0.1% ammonium persulphate (APS) were cast in a *BioRad* gel apparatus and overlaid with 200 µl water saturated isobutanol. Stacking gels, composed of 3% acrylamide, 0.1% bisacrylamide, 115 mM Tris buffer pH 6.8, 0.1% SDS and 0.2% APS were then added on top, and well combs inserted. Gels were transferred to running tanks, and immersed in running buffer (22 mM Tris buffer pH 8.0, 188 mM glycine with 0.1% added SDS).

Protein samples were denatured by addition of loading buffer (64 mM Tris buffer pH 7.0, 2% SDS, 17.5% glycerol, 1 mM DTT and 1.2 mM β-mercaptoethanol) and boiling at 95 ^{O}C for 5 minutes. Approximately 25 µg of each protein sample was added to the wells, and electrophoresis carried out at 120-200 V, depending on gel composition.

Following electrophoresis, gels were inserted in an electroblotting apparatus (*BioRad*), and proteins transferred overnight at 30 V, 4 ^{O}C in buffer (22 mM Tris buffer pH 8.0, 188 mM glycine, 20% methanol) onto nitrocellulose membranes (Hybond C Super, *Amersham*). After transfer, blots were blocked for 1 hr in TBS-Tween solution (25 mM Tris, 1.4 M NaCl, 0.1% Tween 20) with 5% milk powder (*Marvel*). Primary antibodies were added in blocking buffer at concentrations between 40-200 ngml^{-1} for 3 hrs at 4^{O}C. Blots were washed several times in TBS-Tween solution before blotting with secondary antibody conjugated to horse radish peroxidase (goat anti-mouse HRP-conjugated antibody, or donkey anti-rabbit HRP-conjugated antibody [*Amersham*]) at 1:5000 dilution. After 3 hours, blots were washed a further 3 times in TBS-Tween solution and proteins detected by ECL (enhanced chemiluminescence) using a standard ECL protocol (*Amersham*).

4.6. EGF stimulation

For EGF stimulation, cells were first serum starved for 24 hours by immersion in 2 ml DMEM solution with 0.25% essentially fatty acid free BSA (*Sigma*) but without FBS. Cells were stimulated by adding EGF to dishes to final concentration of 100 ngml^{-1}.

4.7. Fixing cells

Prior to fixing cells, the medium was aspirated and cells washed in 2 ml phosphate buffered saline (PBS). Cells were then immersed in 2 ml formaldehyde at 4% concentration in PBS, for 4 minutes. Cells were washed and reimmersed in PBS for imaging.

4.8 Labeling of beads with fluorescent constructs

For studies of FRET between EGFP and different red acceptors, constructs of EGFP linked to each acceptor were purified in *E. Coli* and bound to S-agarose beads before imaging on the microscope. Approximately 50 -150 µl of 50 µm S-agarose beads (*Novagen*) was added to a 1.5 ml epindorf tube. Beads were then washed by adding 400 µl of buffer solution (50 mM Tris/HCl, pH 7.5, 150 mM NaCl, 1 mM DTT, 1% Triton-X-100, 2 $mgml^{-1}$ BSA and 5 mM $MgCl_2$) and centrifuging at 2000 rpm for 3 mins, after which buffer was removed by suction. After repeated washes, beads were resuspended in 400 µl buffer and solutions of purified protein added to make up a final concentration of 50 – 100 µM. The tube was left on a rotating wheel at 4 ^{O}C for 2 hrs, after which the buffer solution and any unbound protein was removed by suction. Beads were washed a further 2-3 times in buffer solution. In order to immobilise the beads for microscopy, beads were mixed with 3 ml of a 6% acrylamide gel solution (see SDS-PAGE and Western Blotting) which was then poured into 3 cm glass bottom dishes (*MatTek*^{TM}) dishes and allowed to set. Beads were then imaged within 3 hrs.

Chapter 5: FLIM-FRET studies of Phospholipase C Epsilon interactions with Ras GTP-ases

5.0. Chapter overview

This chapter introduces the Ras family of GTP-ases as important components in cell signal pathways and discusses the various downstream effectors through which Ras is able to elicit different cellular responses. One of the downstream components addressed in this thesis is the protein Phospholipase C Epsilon (PLCε), a member of the Phospholipase C family of enzymes.

At the time of writing, much of what is known about PLCε and its interactions with Ras has been inferred from biochemical assays performed *in vitro*. Imaging these interactions in a cellular context would therefore be of particular value for understanding the regulatory mechanism that govern these proteins' function. Here, we discuss FLIM-FRET experiments that were carried out using fluorescent constructs of Ras and PLCε and evaluate the scope of this approach for monitoring cellular interactions between these proteins.

5.1. Ras family proteins

Ras family proteins are small (<30kDa) proteins that serve regulatory roles in a variety of cell signaling pathways linked to growth, differentiation, proliferation and survival. This family of proteins has come to prominence owing to the large number of cancers which result, in part at least, from mutations in one or other Ras genes. Current estimates suggest that 30% of all cancers are linked to a Ras gene mutation. These are especially prevalent in pancreatic cancer, with incidences estimated at greater than 90%, whilst 50% or more thyroid and colorectal cancers may stem from such an occurrence [106].

5.1.1. GTP-binding nature of Ras

The Ras family forms a subset of the superfamily of small GTP binding proteins or GTP-ases. These proteins function as molecular switches by alternately binding to the guanonucleotides GDP and GTP (guanosine diphosphate and triphosphate, respectively). The transition between these two states is mediated by two additional families of proteins,

known as GEFs (guanonucleotide exchange factors) and GAPs (GTP-ase activating proteins). These proteins have complementary roles in operating the switch (Figure 5.0).

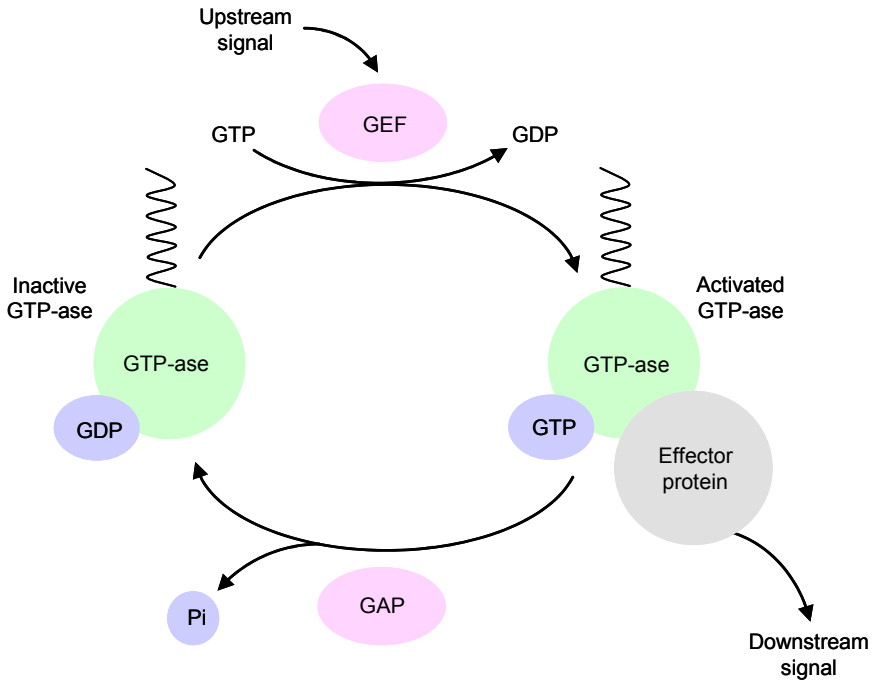


Figure 5.0: Regulation of GTP-ase activity by GEFs and GAPs. GEFs facilitate the transition from a GDP bound state to a GTP-bound state in which the GTP-ase is able to engage with effectors and so propagate downstream signals. GAPs return the protein to an inactive form by helping speed the protein's hydrolysis of GTP back to GDP.

The exchange of GDP for GTP results in a transition from the protein's inactive state to an active one. GEFs facilitate this exchange by destabilising the binding of GDP to the protein, enabling the uptake of free cytosolic GTP to the nucleotide binding site. The additional phosphate group in GTP induces a conformational change in the GTP-ase, allowing it to engage with effectors and so propagate cellular signals. This might involve recruiting downstream effectors to a particular cellular location (e.g. the plasma membrane) or initiating conformational changes in the effectors themselves.

Once activated, the protein will, over time, hydrolyse GTP back to GDP (hence the term GTP-ase). Rates of hydrolysis are increased through interaction with the second group of regulatory proteins, GAPs, which help return the protein to a GDP bound state and so terminate its signaling.

Aside from the Ras family of proteins, the GTP-ase family encompasses 4 other families, those of Rho, Rab, Arf and Ran. Proteins are classified into a particular group primarily on the basis of sequence homology, however, many also share similar functions in the cell

(Table 5.0). A review of these different families and their roles in cell signaling has been given by Takai *et al* [107].

Ras family		Rho family		Rab family			Arf family		Ran
H-Ras	Tc21	RhoA	Rac	Rab1A	Rab9	Rab22	Arf1	Arl1	Ran
K-Ras	Rit	RhoB	Rac2	Rab1B	Rab10	Rab23	Arf2	Arl2	
N-Ras	Rin	RhoC	Rac3	Rab2	Rab11A	Rab24	Arf3	Arl3	
R-Ras	Kir/Gem	RhoD	Cdc42	Rab3A	Rab11B	Rab25	Arf4	Arl4	
M-Ras	Rheb	RhoE	Rnd1	Rab3B	Rab12	Rab26	Arf5	Arl5	
RalA	kB-Ras1	Rho3	Rho6	Rab3C	Rab13	Rab27A	Arf6	Arl6	
RalB	kB-Ras2	Rho8	Rnd2	Rab3D	Rab14	Rab27B	Sar1a	Arl7	
Rap1A	R-Ras	RhoG	Rho7	Rab4	Rab15	Rab28	Sar1b	Ard1	
Rap1B		RhoH	Tc10	Rab5A	Rab16	Rab29			
Rap2A		TTF		Rab5B	Rab17	Rab30			
Rap2B				Rab5C	Rab18	Rab31			
				Rab6	Rab19	Rab32			
				Rab7	Rab20	Rab33A			
				Rab8	Rab21	Rab33B			

Table 5.0: Mammalian small GTP-ases (Adapted from Takai, Sasaki and Matosaki [107])

Within the Ras family, the three classic isoforms H, K and N-Ras are the most prominent members – the majority of Ras mutations can be traced to one or more of these genes and it is these three members that shall be considered in this thesis. The first oncogene to be discovered, H-Ras derives its name from the transforming gene of Harvey Sarcoma Virus, with which it shares a high degree of sequence homology [108]. The K and N isoforms similarly derive their names from the Kirsten Sarcoma and Neuroblastoma viruses respectively. While all three isoforms are implicated in oncogenesis, mutations in K-Ras are by far the most prevalent: of the total number of cancers involving a mutant Ras gene, 85% may be attributable to K Ras. The remaining 15% are mainly accounted for by N Ras, with figures suggesting less than 1% arising from mutations in H Ras [109].

5.1.2. Signaling via Ras: Upstream signaling and Ras activation

Following translation, Ras undergoes a series of post-translational modifications at the C terminal. These modifications, which vary between isoforms, append a lipid moiety to the protein's C-terminus that allows it to associate with different intracellular membranes en route to the plasma membrane [110]. Once at the membrane, Ras proteins are then activated following ligand binding of stimulatory agonists to neighbouring receptors. A key example of this is the activation of the epidermal growth factor receptor (EGFR) in response to epidermal growth factor stimulation (EGF). When activated, these and other tyrosine kinase receptors become phosphorylated, providing docking sites for SH2 domains of secondary,

adaptor proteins. These can in turn recruit other cellular components to the plasma membrane, including Ras GEFs, which will then initiate the exchange of GDP for GTP on Ras anchored at the membrane. This is exemplified by the Grb-2 / Sos pathway shown in Figure 5.1 below.

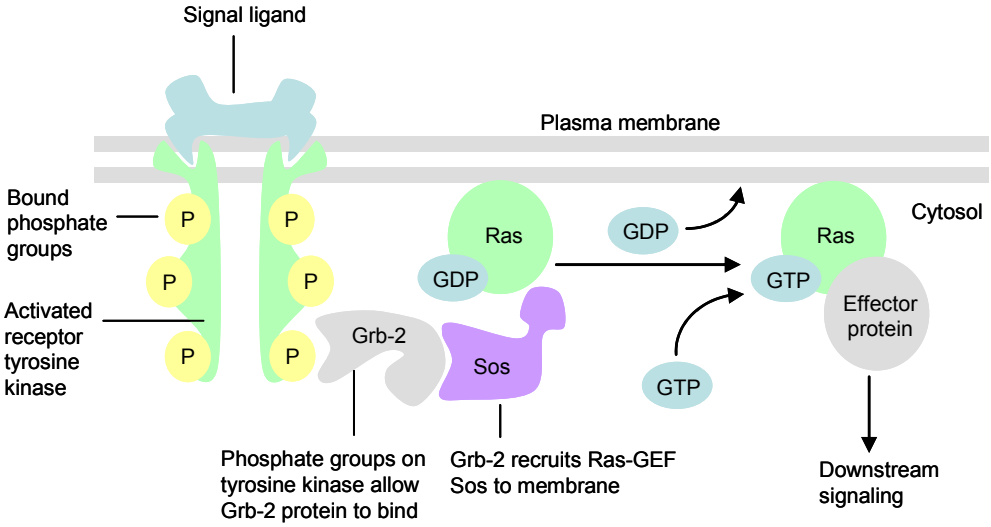


Figure 5.1: Ras is activated in response to signals from outside the cell. Activation of tyrosine receptor kinases by signal ligands initiates the Grb-2-Sos pathway, leading to Ras activation at the plasma membrane (Figure adapted from "Molecular Biology of the Cell [111]").

Besides this common pathway, several other mechanisms for Ras activation have been proposed, including activation via Ca^{2+} or diacylglycerol dependent GEFs. These are also discussed in more detail in Chapter 7.

5.1.3. Signaling via Ras: Downstream Ras effectors

The main Ras effectors and their downstream components are shown in Figure 5.2 below. Many of these have been well characterised over the past two or three decades. Others, most notably Phospholipase C Epsilon (PLCε), are more recent additions to the group of proteins that Ras is understood to interact with in the cell.

The most widely documented Ras effector is the Raf serine-threonine kinase, of which there are several isoforms: A-Raf, B-Raf and C-Raf [109]. Raf proteins lie upstream of the MAP (Mitogen Activated Protein) Kinases ERK1 and ERK2 [112], known to promote gene subscription and subsequent cell division through interaction with the ETS family of transcription factors [113]. Aside from the MAP Kinase pathway, Ras proteins are also known to activate phosphatidylinositol-3-kinase (PI3K), through its recruitment to the plasma membrane [114]. Once brought to the membrane, PI3K is able to interact with its

substrate, phosphatidylinositol-4,5-biphosphate (PIP_2), catalysing its phosphorylation to form phosphatidylinositol-3,4,5-triphosphate (PIP_3). PIP_3 lies upstream of the protein kinase PkB/Akt [115] whose phosphorylation of substrates BAD, glycogen synthase GSK3 and Forkhead transcription factors is a key mechanism for inhibiting apoptosis and promoting cell survival [116-118]. PkB/Akt also lies upstream of NF-Kappa-B, which besides its well documented role in inflammatory response is also involved in promoting cell growth and division [119].

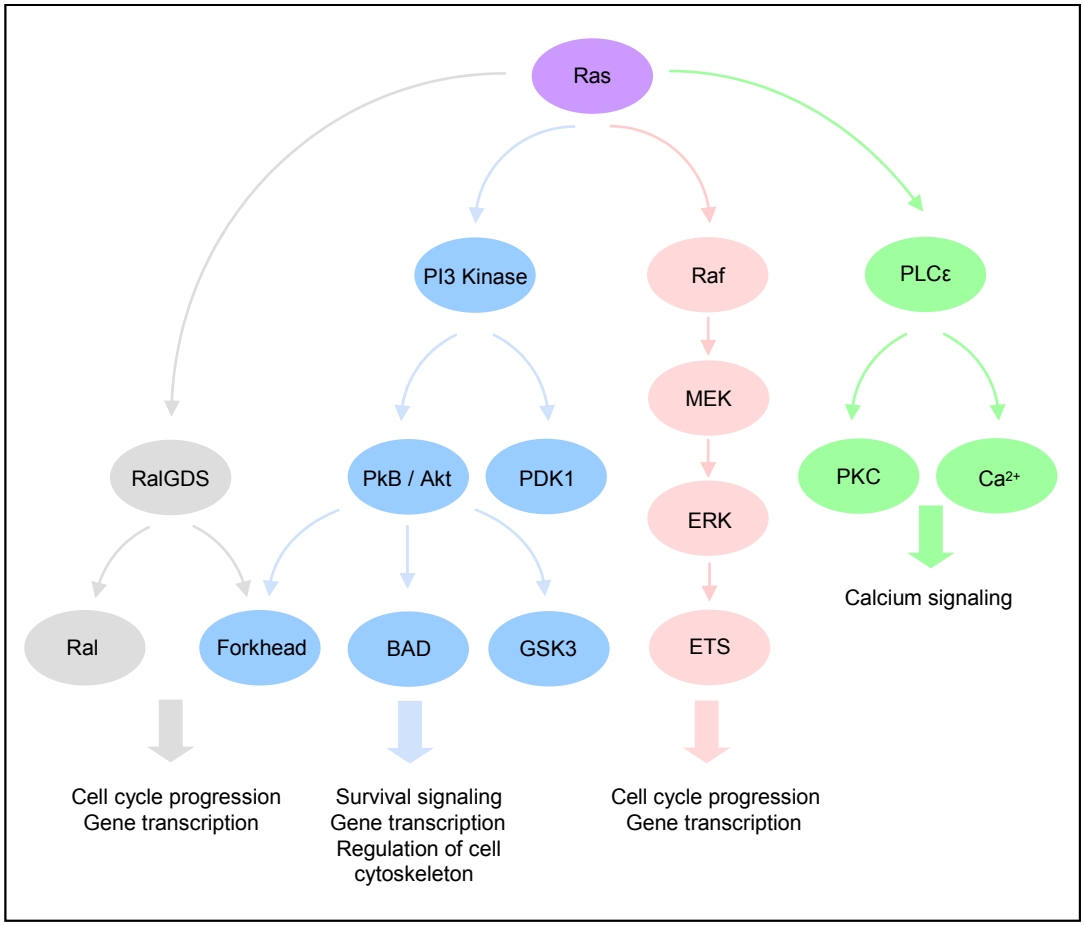


Figure 5.2: Key Ras effectors and downstream signal pathways.

Also downstream of Ras is the exchange factor RalGDS, a GEF for the small GTP-ases RalA and RalB [120]. Like PkB/Akt, Ral proteins are perceived to interact with members of the Forkhead family of transcription factors, and are thought to promote cell survival through inhibition of these proteins pro-apoptotic function [121]. The difference in roles between RalA and RalB are currently the subject of debate; it has been suggested that only RalA is in fact oncogenic, while RalB may function as a tumour suppressor by sequestering Ral GEFs away from RalA [122].

5.2. Phospholipase C Epsilon: A novel Ras effector

The most recent Ras effector to be discovered, Phospholipase C Epsilon belongs to the larger family of phospholipase C enzymes. These proteins play a pivotal role in regulating hormone, growth factor and neurotransmitter initiated cell responses [123, 124]. Following activation by one of several regulatory proteins, Phospholipase C is able to catalyse hydrolysis of the phospholipid phosphatidylinositol-4,5-biphosphate (PIP_2) to the soluble product inositol-1,4,5-triphosphate (IP_3) and the membrane bound diacylglycerol (DAG). The latter is involved primarily in the activation of Protein Kinase C while IP_3 has an important role in calcium signaling, stimulating the release of Ca^{2+} ions from the endoplasmic reticulum (Figure 5.3).

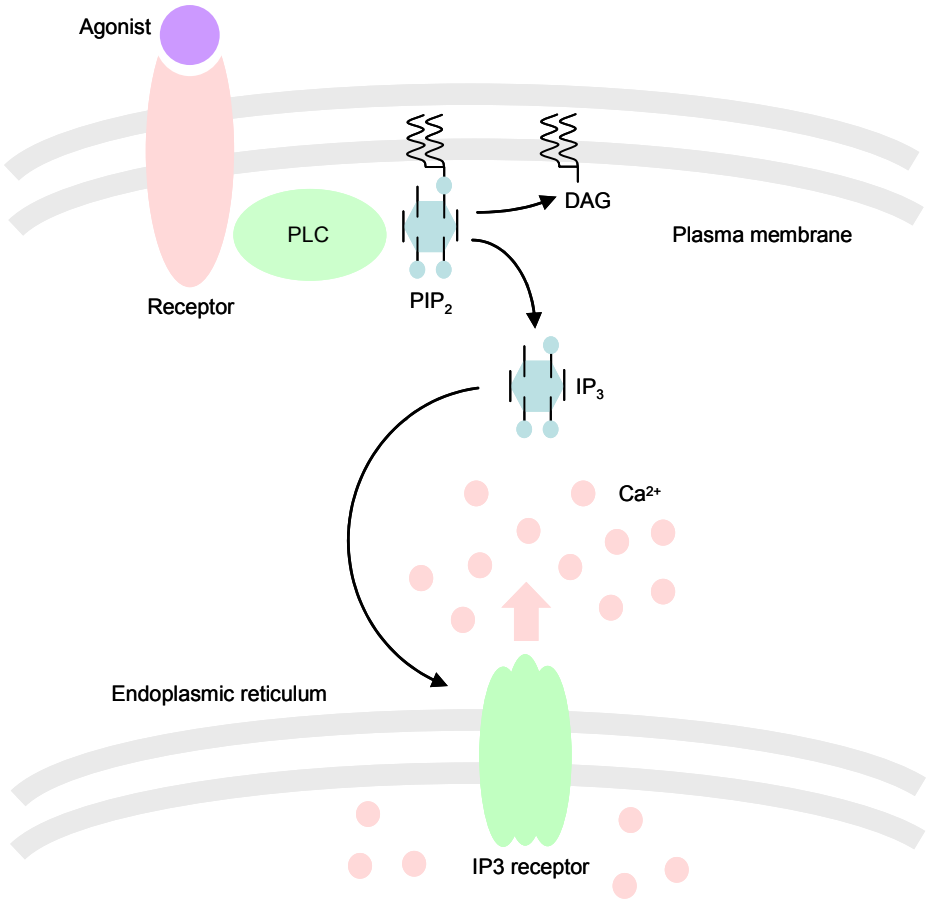


Figure 5.3: Signaling via Phospholipase C (PLC) In response to agonist stimulation of cell surface receptors, PLC is recruited to the membrane where it catalyses hydrolysis of PIP_2, resulting in the soluble product IP_3 and membrane bound diacylglycerol DAG. IP_3 in turn promotes release of Ca^{2+} from intracellular stores through binding to the IP_3 receptor in the endoplasmic reticulum.

The emergence of PLCε as a novel Ras effector has challenged conventional views on the regulatory mechanisms underlying phosphoinositide hydrolysis and subsequent secretion of

second messengers including Ca^{2+} and $Ins(1,4,5)P_3$. Until recently, these processes were thought to be regulated primarily through the interactions of heterotrimeric G proteins with other PLC isoforms. The discovery of a new isoform directly activated by Ras suggests a greater level of cross talk between these pathways than was previously recognised [125].

5.2.1. Mechanism for Ras interactions with PLCε

The suggestion that Ras could directly activate PLCε immediately followed the identification of two Ras association domains at the protein's C terminus (Figure 5.4) [126]. Whilst these do not share a high degree of primary sequence homology with the Ras binding domains from either C-Raf or PI3 Kinase, the secondary structure elements form a highly similar structure to these classical Ras effector domains [127].

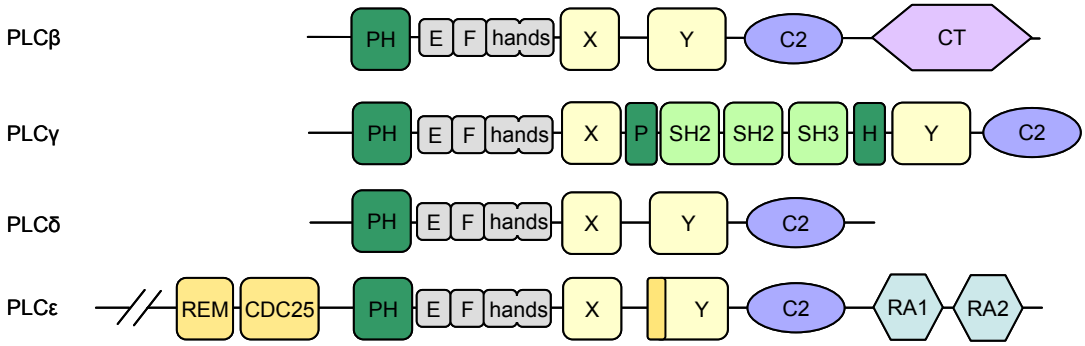


Figure 5.4: Domain structure of Phospholipase C family members PLCβ, PLCγ, PLCδ, and PLCε. The X-Y catalytic domain is conserved across all members, as are the C2 and EF domains. PLCε (bottom) possesses an additional 2 Ras association (RA) domains at the C terminus, while the CDC25 domain at the N terminus has been implicated in GEF signaling to small GTP-ases.

Studies in which cells expressing different deletion mutants of PLCε were stimulated with EGF and assayed for IP_3 production have shown that it is specifically the RA2 domain which is required for Ras activation of PLCε [105]. This result agrees well with structural analysis in which it has been demonstrated that the putative Ras binding interface in RA1 is negatively charged and therefore does not favour an interaction with the (predominantly) negatively charged binding site on Ras. This is in contrast to the RA2 domain, whose surface charge distribution more closely resembles that of other Ras effectors. As such, the RA1 domain appears to be somewhat redundant, at least in regard to regulation of PLCε by Ras [105].

5.3. Imaging interactions between Ras and PLCε

Until now, microscopy studies have played a fairly minor role in our understanding of how Ras regulates PLCε activity. Previous work using fluorescent constructs of PLCε in COS cells showed PLCε to have a cytosolic location, but to translocate to the plasma membrane upon EGF stimulation [125, 128]. This is in keeping with the theory that like other Ras effectors, PLCε is recruited to the membrane following Ras activation by GEFs further upstream. Nonetheless, a direct interaction between Ras and PLCε has not been verified in cells. To investigate whether such interactions could be observed between PLCε and Ras family GTP-ases, we cloned an EGFP fusion of PLCε in which the EGFP fluorophore was tagged to the protein's C terminus. Full length PLCε is a considerably large protein, in excess of 250kD. Possibly as a result of this, transfection of full length PLCε into cells is particularly difficult and usually results in very low expression levels. An appreciable amount of protein degradation may also be observed when cell lysates are analysed by Western blotting. For this reason, it was decided to use a truncated form in which the N-terminal CDC25 and REM domains were removed. This construct, denoted rPLCε-EGFP in the text, is shown below in Figure 5.5.

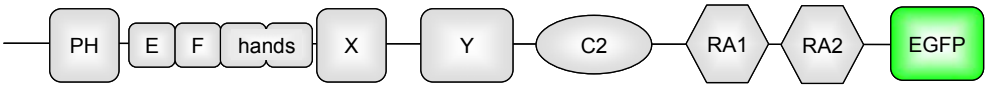


Figure 5.5: Truncated PLCε fusion protein (rPLCε-EGFP)

An mRFP fusion protein was also made for each of the three classic Ras isoforms, H, K and N-Ras. The mRFP was fused to the N terminus of each GTP-ase by a 6 amino acid linker. Each of these constructs was kindly provided by Dr. T. Bunney at the Institute of Cancer Research, London and was prepared as described in Chapter 4.

The Ras-mRFP fusions and the rPLCε-EGFP construct were assayed for expression and degradation in COS cells. Cells were transfected with plasmid DNA using a standard LipofectAmine protocol from *Invitrogen* and left to express for 24 hours, after which the cells were harvested and analysed by Western Blotting (see Chapter 4 for details). Ras proteins were probed using a monoclonal α-His primary antibody and the PLCε constructs were probed using an in-house PLCε monoclonal antibody. The same α-mouse secondary antibody was then used for each blot.

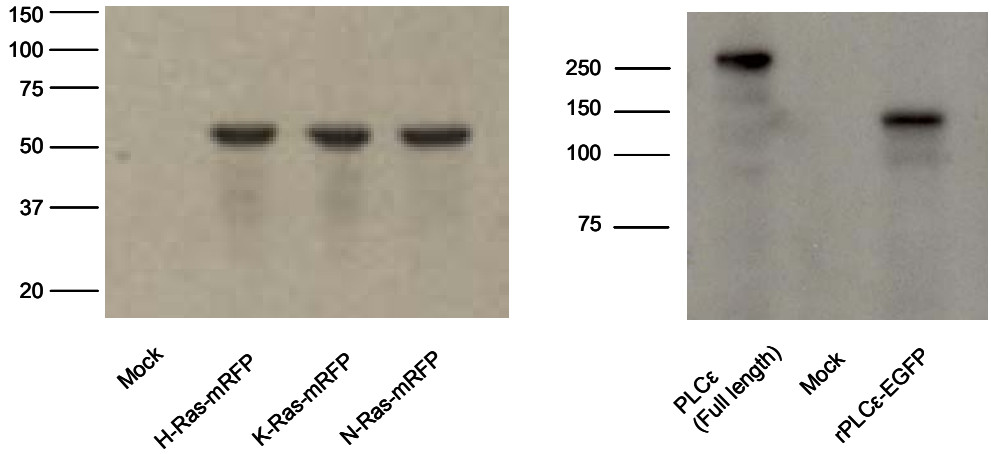


Figure 5.6: Western blots of mRFP-labelled small Ras GTP-ases (left) and rPLCε-EGFP (right), using whole cell lysates from transfected COS cells.

The blots in Figure 5.6 above show that each of the three Ras fusions H-Ras-mRFP, K-Ras-mRFP and N-Ras-mRFP were well expressed in COS cells without signs of any degradation. The rPLCε-EGFP construct was also seen to have negligible degradation, with a molecular weight of 150kD (c.f. 250kD for the full length protein in lane 1).

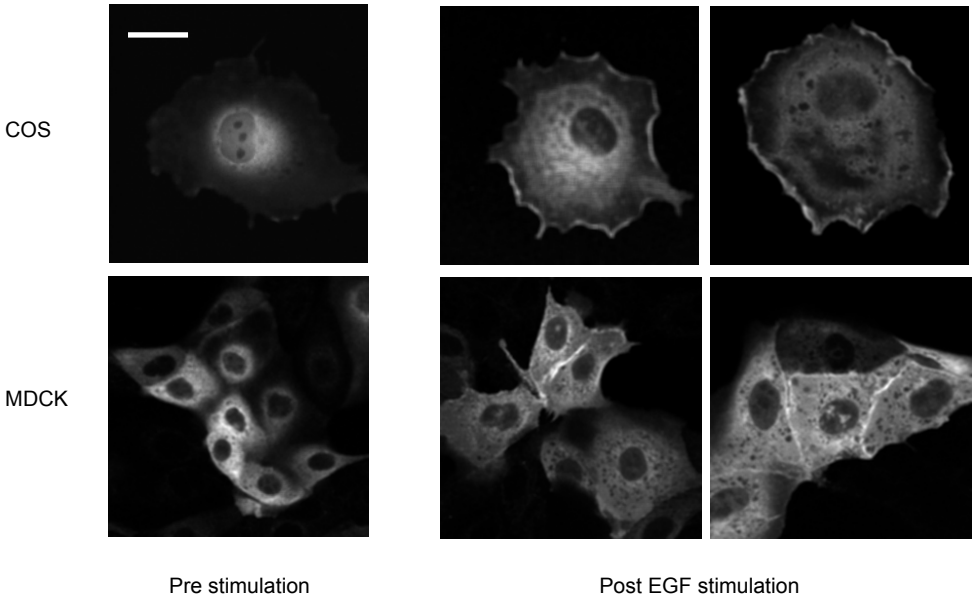


Figure 5.7: Localisation of rPLCε-EGFP in COS cells (top row) and MDCK cells (bottom row). In a small number of cells, rPLCε-EGFP was seen to translocate to the membrane in response to EGF stimulation. The left hand panel shows serum starved cells prior to stimulation. The 4 images in the right hand panel were acquired 10 - 30 mins post EGF stimulation. Scale bar = 15 μm.

Having established the viability of the constructs, we proceeded to image their localisation in cells on the microscope. Figure 5.7 shows images of serum starved COS cells and MDCK cells expressing rPLCε-EGFP prior to and after EGF stimulation. In order to obtain

consistent expression of rPLCε-EGFP, plasmid DNA was delivered directly to the cell nuclei using the technique of microinjection, with cells imaged 5-6 hrs post injection. In serum starved cells, rPLCε-EGFP was seen to have a mainly perinuclear localisation (Figure 5.7 left panel). In a small minority of cells, stimulation with EGF resulted in a sustained translocation to the membrane (Figure 5.7 right panel) – this agreed with previous reports by Song [126] and Sorli [128]. Many of the cells imaged did not respond, however, but maintained a perinuclear localisation.

5.3.1. FLIM-FRET studies of Ras and rPLCε-EGFP

The experiments above had shown that, on occasion, PLCε would undergo membrane translocation in response to EGF stimulation. In order to determine whether this was due to direct interactions between Ras and PLCε, we coexpressed fluorescent constructs of Ras-mRFP and rPLCε-EGFP in MDCK cells and performed FLIM measurements to measure FRET between the two. For FLIM, we used a TCSPC SPC-830 module (*Becker and Hickl GmBH*) in conjunction with a cooled photomultiplier tube (PMC-100, *Hamamatsu*) to obtain FLIM images of the EGFP donor. The PMT was connected to the external port of a Leica TCS SP5 confocal microscope. Single photon excitation was provided by a frequency doubled femtosecond Ti:Sapphire laser (Tsunami, *Spectraphysics*). A 30/70 partially reflecting mirror was used to separate the excitation from fluorescence, together with a 500-550 nm emission filter. Cells were imaged with a x63 1.40NA oil immersion objective.

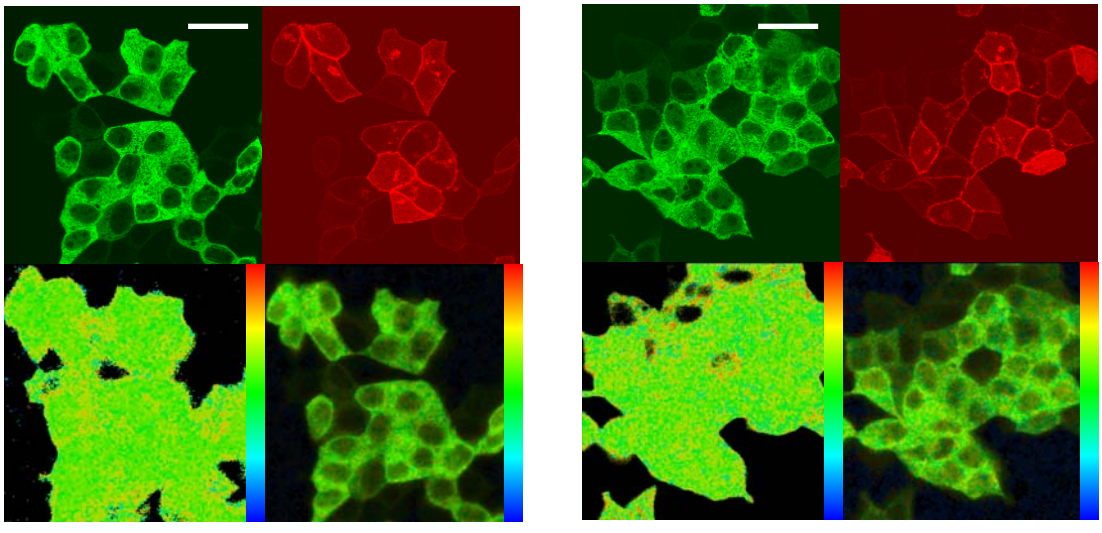


Figure 5.8: FLIM images of MDCK cells expressing rPLCε-EGFP and H-Ras-mRFP. The top row in each panel shows localisation images of rPLCε-EGFP (green) and H-Ras-mRFP (red). The bottom row in each panel shows the fluorescence lifetime map (left) and a merged image of lifetime with donor intensity (right). In both cases, the colorbar bounds are 2000 ps (blue) to 3000 ps (red). Scale bars = 20 μm

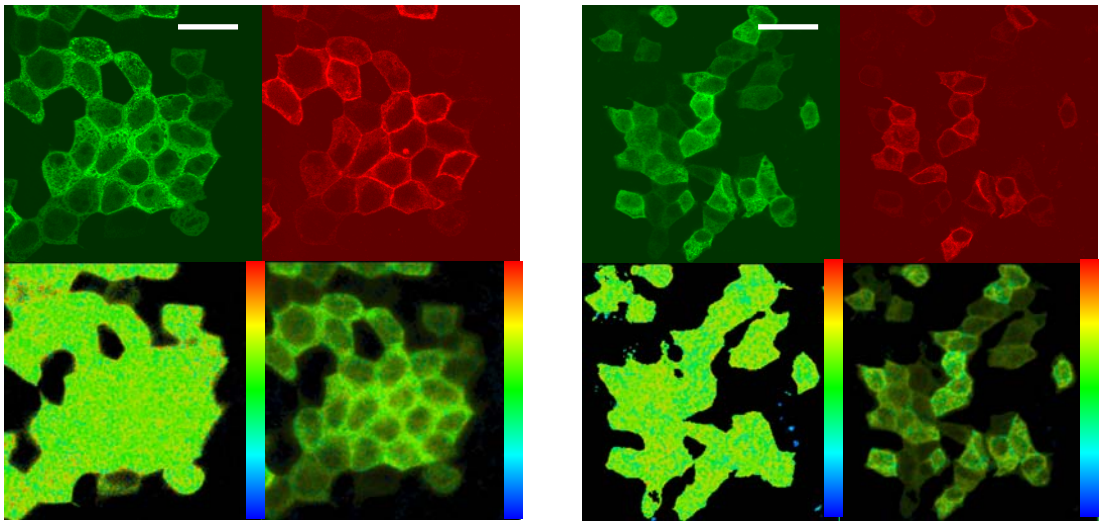


Figure 5.9: FLIM images of MDCK cells expressing rPLCε-EGFP and K-Ras-mRFP. The top row in each panel shows localisation images of rPLCε-EGFP (green) and K-Ras-mRFP (red). The bottom row in each panel shows the fluorescence lifetime map (left) and a merged image of lifetime with donor intensity (right). In both cases, the colorbar bounds are 2000 ps (blue) to 3000 ps (red). Scale bars = 20 μm.

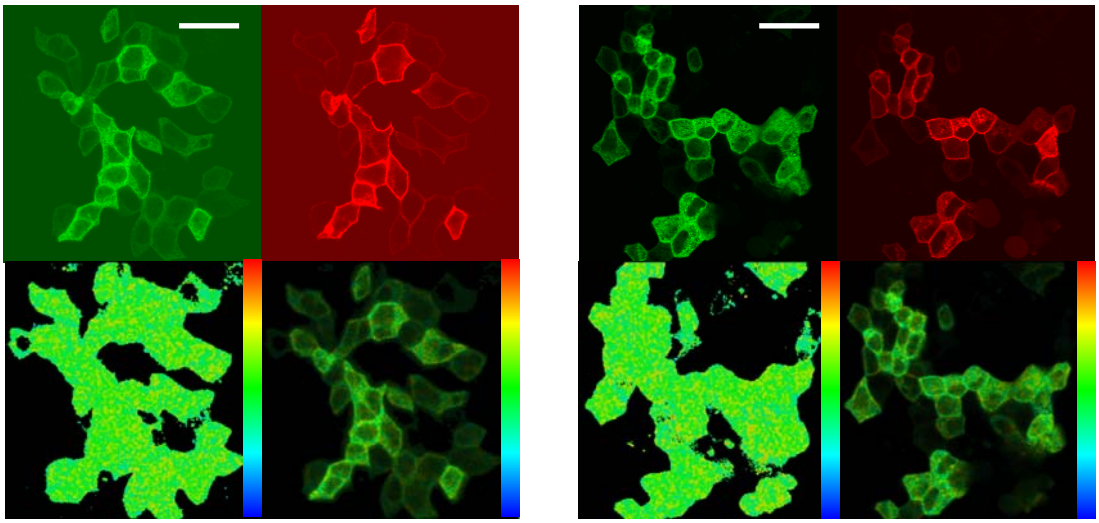


Figure 5.10: FLIM images of MDCK cells expressing rPLCε-EGFP and N-Ras-mRFP. The top row in each panel shows localisation images of rPLCε-EGFP (green) and N-Ras-mRFP (red). The bottom row in each panel shows the fluorescence lifetime map (left) and a merged image of lifetime with donor intensity (right). In both cases, the colorbar bounds are 2000 ps (blue) to 3000 ps (red). Scale bars = 20 μm.

Figures 5.8- 5.10 above show FLIM images of rPLCε-EGFP coexpressed with mRFP fusions of the 3 classic Ras isoforms in MDCK cells prior to and after stimulation with EGF. Each of the three Ras fusions was seen to localise primarily to the plasma membrane. The H and N isoforms were also seen to localise to the Golgi, whereas K-Ras-mRFP did not – this is in

keeping with published findings that K-Ras traffics to the membrane via a different mechanism to H-Ras and N-Ras [129, 130]. The images shown are representative of a number of fields of view. In most cases, lifetimes were found to be homogeneous throughout. In a small minority of cells where translocation of rPLCε-EGFP to the membrane was particularly evident, a small shift in lifetime was visible. Figure 5.11 shows FLIM images of rPLCε-EGFP in which FRET was observed at the cell membrane. Both series of images are of cells stimulated with EGF for 10 minutes.

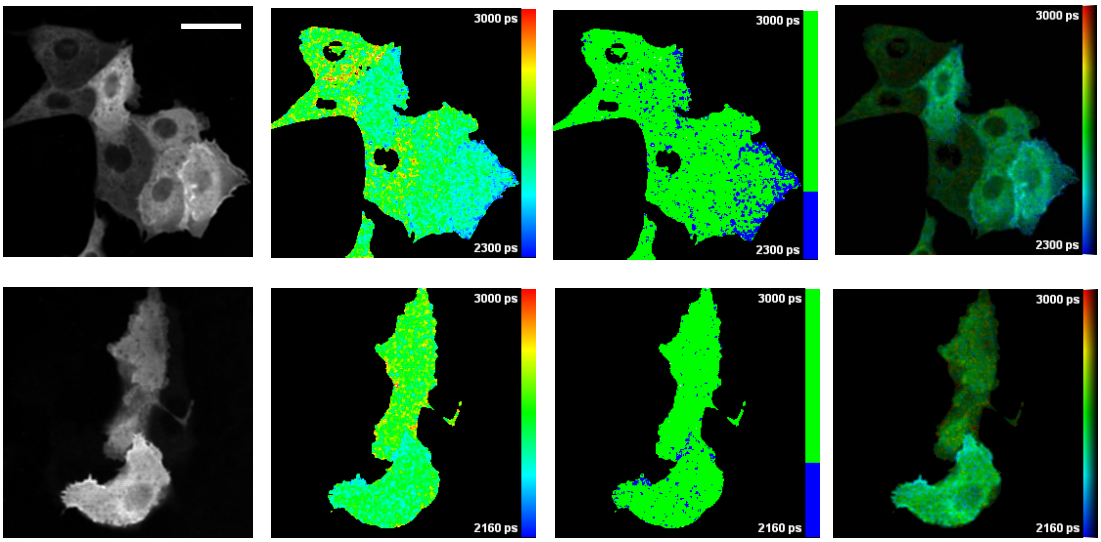


Figure 5.11: FLIM images from two fields of view of MDCK cells expressing rPLCε-EGFP and K-Ras-mRFP. From left: Intensity image of rPLCε-EGFP localisation, with membrane translocation particularly evident. Second from left: Fluorescence lifetime map (continuous color-scale). Third from left: Fluorescence lifetime map (binary color-scale, to emphasise the shorter lifetime seen at the cell membrane). Fourth from left: Intensity image merged with FLIM map (continuous color-scale). Scale bar = 10 μm.

The images in Figure 5.11 provide the first *in vivo* evidence of interactions between rPLCε-EGFP and K-Ras-mRFP at the plasma membrane. Given this result, the question is raised of why FRET was not observed more frequently following EGF stimulation. A possible answer might be that the interaction is highly transient and therefore the chance that the two proteins will be in complex at the point at which the cells are fixed is very small.

5.3.2. Studies of over-expressed Ras and PLCε

The cells imaged in section 5.3.1 were deemed to have a physiological expression level of Ras, as evidenced by its correct localisation to cellular compartments such as the Golgi and plasma membrane. It was found that at later time-points (7 hrs or more post microinjection) the small GTP-ases became heavily overexpressed, presumably owing to the high plasmid

copy number introduced to the cells at time of injection. Such cells exhibited enhanced brightness when viewed in the microscope and more importantly, mislocalisation of Ras to different cellular compartments and the cytosol. This issue of mislocalisation (trafficking of overexpressed proteins away from sites of endogeneously expressed protein) is a common occurrence amongst small GTP-ases that require post-translational modification and so rely on further enzymatic interactions before being targeted to the correct cellular compartment, most often the plasma membrane [130]. High levels of overexpression can cause a backlog of protein waiting to be processed, with result that Ras is retarded on endomembranes or released into the cytoplasm.

In some cases following prolonged expression of Ras, an interesting feature was observed. The rPLCε-EGFP and Ras-mRFP were seen to colocalise within the cytosol, and when FLIM-FRET measurements were performed on the microscope, these cells exhibited a noticeable decrease in mean lifetime of the EGFP donor (Figures 5.12 and 5.13). This was confined to cells in which Ras expression was particularly high and where the contrast between the membrane and cytosolic fractions was quite diminished.

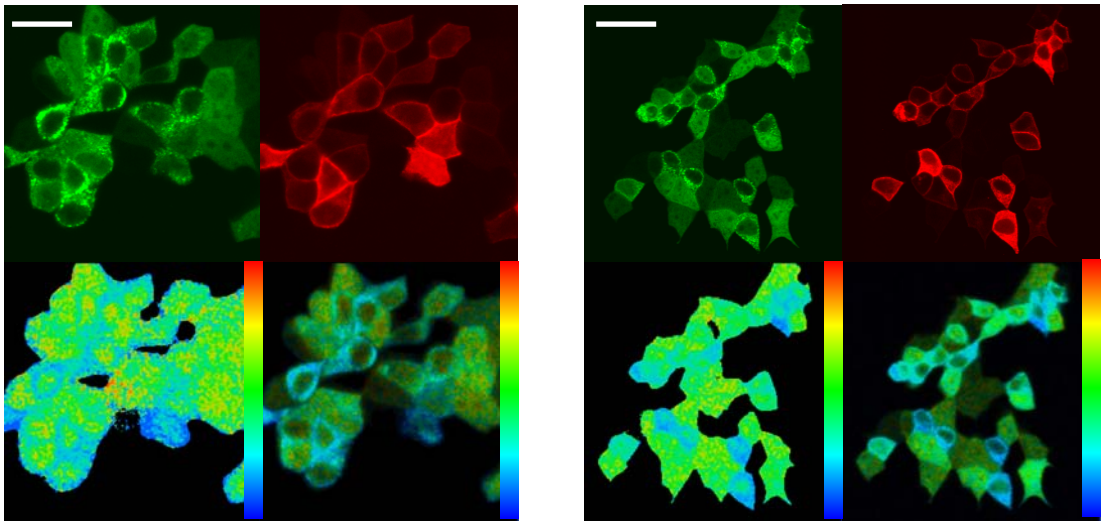


Figure 5.12: FLIM images of MDCK cells overexpressing rPLCε-EGFP and K-Ras-mRFP. The top row in each panel shows localisation images of rPLCε-EGFP (green) and K-Ras-mRFP (red). The bottom row in each panel shows the fluorescence lifetime map (left) and a merged image of lifetime with donor intensity (right). The colorbar bounds are 2000 ps (blue) to 3000 ps (red). EGF was not used to treat the cells in either data set. Scale bars = 20 μm.

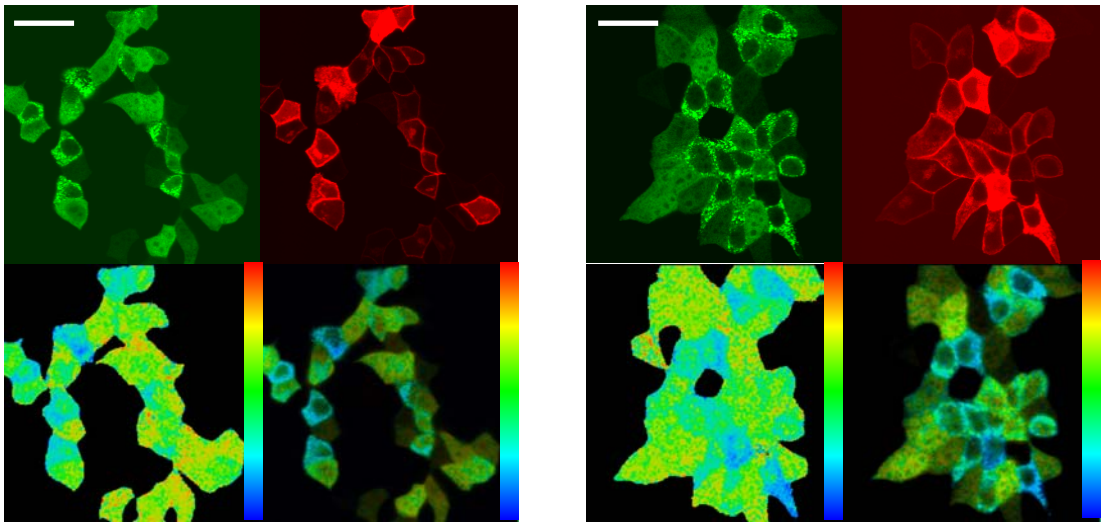


Figure 5.13: FLIM images of MDCK cells overexpressing rPLCε-EGFP and H-Ras-mRFP. The top row in each panel shows localisation images of rPLCε-EGFP (green) and H-Ras-mRFP (red). The bottom row in each panel shows the fluorescence lifetime map (left) and a merged image of lifetime with donor intensity (right). The colorbar bounds are 2000 ps (blue) to 3000 ps (red). EGF was not used to treat the cells in either data set. Scale bars = 20 μm.

The results of any such experiments where Ras or another small GTP-ase is heavily overexpressed must be treated with caution. At any one time, the cellular pool of Ras will exist in an equilibrium between GDP and GTP bound forms. Overexpression of wild type Ras may itself shift this equilibrium towards a higher concentration of activated Ras, with consequences of tumorigenicity [131]. Cells with high overexpression should not therefore serve as examples of physiological behaviour. This said, the data obtained from such experiments can be informative, provided it is interpreted in the correct fashion. The results above suggest interactions do occur between rPLCε-EGFP and H-Ras-mRFP when the latter is expressed at high levels. That this effect is only seen in cells which have particularly high level of Ras expression might reflect an inherently weak affinity of the interaction.

5.3.3. Studies of RA2 domain interaction with Ras

The argument put forward in section 5.3.1 to explain the rare occurrence of FRET between rPLCε-EGFP and Ras-mRFP was that any such interaction would be a transient one, and therefore would only be captured in a small number of cells imaged. An alternative explanation might be that these interactions are of longer duration, but the two fluorescent labels are only spaced within the requisite distance of one another for part of this time. Upon binding, conformational changes in PLCε, or interaction with additional membrane components could shift the orientation of the two fluorophores with result that FRET between them would quickly diminish. Such a conjecture would be difficult to prove in

practice, since it would require evidence of a conformational change in PLCε upon binding to Ras. Nonetheless, one could speculate from this that if only the RA2 domain were expressed, any FRET signal between Ras and RA2 would be more prolonged, since no such conformational change would follow the formation of a complex. To test this hypothesis, we coexpressed pTriEx4/H-Ras-mRFP and pEGFP/PLCε(RA2) in MDCK cells and COS cells which were then fixed prior to and after EGF stimulation. FLIM-FRET experiments were then performed as described above.

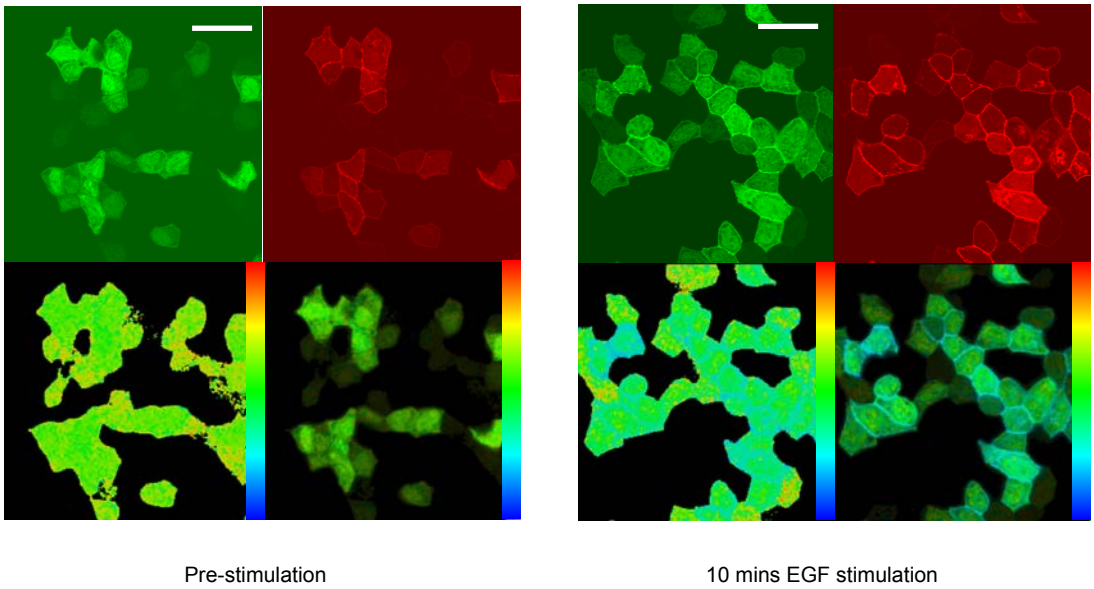


Figure 5.14: FLIM images of MDCK cells expressing PLCε(RA2)-EGFP and H-Ras-mRFP. The top row in each panel shows localisation of PLCε(RA2)-EGFP (green) and H-Ras-mRFP (red). The bottom row in each panel shows the fluorescence lifetime map (left) and a merged image of lifetime with donor intensity (right). The colorbar bounds are 2100 ps (blue) to 3000 ps (red). Scale bars = 20 μm.

Figures 5.14 above and 5.15 below show FLIM images of PLCε(RA2)-EGFP in cells coexpressing H-Ras-mRFP stimulated with EGF. A clear FRET signal was indeed seen in the membrane of these cells, suggesting that the RA2 domain does interact specifically with Ras at the membrane and for a prolonged period of time. Similar results were also seen where K-Ras-mRFP was expressed.

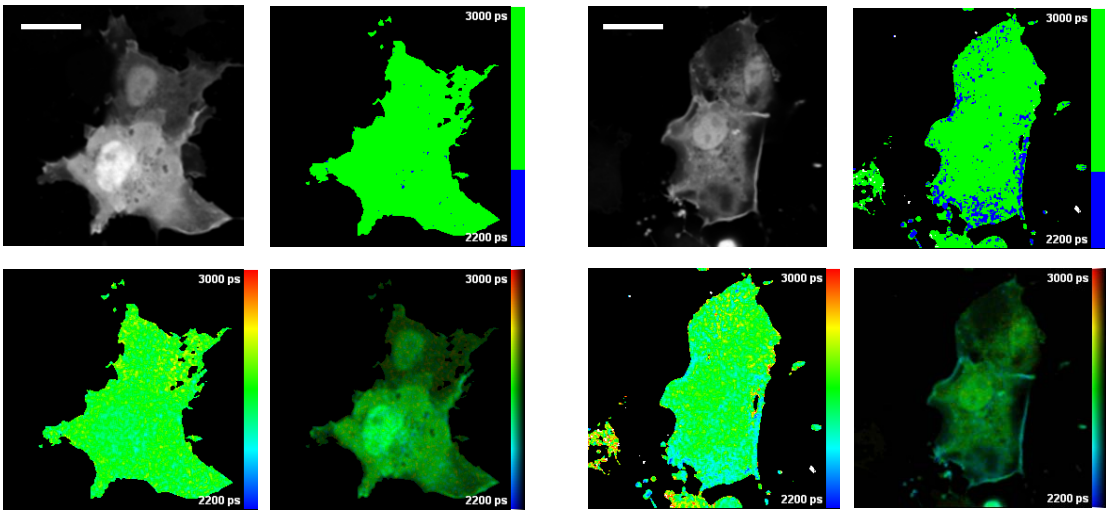


Figure 5.15: FLIM images of PLCε(RA2)-EGFP in COS cells coexpressing H-Ras-mRFP. Top left: Intensity image, top right: Fluorescence lifetime (discrete lifetime scale), bottom left (continuous lifetime scale), bottom right: lifetime merged with intensity image. Scale bars = 10 µm.

5.3.4. Comparison of interactions with Raf-RBD

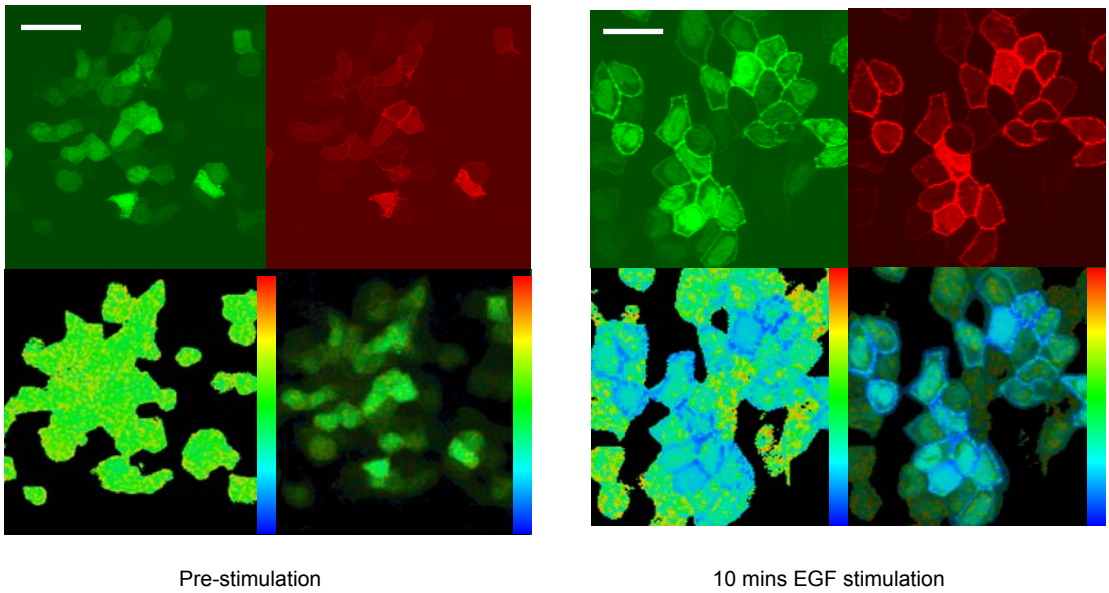


Figure 5.16: FLIM images of MDCK cells expressing Raf-RBD-EGFP and H-Ras-mRFP. The top row in each panel shows localisation images of Raf-RBD-EGFP (green) and H-Ras-mRFP (red). The bottom row shows the fluorescence lifetime map (left) and a merged image of lifetime with donor intensity (right). The colorbar bounds are 2100 ps (blue) to 3000 ps (red). Scale bars = 20 µm.

The FRET signal observed from cells expressing PLCε(RA2)-EGFP and H-Ras-mRFP provided a means to compare this interaction with that of another Ras effector – the Ras binding domain of C-Raf-Kinase (Raf-RBD). MDCK cells were coinjected with DNA

encoding pTriEx4/H-Ras-mRFP and pEGFP/C-Raf-RBD as previously described [104] and FLIM measurements performed (Figure 5.16). These experiments were also repeated in COS cells transfected with the same plasmids (Figure 5.17).

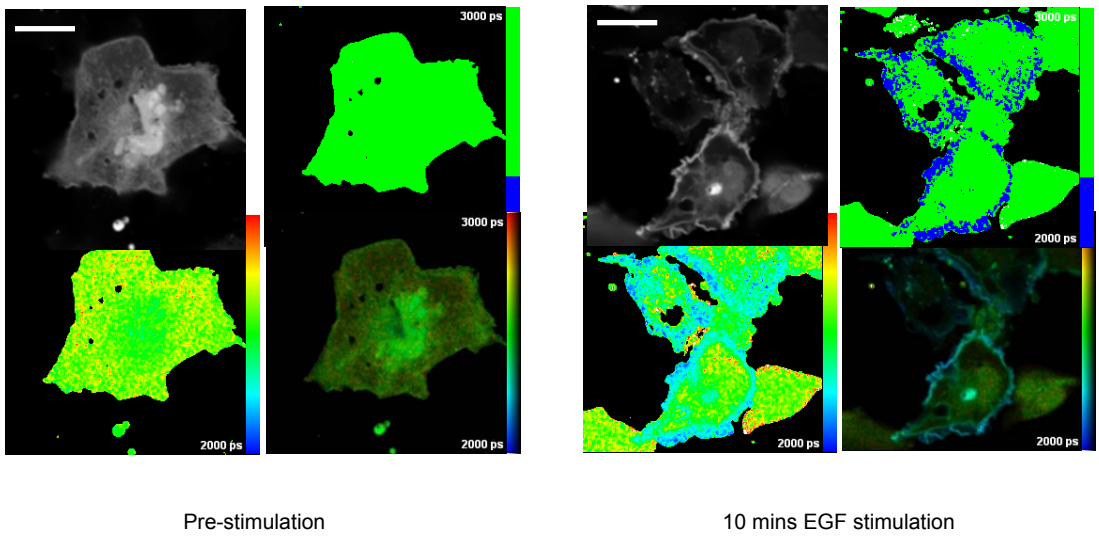


Figure 5.17: Fluorescence lifetime images of Raf-RBD-EGFP in MDCK cells coexpressing H-Ras-mRFP. Top left: Intensity image, top right: Fluorescence lifetime (discrete lifetime scale), bottom left (continuous lifetime scale), bottom right: lifetime merged with intensity image. Scale bars = 10 μm.

To compare the results from cells expressing PLCε(RA2)-EGFP and Raf-RBD-EGFP, a region of interest was defined about the membrane in images of both constructs, and the lifetime histograms compiled for both this region and the image as a whole. Figure 5.18 below shows representative results for the two different effectors.

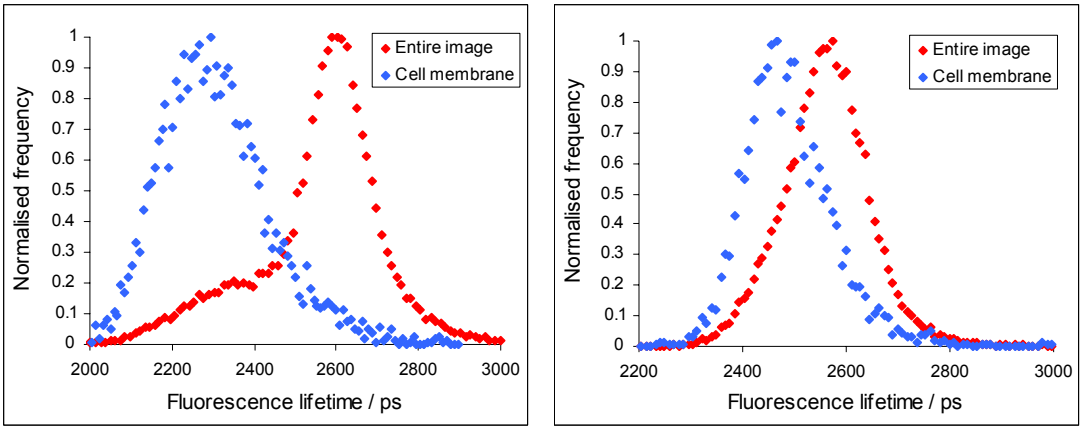


Figure 5.18: Fluorescence lifetime histograms of Raf-RBD-EGFP (left) and PLCε(RA2)-EGFP (right) in COS cells expressing H-Ras-mRFP. Both pairs of constructs showed a fall in lifetime at the membrane compared to the cytoplasmic fraction, although this shift was smaller in the case of PLCε(RA2)-EGFP.

The greater shift in lifetime seen between Raf-RBD-EGFP and H-Ras-mRFP could indicate a closer proximity of the EGFP and mRFP fluorophores (or more favourable orientation) when these two species are in complex. This is perhaps unlikely, since although neither the RA1 nor RA2 domain of PLCε share a high degree of primary sequence homology with the Ras binding domain of Raf, their tertiary structures are highly similar. Given this similarity, it is perhaps more likely that the stronger FRET signal arises instead from a higher binding affinity between Ras and C-Raf RBD, compared to PLCε(RA2). Although reports vary, the dissociation constant for the RA2/Ras complex has been measured to be in the low micromolar range [132] compared to that for Ras/Raf-RBD which is in the nanomolar range. Thus, the results above would seem to confirm that the RA2 domain is a genuine Ras binding domain which will bind to Ras in cells, albeit with lower affinity than C-Raf RBD.

5.4. Summary

This chapter has investigated the scope for imaging the interactions between small Ras GTP-ases and the effector PLCε using FLIM-FRET microscopy. FRET was clearly visible between the EGFP-labelled PLCε(RA2) domain and H-Ras-mRFP at the plasma membrane following EGF stimulation in COS and MDCK cells. Similar results were also seen in the context of a truncated rPLCε –EGFP construct with the N terminal CDC25 and REM deleted, although only in a very small minority of cells imaged. Furthermore, a shorter EGFP lifetime was measured in cells in which rPLCε-EGFP and H-Ras-mRFP or K-Ras-mRFP were overexpressed to a high degree, indicating a possible interaction at non-specific sites within the cell.

Taken together, these results confirm previous work suggesting that Ras/PLCε interactions are mediated by the RA2 domain of the protein, which binds Ras at the plasma membrane. The fact that FRET was only seen between the larger rPLCε-EGFP construct and H-Ras-mRFP or K-Ras-mRFP in a very small number of cells suggests that the dynamics of this interaction differ considerably from the isolated RA2 domain. This discrepancy could be explained in a number of ways. One possibility is that the interaction between rPLCε and Ras is a transient one and that once brought to the membrane, PLCε ceases to bind Ras and instead interacts with other membrane components en route to substrate hydrolysis. Perhaps more likely is that upon binding, rPLCε undergoes some form of conformational change with a resultant change in distance between the two fluorescent labels. Assuming an increase in separation, one would then only detect FRET in the short period between PLCε being recruited to the membrane and its subsequent activation. This hypothesis would also explain

why rPLCε-EGFP was often seen to localise at the membrane without showing signs of FRET, whereas the isolated PLCε(RA2)-EGFP had a sustained FRET signal at all times after binding to Ras at the membrane.

The results of the overexpression studies, whilst treating them with caution, do also provide evidence of a direct interaction between PLCε and Ras. More generally, they highlight an important consideration when using FRET to image protein-protein interactions. In order to successfully resolve the binding between two proteins, one requires a sufficiently high FRET signal that can be disseminated from the background. Here, background relates not only to the underlying noise in the measurement, but also to the additional signal emanating from unbound donors and acceptors. This signal may often mask the underlying FRET if the fractional population of molecules in complex is much smaller than that of the unbound species. The equilibrium between these states will be determined primarily by the binding affinity (the degree to which a complex is more energetically favourable than the two partners remaining apart). That FRET was not observed more frequently between these proteins when expressed at lower concentrations may be a reflection of their small binding affinity; overexpression of Ras would shift this equilibrium towards a greater fraction of bound species, hence a greater proportion of 'FRETting' donors. A similar conclusion can also be drawn when comparing FRET between Ras and Raf-RBD with that between Ras and PLCε(RA2), for which the reported dissociation constant is a magnitude greater.

Chapter 6: High speed optically sectioned FLIM to image FRET in live cells

6.0. Chapter overview

This chapter discusses the use of a quasi wide-field, optically sectioning microscope for fast imaging of FLIM-FRET in live cells. The microscope uses a wide-field time-gated strategy for fluorescence lifetime imaging coupled with a Nipkow spinning disc confocal scan head to obtain optically sectioned images. A comparison is made between this system's performance and that of the commercially available laser scanning confocal microscope discussed in the previous chapter. Here, performance is assessed with respect to the error in the measured lifetime across an image when different integration times are used. The enhanced speed of this instrument permitted us to obtain images with greater signal-to-noise for shorter acquisition times and shows promise for increasing the temporal resolution of FLIM-FRET time-lapse imaging.

6.1. Motivation for this work

To date, the majority of live cell FRET experiments reported in the literature have relied on spectral ratiometric imaging of donor / acceptor pairs. Whilst certainly valid, this approach possesses the drawback that differences in donor and acceptor concentration can give rise to artefacts in the measured intensity ratio. It is therefore mainly applicable to intramolecular FRET studies, where the donor/acceptor stoichiometry is always constant. FLIM-FRET, which is applicable to both intra- and intermolecular FRET studies, has by contrast been under-utilised. This is in part owing to the more complex nature of fluorescence lifetime measurements and instrumentation but also to the comparatively long acquisition times required on commercially available FLIM microscopes, the majority of which use TCSPC.

One of the main issues that arose during the course of experiments discussed in Chapter 5 was in fact the length of time required for each acquisition. Although this could partly be explained by the low expression levels of rPLCε-EGFP, the same can not be said for other constructs studied, for example EGFP-Raf-RBD, for which acquisition times were still on the order of minutes. In this case, the long acquisition time was not attributable to the inherent sample brightness, but rather to other factors that limited the rate of photon collection at the detector. These factors included the need to avoid pulse-pile-up effects, amd

the necessity for low excitation powers in order to prevent extensive photobleaching of the sample. Through use of a different FLIM strategy, we have shown that it is possible to overcome these limitations and so achieve the fast acquisition times required for imaging these interactions in live cells.

6.2. Considerations for high speed FLIM

For high speed FLIM-FRET microscopy, two main criteria must be satisfied. First, the spatial resolution must be sufficient to resolve the various organelles under observation and secondly, the signal to noise in each pixel must be high enough to ensure an accurate measurement of fluorescence lifetime on the desired timescale. This second point will depend on the number of photons that can be collected from the sample in a given time and the noise from the detector used to temporally resolve the fluorescence.

Although TCSPC offers the highest signal to noise measurement (per emitted photon) of any FLIM technique, it is by its nature a point detection method, hence choosing this as a means for resolving the fluorescence decay places a restraint on the number of pixels that can be imaged in parallel. Wide-field excitation and detection enables one to gather light from multiple pixels at once and maximise the overall photon collection rate, but conventionally this is at the expense of optical sectioning. A system that combined the elements of parallel pixel acquisition with optical sectioning would be highly desirable for live cell FLIM-FRET studies of protein-protein interactions, including those between Ras and its effectors. This was the motivation for the work discussed in this chapter.

6.3. Wide-field Fluorescence Lifetime Imaging

Wide-field fluorescence lifetime imaging has been described in both the time-domain and frequency-domain [64, 68]. Traditionally, wide-field time domain FLIM has been the more expensive and therefore less frequently used option. This was largely owing to the need for an ultrafast laser for pulsed excitation. More recently, the growing availability of such lasers and the additional benefits they provide has worked to redress the balance. These advantages include the spectral tunability achievable through non-linear processes (second harmonic generation, optical parametric amplification, etc) as well as the potential for multiphoton excitation where deep penetration into thick samples is required.

The principal components used for wide-field time domain FLIM are shown in Figure 6.0. Wide-field FLIM images are captured by using an ultrafast laser for pulsed excitation and a gated optical intensifier (GOI) for temporally resolving the fluorescence decay. The GOI functions as a shutter which opens at a specific point during the course of the fluorescence decay, allowing the intensity at that part of the decay to be captured on the CCD. The shutter is triggered by a signal from the laser, and can be set to open at different time points by changing the delay on the delay generator.

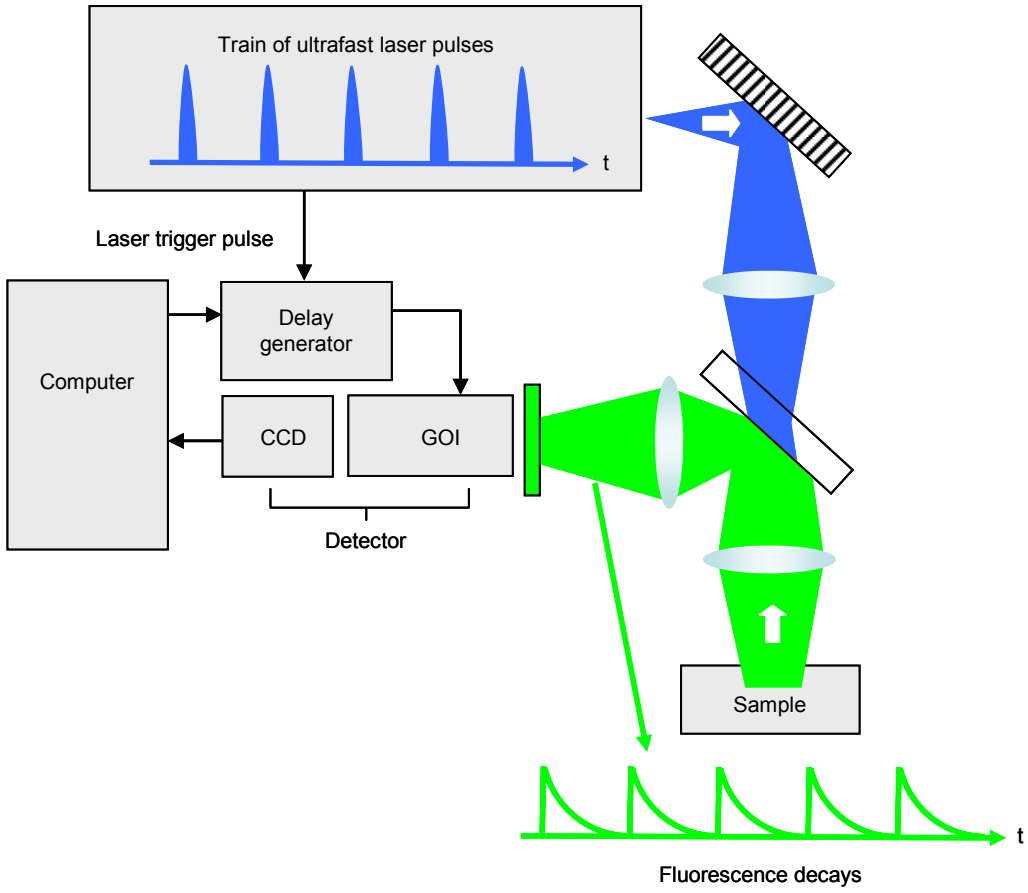


Figure 6.0: Instrumentation for wide-field time-gated fluorescence lifetime imaging.

6.4. Implementing optical sectioning in wide-field microscopy

A number of methods now exist for implementing optical sectioning in a wide-field microscope. These include deconvolution and structured illumination microscopy, both of which have been demonstrated to provide high resolution sectioned images at fast frame rates [48-50]. These techniques require post processing of multiple images, however, which can dramatically reduce the bit depth in the final image. This is especially important when combined with FLIM [133]. It is generally preferable to use a method in which a truly

sectioned image is acquired on the detector. One device that provides this to a good approximation is the spinning disc or Nipkow disc microscope, which can acquire optically sectioned images at far higher frame rates than that possible in a standard point scanning confocal microscope. The first example of this type of instrument was developed in the 1960s by Petran and Hadravsky, known as the Tandem Scanning Microscope [134]. This was later refined in the Real Time Scanning Optical Microscope of Kino and Corle [135]. The main feature of these instruments is a disc perforated with a series of pinholes, such that when an expanded laser beam is shone through the disc, a number of individual beams are formed. Each of these beams is focussed to a different point on the sample and the fluorescence from each point imaged back through the same pinhole to a detector. The principle is therefore akin to a confocal microscope, except that multiple points are imaged in parallel. Rotating the disc causes the position of each beam at the sample to change, illuminating a new series of points in the sample plane. This parallelism reduces the time taken to scan a field of view to the extent it becomes possible to use a wide-field detector such as a CCD. The Nipkow disc can achieve similar axial resolution to that of a confocal microscope while maintaining the benefits of speed provided by parallel pixel acquisition.

6.5. High power supercontinuum sources for FLIM

The discussion above suggests that a wide-field FLIM strategy, coupled with a spinning disc microscope should meet the necessary requirement for fast, optically sectioned fluorescence lifetime imaging and indeed, this approach has already been demonstrated in both the time [136] and frequency domains [137, 138]. To date, however, these systems have had limited application in imaging of live cell protein-protein interactions. One might question why this is the case – given the parallel pixel acquisition, speed should not be an issue. This is to overlook one vital aspect, however: the amount of light available for excitation.

In order for the Nipkow disc to provide optimal sectioning, it is necessary that the holes in the disc be placed sufficiently far apart. If spaced too close together, light from outside of focus might then reach the detector by passing through pinholes adjacent to that used for excitation of a particular spot. The distance between adjacent pinholes must therefore be large enough to offset this, which will in turn limit the amount of excitation light. The issue of low disc transmission has been addressed to large degree in the CSU series of microscopes released by *Yokogawa Electric Corporation* (Japan). In this system, a second array of microlenses is used to focus light more efficiently through each pinhole, increasing the disc's transmission by an order of magnitude. (Figure 6.1) [139].

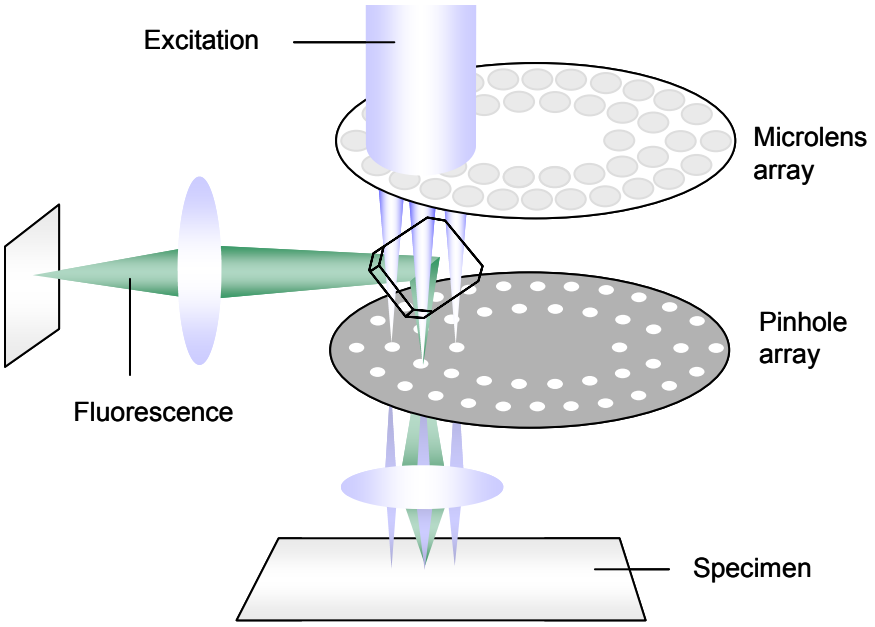


Figure 6.1: The Yokogawa CSU10 microscope series uses an array of microlenses to focus light through each hole in the Nipkow disc. Each microlens is aligned with a single pinhole and the two discs rotate together in synchrony This increases the transmission of excitation light through the disc whilst keeping the spacing between pinholes large enough the preserve the optical sectioning effect.

Even allowing for the increased transmission efficiency of the CSU, a particularly powerful light source is required in order to overcome the loss at the disc and to date, this has been a limiting factor in realising the promise of such systems for live cell FLIM-FRET. This is particularly true in the time domain where the need for pulsed excitation places further constraints on the sources that can be used. For visible fluorophores such as EGFP, one might consider using a frequency doubled Ti:Sapphire laser, however, the gain profile of such lasers tails off toward 950 nm, with a concurrent fall in the efficiency of second harmonic generation at wavelengths used to excite such fluorophores. Pulsed laser diodes also cannot offer sufficient power for this application.

A solution to this problem has, nonetheless, recently become available. Novel laser sources, based on supercontinuum generation in microstructured “photonic crystal fibre” (PCF) can now provide output powers of several mW/nm across the entire visible spectrum [140, 141]. The term supercontinuum generation encompasses a series of non-linear optical processes that combine to result in the spectral broadening of an input light signal, usually a femtosecond or picosecond pulse from a mode-locked fibre laser / solid state laser, although continuum generation based on nanosecond pulses has also been demonstrated [142]. Spectral broadening of the pulse within the PCF arises from a complex interplay of self phase modulation (SPM), four wave mixing (FWM), raman scattering and soliton formation and subsequent fission [143, 144]. These non-linear processes require high intensities of

light, hence the need for tight confinement of the pulse within a particular waveguide structure. That such lasers have now become commercially viable owes much to developments in both microstructured fibre technology and high power ultrafast fibre lasers [145-147] and their application in microscopy, including FLIM, is a growing source of interest [148-150].

6.6. Set up for high speed Nipkow disc FLIM microscope

Based on the above discussion, we decided to revisit the concept of using a Nipkow disc to obtain optical sectioning in a wide-field FLIM microscope, using a high power supercontinuum source to ensure sufficient light for excitation. Figure 6.2 shows the instrumental set up.

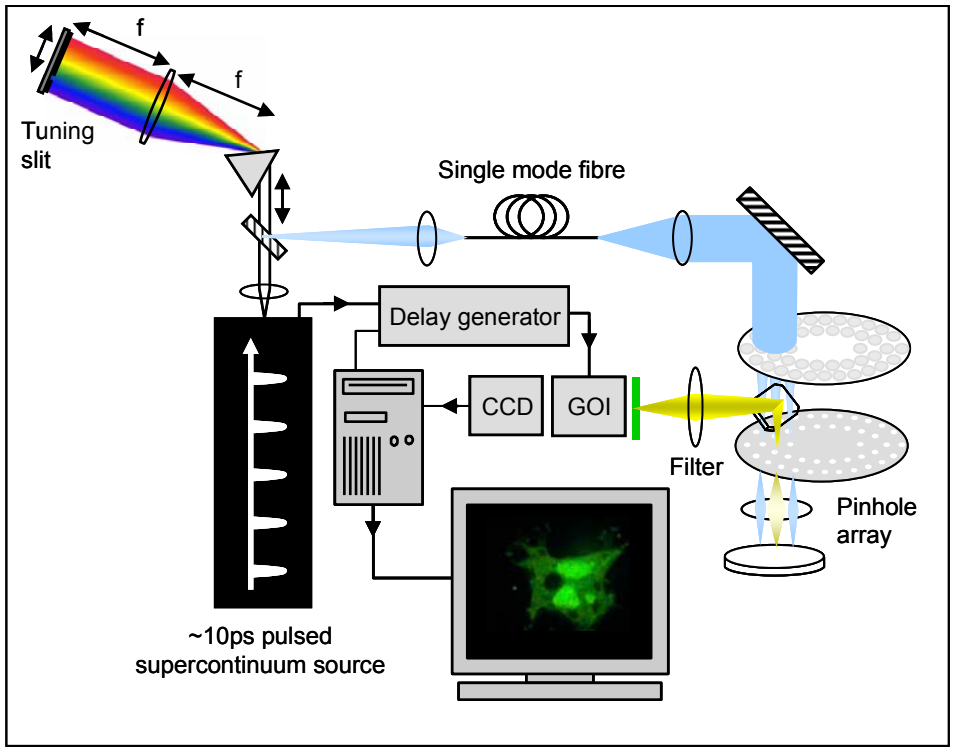


Figure 6.2: Optical set up for wide-field optically sectioning FLIM microscope.

For efficient excitation of EGFP labelled constructs, we employed a 50 MHz pulsed supercontinuum (*Fianium*, model SC450-2), with spectral power density 2 mW / nm in the wavelength range 470-490 nm. The laser output spectrum was dispersed by a prism on to a mirror and the excitation wavelength band selected by varying the position and width of a slit directly in front of the mirror, before recollimating the back reflected light. This was then coupled into a single mode fibre using a 0.17NA aspheric objective, and the fiber connected to the input of a CSU10 confocal spinning disc unit (*Perkin Elmer*, UK).

The CSU scan head itself is a stand-alone unit that can be connected at the camera port of an inverted laboratory microscope. Excitation light is introduced to the unit by a single mode fiber from where it is directed to the sample plane of the microscope (Figure 6.3).

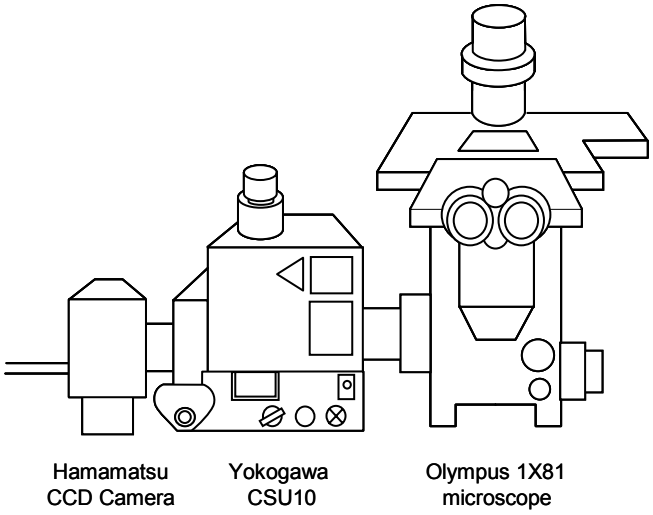


Figure 6.3: Schematic of Yokogawa CSU10 scan head, microscope and CCD camera. (The GOI, which for FLIM measurements is placed between the CSU10 and CCD, is not shown in this figure).

The excitation and fluorescence light paths inside the CSU10 are shown in Figures 6.4 and 6.5 below. Light is coupled into the unit through a single mode fibre. The beam is collimated and reflected off a series of mirrors to the microlens array and pinhole disc. The fluorescence is imaged back through the disc, and reflected by the dichroic mirror to the camera port.

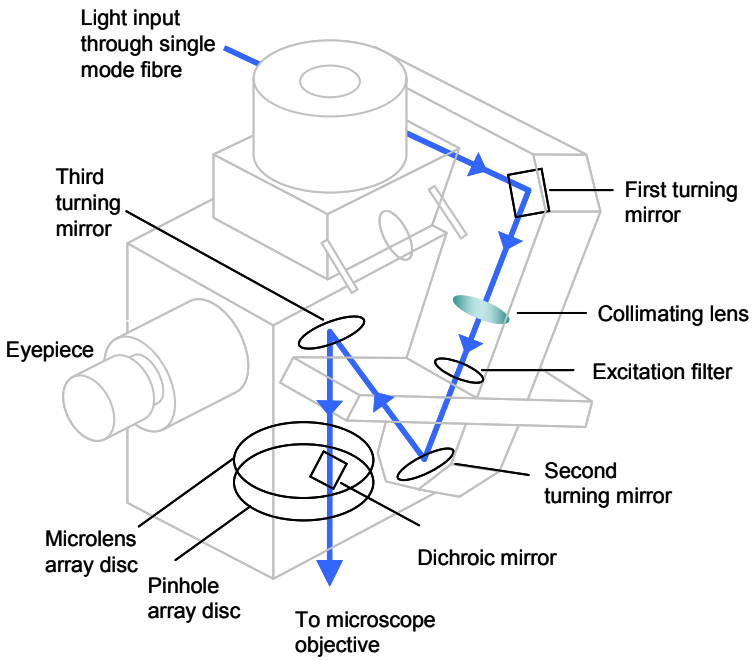


Figure 6.4: Excitation light path in Yokogawa CSU10 scan head

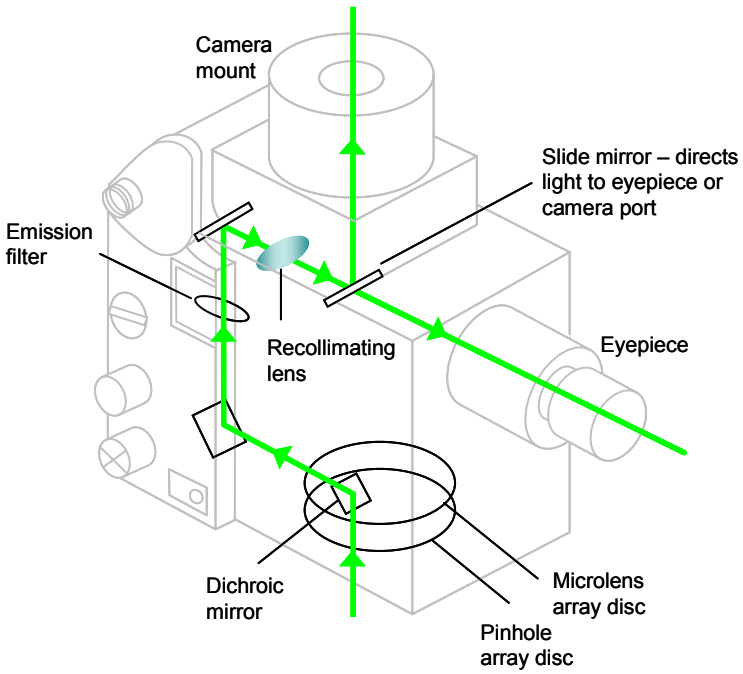


Figure 6.5: Fluorescence light path in the Yokogawa CSU10 scan head

For fluorescence lifetime measurements, we used a gated optical intensifier (*Kentech Instruments*, model number HRI) in conjunction with a solid state electronic delay box (HDG, also from *Kentech Instruments*). The latter can switch between delays in approximately 1 ms, permitting images to be acquired at numerous time gates without substantial penalty in acquisition time. The phosphorescence from the HRI was imaged by a set of camera relay lens onto a 12 bit high resolution Peltier cooled ORCA-ER camera (*Hamamatsu*). This camera has a chip size of 8.58 mm x 6.86 mm with 1344 x 1024 pixel elements. The dark current in the camera is quoted at 0.1 electrons / pixel / second.

6.7. Preliminary FLIM experiments

As a preliminary test of the system, we acquired a z-stack of FLIM images from COS cells expressing EGFP labelled Raf-RBD and H-Ras-mRFP which were stimulated with EGF for 10 minutes. A series of 5 time-gated images was acquired for each layer in the stack, with a 1 second integration time per image, using the maximum 1000 ps gate width on the HRI. The results of this are shown in Figure 6.6, for which the total acquisition time was 120 seconds. By comparison, a 3D FLIM stack acquired on our confocal TCSPC FLIM microscope would typically take tens of minutes. Figure 6.6 highlights both the optical sectioning capabilities of the microscope and the temporal resolution in the lifetime decays, as evidenced by the clear FRET signal around the cell membrane.

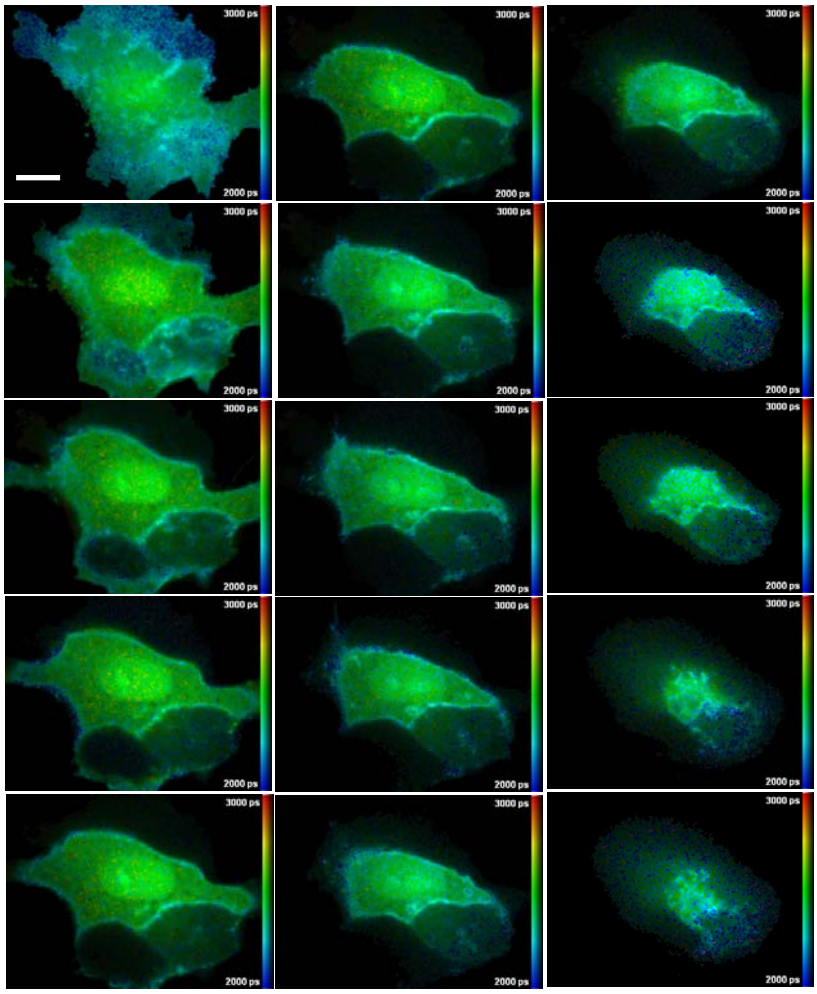


Figure 6.6: Sectioned image stack through a COS 7 cell expressing H-Ras-mRFP and Raf-RBD-EGFP, displaying FRET at the plasma membrane following stimulation by epidermal growth factor EGF. Each image was recorded in 5 s, with a 120 s total acquisition time (Scale bar = 10μm)

6.8. Comparison of wide-field system with confocal TCSPC

A comparison was made between the signal to noise in FLIM images obtained with the Nipkow disc FLIM microscope and those using a commercial confocal microscope with time correlated single photon counting. For these experiments, we used an SPC-830 TCSPC module (*Becker and Hickl GmBH*) in conjunction with a PMC-100 cooled photomultiplier tube (*Hamamatsu*) to obtain fluorescence lifetime images. The PMT was connected to the external port of a Leica SP2 confocal microscope. Single photon excitation was obtained by frequency doubling of a Ti:Sapphire Laser (Tsunami, *Spectraphysics*) which was coupled into the microscope. A 490 nm dichroic mirror was used in both the Nipkow disc microscope and SP2 confocal microscope, together with a 500-550 nm band pass filter in the emission channel. To account for the slight difference in axial resolution, the pinhole in the SP2 microscope was opened to obtain an equivalent axial PSF to that of the Nipkow disc.

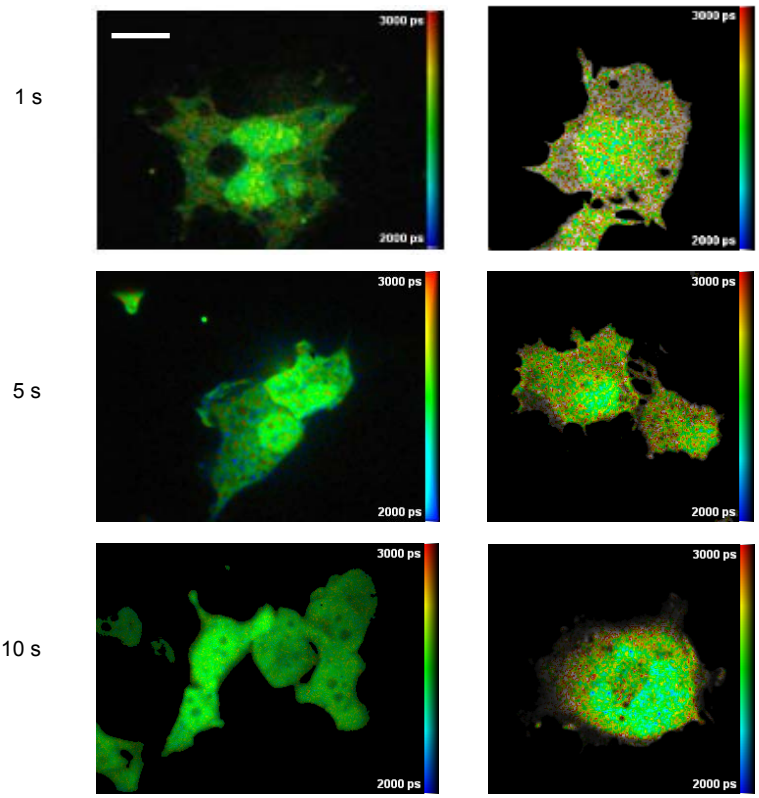
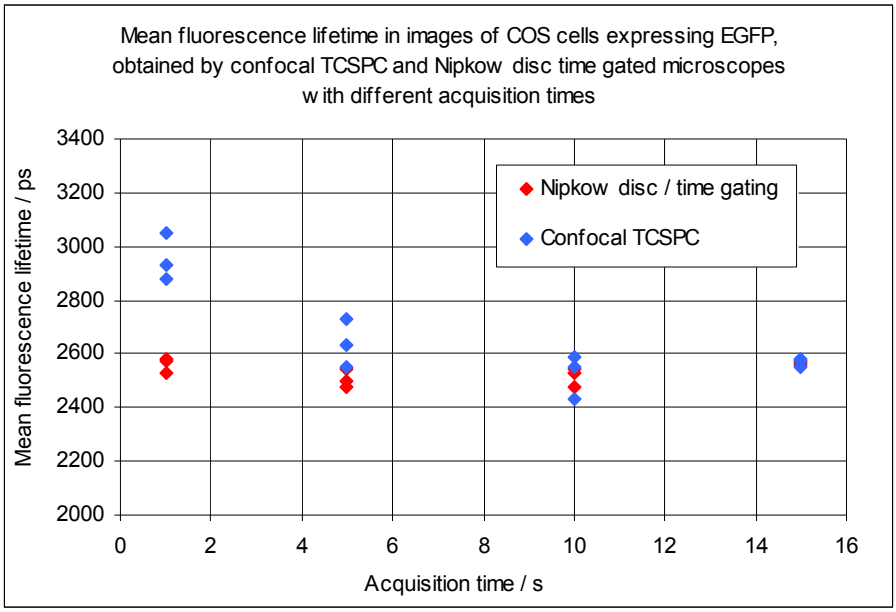


Figure 6.7: Representative images of EGFP expressing cells captured on the Nipkow disc microscope (left column) and confocal system (right column) with acquisition times shown alongside. Note that the noise is far more prevalent in the images of cells obtained on the TCSPC. Pixels in white are those for which an erroneous lifetime beyond the bounds of the color scale has been calculated. (Scale bar = 10 μm).

Although both systems will ultimately be limited by photobleaching considerations (particularly when acquiring time lapse sequences) the goal here was to compare the maximum signal to noise of the two instruments. For this reason, the laser power was chosen so as to provide the maximum signal in each case. For the confocal microscope this coincided with the pulse pile up limit of 10^6 counts per second, and was measured as 8 μW at the sample. For the CSU10, the laser power was the maximum 8 mW obtainable from the supercontinuum source through the single mode fiber.

Images of cells were acquired at integration times of 1-30 seconds, and the spatial resolution set to be equal in both systems. Images were smoothed with a 3x3 kernel and lifetimes fitted in a custom written LabView program (*National Instruments*). The intensity in each image was thresholded so that only those pixels which had 25% or more of the peak intensity were included in the analysis. Lifetimes were fitted using a least squares iterative Levenberg Marquadt algorithm, and the mean lifetimes and standard deviations compared. Representative images and derived plots are shown in Figures 6.7 and 6.8, respectively.



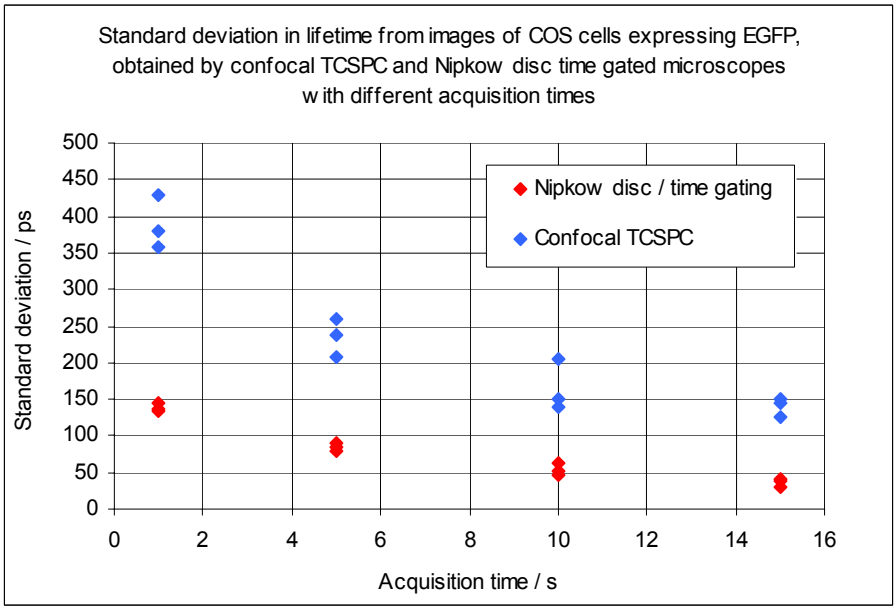


Figure 6.8: Plots of the mean fluorescence lifetime and standard deviation measured from cells expressing EGFP using confocal TCSPC, and time-gated Nipkow disc microscopy. The mean lifetime recorded on the Nipkow disc is constant across the range of acquisition times, even with as short an acquisition time as 1 second. In contrast, on the confocal TCSPC system an artefact is seen for acquisition times below 10 seconds, owing to the reduced number of photons detected. This shortage of fluorescence photons is further highlighted in the plot of standard deviation, where the increased width of the lifetime distribution is evident across the full range of acquisition times.

6.9. Noise characterisation of wide-field detector

The results shown in Figure 6.8 are empirical though nonetheless informative measures of system performance. To aid this comparison, a series of simulations was carried out to model

the accuracy in lifetime determination for the two systems at different acquisition times. The first step in this was to determine the noise characteristics of each detector. In the case of TCSPC, where one measures photon events per second and the signal is shot-noise limited, both the noise and the flux on the detector are easy to determine. For the wide-field detector, the situation is more complex as the noise may vary depending on the gain on the multichannel plate. Modelling this detector therefore requires knowledge of how the noise varies with gain voltage.

Prior to characterising the GOI / camera system, two assumptions were made:

a) The main source of noise stems from the multichannel plate GOI. The cooled CCD camera does not contribute significant noise to the measurement once background images are subtracted (readout noise is insignificant compared to the GOI noise).
b) The camera has a linear operating range for integration times <5 seconds. At intervals above this, fixed pattern noise becomes an issue.

The noise on the intensifier was characterised by observing the intensity distribution in images recorded at different gains when the photocathode was illuminated by a continuous wave diode laser, which was expanded to fill the full aperture of the detector (Figure 6.9).

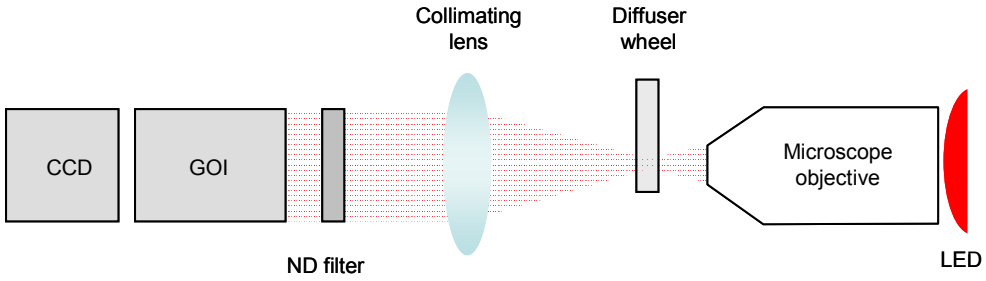


Figure 6.9: Optical set-up for characterising the intensifier noise. A CW LED was focussed onto a diffuser wheel and then collimated to fill the aperture of the photocathode. The total flux incident on the GOI was adjusted by use of different ND filters placed before the detector.

The LED power was set so as to produce a flux on the GOI equivalent to that seen in typical cellular imaging experiments, assuming a fairly bright sample. This was achieved by inputting typical acquisition parameters for a FLIM acquisition, and increasing the LED voltage until the camera reached saturation. Typical values for these parameters when imaging EGFP cells were a gate width of 1000 ps, an MCP gain of 500-550 V and a camera integration time per gate of 0.1 – 0.2 seconds. Once set up, the LED voltage was not adjusted

for the remainder of the experiments. A period of 30 mins was also allowed to pass before beginning any acquisitions, to allow the LED power to stabilise.

6.9.1. Measurements of LED flux on detector

The first stage in characterising the detector was to determine the actual flux incident upon it. This was measured by carrying out single photon counting measurements on the CCD. To begin with, a 0.0076% ND filter was placed in front of the GOI and the camera integration time reduced to below 30 ms. The goal here was to ensure that, in accordance with requirements for single photon counting, no more than one photon was detected per camera pixel during the integration time. Single photon counting was then performed as follows: A series of 100 images was taken for integration times varying from 1 ms up to 30 ms on the CCD. For each series of images, a threshold was applied, such that only bright events corresponding to a detected photon (and not dark events in the camera) were recorded. It was found that at the maximum MCP voltage of 850 V, the measured signal on the camera from one such event was high enough to distinguish above the camera dark noise. Typical images, at two different thresholds are shown in Figure 6.10 below.

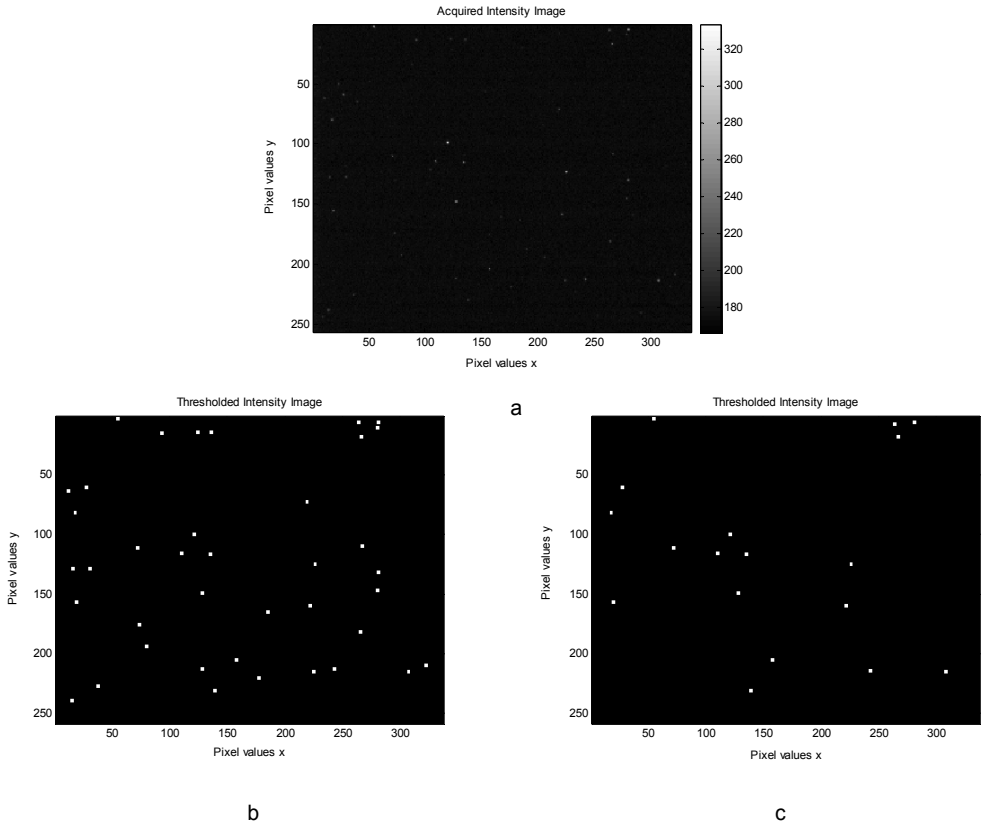


Figure 6.10: a) Acquired intensity image at 850 V, 1 ms integration time with a 0.0076% transmission filter. Figures b and c show the same image thresholded at 200 DN and 250 DN, respectively.

The total number of single photon events detected in each of the 100 frames was recorded, and the mean and standard deviation calculated. The same was then repeated for each integration time. To check that these were true single photon events being measured, the mean number of photons per camera integration time was compared to the variance across the series of 100 images. In the case where only single photons are detected, the square of the noise (standard deviation squared) should scale with the mean. This was indeed seen to be the case (Figure 6.11).

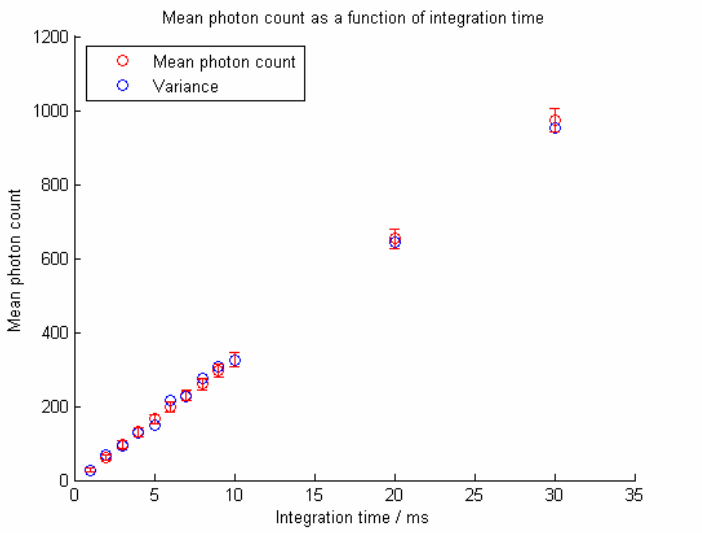


Figure 6.11: Mean photon count as a function of integration time, for ND 0.0076% transmission.

These measurements were next repeated with a series of different ND filters. In each case, plots of mean photon count and variance were compiled for the different integration times.

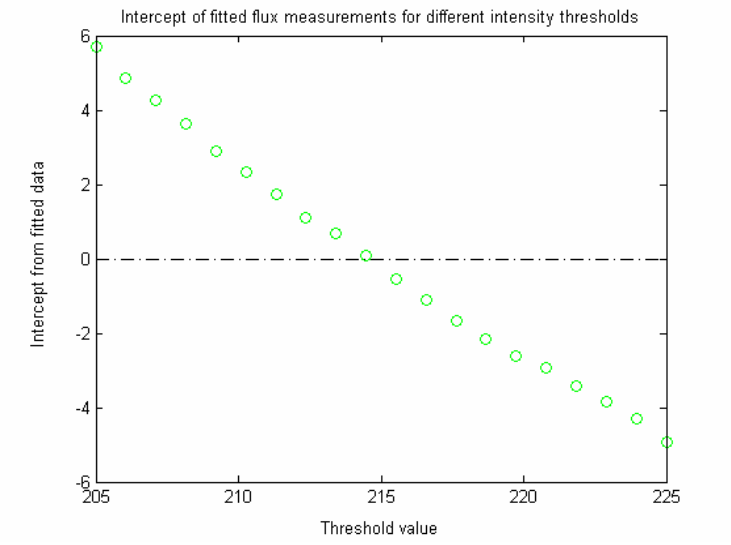


Figure 6.12: Intercept of fitted function for different threshold values, at ND 0.0076% transmission.

The optimum threshold was taken as that at which line of mean photon count versus time was seen to pass through the origin (intercept = 0). Figure 6.12 shows the measured intercepts for different threshold values, using the 0.0076% transmission filter. In this case, the optimal threshold was found to be at 214 DN, with a fitted gradient of 33 photons / ms. The results from 3 ND filter combinations are summarised in Table 6.0 below:

Percentage Transmission	Optimal threshold value (DN)	Measured flux (photons / ms)	Calculated flux (allowing for transmission of filters) 10^5 photons / ms
0.0076	214	33	4.34
0.0035	207	19.4	5.54
0.0020	203	12.4	6.20
		Mean flux	5.36

Table 6.0: Calculated photon flux for different ND filter combinations.

6.9.2. Signal to Noise Ratio Measurements

Having determined the flux incident on the GOI, we removed the ND filters and commenced measurements of signal to noise ratio at different gain values. At each gain, a series of 10 integration times were chosen, the maximum of which ensured that the CCD just reached saturation. For each integration time, a total of 100 images was captured on the CCD. The mean background dark count was measured by repeating the same measurements with a light proof cap on the camera. This value was then subtracted from the original image stack. Once corrected, the mean intensity and standard deviation was calculated for each individual pixel in the image stack. This resulted in two 225 x 336 arrays, the first containing mean intensities, the second the standard deviations. Single values for the mean and standard deviation were then obtained by averaging a 100 x 100 region of pixels in the centre of these two arrays. These values were taken as the signal and noise respectively for that integration time. It was found that for all MCP gain voltages used, the square of the noise varied linearly with digital number / integration time (Figure 6.13 below).

Figure 6.14 shows the mean standard deviation as a function of digital number for the different gain settings used. As one would expect, there is an increase in the noise (standard deviation) with higher gain voltage.

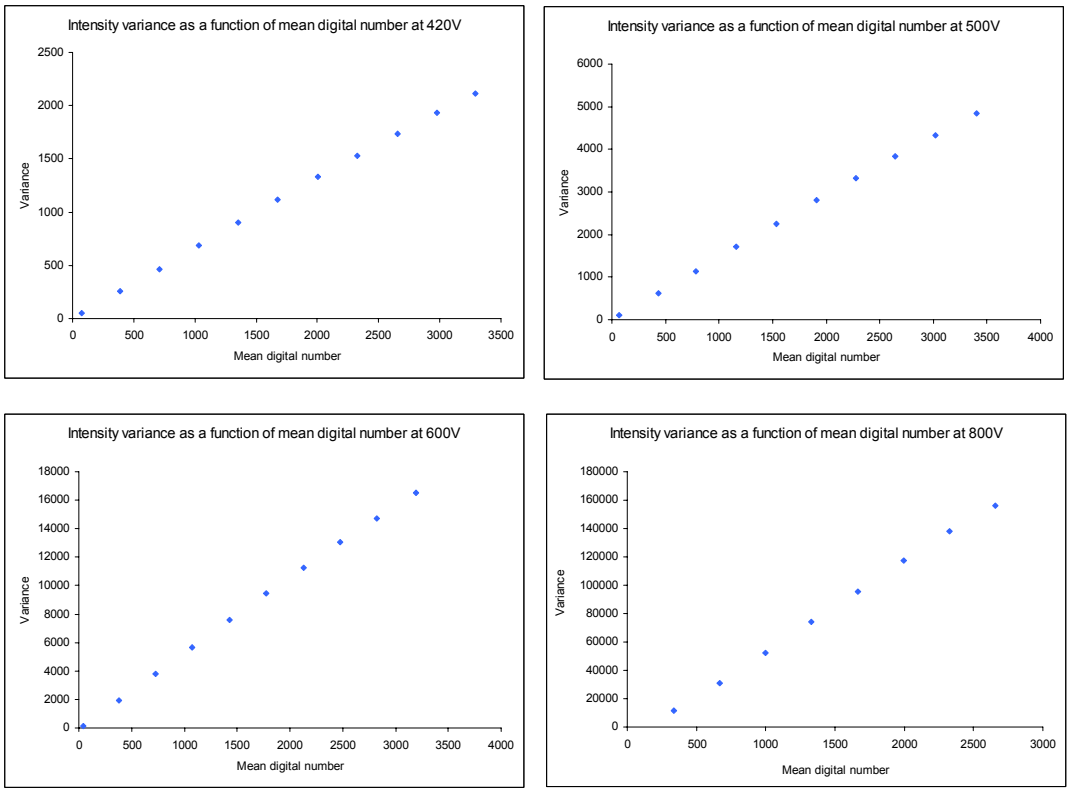


Figure 6.13: Variation in standard deviation squared with digital number, at different gain settings.

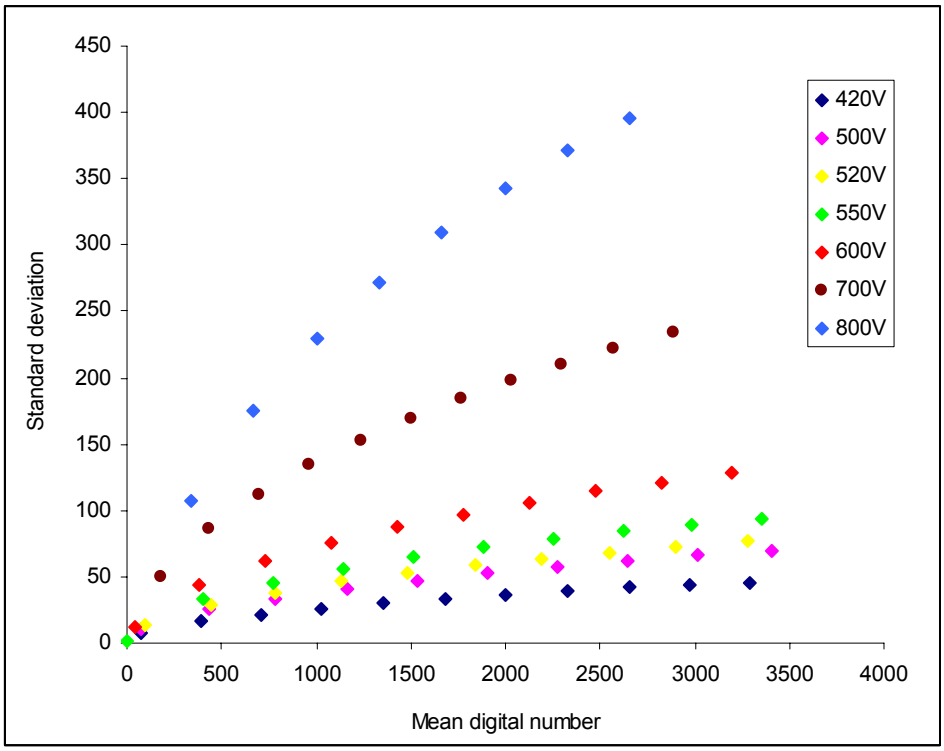


Figure 6.14: Standard deviation measured for different gain settings.

The signal to noise ratio SNR for a given gain / integration time was calculated from:

$$SNR = \frac{\overline{DN}}{\sigma_{DN}} \qquad \text{(Equation 5.0)}$$

where $\overline{DN}$ is the mean digital number, and σ_{DN} the standard deviation on the mean. The results are shown in Figure 6.15 below.

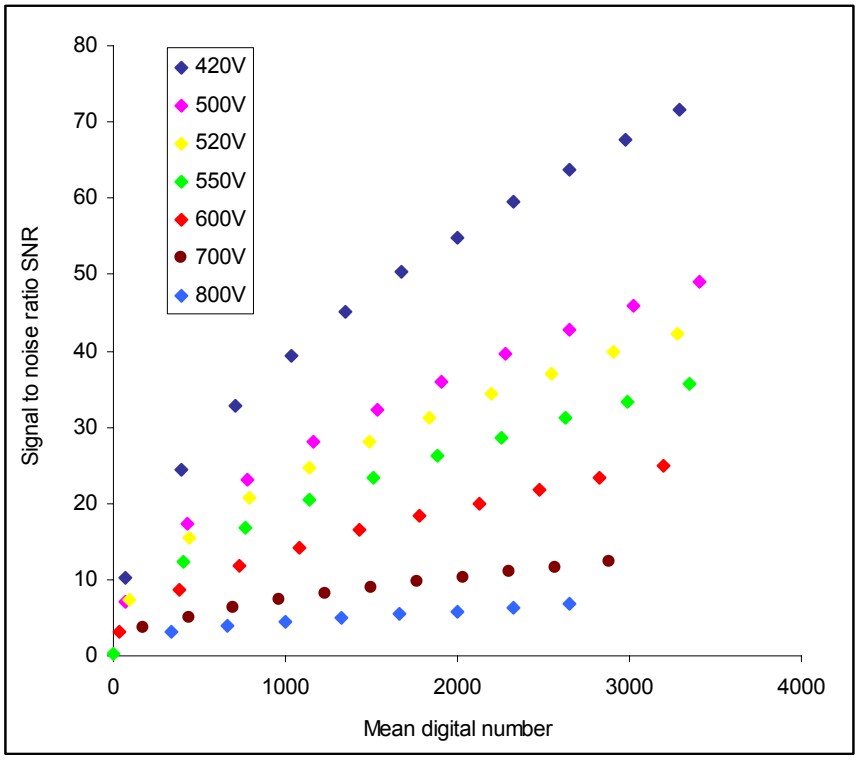


Figure 6.15: Signal to noise ratio SNR as a function of digital number for different gain settings.

6.9.3. Calculating SNR as a function of photon number

In order to make a quantitative comparison with TCSPC, it would be necessary to evaluate the SNR as a function of the actual number of detected photons. Having previously measured the flux incident on the GOI, it was possible to determine the number of photons detected at each integration time on the camera. For each gain, the scaling factor *k*, linking the digital number readout to the actual number of photons *S* was calculated:

$$k = \frac{\overline{DN}}{S} \qquad \text{(Equation 5.1)}$$

Figure 6.16 below shows the measured values of k for each gain setting:

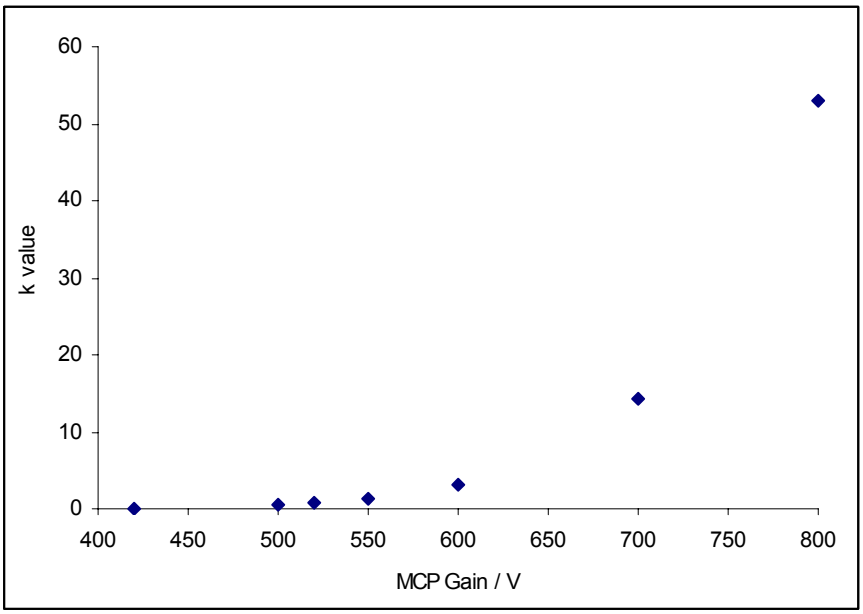


Figure 6.16: k values for different MCP gain settings.

As was seen earlier, the variance $(\sigma_{DN})^2$ scaled linearly with digital number for each MCP gain. Thus, assuming the digital number *DN* on the camera is a linear function of the number of detected photons, it follows that $(\sigma_{DN})^2$ also scales linearly with the number of photons. On this basis on can define a parameter *B* linking the measured variance with the number of detected photons:

$$B = \frac{(\sigma_{DN})^2}{S} \qquad \text{(Equation 5.2)}$$

The signal to noise SNR can then be inferred from the following:

$$SNR = \frac{\overline{DN}}{\sigma_{DN}} = \frac{k\,S}{\sqrt{B\,S}} = k\sqrt{\frac{S}{B}} \qquad \text{(Equation 5.3)}$$

This is shown for the different gain settings in Figure 6.17 below:

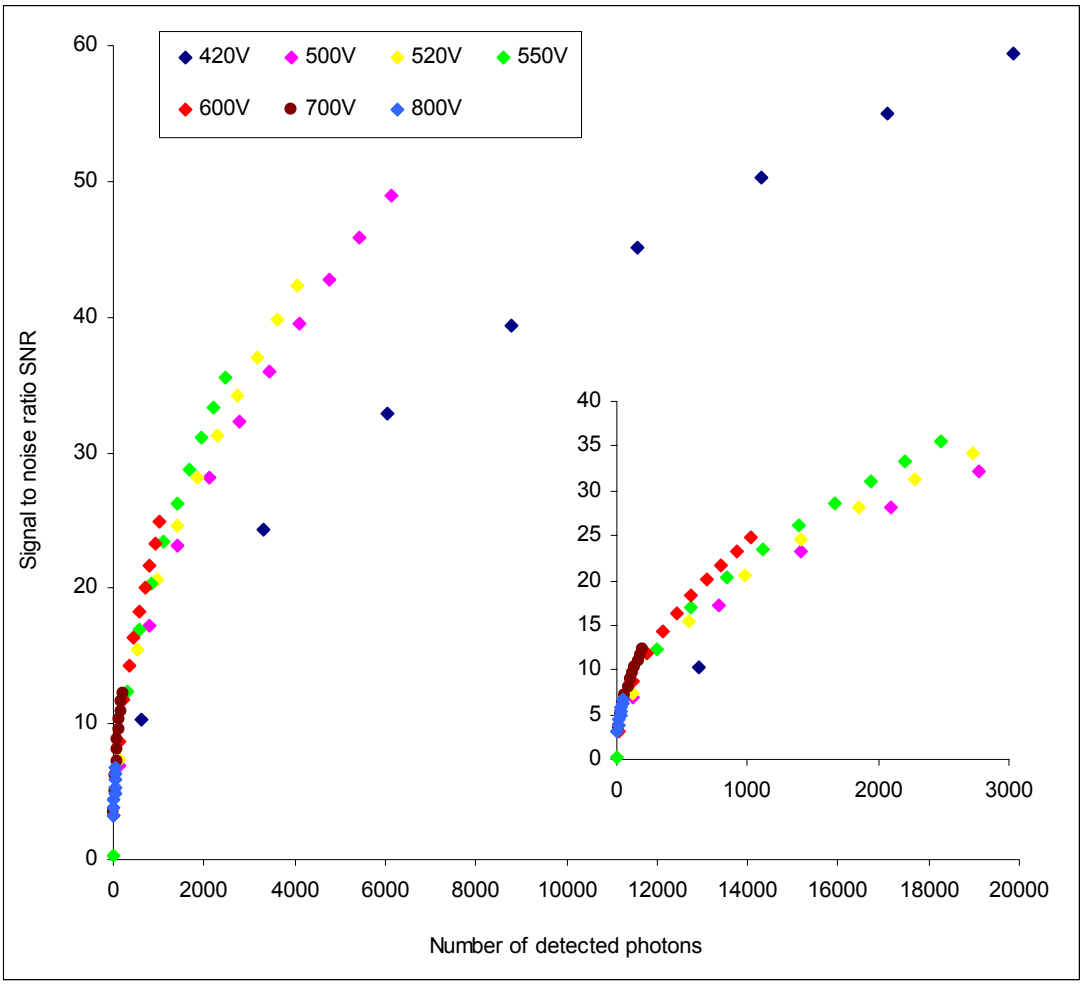


Figure 6.17: Signal to noise ratio as a function of detected photons for different MCP gain settings. Inset: An expanded region of the graph for lower numbers of detected photons.

6.9.4. Comparison of wide-field time-gating and TCSPC: Simulations

The data in Figure 6.17 provide a look-up table of noise per given number of photons for a specific MCP gain. Using these values, and assuming a known value of flux on the detector, it was now possible to estimate the noise on the intensity in each gate during a wide-field FLIM acquisition.

Following this, a series of simulations were run in which lifetime decays were compiled for both the wide-field system and TCSPC. For the purpose of these simulations, the flux on the detector was taken to be that obtained when using the maximum laser power possible on the sample (when not taking into account photobleaching). In the case of TCSPC, this was determined by the pulse pile up limit - a rate of approximately 10^6 counts per pixel per second (for a single TCSPC card). For the Nipkow disc microscope, one could envisage using a much higher power on the sample, even if taking photobleaching into consideration,

since this will be distributed across the entire field of view. In practice however, one is limited by the amount of available laser power. We therefore took the flux to be the maximum obtained in practice from cells expressing EGFP (Figure 6.7). This was calculated from the integration time required to reach camera saturation at a gain of 550 V, using the maximum 1000 ps gate width on the HRI and was of the order 10^5 counts per second. The total flux on the detector will be a factor 300 times greater than this, owing to the number of beams that scan the sample in parallel.

Using these values of flux, and the noise characteristics of each detector, we were able to simulate a series of decays for the two systems. Code for running these simulations was written in *MatLab* by Dr. J. McGinty at Imperial College London. For TCSPC, we modelled 64 time bins, as typically used in the *Becker & Hickl* TCSPC acquisition. In the wide-field system, a series of 5 time gates was used, in accordance with experimental practice. The number of photons in each bin / gate was determined from the maximum flux per pixel, and noise was added accordingly. This was then repeated for different acquisition times. Each series was fed into our in-house fitting software, and histograms of lifetime obtained for these acquisition times. Results of this are shown in Figure 6.18.

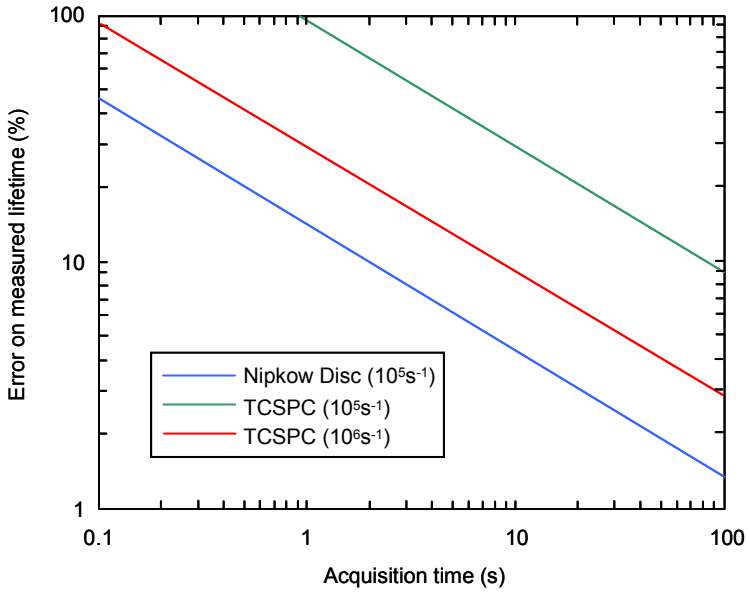


Figure 6.18: Accuracy in lifetime as a function of acquisition time for three cases: i) confocal time correlated single photon counting with a count rate of $10^6 s^{-1}$; ii) confocal time correlated single photon counting with a count rate of $10^5 s^{-1}$; iii) the Nipkow disc system, assuming a flux per pixel equal to that calculated from cells expressing EGFP.

The results in Figure 6.18, coupled with the experimental data presented in Figure 6.8, highlight the advantages of parallel pixel acquisition: although the signal to noise per photon is less than that which could be obtained in a single photon counting module, the collection

rate of photons from the sample is much higher. It follows that for short acquisition times, the wide-field Nipkow system has an improved overall signal to noise ratio.

It is worth noting that for the short (<10 second) acquisition times under consideration, it is exceedingly difficult to obtain sufficient photons for multiexponential analysis; hence no benefit is lost in sampling the decays with wide gates and fitting a simple monoexponential decay model. Where more complex decay analysis is required, global analysis (discussed in section 3.3.3) can be used, allowing one to determine the relative amplitudes of different lifetime components whilst still only using a small (<6) number of gates.

These simulations also do not account for the effects of photobleaching. In experiments, this was found to be more prevalent in the case of the confocal microscope than the Nipkow disc, most likely as a result of the higher peak intensity at the sample [151]. In practice therefore, one often needs to limit the laser power on the confocal microscope below the pulse pile-up limit with the consequence of a lower count rate at the detector. The green line in Figure 6.18 shows the results for TCSPC with a typical reduced count rate of 10^5 counts per second. One can see that in this case, the acquisition time would need to increase 10 fold to achieve the same signal to noise as the Nipkow disc microscope.

6.10. Application to imaging Ras activation in live cells

The results above show that the Nipkow disc time-gated instrument can acquire FLIM images with higher signal to noise at short acquisition times. This increase in temporal resolution allowed us to study the dynamics of Ras activation in living cells by time-lapse FLIM imaging of FRET between mRFP labelled H-Ras and EGFP labelled Raf-RBD. Such experiments had been reported in the past [152, 153], however, this was the first time optical sectioning had been incorporated in the measurement – a key milestone for live cell imaging of protein-protein interactions.

For the experiments below, live MDCK cells coexpressing H-Ras–mRFP and an EGFP labeled Raf-RBD were imaged at different time points following EGF stimulation. EGFP was excited with a wavelength excitation band of 470-490 nm, and fluorescence detected through a 500-550 nm band pass filter. Images of H-Ras-mRFP were obtained by mercury lamp excitation, using a 550-590 nm excitation filter with 600LP emission filter (Figure 6.19). Previously, we had seen a shortening of the donor lifetime at the cell membrane 5-10

minutes after treatment with EGF. By using the Nipkow disc microscope, this activation profile could now be followed within individual cells.

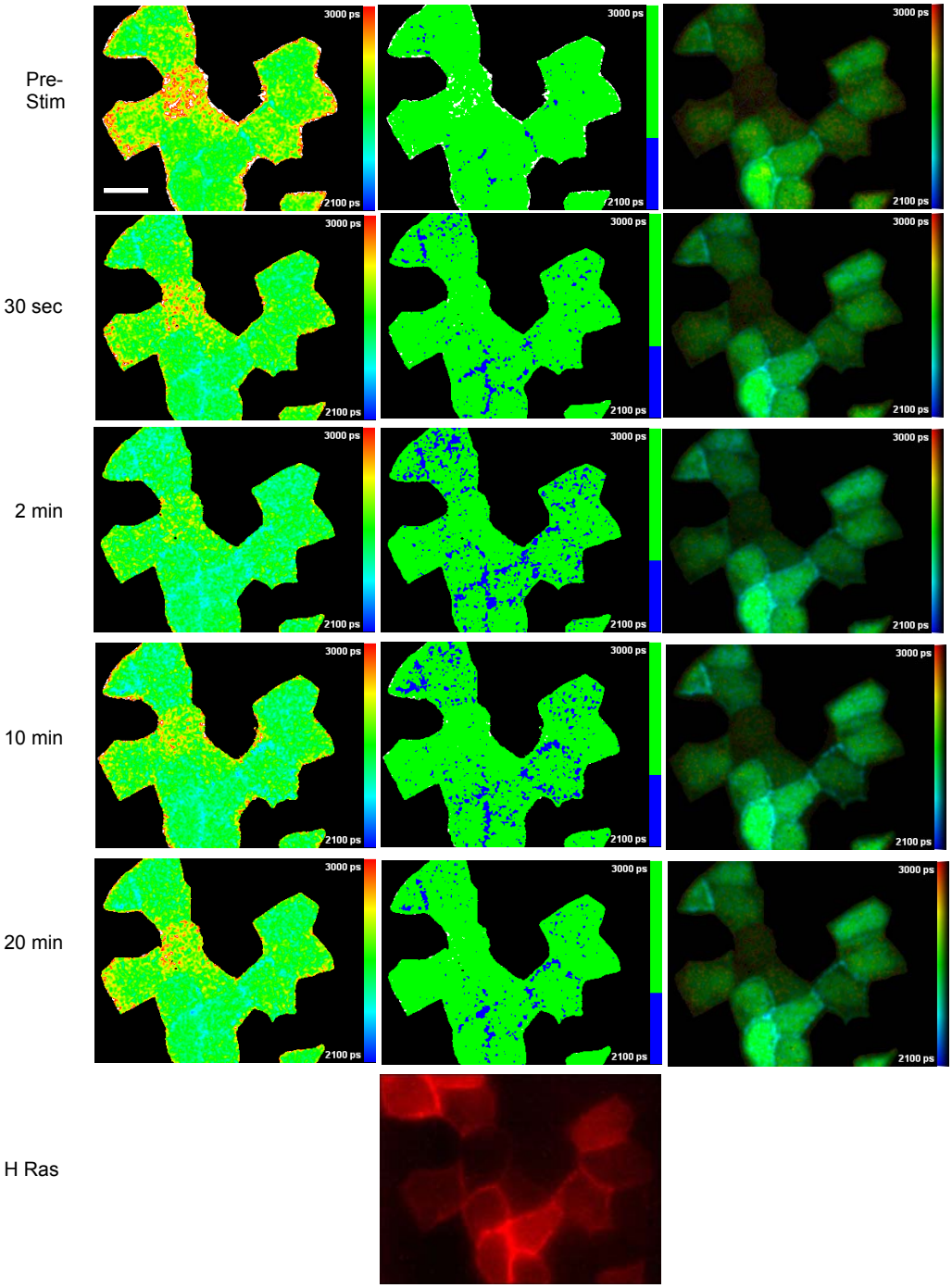


Figure 6.19: Time-lapse fluorescence lifetime imaging of Raf-RBD-EGFP interacting with H-Ras-mRFP at the cell membrane in MDCK cells. Within 30 seconds of adding EGF, a shortening of the EGFP donor lifetime was observed at the cell membranes, indicating activation of H-Ras-mRFP. The maximum shift in lifetime was seen at 10 mins, after which the lifetimes began to rise, indicating a transient activation profile. Left column: Donor fluorescence lifetime (continuous scale); middle column: donor fluorescence lifetime (binary scale, thresholded at 2400 ps); right column: merged fluorescence lifetime with intensity; bottom: H-Ras-mRFP localization. (Scale bar = 10 μm)

The images in Figure 6.19 show a fall in donor lifetime at the cell membrane within the first few minutes of stimulation. This fall in lifetime peaked around 10 mins, after which the FRET signal was seen to diminish slightly – this is in keeping with other published findings on the dynamics of H-Ras activation at the plasma membrane [152]. These results represent an important advance in our ability to study activation profiles of different cellular species.

6.11. Application to high throughput screening

Aside from time-lapse imaging of protein-protein interactions, the fast acquisition speed of the Nipkow disc microscope offers opportunities for high throughput screening applications. The use of microscopy for screening effects of drug compounds in multi-well plates is not itself a novel concept, however, the systems currently in use would greatly benefit from the ability to perform spectroscopic measurements, including FLIM-FRET. This idea has already been demonstrated by Esposito *et al* who used an automated wide-field frequency domain FLIM microscope to image the ubiquitination of different alpha-synuclein mutants in multi-well plates [154]. The Nipkow disc microscope could enhance this capability by providing the benefits of optical sectioning in addition to FLIM.

One caveat to this relates to the method used to sample and fit the lifetime data in each well. Up until this point, the data sets presented have all been obtained using a standard FLIM procedure, in which several time-gated images are collected and the intensities in each image fit to an exponential decay model by a weighted least squares fitting routine (section 2.8.1). Although manual fitting of decays is possible for these small data sets, the large number of data sets acquired in high-throughout applications makes automated lifetime analysis essential. This can be greatly helped through implementation of a Rapid Lifetime Determination (RLD) method [65, 155, 156]. The RLD is an alternative strategy for FLIM acquisitions, which removes the need for iterative fitting of decays, and so reduces the burden on computing power needed to process the data sets. In this case, rather than collecting an entire series of time-gated images, intensities are recorded in two or more time gates and the fluorescence lifetimes are calculated analytically. Assuming the fluorescence decay approximates a monoexponential function, the intensities in the first and second gates, I_{g1} and I_{g2} can be expressed as:

$$I_{g1} = I_O \tau \exp\left(\frac{-t_1}{\tau}\right)\left(1 - \exp\left(\frac{-\Delta T}{\tau}\right)\right) \qquad \text{(Equation 5.4)}$$

$$I_{g2} = I_O \tau \exp\left[\frac{-t_1 + s}{\tau}\right]\left[1 - \exp\left[\frac{-\Delta T}{\tau}\right]\right] \qquad \text{(Equation 5.5)}$$

where I_O is the intensity at the start of the decay, τ is the fluorescence lifetime, s is the separation in time between the two gates and ΔT is the gate width. The lifetime τ can then be derived analytically from the ratio of the two intensities:

$$\tau = \frac{s}{\ln\left[\frac{I_{g1}}{I_{g2}}\right]} \qquad \text{(Equation 5.6)}$$

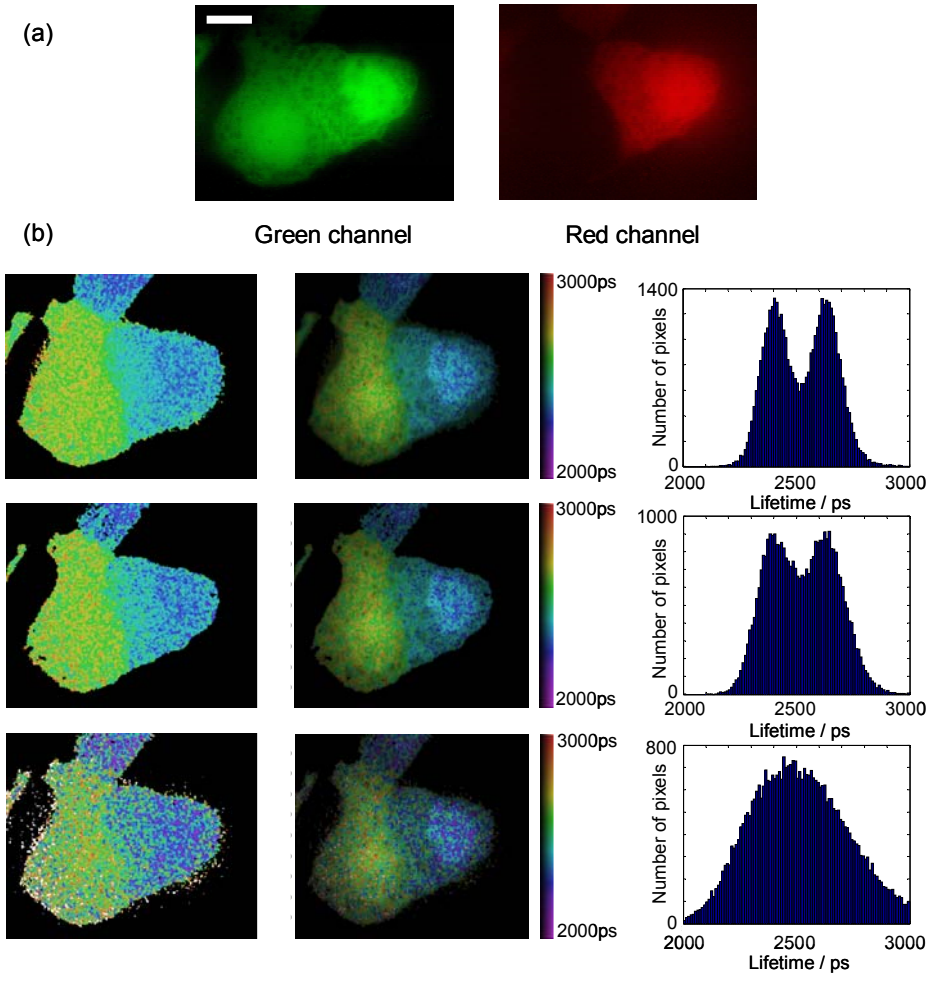


Figure 6.20: a) Mercury lamp images of live MDCK cells expressing either EGFP or a tandem construct of EGFP-mRFP. The fluorescence in the red channel shows only this cell expresses both fluorophores. b) Fluorescence lifetime images of the same field of view, captured at frame rates of 1 Hz (top row), 5 Hz (middle row) and 10 Hz (bottom row). Also shown are the lifetime histograms for each image. Lifetimes were measured using a two gate RLD method. The shorter lifetime in the cell expressing both fluorophores is evident even when imaging at 10 Hz. (Scale bar = 10 μm)

Since one only acquires images in two gates, the information obtained may be less than that provided by a standard FLIM acquisition. Nonetheless, the RLD approach can still provide

high quality data. Figure 6.20, for example, shows FLIM image of cells acquired using the RLD approach. The cell on the left is expressing EGFP alone, while the cell on the right is expressing the tandem construct EGFP-mRFP introduced in Chapter 3. The difference in lifetime between the two cells is obvious, and can be resolved as two distinct peaks in the histogram when imaging at 5 frames per second. It is possible that by averaging over multiple cells, one would be able to discern this difference even when imaging at 10 frames per second.

6.12. Summary

This chapter has discussed the implementation of an optically sectioning fluorescence lifetime imaging microscope for studies of live cell signaling. A key step in achieving this has been the incorporation of a high power, pulsed supercontinuum source for efficient excitation of EGFP labelled fluorescent constructs. The acquisition times are significantly shorter than that achievable by TCSPC for equivalently bright specimens, and permit the study of dynamic changes in cell activation and function with greater temporal and spatial resolution than previously possible. The system also holds promise for high throughput screening, including pharmaceutical applications, such as for evaluating the effects of different inhibitors of Ras activity.

Chapter 7: Multiplexed FRET to image dual FRET sensors

7.0. Chapter overview

The ability to resolve molecular interactions within cells has made FRET a highly valuable technique for biologists. A positive FRET result is a strong indication that two proteins which are observed to bind in *in vitro* assays do genuinely interact within the context of the cell and thus are physiologically linked. This feature has often been argued as the unique selling point of FRET microscopy. In recent years, however, it has become increasingly evident that it is not only the spatial localisation of signals that determines cellular response, but also the temporal dynamics of these signals. Imaging of single interactions in fixed cells is therefore only the first step towards understanding the role two such proteins have in the cell.

In this chapter, we discuss the implementation and characterisation of a wide-field fluorescence microscope, together with design of suitable fluorescent probes, for imaging two FRET pairs within a single live cell, with each pair being used to report on a different aspect of cell signaling (in this case, calcium flux and activation of Ras GTP-ases at the membrane). The ability to resolve the temporal and spatial dynamics of these separate events in live cells following stimulation represents an important step forward in correlating distinct elements in a signal pathway. The technology described will also be applicable to a wide range of other signal pathways, using different FRET sensors to report on these other signaling events.

7.1. Motivation for multiplexed FRET experiments

In Chapter 5, we discussed the use of FRET to image interactions between PLCε and members of the Ras GTP-ase family of proteins. Numerous studies have suggested possible interactions between PLCε and these different proteins, although scant evidence of FRET was seen in these studies (excluding the interaction of the isolated RA2 domain with Ras). This posed the question of whether the strength or longevity of such interactions was below the threshold of that detectable in the microscope. To learn more of the biology of PLCε therefore requires an alternative approach, using more established FRET sensors to report on associated signaling events.

7.1.1. Basis for investigating PLCε activity by multiplexed FRET

The prime mode of activation of PLCε is thought to occur through its interaction with Ras at the plasma membrane. Nonetheless, recent experiments have shown that a more diverse series of events may lead to PLCε activation, independently of Ras. Interestingly, it has even been suggested that calcium release following PLCε activation by other routes may itself lead to Ras activation, through calcium activated Ras GEFs.

Calcium and Ras activity have long been known to be implicated in similar cell processes, including survival, differentiation and proliferation. Rosen *et al* were able to offer definitive evidence of calcium regulated Ras activation, which occurred following release of calcium from internal stores and also from outside the cell via voltage operated channels, in PC12 cells and primary rat neurons [157]. The demonstration that an oncogenic Ras could bypass calcium regulated aspects of cell cycle suggested a clear link between Ras and calcium signaling, which in the time since has been confirmed by the identification of a number of calcium regulated Ras GEFs and GAPs [158, 159].

The first GEF to be discussed here is the Ras guanine-nucleotide-releasing factor (Ras GRF1, or CDC25Mm) and the highly similar Ras-GRF2 protein. In both cases, it is the presence of the CDC25 C-terminal domain, a highly conserved sequence amongst Ras GEFs that identifies them as such. Other regulatory domains comprise an N-terminal PH domain, calmodulin binding IQ region and additional regulatory domains with suggested roles in protein-protein interactions. It is envisaged that GEF activity is initiated by calcium dependent calmodulin binding to the protein's IQ domain [160]. In contrast to the quintessential Ras GEF Sos, which has a cytosolic localisation and is only recruited to the plasma membrane following ligand binding to membrane receptors, RasGRF1 is localised to the plasma membrane by interactions of its PH domain with phospholipids, or possibly the βγ subunits of G-proteins. Its activation of Ras may therefore be accomplished by calcium binding alone. RasGRF2 meanwhile has a cytosolic localisation and the mechanics which drive this protein's recruitment to the plasma membrane are unknown [161].

Other Ras GEFs with alternative regulatory factors have also been identified. We mention them here because these other factors have crossover into PLC regulated signal pathways, and thus highlight further interplay between Ras and PLC signaling. Ras guanine-nucleotide-releasing protein (RasGRP), also known as calcium and diacylglycerol-regulated guanine-nucleotide exchange factor II (CalDag GEF II) binds calcium through an EF-hands domain,

although this alone is insufficient for Ras activation. An additional interaction with diacylglycerol is also required, mainly to provide anchorage in the membrane. This has been confirmed by substitution of the DAG binding domain with other membrane localisation signals, such as the C-terminal region from K-Ras [162].

CalDAG GEF I meanwhile has been identified as a GEF for the small GTP-ase Rap1A, which catalyses Rap activation in response to cell treatment with phorbol ester, causing its translocation to the plasma membrane. This too can stimulate Ras, although only after prolonged treatment of the cells [163].

CalDAG GEF III functions as a GEF for several Ras family members, binding to phorbol ester and resulting in heightened activation of MAP Kinase [164]. Diacylglycerol would seem to be the dominant factor in regulating this protein's GEF activity by recruiting it to the cell membrane.

In addition to these GEFs, several Ras GAPS have also been identified in the literature. Indeed, the activity of such proteins is evident in the exchange between calcium free and calcium containing media, which in some studies has been sufficient to inhibit MAP Kinase activation and cell proliferation. A prominent Ras GAP is p120 RasGAP, which is understood to translocate to the plasma membrane following calcium flux into the cell [165]. Translocation is thought to occur via the protein's C2 domain. Whilst some studies have suggested p120 GAP activity to be directly activated by calcium, these have met with opposing views by others, particularly in light of the consideration that the C2 domain does not contain the typical aspartate residues commonly found in other C2 calcium binding domains [166]. An alternative, indirect mode of activation has been suggested through interaction with Annexin VI, itself having a well characterised response to calcium [167].

Elsewhere, proteins of the GAP1 family have been shown to inhibit Ras activation in response to calcium flows. The most prominent of these is the calcium promoted Ras inactivator (CAPRI), which, in addition to its Ras GAP domain, has two C2 domains, complete with aspartate residues normally expected in such calcium binding domains [168]. Once again, inactive CAPRI has a cytosolic localisation, but upon cell stimulation is recruited to the plasma membrane through the interaction of its two calcium bound C2 domains with membrane phospholipids. A more complex picture of calcium regulated Ras inactivation arises in considering the $GAP1^{IP4BP}$ protein. This protein is activated through interaction with the second messenger 1,3,4,5-tetrakisphosphate, itself generated from IP_3 by $Ins(1,4,5)P_3$-3-kinase in a calcium dependent manner. This rather convoluted path of steps

has led it to be posited that GAP1P1^{IP4BP} functions as a PLC dependent GAP which is able to switch off Ras activity following production of IP_3 in response to different cellular agonists [169].

In the context of this discussion, the emergence of PLCε as a possible node for integrating calcium and Ras related signal processes [170] is particularly interesting. In addition to its direct interaction with Ras, the downstream products of its substrate hydrolysis, namely diacylglycerol and calcium, may themselves serve to upregulate Ras activity through CalDAG-GEFs or RasGRF, resulting in prolonged PLC activity and changes in temporal modulation of the ensuing calcium flux. Depending on the duration and amplitude of the initial calcium flux and diacylglycerol release, the reverse might also be true, i.e. Ras GAPs such as Ras GRP1 may become activated, switching off the Ras signal cascade. Investigating the temporal dynamics of Ras activity and calcium fluxes in cells expressing PLCε is therefore of great interest in understanding its role in cell physiology. Moreover, it would move us one step forward to better understanding the complex interplay between Ras activation and calcium signaling in general.

7.2. Imaging calcium flux in cells

Calcium imaging has been a mainstay of cell biology research for the past two decades. The most widespread method for calcium imaging is the use of fluorescent dyes – small, inorganic molecules that are usually conjugated to a calcium chelator, such as EDTA or more commonly BAPTA. When bound to calcium in cells, the attached fluorophore may undergo either a shift in fluorescence intensity or emission wavelength. Dyes that show a change in intensity upon calcium binding include Oregon green, calcium-green-1 and calcium green-2. Those that show a change in emission wavelength can be used for ratiometric measurements and are therefore less prone to artefacts arising from photobleaching – these include the Fura-2 and Indo-1 dyes [171, 172].

The main alternative to calcium dyes involves the use of genetically encoded indicators. The first of these to be used, dating back to the 1970s is the endogenous protein aequorin derived from marine jellyfish [173]. (GFP was later derived from a jellyfish of the same species). Aequorin is a bioluminescent molecule that emits light in the presence of calcium. The main drawback of this protein is its low dynamic range – the low light signals generated upon calcium binding require exceptional detector sensitivity in order to measure them. During the late 1980s and 1990s, following the introduction of GFP, a new range of calcium sensors

became available. A fortuitous discovery by Baird *et al* [174] showed that in addition to C or N terminal fusions, GFPs could also tolerate insertions of calcium sensitive domains at other sites in their Beta Barrel structure. The change to 'circularly permutated' mutants of GFP provided fusion proteins whose fluorescence was much more sensitive to calcium binding in the inserted domain (in this case, calmodulin). Currently, several probes based on this principle have been developed, including camgaroo [175], pericam [176] and G-Camp [177]. Calcium binding to these domains can affect the protonation state of the chromophore, with a resultant change in fluorescence intensity or occasionally a shift in emission wavelength.

Following the development of the CFP and YFP spectral variants of GFP, the first ratiometric FRET calcium probe 'cameleon' was reported by Miyawaki *et al* [72]. Substitution of the ECFP and / or EYFP fluorophores for alternative cyan and yellow variants (and their circularly permutated equivalents) has given rise to an entire family of cameleons. Currently, the most favourable variant in terms of its dynamic range (and the first to be sold commercially) is the YCAM 3.6. cameleon, also developed in the lab of Miyawaki [178]. An excellent review of these different indicators, and their advantages and disadvantages has been given by Palmer and Tsien [179].

7.2.1. Choice of FRET sensors for imaging calcium

Calcium Ca^{2+} indicator	Advantages	Disadvantages
Calcium dyes (Fura, Indo)	• Easy to load into cells • Highest dynamic range of all calcium sensors • High brightness	• May be toxic to cells. • Will eventually leak out of cells not suitable for long term imaging experiments • Can not be targeted to specific cell locations • May aggregate in certain cellular compartments over time
Aequorin	• Suitable for imaging single cells	• Requires gene expression within cells • Poor quantum yield and low dynamic range
Cameleon	• Suitable for imaging single cells • Good cell viability • Possible to design stable cell lines	• Requires gene expression within cells • Dynamic range is lower than small molecule calcium sensitive dyes

Table 7.0: Pros and cons of different calcium imaging methods (adapted from [180]).

Table 7.0 above lists some of the main advantages and disadvantages of the different approaches for imaging calcium in live cells. Given the higher dynamic range of calcium dyes, one might argue that use of a genetically encoded FRET sensor for tissue culture studies is somewhat redundant. For straightforward calcium imaging, this is perhaps true. Nonetheless, it is important to remember that in pursuing these experiments, our goal was not only to image calcium transients, but more generally to explore the potential for imaging multiple FRET sensors within single cells. At the present time, a large number of different FRET sensors based on ECFP/EYFP or their spectral equivalents have been reported in the literature [72-76]. The vast majority of these possess no chemical analogue capable of reporting on the same cellular process. Being able to image the cameleon probe and a second FRET sensor within the same cell successfully would therefore represent not only a result in terms of correlating these two signaling components but in addition would show the way forward for correlating other signaling events using the many other available FRET sensors. On this basis, we decided to investigate whether YCAM 3.6 could be used as an indicator for calcium signals associated with PLC activity, and if so, to combine this with an additional FRET sensor for imaging Ras activation within these same cells.

7.3. Preliminary studies: Cameleon imaging with PLCs

For imaging YCAM 3.6 in cells, we used an Olympus 1X81 microscope with illumination provided by a 447 nm diode pumped solid state laser (*Crystalaser,* USA). The fluorescence emission was spectrally resolved using a Dual View Imager (*Optical Insights,* USA*)* placed at the camera port of the microscope and coupled to a Hamamatsu ORCA ER CCD.

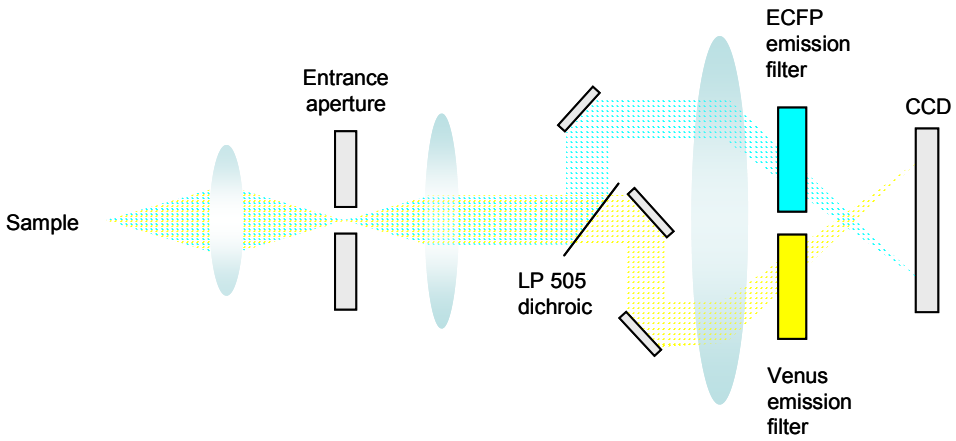


Figure 7.0: Schematic of the Dual View Imager from Optical Insights. The Dual View can be used to spectrally resolve fluorescence from the sample into two channels, imaged onto the same CCD chip.

The Dual View is an optical component that resolves the fluorescence signal into two spectral channels, which are then imaged onto two halves of the same CCD chip. A schematic is shown in Figure 7.0 above. For the experiments discussed, a LP 505 nm dichroic was used to spectrally resolve the ECFP and Venus fluorescence. A 535/40 nm emission filter was used in the Venus spectral channel and a 483/20 filter in the ECFP channel. An example image of cells expressing YCAM 3.6, excited at 450 nm is shown below in Figure 7.1.

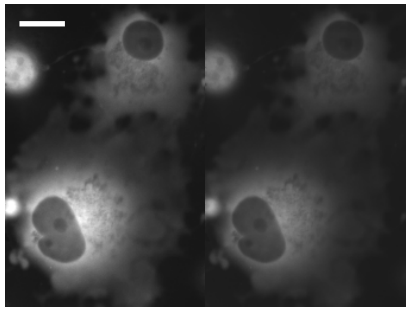


Figure 7.1: Dual channel image of COS cells expressing the YCAM 3.6 sensor (Scale bar = 10μm).

7.3.1. Image analysis

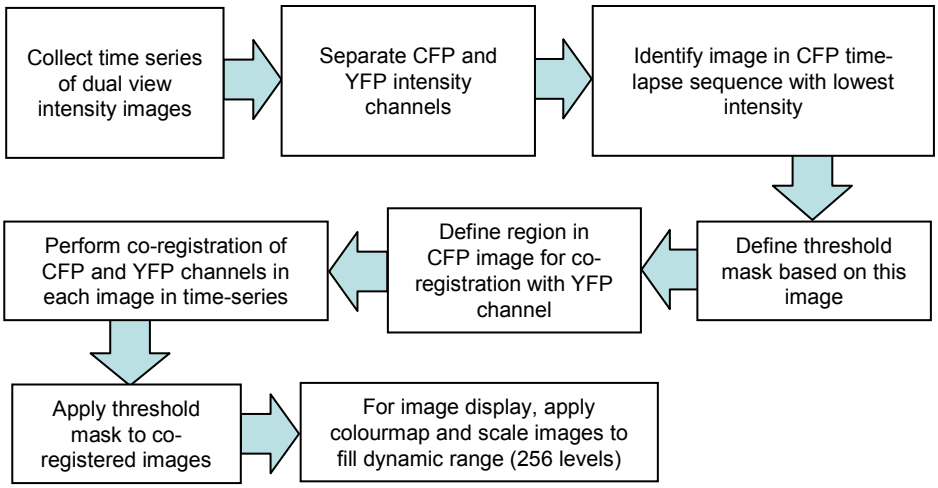


Figure 7.2: Flow chart for batch analysis of dual view time-lapse sequence images.

Analysing the FRET signal from the cameleon probe requires accurate ratioing of pixel intensities across the two halves of the image. The main issue here is correct registration of the two channels when dividing one by the other. A custom program for this purpose was written in LabView (*National Instruments)* by Sunil Kumar, and was incorporated into a

second batch processing program for analysing time-lapse sequences of dual channel images. The main steps in this analysis are shown in the flow chart in figure 7.2. Figure 7.3 below shows one such time lapse sequence, for the cells pictured earlier. These cells were also cotransfected with a plasmid encoding full length (untagged) PLCε. Following EGF stimulation, images captured at 1s intervals for 5 minutes.

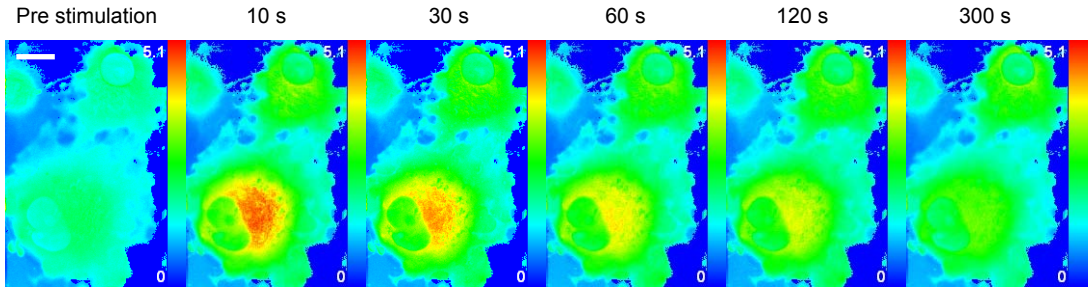


Figure 7.3: Time-lapse sequence of ratiometric FRET images of cells expressing full length (untagged) PLCε and YCAM 3.6, stimulated with EGF. Immediately after stimulation, a large calcium flux was seen to occur in the perinuclear region of the cell, as seen here from the increased ratio of the Venus / ECFP channel intensities, which gradually subsided over the course of 5 minutes. (Scale bar = 10 μm)

7.3.2. Results of dual view calcium imaging

To investigate the potential for imaging calcium fluxes associated with PLC activity, we contransfected COS cells with plasmids encoding YCAM 3.6 and full length (untagged) PLC isoforms PLCε, PLCγ1 and PLCβ. Following transfection, cells were placed in serum free media overnight and imaged the following day using dual channel detection as described above. Time-lapse sequences of cells were acquired for up to 5 minutes, with EGF added to the cell medium 10 seconds after the start of the acquisition. Images were then batch processed using the series of steps shown in Fig 7.2 and intensity ratios from the cytosolic region of the cells analysed. Trends in intensity ratio were compared for cells co-expressing the 3 PLC isoforms and YCAM 3.6, with cells expressing YCAM 3.6 alone, when stimulated by EGF. Figure 7.4 shows representative traces from a number of fields of view for each of these cases.

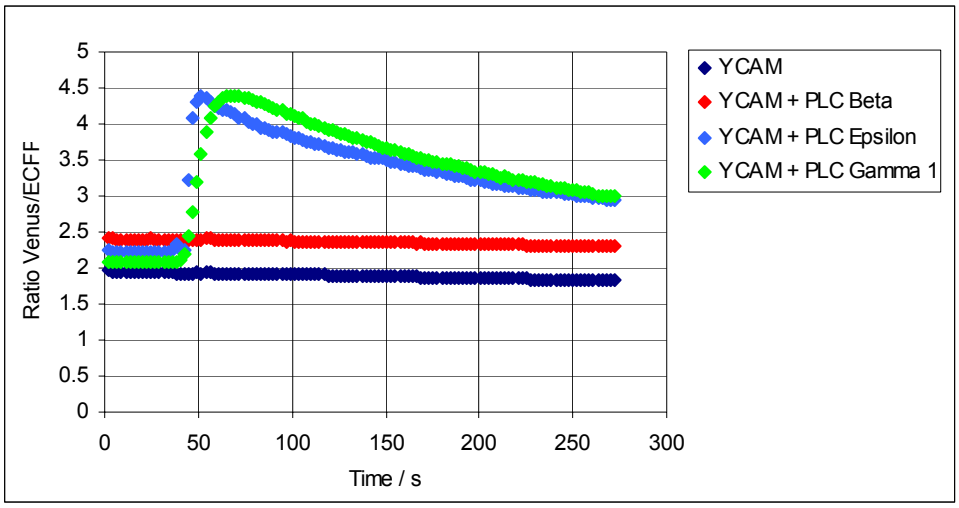


Figure 7.4: Variation in Venus/ECFP intensity ratio for live COS cells coexpressing YCAM 3.6 and the three PLC isoforms, or YCAM 3.6 alone, when stimulated with EGF.

Since calcium fluxes can be triggered by a number of different mechanisms in response to EGF stimulation, one must proceed with caution in interpreting the above data. One point is clear however - these experiments highlight the potential of dual channel imaging of YCAM for discriminating calcium signals associated with PLC expression. A key finding from these experiments is the difference in signals seen between cells cotransfected with PLCγ or PLCε and those expressing the YCAM construct alone. This suggests the observed increase in cytosolic calcium levels does follow as a direct consequence of the coexpression of PLCs. This conjecture would also seem to be confirmed by the difference in response to EGF of the PLCε and PLCγ isoforms, compared to PLCβ (unlike PLCε and PLCγ, the regulatory domains of PLCβ are not believed to function downstream of the EGF receptor).

In summary, these experiments demonstrate that dual channel intensity imaging of cell populations expressing YCAM offers a robust method for monitoring calcium flux with high spatial and temporal resolution, and one which can be used to report on specific responses in cells coexpressing different PLC isozymes.

7.4. Extension to multiplexed FRET

The data in section 7.3.2 confirmed that the YCAM 3.6 FRET probe could be used successfully to assay calcium fluxes associated with over-expressed PLC enzymes. With this outcome established, we proceeded to develop an additional FRET sensor to report on Ras activation in combination with the YCAM sensor. In what follows, we discuss the technical challenges this presented, and how this outcome was successfully achieved.

7.4.1. FRET Sensors for imaging Ras activity in live cells

A number of sensors have been developed to image Ras activation in cells, although to date these have all been used in isolation (i.e. without additional signal components also being imaged). The basic strategy is that discussed in Chapters 5 and 6. The Ras protein is fused to a suitable fluorophore and coexpressed with a fluorescently labelled Raf-RBD, such that upon activation of Ras, the two proteins will couple together and FRET will occur between the two. These proteins may be expressed as separate constructs [152, 153], or alternatively as a single intramolecular FRET sensor, as that developed by Mochizuki *et al* [181] (Figure 7.5). Named 'Raichu', for 'Ras Interacting Chimeric Unit', this sensor is similar to the cameleon probe and comprises a single construct in which the Ras protein and Raf RBD are covalently linked by a peptide sequence.

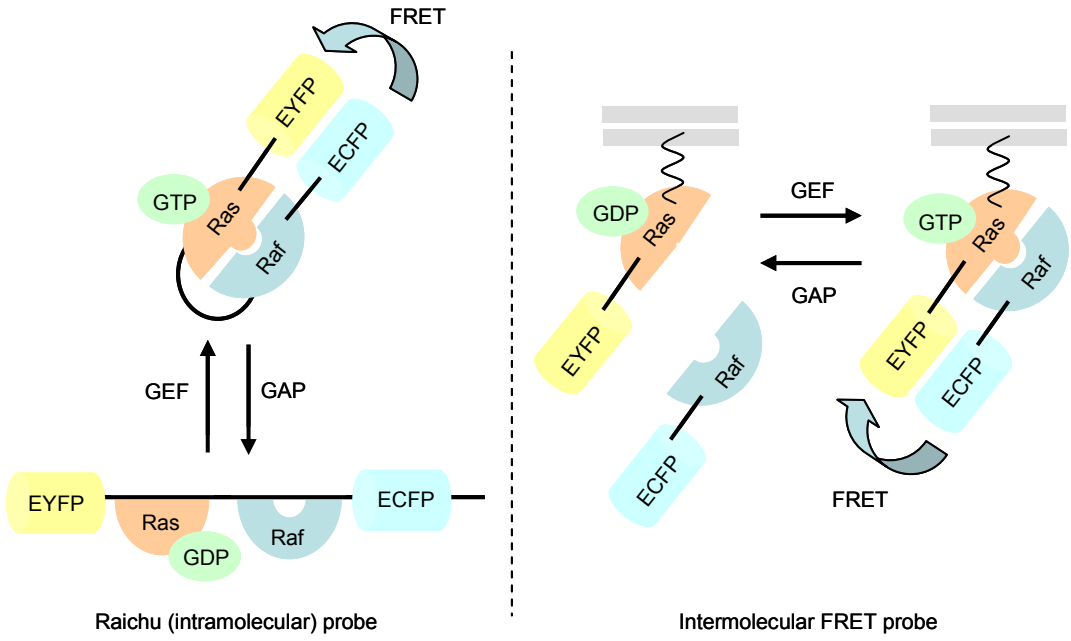


Figure 7.5: FRET probes for sensing Ras activation. Left: The Raichu intramolecular FRET sensor designed by Miyawaki et al [181]. Right: An intermolecular FRET sensor consisting of separately labelled Ras and Raf constructs. (Note that the domain labelled Raf here refers only to the Ras binding domain of Raf Kinase and not the full length protein).

Although both kinds of sensor comprise the same components, there are important differences between them. The Raichu was originally designed as a biosensor to report on endogenous Ras activity; since each Ras molecule is covalently bound to a Raf RBD there is little chance of the exogenous Ras interacting with other cellular components. Instead, the observed FRET signal can be considered an indicator of proximity to Ras GEFs and GAPs. The intermolecular FRET pair, on the other hand, provides a readout of exogenously expressed Ras activity.

From an imaging perspective, Raichu probes have the advantage of an equal donor/acceptor stoichiometry. Assuming the acceptor has sufficient quantum yield, one can therefore detect FRET by simple ratiometric imaging of donor/acceptor intensities. For the case of separately expressed constructs, one must either revert to lifetime measurements or perform intensity calibration measurements in order to eliminate artefacts arising from different donor/acceptor concentrations. This method does however provide a higher dynamic range compared to the single molecule probes, since the latter may sustain a residual FRET signal even in the inactive conformation. These points are summarised in Table 7.1 below:

	Intramolecular FRET sensor (Raichu-Ras)	Intermolecular FRET sensor
Advantages	• Both fluorophores are contained within a single plasmid – no problems of co-expression • Should not interfere with endogenous signaling	• High dynamic range in FRET signal: FRET will only occur upon Ras activation
Disadvantages	• Dynamic range may be compromised by FRET in the inactive state of the probe	• Need to coexpress multiple plasmids within same cell • Over-expression of Ras may influence cell behaviour • In addition to endogenous GEF activity, FRET read-out may also be affected by relative expression levels of two species

Table 7.1: Advantages and disadvantages of intramolecular (Raichu) sensors and intermolecular FRET probes for imaging Ras activity.

In the first instance, it was decided to base the design for the second FRET sensor around a single molecule Raichu construct. This would have the advantage of only requiring one construct to be coexpressed as well as avoiding the issue of balancing the concentrations of donor and acceptor, as in the case of intermolecular FRET.

7.5. Choice of second FRET pair for the Ras sensor

Recent developments have led to an increased number of fluorescent proteins towards the red end of the visible spectrum. In 2004, Shaner *et al* published a landmark paper in which an entire array of novel fluorescent proteins spanning the visible spectrum from yellow to red had been produced and sequenced [21]. Around this time an additional red shifted fluorescent protein, mPlum, was also developed in the same laboratory [182]. The spectra of proteins that were available at the beginning of these experiments are shown in Figure 7.6 below.

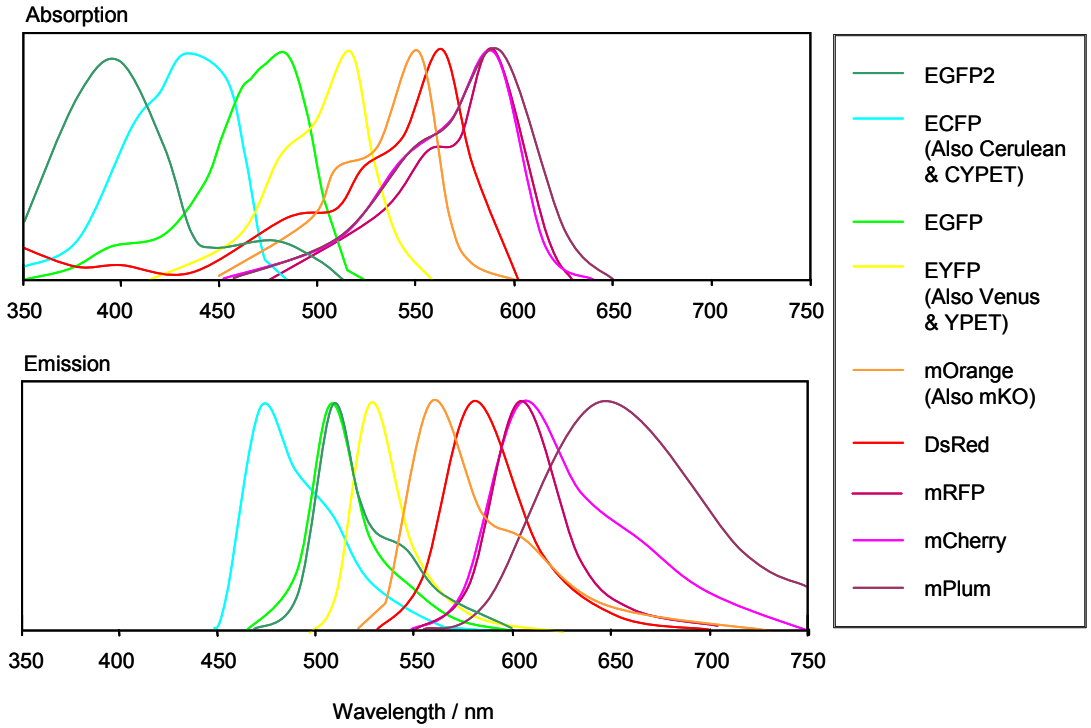


Figure 7.6: Absorption and emission spectra of visible fluorescent proteins.

7.5.1. Considerations for fluorophores

In choosing a pair of fluorophores for the second FRET sensor, a number of criteria must be satisfied. These mostly concern the need to avoid cross talk between the different spectral channels used to image the two FRET pairs. The following list highlights some of these points. Note that the first two points are true of any FRET scenario, the last two reflect extra considerations which arise when imaging the FRET pair alongside the YCAM sensor.

a) The overlap between the excitation spectra of the second donor and that of the second acceptor should be as small as possible, in order to minimise direct excitation of this acceptor. In practice, since most orange and red proteins exhibit a tail in their absorption spectra towards shorter wavelengths, some degree of direct acceptor excitation will be inevitable.
b) The second donor and acceptor pair must possess adequate spectral overlap for FRET to occur between them whilst not giving rise to spectral cross talk - one must avoid acceptor emission contaminating the donor filter channel, and vice versa.
c) The donor and acceptor emission spectra should be distinct from the emission spectrum of Venus in order to avoid spectral contamination of the second FRET pair by this fluorophore.
d) The donor excitation spectrum should be spectrally distinct from that of Venus to prevent coexcitation (and subsequent photobleaching) of the Venus fluorophore when imaging the second donor.

In addition to spectral considerations, the choice of proteins will also be affected by other criteria. Some of these will be common to both the donor and acceptor (quantum yields, photostability, maturation time), whilst others will be specific to one or the other (donor fluorescence lifetime, acceptor absorption coefficient). One point to mention is that different criteria may vary in importance depending on the means used to image the FRET signal. For example in a spectral ratiometric sensor it is vital that the acceptor have a high quantum yield in order to maximise the signal from sensitised emission. This is not necessary in FLIM-FRET where only the donor fluorescence is recorded. Indeed, in such a case it may often be that a low quantum yield acceptor is preferable to avoid bleed-through artefacts into the donor channel. For FLIM-FRET measurements it is also preferable for the donor to exhibit a mono-exponential decay profile, whereas this is inconsequential for measurements based solely on intensity. Obviously, no single pair of fluorophores will optimally fulfil all of these criteria – the task is therefore one of identifying a pair that can be imaged with sufficient signal to noise when all of these possible limitations are taken into account.

7.5.2. Choice of donor for the second FRET pair

The choice of a suitable donor for the second FRET pair will be largely determined by its brightness and spectral separation from the Venus fluorophore in the YCAM probe. A glance at the spectra in Figure 7.6 suggests an orange/red spectral variant could be a suitable donor,

whilst one of the longer red emitters (mCherry, mPlum etc) could act as the second acceptor. Table 7.2 below summarise the prospective choices for the donor in the second FRET pair.

Donor	Advantages	Disadvantages
mOrange	• High quantum yield • Long fluorescence lifetime (2.7 ns) • Large spectral overlap with potential acceptors mCherry, mPlum	• Low photostability • Large spectral overlap with Venus • Long maturation time
mKO	• High quantum yield • Very long fluorescence lifetime (3.5 ns) • Exceptional photostability • Large spectral overlap with potential acceptors mCherry, mPlum	• Large spectral overlap with Venus • Will undergo photoconversion to green emitter under short wavelength excitation (<500 nm) • Long maturation time
mRFP	• Larger spectral separation from Venus spectral channel	• Poor photostability • Low brightness (particularly, quantum yield) • Short fluorescence lifetime (<2 ns)
DsRed	• Larger spectral separation from Venus spectral channel	• Forms oligomers • Long maturation time • Multiple spectral components (matures through an initial green emissive state)

Table 7.2 Advantages and disadvantages of prospective donors for second FRET pair in multiplexed FRET.

From the left hand column of Table 7.2, mKO would seem to offer the best choice for the second donor, having good photostability, quantum yield and long fluorescence lifetime [183]. Unfortunately, a recent finding by Goedhart *et al* showed that mKO can undergo photoconversion to a green emitting state, following prolonged excitation at wavelengths below 500 nm [184]. While this does not preclude its use as a FRET donor is its own right, it renders it unsuitable for multiplexed FRET experiments where one would also need to illuminate the sample at shorter wavelengths in order to excite the ECFP donor. Of the two red fluorescent proteins, mRFP lacks sufficient brightness to act as a donor, whilst DsRed can be disqualified on the basis of its tetramerisation and issues concerning its maturation. For these reasons, the remaining orange fluorophore, mOrange was deemed the best choice.

7.5.3. Choice of acceptor for the second FRET pair

Choice of a suitable acceptor follows a slightly different set of criteria to the donor. One factor to consider is the size of the absorption coefficient, although the minimal difference in FRET efficiency between mRFP and mCherry as acceptors (see Chapter 3) suggests that a lower absorption coefficient should not necessarily be used to discriminate against a protein if it has other beneficial features.

Looking back at Figure 7.6, three possible candidates for pairing with the mOrange donor arise: mCherry, mPlum and HcRed. Of these 3, mCherry is the brightest and has the largest absorption coefficient. Each of the three has a similar absorption spectrum, meaning the overlap between the donor emission and acceptor absorption spectra will be approximately the same in all three cases. The larger stokes shift of mPlum and HcRed is certainly an advantage, since this will allow one to choose a donor emission band further removed from Venus, without detecting fluorescence from the second acceptor in this same channel. HcRed, however does have a tendency to dimerise [185].

In 2007, Goedhart *et al* published a comparison of FRET efficiencies between different pairs of yellow/orange donors and red acceptors [184]. Of those tested, mKO-mCherry was reported as having the highest dynamic range, followed by mOrange-mCherry. This report did not, however, mention use of either mPlum or HcRed as an acceptor, leaving it unclear as to what sort of dynamic range might be obtained using these two fluorophores. As a first choice, therefore, we chose to investigate the combination mOrange/mCherry for the second FRET pair.

Using the original Raichu construct designed by Mochizuki *et al* as a template, a novel Raichu construct labelled with the mOrange/mCherry FRET pair was cloned by Dr. W. Zhang at the Institute of Cancer Research.

7.6. Imaging the second FRET pair

Having chosen the fluorophores mOrange and mCherry, an important question arose over how best to image FRET between this pair. For the YCAM 3.6 construct, spectral ratiometric imaging is both suitable and straightforward, mainly because of the broad spectral separation between the ECFP and Venus emission spectra and also the high brightness of Venus which ensures a strong signal from sensitised emission. In common with YCAM 3.6, the Raichu

construct has the benefit of equal stoichiometries of donor and acceptor and so fulfils one criterion for ratiometric imaging. Nonetheless, such an approach is problematic for other reasons discussed below.

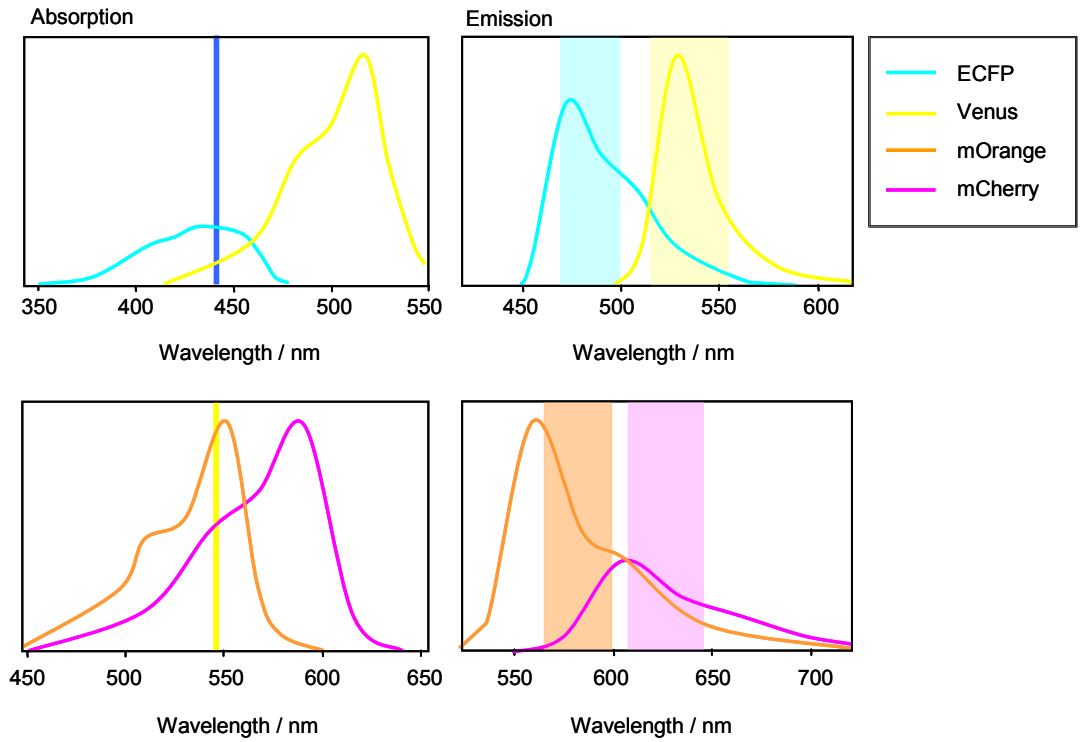


Figure 7.7: Absorption and emission spectra for ECFP/Venus and mOrange/mCherry FRET pairs. The absorption spectra have been normalised to the respective absorption coefficient of each fluorophore and the emission spectra normalised to their respective quantum yields. The vertical lines in the absorption spectra indicate possible choices for the excitation wavelength. The shaded regions in the emission spectra are suggested filters for dual channel intensity measurements.

Figure 7.7 highlights the difference in spectral properties of the two FRET pairs ECFP / Venus and mOrange / mCherry. Note in particular the separation between the two peaks in the emission spectrum for ECFP and Venus. If we now compare this with the mOrange / mCherry pair, we see a different situation. In this case, the low quantum yield of mCherry means that any sensitised emission from this fluorophore will occur against a relatively high noise background. A second issue is the possibility of acceptor (mCherry) fluorescence being detected in the donor (mOrange) filter channel. In most FRET experiments, this should be easy to avoid by choosing a shorter wavelength filter which cuts off before the emission spectrum of the acceptor begins (as is shown here for the ECFP / Venus pair). In the context of multiplexing, however, the overlap in emission and absorption spectra of Venus and mOrange necessitates using a longer wavelength filter set for imaging mOrange, to avoid yellow fluorescence contaminating the signal. Unfortunately, this runs into the problem of collecting mCherry fluorescence in this donor channel.

The above factors indicate that ratiometric measurements of FRET between mOrange / mCherry could offer a substantially lower dynamic range than ECFP / Venus. It was not known at this time whether lifetime measurements might offer an improved dynamic range. Nonetheless, based on relative quantum yields and spectra, the fractional contribution of mCherry fluorescence to this channel could be estimated to be much less than that from mOrange fluorescence. It was therefore posited that lifetime imaging of the mOrange donor would provide a useful measure of FRET between these species.

7.6.1. Fluorescence lifetime analysis of mOrange-Raichu-Cherry

As a first step towards evaluating the mOrange / mCherry Raichu's potential for multiplexed studies, we expressed the probe in COS cells by lipofection, and compared the lifetime of cells expressing the probe with those expressing the mOrange donor only. To check for FRET in the Raichu probe, cells were serum starved overnight, then imaged on the microscope following stimulation with 150 $ngml^{-1}$ EGF. Figure 7.8 shows representative images of these cells. Cells were excited using a supercontinuum source from Fianium, which was spectrally filtered to provide excitation light in the wavelength band 530-557 nm, with an emission filter at 563-603 nm.

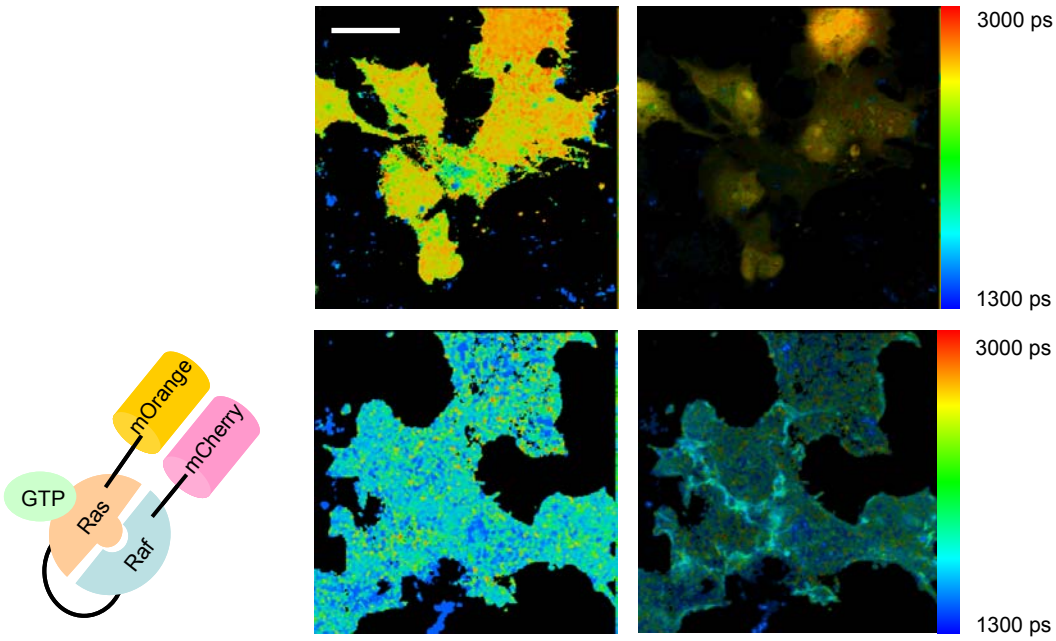


Figure 7.8: Fluorescence lifetime images of mOrange (top row) and mOrange-Raichu-mCherry (bottom row) in COS cells stimulated by EGF. Images on the right are the lifetime maps merged with the intensity image. Inset: Illustration of the mOrange-Raichu-mCherry probe. (Scale bar = 10 µm)

In comparing the FLIM maps of the mOrange/mCherry construct to that of mOrange alone, a clear shortening of lifetime (~ 1.2 ns) was evident. Whilst part of this fall in lifetime may have been accounted for by FRET between the two fluorophores, the size of the shift suggested additional factors besides FRET might be involved. In particular, the question arose as to what extent fluorescence from mCherry might be contaminating the mOrange spectral channel. To examine this, cells expressing the mOrange-Raichu-mCherry construct were imaged using a second filter set (F2) which was selected so as to minimise detection of mCherry fluorescence. Lifetimes measured using this filter set (F2) were then compared to those measured using the original filter set (F1). The spectral bands for the two filter sets are shown in Figure 7.9 and Table 7.3.

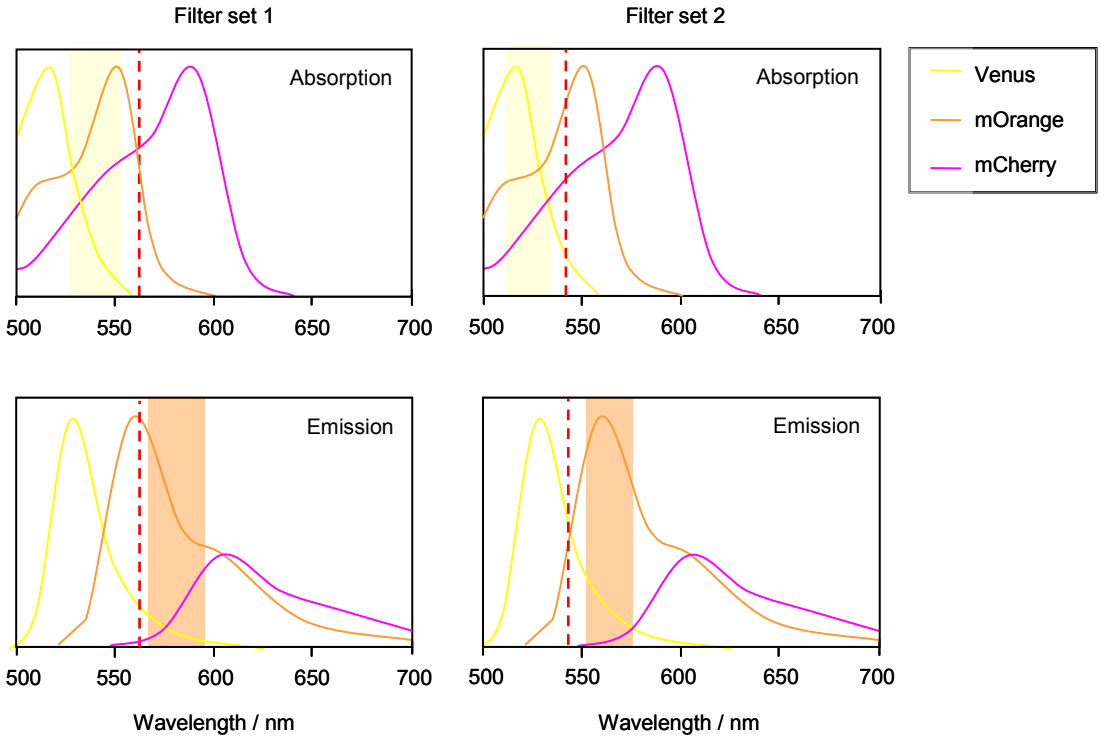


Figure 7.9: Absorption and emission spectra of Venus, mOrange and mCherry, with the spectral bands used in Filter set 1 (left column) and set 2 (right column) shown in the shaded regions. The dotted lines indicate the dichroic cut-off wavelength in the two cases.

Filter set	Excitation band / nm	Dichroic cut off	Emission band / nm
F1	542/27	560	580/30
F2	525/22	545	565/22

Table 7.3: Pass bands for two filter sets used to image mOrange-Raichu-mCherry.

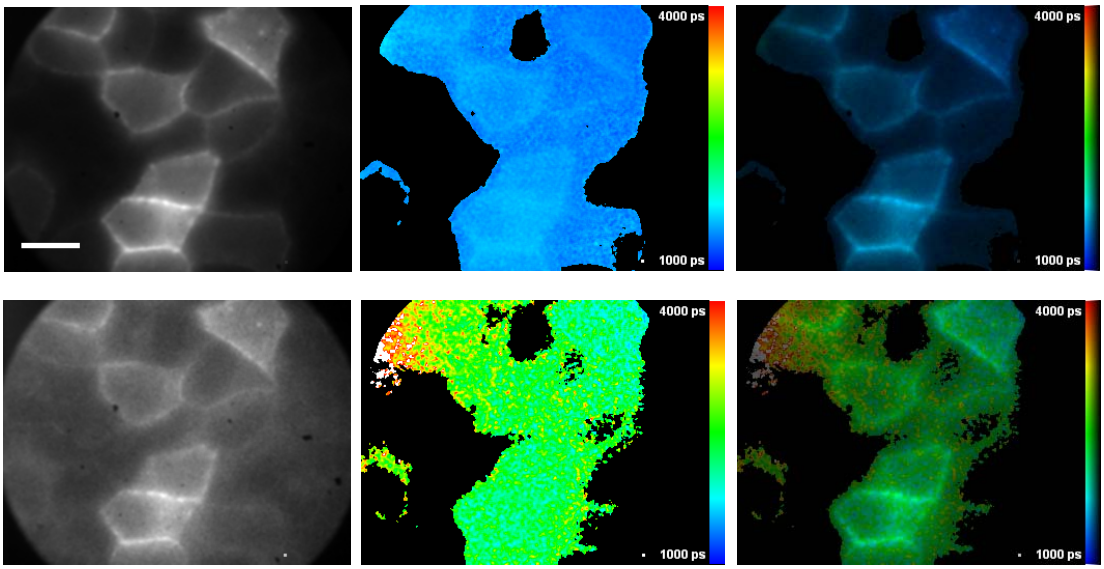


Figure 7.10: Fluorescence intensity and lifetime images of mOrange-Raichu-mCherry expressed in MDCK cells, imaged using the two filter sets F1 (top row) and F2 (bottom row). Scale bar = 10 µm.

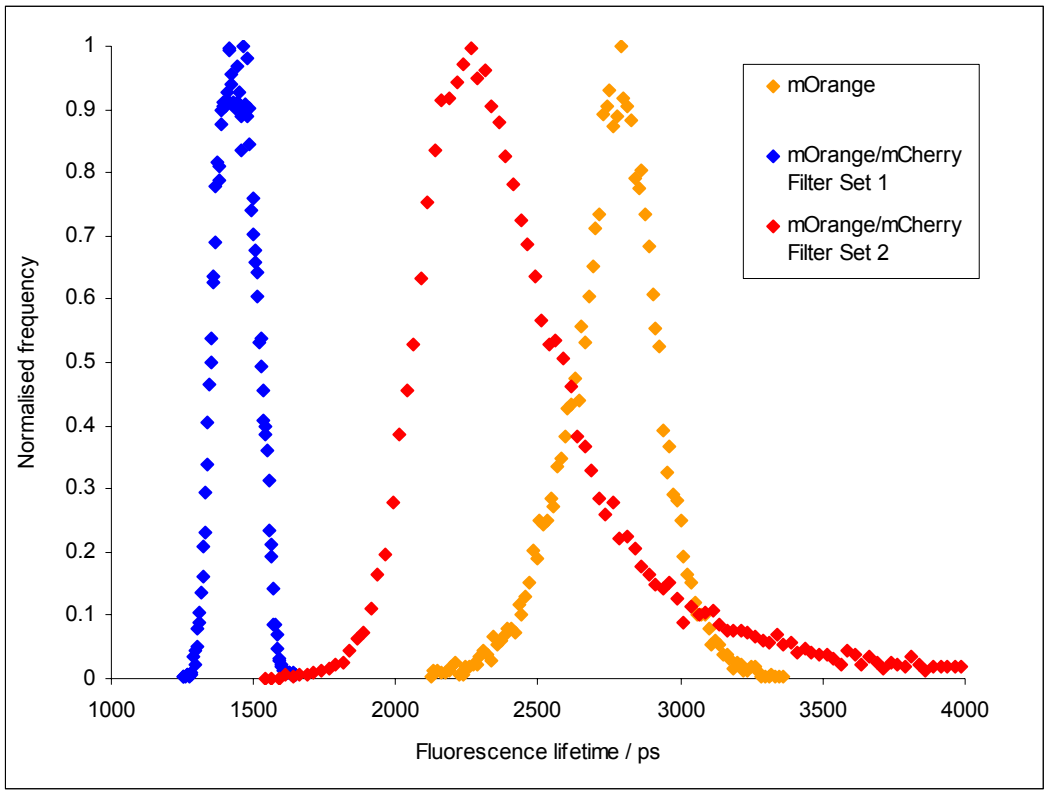


Figure 7.11: Lifetime histograms for the images in Figure 7.10 above.

The images in Figure 7.10 show a pronounced difference in lifetime between the two filter sets. This does indeed confirm that it is not just mOrange fluorescence that is contributing to the lifetime decay measured using filter set F1 (in the absence of other spectral components the lifetime would not vary to the extent it does when using the second filter set). In Figure

7.11, the histogram for the second, longer emission channel in F2 shows a mean lifetime of 1.4 ns, equivalent to that reported for mCherry alone [186]. This suggests that the signal in this channel is almost entirely mCherry fluorescence. The lifetime measured using the second filter set (which should reject most of the mCherry fluorescence) also seems to confirm this - this lifetime is closer to that of mOrange expressed by itself, while the smaller shift could be a genuine sign of FRET between mOrange and mCherry. These findings cast doubt on the original assumption that mCherry fluorescence would be low compared to the signal from mOrange, given the difference in quantum yield between the two. The comparative weakness of mOrange fluorescence might be explained by incomplete maturation – this would also explain the much weaker fluorescence signal detected when using filter set F2, despite collecting fluorescence nearer the emission peak of mOrange and the broader width of the lifetime histogram in this case.

7.7. Effects of spectral bleed-through on measured lifetimes

The data in section 7.6.1 show that in using a shorter wavelength filter channel, one can negate the effects of mCherry fluorescence being detected in the mOrange spectral channel. These results do not, however, take into consideration possible contamination by Venus, as was alluded to earlier. Taken together, these findings begin to suggest that the mOrange / mCherry pair lack the spectral bandwidth for multiplexing with ECFP and Venus.

To confirm this, we examined the extent to which the lifetime measured in the mOrange spectral channel varied when mOrange was coexpressed with either YCAM or mCherry constructs, and imaged using the two filter sets F1 and F2. Using constructs available in the lab, cells were cotransfected with either mOrange and YCAM, or mOrange and mCherry. Cells were left for 36 hrs in order to ensure maximum maturation of the respective fluorophores. Following this, cells were imaged on a wide-field microscope using the two filter sets F1 and F2, with laser excitation supplied by the same supercontinuum source discussed in the previous chapter. The mean lifetime in each image was measured and the data from a series of 15 images compiled in the box plot in Figure 7.12 below. Since none of these constructs should undergo FRET with one another, any deviation in mean lifetime would reflect a systematic error arising from spectral cross talk.

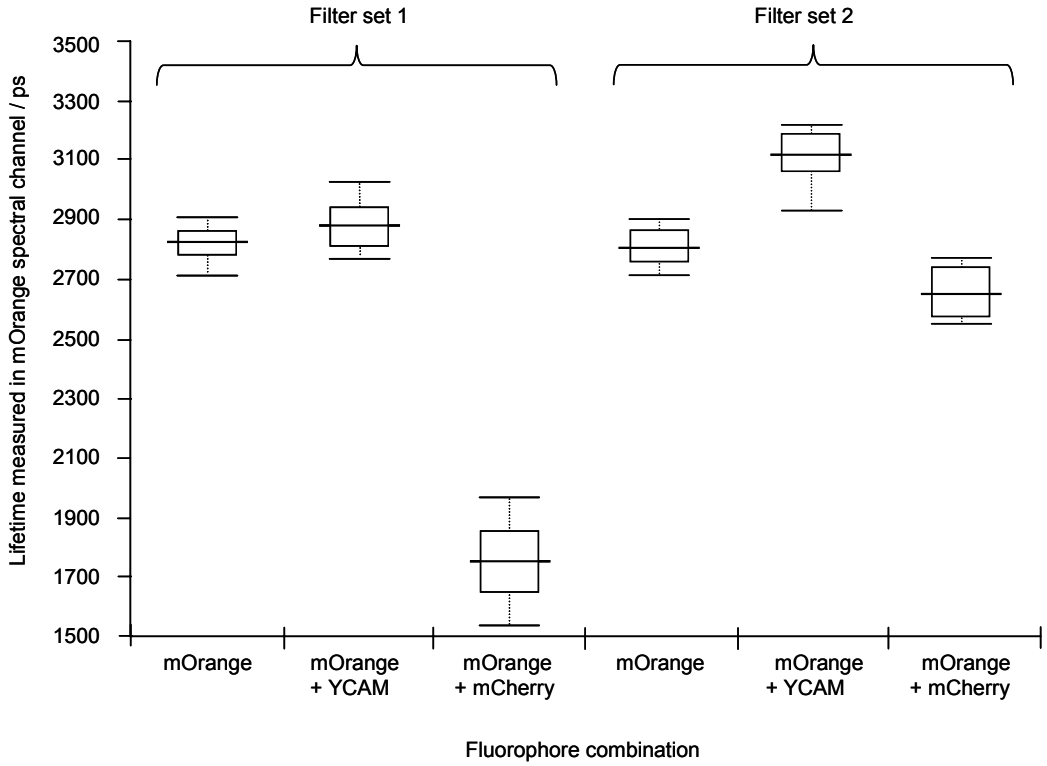


Figure 7.12: Box plot showing the distribution of mean lifetimes in the mOrange spectral channel, when imaging cells expressing different combinations of mOrange, YCAM and mCherry with the two filter sets F1 and F2.

The results shown above highlight the limited spectral bandwidth available when using mOrange and mCherry as a second FRET pair. The broad overlap in absorption and emission spectra means that a significant amount of spectral bleed-through is inevitable, either from Venus emission (if short wavelength filters are used) or mCherry (where more red-shifted filters are used). Piljic and Schultz, who in the time since then have published a dual FRET result using these FRET pairs have themselves pointed out the need to extend the excitation of mOrange to 565 nm to avoid excitation of EYFP, with a compromise made in terms of mCherry excitation [187]. In this case, the change in FRET upon conformational change could be detected above the cross talk between mOrange and mCherry, however it is arguable that this will only be true in certain sensors with particularly high dynamic range. More generally, it is likely that this bleed-through would present too high a noise background to measure genuine ratiometric changes in intensity arising from FRET, with lifetime measurements similarly compromised.

7.8. Increasing the spectral bandwidth for multiplexing

Following on from this discussion, the obvious step would be to obtain fluorophores with greater spectral separation. One possibility for expanding the spectral gap between pairs

might be to replace the ECFP / Venus pair with a shorter wavelength excited pair, such as blue fluorescent protein with an EGFP acceptor, as demonstrated by Mahajan *et al* [188]. This would then allow one to excite and detect the mOrange donor at shorter wavelengths, without encountering the issue of Venus fluorescence being detected in the same channel. This approach would be unfavourable for two reasons, however. First, moving to shorter wavelengths would require excitation in the UV region of the spectrum, with accompanying issues of cell viability and background autofluorescence. Secondly, this would necessitate re-labelling of the cameleon probe, which could in turn reduce the probe's dynamic range. Instead, we chose to expand the spectral separation by use of further red-shifted FRET pairs.

During the time this second FRET sensor was under development, several new red fluorescent proteins had become available. Of particular note was the publication in July 2007 of two novel far red emitting species, a dimeric form named Katushka, and a monomeric alternative mKate [189]. The properties of these and other possible acceptors are summarised in Table 7.4 below.

Protein	Excitation maximum / nm	Emission maximum / nm	Quantum yield	Extinction coefficient / $M^{-1}cm^{-1}$	Brightness (relative to EGFP)
mCherry	587	615	0.22	72000	0.48
mRaspberry	598	625	0.15	86000	0.39
Katushka	588	635	0.34	65000	0.67
mKate	588	635	0.33	45000	0.45
mPlum	590	649	0.10	41000	0.12
HcRed	594	649	0.05	70000	0.10

Table 7.4 Spectral properties of far-red emitting fluorescent proteins.

Of those proteins listed in Table 7.4, mCherry has already been discussed and dismissed on grounds of its spectral overlap with the mOrange donor. The monomeric protein mRaspberry, having been developed by evolutionary mutagenesis at the same time as mCherry possesses a slightly further red-shifted emission, nonetheless, the same problem of detecting its fluorescence in the mOrange channel may still occur.

Katuskha was designed primarily for *in-vivo* imaging, being particularly bright and possessing an emission spectrum which coincides with the optical window for efficient transmission through tissue. As the brightest of all the variants, it might serve as a possible candidate for ratiometric FRET measurements with mOrange, although issues could arise from its dimerisation. Its derivative, mKate, while not as bright is nonetheless monomeric

and may therefore present a more favourable alternative. The last two proteins in the table, mPlum and HcRed afford the greatest spectral separation from mOrange. Although the low brightness of these proteins precludes their use as acceptors for ratiometric FRET measurements, FRET between mOrange and either one of these should still be possible using lifetime imaging of the mOrange donor. Although HcRed has a higher absorption coefficient, its tendency to dimerise makes mPlum a more suitable choice for cell imaging.

On the basis of these arguments, it was decided to use mPlum as the acceptor in the second FRET pair with the mOrange donor. This in turn would necessitate using FLIM to image FRET between this pair of proteins, since the signal from sensitised emission of mPlum would likely be too low to achieve sufficient signal to noise. It is interesting to speculate whether the same might not be true of an mOrange / mKate pair, in which the enhanced brightness of mKate might permit ratiometric measurements to be utilised. This pair might therefore offer a second valid alternative to mOrange / mCherry. Ultimately, however, the need to maximise the spectral bandwidth meant choosing the pairing of mOrange with mPlum, the latter having the furthest red-shifted emission of all available proteins.

7.9. Comparing spectral bleed-through of mPlum with mCherry

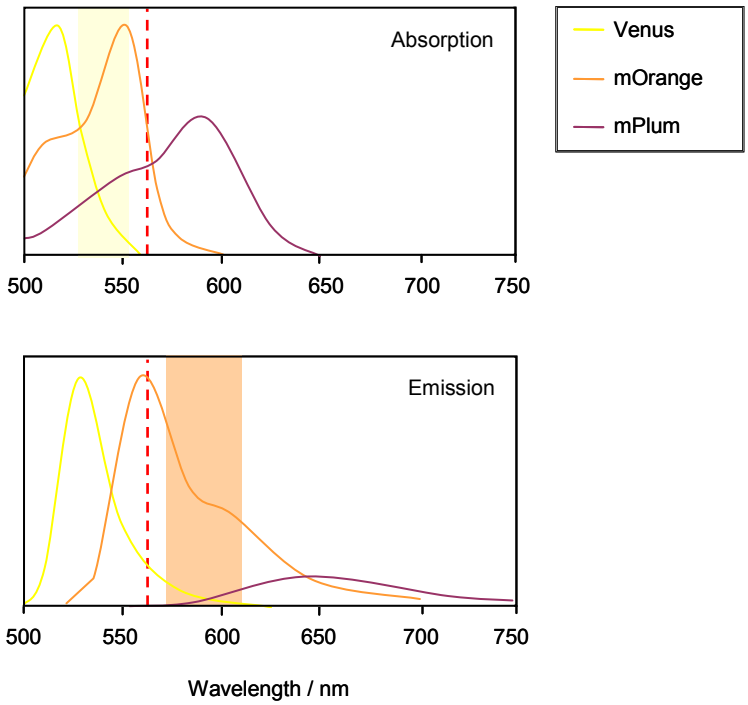


Figure 7.13: Absorption and emission spectra of Venus, mOrange and mPlum with the spectral bands used to excite and detect shown in the shaded regions. The dotted lines indicate the dichroic cut-off.

Having already encountered the issue of spectral contamination by mCherry in the first Raichu probe, we sought to evaluate whether mPlum could offer a better option. In order to confirm that mPlum did not contaminate the mOrange spectral channel, we measured the lifetimes of cells expressing both these proteins and observed whether or not these were impacted by fluorescence from mPlum. Figure 7.13 shows the spectra and filter set used. Note that the longer emission of mPlum fluorescence enabled us to use a longer emission filter for the mOrange channel, preventing the detection of Venus fluorescence in the same spectral window. Cells were cotransfected with plasmids encoding the mOrange and mPlum fluorophores and were imaged using a 542/22 excitation filter, 560LP dichroic and 593/40 emission filter. The mean lifetime from a number of cells was calculated and compared to that from cells expressing mOrange alone. To validate this as a suitable pair for multiplexing, cells coexpressing the YCAM plasmid were also imaged. Figure 7.14 shows the compiled data for each combination of flurophores when using this filter set. The data set for mCherry / mOrange is also shown for comparison.

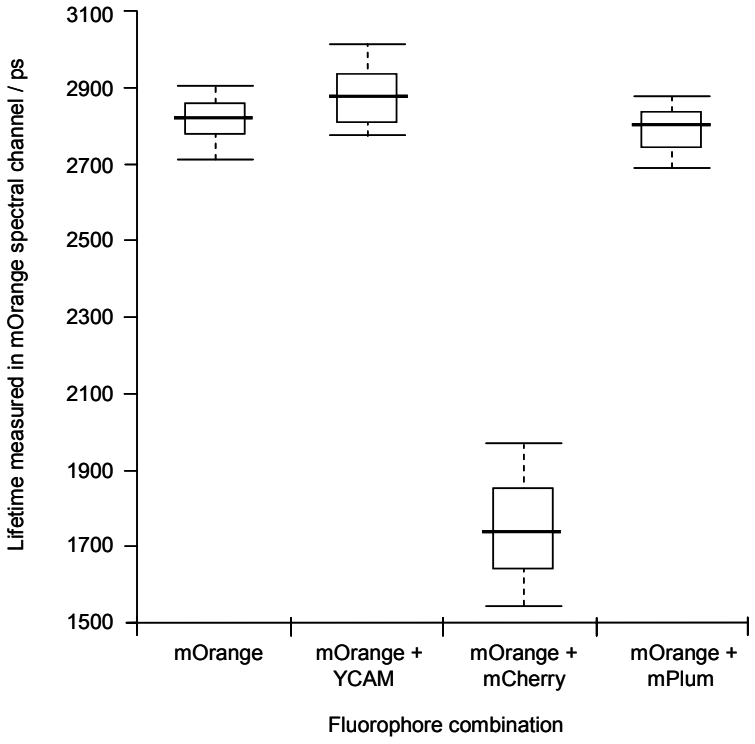


Figure 7.14: Box plot showing distributions of mean lifetime in cells expressing different combinations of mOrange, YCAM and mPlum.

These results suggested that by using mPlum instead of mCherry, the mOrange fluorescence could be successfully resolved in the longer wavelength channel without incurring issues of bleed-through of the acceptor fluorescence. Following this, a second Raichu construct was cloned by Dr. Zhang, this time replacing mCherry with mPlum.

7.10. Imaging the mOrange-Raichu-mPlum construct

To assay the new Raichu construct for FRET between mOrange and mPlum, COS cells were transfected with the Raichu plasmid and serum starved for 24 hrs. Following this, cells were stimulated for different periods with EGF and fixed in paraformaldehyde, before being imaged on the microscope. Representative images and lifetime histograms are shown in Figures 7.15 and 7.16 respectively.

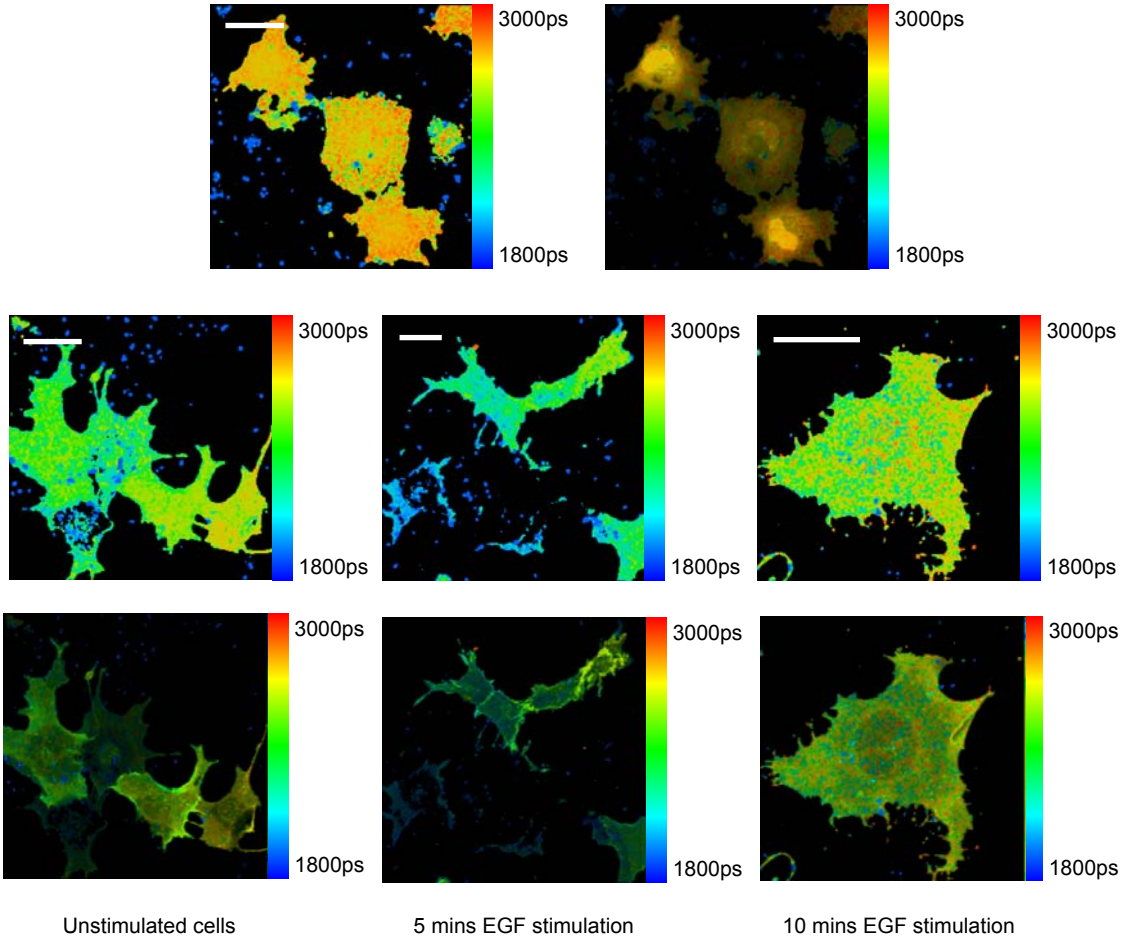


Figure 7.15: Fluorescence lifetime images of mOrange and mOrange-Raichu-mPlum in COS cells. Top row: FLIM map and intensity merged image of mOrange. Middle and bottom rows: FLIM maps and intensity merged images of mOrange-Raichu-mPlum fixed after different periods of stimulation by EGF. (Scale bars = 10 μm).

The results show that the mOrange-mPlum pair does function as an efficient FRET pair, with cells showing consistently short lifetimes. This alleviated concerns that the low absorption coefficient of mPlum would render it a poor acceptor for mOrange compared to mCherry. Unfortunately, it was found that in the vast majority of cells this signal remained constant prior to and after stimulation, suggesting a low dynamic range in FRET signal. This could be explained by one or two different reasons: firstly, that the probe's conformation in both its

active and inactive forms was such that efficient FRET could occur between the two fluorophores. Alternatively, that the probe had folded in such a way that it could not be activated or deactivated (i.e. was in one permanent conformation with a constant FRET signal). The folding of the Raichu construct is a complex process and could be highly sensitive to slight changes in primary sequence. It is possible that in redesigning this probe, the Ras domain had become occluded from endogenous GEF activity, leaving it in an unaltered conformation upon cell stimulation.

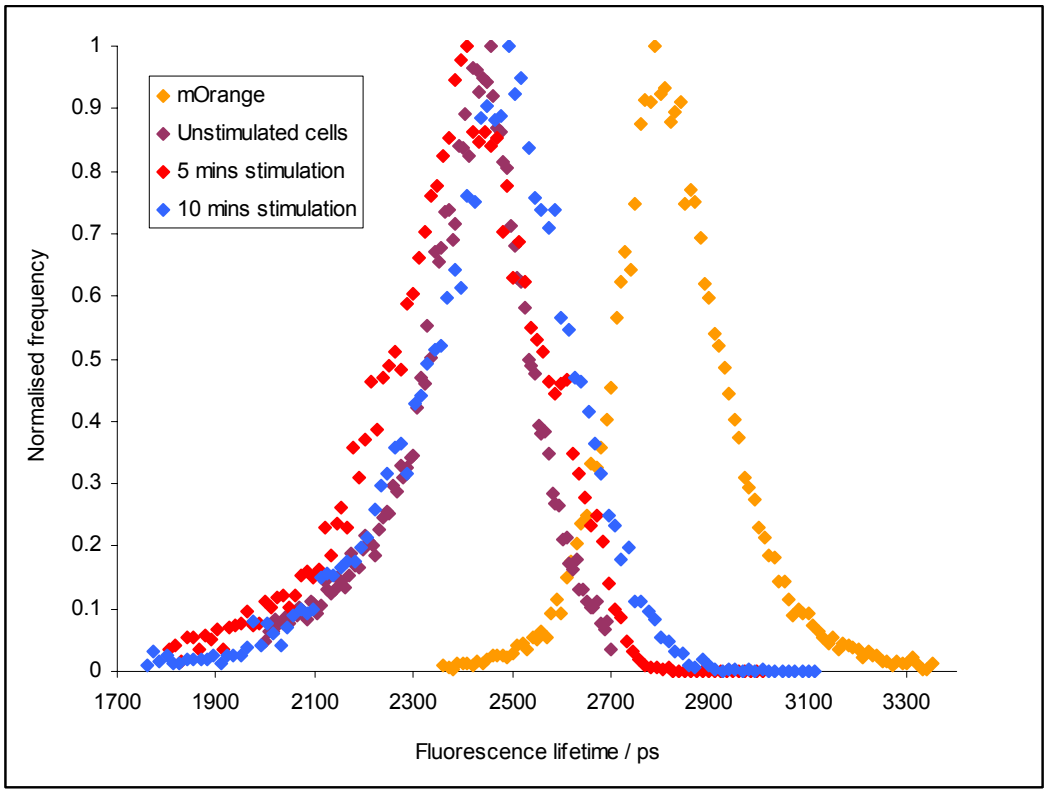


Figure 7.16: Fluorescence lifetime histograms from cells expressing mOrange, and mOrange-Raichu-mPlum stimulated for different periods with EGF.

In summary, these measurements marked a partial success: a probe had been designed with measurable FRET signal, which could be spectrally resolved from the cameleon FRET pair. Nonetheless, the lack of any change in FRET signal upon cell stimulation argued that further engineering of the linker sequences would be required before this could be developed into a second viable FRET biosensor.

7.11. Use of separately labelled constructs

The problem of low dynamic range in the mOrange-Raichu-mPlum FRET sensor is not uncommon in developing such probes. There are a number of ways this problem can be

addressed, usually involving extended trialling of mutant versions of the probe with different linker lengths between domains and the introduction of different circular permutations of the fluorescent labels with change in fluorophore orientation and resultant FRET signal. Such methods are quite time intensive, however, and rely on a high throughput strategy for first cloning and then monitoring the different mutants' behaviour. The decision was therefore made to opt for an intermolecular sensor consisting of isolated Raf RBD and H-Ras. Although this would mean expressing 3 plasmids (or possibly 4 if PLC was also to be used) within the same cell and would therefore necessitate all experiments be carried out using microinjection, the possibility for increasing the dynamic range in the second FRET sensor made this worthwhile.

7.12. TagRFP: An alternative donor for the second pair

The data in section 7.9 had shown that mOrange fluorescence could be successfully resolved from YCAM 3.6 and mPlum provided one used the correct filter combinations. The caveat associated with this was one had to excite and detect the orange fluorescence away from the respective peaks in absorption and emission spectrum.

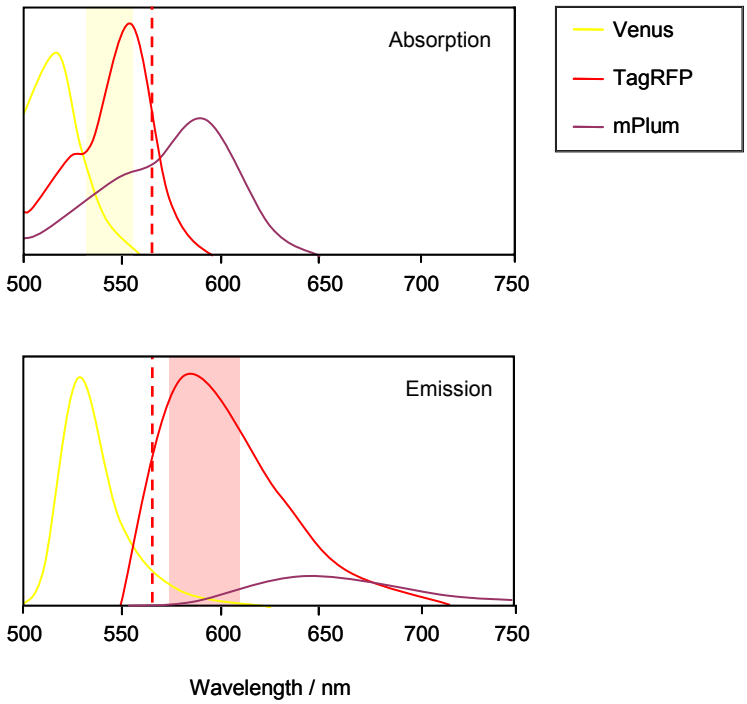


Figure 7.17: Absorption spectra and emission spectra for TagRFP, YCAM and mPlum. Shaded areas indicate filters used to excite and detect TagRFP fluorescence.

During the time the constructs discussed above were being characterised, a novel red fluorescent protein was developed in the lab of Dmitriy Chudakov in Moscow [186]. Named TagRFP, this fluorophore was subsequently commercialised and made available through *Evrogen*. The fluorophore is one of several mutants developed by mutagenesis of an original clone from the sea anemone *Entacmaea quadricolor* and possesses an enhanced brightness and maturation time compared to other proteins in the same spectral range (mRFP, DsRed etc). TagRFP also has the fortuitous advantage that its absorption and emission spectra peaks coincide well with the filter combinations chosen to resolve mOrange from Venus and mPlum (Figure 7.17). This prompted us to replace mOrange with TagRFP as the donor in the second FRET pair.

7.12.1. Investigating FRET between TagRFP and mPlum

To validate the new red fluorescent donor, cells expressing mixtures of TagRFP / YCAM or TagRFP / mPlum were imaged on the wide-field FLIM microscope and lifetimes in the TagRFP spectral channel measured to check for artefacts from spectral bleed-through. The results are shown in Figure 7.18 below.

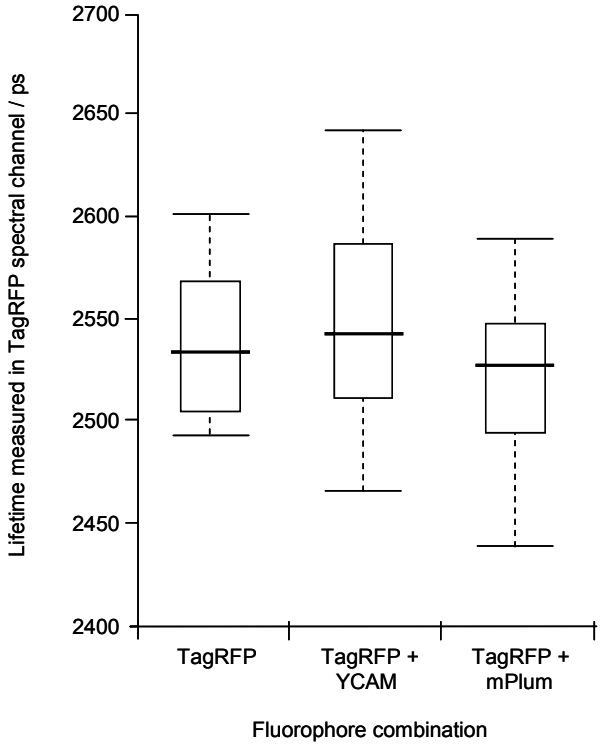


Figure 7.18: Box plot showing distributions of mean lifetime in cells expressing different combinations of TagRFP, YCAM and mPlum.

The data in Figure 7.18 show that TagRFP fluorescence can be successfully resolved with minimal bleed-through from either mPlum or YCAM. Following this, constructs of TagRFP-Raf-RBD and H-Ras-mPlum were cloned (courtesy, Dr. W. Zhang) and coexpressed in live cells. These were then stimulated with EGF and imaged on a wide-field FLIM microscope. Figure 7.19 shows a representative fluorescence lifetime image of TagRFP-Raf-RBD.

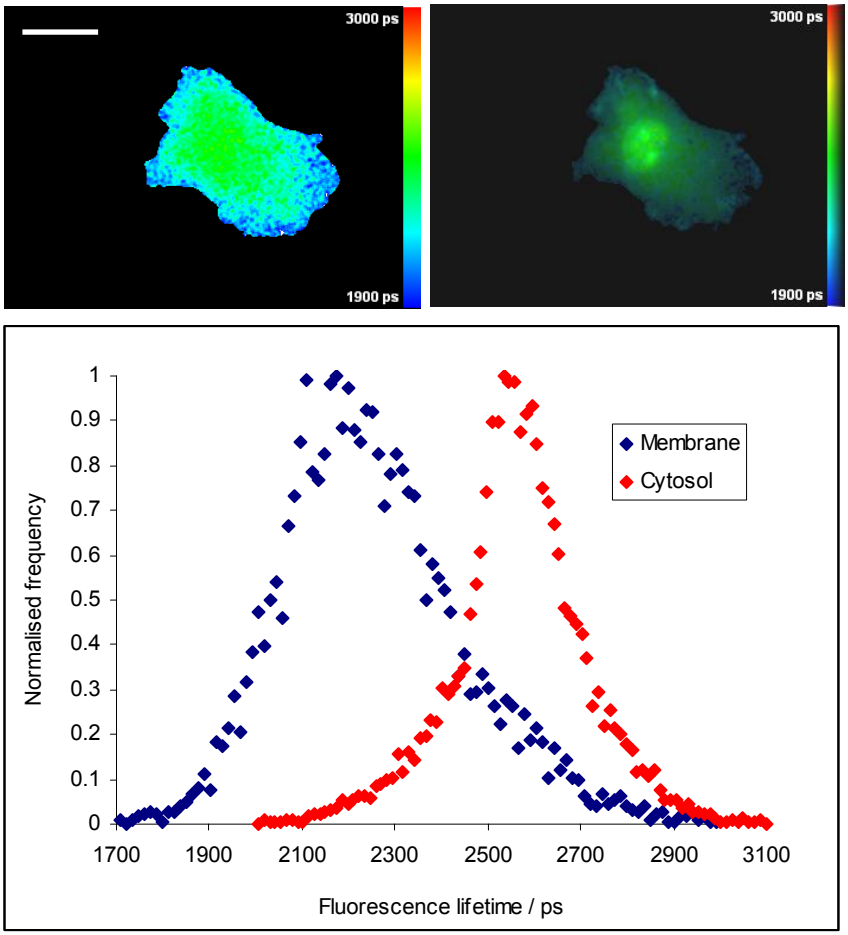


Figure 7.19: Top: Fluorescence lifetime images of TagRFP-Raf-RBD in COS cells coexpressing H-Ras-mPlum, after 10 mins EGF stimulation. Bottom: Lifetime histograms for the above images, from a region in the cytosol and the plasma membrane. The lifetime shift at the membrane is evidence of FRET between TagRFP-Raf-RBD and H-Ras-mPlum. (Scale bar = 10 µm)

The large shift in lifetime between the cytosol and the membrane is clear evidence of FRET and highlights the increased dynamic range of this sensor compared to the single molecule Raichu probe.

From this, we were able to conclude that the combination of the YCAM 3.6 FRET sensor with an intermolecular FRET pair of TagRFP labelled Raf-RBD and H-Ras-mPlum could provide both the necessary spectral bandwidth and dynamic range in FRET signal to

successfully resolve two, independent signaling events in live cells. This pairing of probes and the spectral filters used is summarised in Figure 7.20 below.

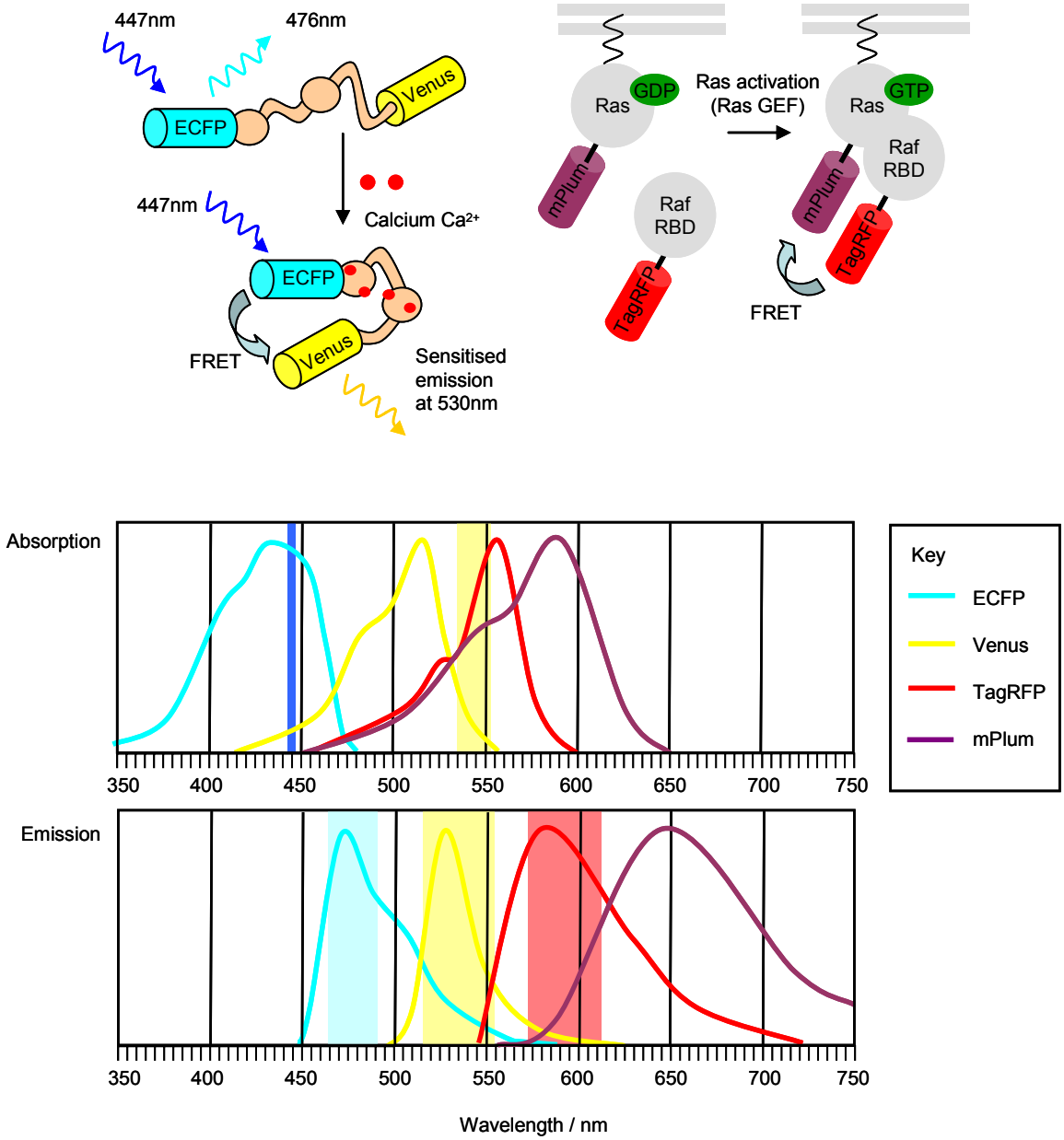


Figure 7.20: Top: Final probe selection for multiplexed FRET: An ECFP/Venus YCAM 3.6 cameleon and TagRFP-Raf-RBD/H-Ras-mPlum intermolecular FRET pair for sensing Ras activation at the membrane. Bottom: Full absorption and emission spectra showing excitation wavelengths and spectral detection channels for multiplexed imaging.

7.13. Experimental set-up for multiplexed FRET

The final set up used for multiplexing is shown in Figure 7.21. The system is built around an inverted Olympus microscope into which are coupled a continuous wave diode pumped solid state laser for blue excitation of ECFP and a spectrally filtered pulsed supercontinuum source

used to excite the second donor, TagRFP. The microscope is set up under standard wide-field illumination, in which the excitation beam is collimated and expanded to fill the diameter of the tube lens in the back port of the microscope. From here it is focussed into the back aperture of the microscope objective providing collimated light at the sample with even illumination across the field of view. To counter interference effects in the image which might give rise to artefacts, a rotating diffuser wheel is placed in the light path to disrupt the spatial coherence of the laser beam.

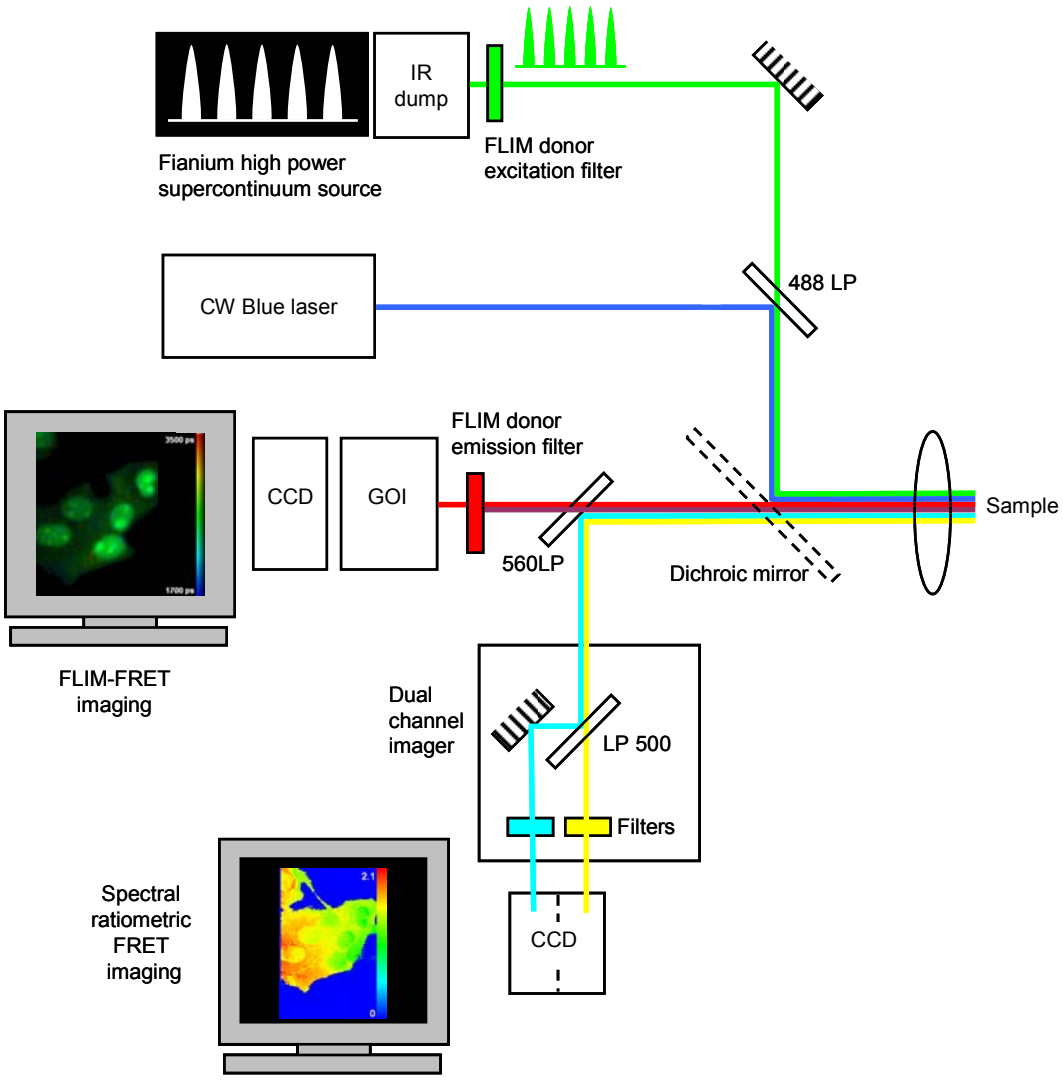


Figure 7.21: Instrumental set up for multiplexed FRET

Fluorescence from the ECFP and Venus emission is separated from TagRFP emission by the 560LP dichroic and spectrally resolved into two channels as before using the dual channel imager from Optical Insights. The TagRFP lifetime meanwhile is measured using the same wide-field gating strategy described in Chapter 6.

In order to coordinate exposures of the two FRET pairs, a shutter was installed in each laser excitation path. The acquisition program was updated by Dr. C. B. Talbot so that the shutters would trigger off the same signals used to start acquisitions on each of the two cameras. In this way it was possible to ensure that the blue laser only illuminated the sample when fluorescence from the YCAM 3.6 probe was being read out and similarly the supercontinuum source only illuminated the sample during FLIM acquisitions of TagRFP. It is feasible that this could be extended to automatically select the dichroic for each of the two lasers, however, it was found that this could be done manually without disrupting the experiment.

7.14. Results of multiplexing

Figure 7.22 shows time-lapse images from a field of view containing cells which were coinjected with the 4 plasmids: YCAM 3.6, TagRFP-Raf-RBD, H-Ras-mPlum and full length PLCε.

Following stimulation by EGF, a fast, transient rise in cytosolic calcium levels occurred, as seen from the increase in intensity ratio between the Venus and ECFP channels in the dual channel imager. The FLIM images of the TagRFP donor meanwhile showed a sustained shortening of the donor lifetime at the cell membrane, indicating FRET between this probe and the membrane bound H-Ras following cell stimulation. Unfortunately, owing to the poor photostability of the TagRFP donor (which became apparent during the course of these experiments), only 4 - 5 FLIM images could be acquired before photobleaching rendered the photon count too small for accurate lifetime determination.

Given the absence of any observed rise in calcium levels in cells which were not coinjected with the full length PLCε enzyme, it seems reasonable once again to posit a link between the calcium spike in Figure 7.22 and a heightened PLC activity. At this point, it is not clear whether this is a direct downstream effect arising from gross release of IP_3 or arises through a different mechanism in which the overexpressed PLCε also has a role to play. Similarly, the FRET signal between TagRFP-Raf-RBD and H-Ras-mPlum, although indicative of Ras activation, is not in itself evidence of a link between these other signaling events, but rather a downstream effect of EGFR phosphorylation. With further experiments, in particular, use of gene knock-downs or inhibitors, it might become possible to unravel the complex interplay between calcium signals and Ras activity.

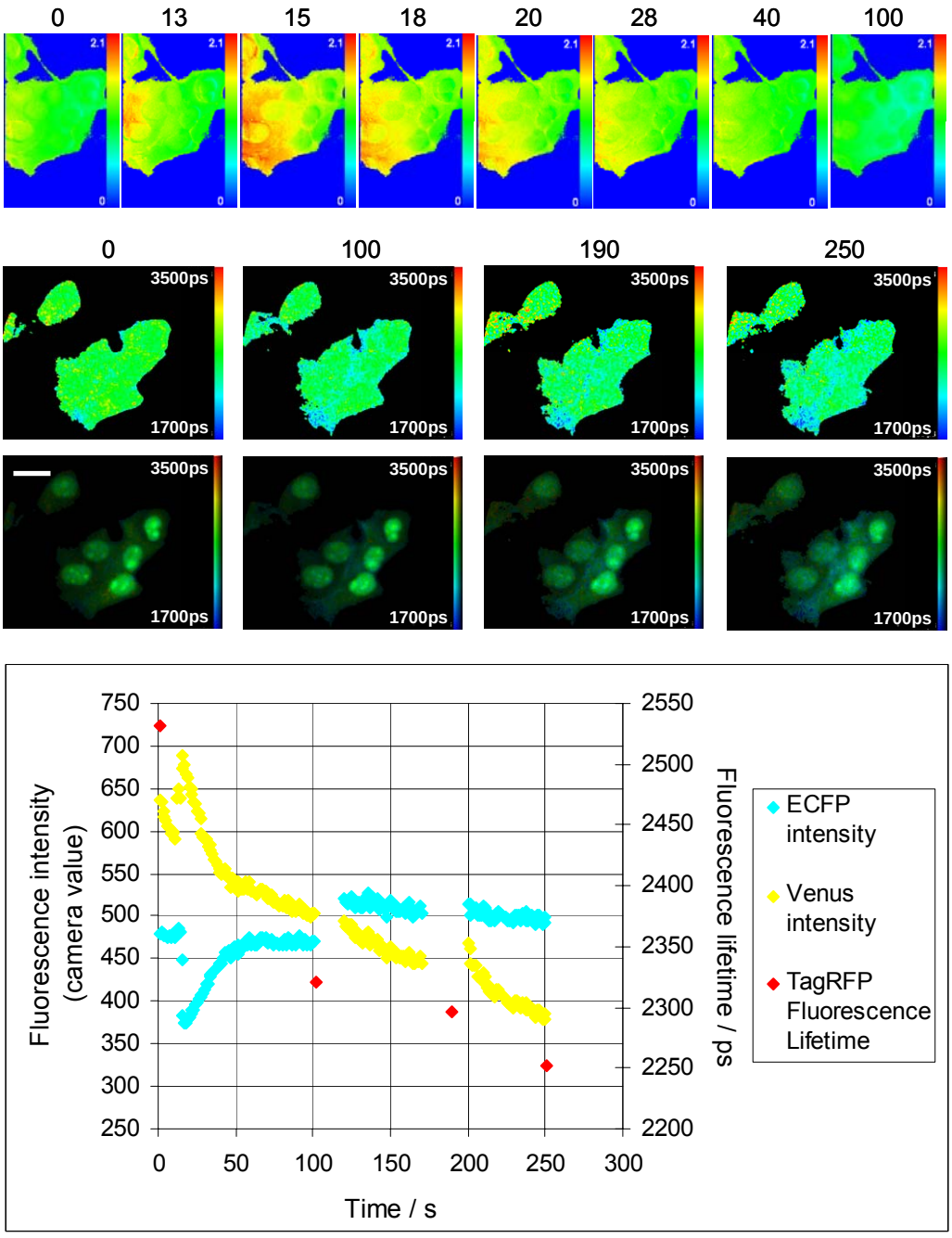


Figure 7.22: Multiplexed FRET imaging of cells expressing the two FRET sensors and full length PLCε. Top: Ratiometric images of YCAM acquired using the Dual-View at intervals before and after stimulation (numbers above indicate time in seconds after cell stimulation with EGF). Middle: FLIM images and merged intensity images of TagRFP in the same cells, at the time points shown above. Bottom: Graphs of ECFP and Venus intensity from a region in the cytosol, and TagRFP lifetime from a region in the cell membrane. (Scale bar = 10 μm).

7.15. Conclusion

This chapter has examined the potential for monitoring multiple key signaling events in live cells using FRET and has demonstrated how through judicious choice of filter sets, fluorophores and probe design, such a goal can be achieved.

In the time since this work was undertaken, several approaches to imaging multiple FRET pairs have been reported in the literature. Ai *et al* have reported on a method relying on dual ratiometric imaging of two donor and acceptor pairs [190]. The large spectral overlap of the existing fluorescent proteins discussed earlier prompted them to design a deep blue excited fluorescent protein with large stokes shift. This permitted them to excite both a CFP derivative (mTFP1) and this new protein (mAmetrine) at the same wavelength. The long stokes shift of the mAmetrine made it possible to resolve the fluorescence from the two donors in separate channels, together with the sensitised emission from their respective acceptors (mCitrine and tDtomato) with enhanced signal to noise compared to the mOrange / mCherry combination. Piljic and Schultz too have published the first report of a multiplexed experiment, using ratiometric imaging of an ECFP / EYFP and mOrange / mCherry pair [187]. Although successful, this paper did highlight the spectral bleed-through between the fluorophores EYFP, mOrange and mCherry as a significant source of noise. That such experiments were successful no doubt owes much to the groups' experience in probe design, which may have helped ensure a large enough change in FRET between active and inactive conformations to be detected above the noise background. Arguably, though, this might not be the case in the majority of FRET sensors.

The method put forward in this chapter yields multiple benefits over these other approaches. It is not compromised by spectral bleed-through to the same extent and the use of FLIM for at least one of the measurements means it is applicable to intermolecular as well as intramolecular FRET sensors. The results shown here hold promise for elucidating the role of calcium signaling in Ras activation and how the spatial and temporal modulation of calcium concentration give rise to different cellular outputs. This represents an important step forward in understanding how these events are related in cell signaling processes, and the role of PLCε in regulating such events.

At the time of writing, a novel mutant of the TagRFP with enhanced photostability has been described by Shaner *et al* [25] – this holds promise for increasing the rate and number of exposures possible in a multiplexed experiment. In addition, a novel Yokogawa confocal scan head has also recently become available with the ability for fast automated switching

between different fluorescent dichroics. In future, this should enable one to perform similar experiments with the benefits of optical sectioning, as discussed in Chapter 6.

Chapter 8: Conclusions

8.0. Chapter overview

In the past several years, Förster Resonance Energy Transfer (FRET) has become a sought-after method for studying cell signaling and function. The information afforded by FRET measurements is particularly valuable since it is one of the few methods by which molecular interactions can be verified in the context of the intact cell. In this thesis, we have focused on the development of new microscopy tools and fluorescent probes in order to expand the potential of FRET for exploring different aspects of cell signaling. Although much of this work is related to signal pathways involving Ras small GTP-ases, the conclusions drawn from it extend to the study of signal pathways in general. The main findings of this work and possible future directions are discussed below.

8.1. Results summary and discussion

A key theme of this thesis has been the design and characterisation of new tools for imaging FRET in live cells. Using a combination of wide-field time-gated fluorescence lifetime imaging technology, a Nipkow spinning disc confocal scan head and a high power supercontinuum source, we have been able to image protein activation in live cells at frame rates far exceeding those possible with commercially available time correlated single photon counting confocal microscopes. Comparisons of the signal-to-noise of FLIM images obtained using these different approaches yielded a favourable outcome for the wide-field time-gated system, which in the presence of sufficiently bright samples can achieve FLIM-FRET frame rates of 10 Hz, adequately distinguishing lifetimes in cells expressing EGFP alone and those expressing an EGFP-mRFP tethered construct. Refinements in supercontinuum sources, should, it is envisaged allow for higher power outputs, with potential for even faster imaging of cell signaling events. This system should continue to provide opportunities for probing interactions in live cells, with additional applications in high throughput imaging for screening drug candidates.

This theme extended to the design and implementation of a ‘multiplexed FRET’ microscope, capable of monitoring FRET signals from two, independent FRET sensors expressed within the same cell. The ability to resolve interactions between multiple cellular species, and the

respective timing and spatial organisation of these events should help to uncover the mechanisms involved in complex signaling networks.

A second key theme of this work has been the evaluation of different fluorescent protein pairs for FRET. In early work, we examined using EGFP as a donor with several recently available red fluorescent proteins. Fluorescence lifetime measurements of constructs fusing EGFP to one of the orange/red fluorophores, mRFP, mCherry and mOrange, showed that both EGFP-mRFP and EGFP-mCherry could provide a robust FRET signal, while the EGFP-mOrange combination had a far more limited dynamic range. It should be noted that, at the time these constructs were made, only the EGFP-mRFP pair had been used and reported in the literature - the measurement of FRET in the EGFP-mCherry construct was therefore one of the first demonstrations of this FRET pair. The identification of suitable FRET pairs for imaging was key to the work on multiplexed FRET, for which it was necessary to maximise the available spectral bandwidth between the two sensors. This was realised by implementing a further two, previously unreported, FRET pairs – mOrange/mPlum and TagRFP/mPlum. Such pairs should provide new opportunities for imaging cellular interactions, particularly in the context of multiplexed imaging.

The advances made above, coupled with hardware already available in the lab, have allowed us to probe interactions associated with Ras and PLCε signal pathways. Using constructs of Ras fused to mRFP in conjunction with an EGFP labelled PLCε construct, we have been able to image their direct interaction in a small number of MDCK cells stimulated with EGF. The infrequency of this occurrence suggests that whilst direct interactions may occur between Ras and PLCε, they are highly transient and hard to capture unless imaging at very high speed (a problem exacerbated by typically low expression levels of PLCε). A second possibility might be that interactions occur through a number of different stages involving conformational changes in the complex, with the probes only being suitably orientated for FRET during one, short-lived stage of the process. Some evidence for this has been given by the observation of a sustained FRET signal seen when H-Ras-mRFP was coexpressed with the isolated RA2 domain from PLCε (as a single protein domain, this would not undergo the same changes in conformation as the full length protein). It is possible therefore, that in addition to recruitment of PLCε to the plasma membrane, Ras may also facilitate its activation through changes in its overall conformation.

Experiments using the multiplexed FRET microscope show further promise for exploring these proteins' functionality. Using this system, we have successfully imaged activation of H-Ras alongside calcium transients following EGF stimulation in live cells, in which

untagged full length PLCε was also expressed. This technology holds potential for elucidating the regulatory mechanisms underlying Ras and PLC activity.

8.2. Future directions

The work in this thesis has contributed to the development of new tools for imaging cell signaling pathways in live cells. Many opportunities now exist for exploiting these developments in order to learn more about cell function and behaviour.

With regard to the studies of FRET between PLCε and Ras GTP-ases in Chapter 5, one possibility might be to investigate using different labelling strategies to maximise the FRET signal seen during the course of an interaction. In this respect, the FlAsH technology pioneered in the group of Professor R. Tsien could be worth exploring, since this will provide opportunities to position the fluorophores at other sites where they may adopt a closer proximity to one another. Although experiments in live cells are currently limited by the low fluorescence signal from the rPLCε-EGFP construct, it is conceivable that the introduction of brighter fluorophores may overcome this limitation. In future, therefore, it may be possible to revisit using the high speed microscope to capture these transient interactions with greater temporal resolution. A further avenue of exploration would also be to look more closely into the posited conformational changes associated with this interaction. One method might be to design a FRET probe based on PLCε itself. While certainly challenging, this is not without precedent [191] and would be highly informative in understanding the mechanism behind Ras mediated activations of this enzyme.

These studies of PLCε and Ras signaling could be further complemented by experiments using the multiplexed FRET microscope. Having demonstrated the viability of this approach for imaging signaling events associated with Ras and PLCε activity, thought can now be given to investigating the temporal dynamics of these signaling events under different cellular conditions. SiRNA techniques could be employed to examine the changes in response during knock-out or knock-down of different signaling components. Similarly, overexpression of the same genes should help elicit further information on the interplay between these different components. One question that does arise is the ease which these experiments could be repeated, given the large number of genes that must be co-expressed in any one cell. Although microinjection has been used successfully throughout this work, it is likely that such an approach will not provide the necessary throughput for longer term studies, in which much larger numbers of cells would need to be looked at. For this reason, it

might be worth returning to the question of designing a long wavelength unimolecular probe for imaging Ras activity. Reducing the number of individual genes that need to be expressed could allow experiments to be performed using conventional transfection protocols which target a much larger number of cells.

Aside from time-lapse imaging of protein-protein interactions, an obvious application for the high speed microscope will be in the high content screening of multi-well plates. In its simplest form, this could involve treating the wells in each plate with different drug compounds and using the FLIM images obtained from each cell to report any changes in binding between cellular components (the interaction of Ras with its effector Raf RBD is a case in point). Automation of the microscope will play a large part in this process: stage scanning functions, auto-focussing and cell-finder capabilities will need to be built in to the microscope controller software, while gain settings on the GOI will also need to be chosen depending on the brightness of the current field of view. The same will also apply for image analysis – image segmentation and auto-fitting routines will need to be employed in order to dissect the lifetimes in different parts of the cells and so validate the effects of these different drug compounds. Many of these steps are now currently underway and should continue in future.

It is clear that there are a large number of possibilities for continuing the work discussed in this thesis. Any such experiments will of course necessitate the close collaboration of scientists in different fields of biology, chemistry and physics - a trend that is certainly likely to continue into the future.

Publications and conference presentations arising from the work presented in this thesis

Journal publications

1. Multiplexed FRET to image multiple signaling events in live cells **D. M. Grant**, W. Zhang, E. J. McGhee, T. D. Bunney, C. B. Talbot, S. Kumar, I. Munro, C. Dunsby, M. A. A. Neil, M. Katan, and P. M. W. French, *Biophys. J.* 95(10) L69-71 (2008)

2. High speed optically sectioned fluorescence lifetime imaging permits study of live cell signaling events **D. M. Grant**, J. McGinty, E. J. McGhee, T. D. Bunney, D. M. Owen, C. B. Talbot, W. Zhang, S. Kumar, I. Munro, P. M. Lanigan, G. T. Kennedy, C. Dunsby, A. I. Magee, P. Courtney, M. Katan, M. A. A. Neil, and P. M. W. French, *Opt. Express* 15, 15656-15673 (2007)

3. A compact, multidimensional spectrofluorimeter exploiting supercontinuum generation H. B. Manning, G. T. Kennedy, D. M. Owen, **D. M. Grant**, M. Katan, A. I. Magee, M. A. A. Neil, C. Dunsby, Y. Itoh and P. M. W. French *J. Biophotonics* (Nov 2008)

4. High speed unsupervised fluorescence lifetime imaging confocal multiwell plate reader for high content analysis C.B. Talbot, J. McGinty, **D. M. Grant**, E. J. McGhee, D. M. Owen, W. Zhang, T. D. Bunney, I. Munro, B. Isherwood, R. Eagle, A. Hargreaves, M. Katan, C. Dunsby, M. A. A. Neil and P. M. W. French *J. Biophotonics* (2008 - *submitted)*

5. Fluorescence lifetime imaging provides enhanced contrast when imaging the phase-sensitive dye di-4-ANEPPDHQ in model membranes and live cells D.M. Owen, P. M. P. Lanigan, C. Dunsby, I. Munro, **D. M. Grant**, M.A.A. Neil, P.M.W. French and A.I. Magee. *Biophys J.* 90(11), L80-L82 (2006)

Conference oral presentations

1. High-speed optically-sectioned fluorescence lifetime imaging of live cells **D. M. Grant**, S. Kumar, J. McGinty, C. B. Talbot, E. J. McGhee, D. M. Owen, P. A .A. De Beule, I. Munro, G. T. Kennedy, P. Courtney, D. M. Davis, M. Katan, C. Dunsby, M. A. A. Neil and P. M. W. French. BiOS, Photonics West, San Jose, US (2008)

2. High speed, optically-sectioned fluorescence lifetime imaging utilizing time-gated Nipkow disk or multifocal multiphoton time correlated single photon counting microscopy C. B. Talbot, J. McGinty, E. J. McGhee, **D. M. Grant**, S. Kumar, D. M. Owen, G. T. Kennedy, I. Munro, P. Courtney, W. Zhang, T. Bunney, A. I. Magee, D. M. Davis, M. Katan, C. Dunsby, M. A. A. Neil and P. M. W. French. OSA Biomedical Optics, St. Petersberg, US (2008)

3. High speed wide-field optically sectioned FLIM and multiplexed FRET for live cell studies E. J. McGhee, **D. M. Grant,** W. Zhang, T. D. Bunney, C. B. Talbot, J. McGinty, I. Munro, C. Dunsby, M. A. A. Neil, M. Katan and P. M. W. French. Focus on Microscopy, Osaka, Japan (2008)

4. High-speed, wide-field optically-sectioned, live cell fluorescence lifetime imaging **D. M. Grant**, S. Kumar, D. M. Owen, P. M. P. Lanigan, C. B. Talbot, J. McGinty, J. Requejo-Isidro, I. Munro, D. S. Elson, C. Dunsby, A. I. Magee, T. Bunney, M. Katan, P. Courtney, M. A. A. Neil and P. M. W. French. BiOS, Photonics West, San Jose, US (2007)

5. Application of tunable continuum sources to fluorescence imaging and metrology E. Auksorius, D. M. Owen, H. B. Manning, P. De Beule, **D. M. Grant**, S. Kumar, P. M. P. Lanigan, C. B. Talbot, J. McGinty, C. W. Dunsby, M. A. A. Neil and P. M. W. French. BiOS, Photonics West, San Jose, US (2007)

6. High-speed wide-field FLIM applied to Nipkow disk microscopy J. McGinty, C. B. Talbot, **D. M. Grant**, G. Kennedy, S. Kumar, D. M. Owen, I. Munro, P. Lanigan, C. Dunsby, A. I. Magee, M. Katan, P. Courtney, M. A. A. Neil and P. M. W. French. FOM, Valencia, Spain (2007)

7. High-speed wide-field optically-sectioned live cell fluorescence lifetime imaging **D. M. Grant**, S. Kumar, D. M. Owen, P. M. P. Lanigan, C. B. Talbot, J. McGinty, J. Requejo-Isidro, I. Munro, D. S. Elson, C. Dunsby, A. I. Magee, M. A. A. Neil, P. Courtney and P. M. W. French. EOS, Paris, France (2006)

8. A compact, multidimensional spectrofluorimeter exploiting supercontinuum generation H. B. Manning, G. T. Kennedy, D. M. Owen, **D. M. Grant**, M. A. A. Neil, C. Dunsby, Y. Itoh and P. M. W. French. BiOS, Photonics West, San Jose, US (2009) (*submitted*)

Poster presentations

1. Multiplexed FRET for imaging cell signaling and high speed optically sectioned FLIM for high throughput screening applications **D. M. Grant**, W. Zhang, E. J. McGhee, C. B. Talbot, J. McGinty, T. D. Bunney, I. Munro, C. Dunsby, P. Courtney, M. Katan, M. A. A. Neil, and P. M. W. French. 7th International Weber Symposium, Lihue US (2008)

2. Imaging membrane lipid microdomains using multidimensional fluorescence microscopy D. M. Owen, M. Cebecauer, S. Kumar, S. Oddos, H. B Manning, **D. M. Grant**, M. Purbhoo, M. A. A. Neil, P. M. W. French and A. I. Magee. 7th International Weber Symposium, Lihue, US (2008)

3. High-speed wide-field FLIM applied to Nipkow disk microscopy J. McGinty, C. B. Talbot, **D. M. Grant**, G. Kennedy, S. Kumar, D. M. Owen, I. Munro, P. Lanigan, C. Dunsby, A. I. Magee, M. Katan, P. Courtney, M. A. A. Neil and P. M. W. French. ECI, Naples, US (2007)

4. Novel imaging and biological applications of the phase-sensitive membrane dye di-4-ANEPPDHQ D. M. Owen, H. B. Manning, S. Kumar, **D. M. Grant**, J McGinty, P. M. P. Lanigan, S. Oddos, C. Talbot, P. De Beule, E. Jury, M. A. A. Neil, P. M. W. French and A. I. Magee. EBSA, London, UK (2007)

5. High-speed wide-field optically-sectioned live cell fluorescence lifetime imaging **D. M. Grant**, S. Kumar, D. M. Owen, P. Lanigan, C. B. Talbot, J. McGinty, J. Requejo-Isidro, I. Munro, D. S. Elson, C. Dunsby, A. I. Magee, M. A. A. Neil and P. M. W. French and P. Courtney. EMBL, Heidelberg, Germany (2006)

6. Application of tunable continuum sources to fluorescence imaging E. Auksorius, C. Dunsby, P. M. P. Lanigan, D. M. Owen, **D. M. Grant**, H. B. Manning, P. De Beule, C. B. Talbot, J. McGinty, M. A. A. Neil and P. M. W. French. EMBL, Heidelberg (2006)

Book chapters

1. Multidimensional fluorescence imaging J. McGinty, C. Dunsby, E. Auksorius, R. K. P. Benninger, P. A. A. De Beule, D. S. Elson, N. Galletly, **D. M. Grant,** O. Hofmann, G. T. Kennedy, S. Kumar, P. M. P. Lanigan, H. B. Manning, I. Munro, B. Önfelt, D. M. Owen, J. Requejo-Isidro, K. Suhling, C. B. Talbot, P. Soutter, M. J. Lever, A. J. De Mello, G. S. Stamp, M. A. A. Neil and P. M. W. French in FRET and FLIM imaging, Edited by T. W. J. Gadella, part of Laboratory techniques in biochemistry and molecular biology, Edited by P. C. van der Vliet. Elsevier BV, Amsterdam, NL (2008)

References

1. Lakowicz, J.R., "Principles of Fluorescence Spectroscopy". New York: Kluwer Academic Press. (1999)

2. Schmidt, R. "Photosensitzed generation of singlet oxygen" *Photochem. Photobiol.* 82(5) p1161-77 (2006)

3. Patterson, G. H. and Piston, D. W., "Photobleaching in two-photon excitation microscopy" *Biophys J.* 78(4) p2159-2162 (2000)

4. Dittrich, P.S. and Schwille, P., "Photobleaching and stabilization of fluorophores used for single molecule analysis with one and two photon excitation" *Appl. Phys. B.* 73 p829-837 (2001)

5. Coons, A. A., "The demonstration of Pneumococcal Antigen in tissues by the use of fluorescence antibody" *J. Immunol.* 45 p159-170 (1942)

6. Bagatolli, L.A., and Gratton, E. "Two-photon fluorescence microscopy observation of shape changes at the phase transition in phospholipid giant unilamellar vesicles" *Biophys J.* 77(4) p2090-101 (1999)

7. Stosiek, C., Garaschuk, O., Holthoff, K., and Konnerth, A. "In vivo two-photon calcium imaging of neuronal networks" *Proc. Natl. Acad. Sci. U.S.A.* 100(12) p7319-24 (1999)

8. Tsien, R. Y., "The green fluorescent protein" *Annu. Rev. Biochem.* 67 p590-44 (1998)

9. Prasher, D. C., Eckenrode, V. K., Ward, W. W., Prendergast, F. G., and Cormier, M. J. "Primary structure of the Aequorea Victoria green fluorescent protein" *Gene* 111(2) p229-33 (1992)

10. Chalfie, M., Tu, Y., Euskirchen, G., Ward, W. and Prasher, D.C., "Green fluorescent protein as a marker for gene expression," *Science* 263 p802-5 (1994)

11. Ormö, M., Cubitt, A. B., Kallio, K., Gross, L. A., Tsien, R. Y., and Remington, S. J., "Crystal structure of the Aequorea victoria green fluorescent protein" *Science* 273(5280) p1392-5 (1996)

12. Yanf, F., Moss, L. G., and Phillips, G. N. Jnr, "The molecular structure of green fluorescent protein" *Nat. Biotechnol.* 14(10) p1246-51 (1996)

13. Cody, C. W., Prasher, D. C. , Westler, W.W., Pendergast, F. G., and Ward, W. W., "Chemical Structure of the hexapeptide chromophore of the Aequorea Green fluorescent protein" *Biochemistry* 32 p1212-18 (1993)

14. Heim, R., Prasher, D. C. and Tsien, R. Y., "Wavelength mutations and post translational autoxidation of green fluorescent protein" *Proc. Natl. Acad. Sci. U.S.A.* 91 p12501-04 (1994)

15. Cubitt, A. B., Heim, R., Adams, S. R., Boyd, A. E., Gross, L. A., and Tsien, R. Y., "Understanding, improving and using green fluorescent proteins" *Trends Biochem. Sci.* 20(11) p448-55 (1995)

16. Heim. R., Cubitt, A., and Tsien, R. Y., "Improved green fluorescence" *Nature* 373 p663-64 (1995)

17. Heim, R. and Tsien, R. Y. "Engineering green fluorescent protein for improved brightness, longer wavelengths and fluorescence resonance energy transfer" *Curr. Biol.* 6(2) p178-82 (1996)

18. 18. Wachter R. M., Elsliger, M. A., Kallio, K., Hanson, G. T., and Remington, S .J. Structural basis of spectral shifts in the yellow-emission variants of green fluorescent protein. *Structure* 6 p1267-77 (1998)

19. 19. Cubitt A. B., Woollenweber, L. A., and Heim, R. "Understanding structure function relationships in the aequorea victoria green fluorescent protein" Methods in Cell Biology. San Deigo. Academic Press Vol 58 p19-30 (1999)

20. Matz, M.V., Fradkov, A. F, Labas, Y. A., Savitsky, A. P., Zaraisky, A. G., Markelov, M. L., Lukyanov, S.A. "Fluorescent proteins from nonbioluminescent Anthozoa species" *Nat. Biotechnol.* 17(10) p969-73 (1999)

21. Shaner, N. C., Campbell, R. E., Steinbach, P. A., Giepmans, B. N., Palmer, A. E., and Tsien, R. Y. "Improved monomeric red, orange and yellow fluorescent proteins derived from Discosoma sp. red fluorescent protein" *Nat Biotechnol.* 22(12) p1567-72 (2004)

22. Gurskaya, N. G., Fradkov, A. F., Terskikh, A., Matz, M. V., Labas, Y. A., Martynov, V. I., Yanushevich, Y. G. , Lukyanov, K. A. and Lukyanov, S.A. "GFP-like chromoproteins as a source of far-red fluorescent proteins" *FEBS Lett.* 507(1) p16-20 (2001)

23. Kremers, G. J., Goedhart, J., van den Heuvel, D. J., Gerritsen, H. C., and Gadella, T.W. Jr. "Improved green and blue fluorescent proteins for expression in bacteria and mammalian cells" *Biochemistry* 46(12) p3775-83 (2007)

24. Verkhusha, V. V., Otsuna, H., Awasaki, T., Oda, H., Tsukita, S., and Ito, K., "An enhanced mutant of red fluorescent protein DsRed for double labeling and developmental timer of neural fiber bundle formation" *J Biol Chem* 276(32) p29621-4 (2001)

25. Shaner, N. C., Lin, M. Z., McKeown, M. R., Steinbach, P. A., Hazelwood, K.L, Davidson, M. W., and Tsien, R.Y. "Improving the photostability of bright monomeric orange and red fluorescent proteins" *Nat Methods* 5(6) p545-51 (2008)

26. Ai, H.W., Henderson, J. N., Remington, S. J., and Campbell, R. E., "Directed evolution of a monomeric, bright and photostable version of Clavularia cyan fluorescent protein: structural characterization and applications in fluorescence imaging" *Biochem J*. 400(3) p531-40 (2006)

27. Rekas, A., Alattia, J. R., Nagai, T., Miyawaki, A. and Ikura, M. "Crystal structure of venus, a yellow fluorescent protein with improved maturation and reduced environmental sensitivity" *J Biol Chem*. 277(52) p50573-8 (2002)

28. Kogure, T., Kawano, H., Abe, Y., and Miyawaki, A. "Fluorescence imaging using a fluorescent protein with a large Stokes shift" Methods. 45(3) p223-6 (2008)

29. Scruggs, A. W., Flores, C. L., Wachter, R., and Woodbury, N. W., "Development and characterization of green fluorescent protein mutants with altered lifetimes" *Biochemistry* 44(40) p13377-84 (2005)

30. Habuchi, S., Ando, R., Dedecker, P., Verheijen, W., Mizuno, H., Miyawaki, A., and Hofkens, J., "Reversible single-molecule photoswitching in the GFP-like fluorescent protein Dronpa" *Proc Natl Acad Sci U S A.* 102(27) p9511-6 (2005)

31. Lippincott-Schwartz, J., and Patterson, G.H., "Fluorescent proteins for photoactivation experiments" *Methods Cell Biol*. 85 p45-61 (2008)

32. Chudakov, D. M., Lukyanov, S., and Lukyanov, K. A., "Tracking intracellular protein movements using photoswitchable fluorescent proteins PS-CFP2 and Dendra2" *Nat Protoc*. 2(8) p2024-32 (2007)

33. Bates, M., Huang, B., Dempsey, G. T., and Zhuang, X. "Multicolor super-resolution imaging with photo-switchable fluorescent probes" *Science* 317(5845) p1749-53 (2007)

34. Shroff, H., Galbraith, C. G., Galbraith, J. A., and Betzig, E., "Live-cell photoactivated localization microscopy of nanoscale adhesion dynamics" *Nat. Methods* 5(5) p417-23 (2008)

35. Jamieson, T. Bakhshi, R., Petrova, D., Pocock, R., Imani, M., and Seifalian, A. M., "Biological applications of quantum dots" *Biomaterials* 28(31) p4717-32 (2007)

36. Medintz ,I. L., Uyeda, H. T., Goldman, E R., Mattoussi, H., "Quantum dot bioconjugates for imaging, labelling and sensing" *Nat Mater* 4(6) p435-46 (2005)

37. Skala, M. C., Riching, K.M., Gendron-Fitzpatrick, A., Eickhoff, J., Eliceiri, K. W., White, J. G., and Ramanujam, N. "In vivo multiphoton microscopy of NADH and FAD redox states, fluorescence lifetimes, and cellular morphology in precancerous epithelia" *Proc Natl Acad Sci U S A*. 104(49) p19494-9 (2007)

38. Levitt, J. M., Baldwin, A., Papadakis, A., Puri, S., Xylas, J., Münger, K., and Georgakoudi, I. "Intrinsic fluorescence and redox changes associated with apoptosis of primary human epithelial cells" *J Biomed Opt* 11(6) 64012 (2006)

39. Minsky, M. Microscopy Apparatus. In *U. S. Patent* U. S. A (1961)

40. White, J. G., Amos, W. B., and Fordham, M., "An evaluation of confocal versus conventional imaging of biological structures by fluorescence light microscopy" *J. Cell. Biol.* 105(1) p41-8 (1987)

41. Pawley, J. B. "Handbook of Biological Confocal Microscopy" - J.B. Pawley, New York, Plenum Press (1995)

42. Williams, R. M., Zipfel, W. R., and Webb, W. W., "Multiphoton microscopy in biological research" *Curr. Opin. Chem. Biol.* 5(5) p603-8 (2001)

43. Petran, M., Hadravsky, M. Egger, M. D., and Galambos, R. "The Tandem Scanning Reflected Light Microscope" *J.O.S.A.* 58 p661-664 (1968)

44. 43. Kino, G. S., Corle, T. R., and Xiao, G. Q., "Real Time Confocal Scanning Optical Microscope" *Appl. Phys. Lett.* 53 p716-718 (1988)

45. Wolleschensky, R., and Zimmermann, B. “High-speed confocal fluorescence imaging with a novel line scanning microscope” *J. Biomed. Opt.*.11 p064011 (2006)

46. Strauba, M., Lodemannb, P., Holroydb, P., Jahnb, R., and Hell, S. W. “Live cell imaging by multifocal multiphoton microscopy” *Euro. J. Cell Biol.* 79(10) p726-34 (2000)

47. Kumar, S., Dunsby, C., De Beule, P. A. A., Owen, D. M., Anand, U., Lanigan, P. M. P., Benninger, R. K.P., Davis, D. M., Neil, M. A. A., Anand, P., Benham, C., Naylor, A., and French, P. M. W., “Multifocal multiphoton excitation and time correlated single photon counting detection for 3-D fluorescence lifetime imaging," *Opt. Express* 15, p12548-12561 (2007)

48. Neil, M. A. A., Juskaitis, R., and Wilson, T., “Method of obtaining optical sectioning by using structured light in a conventional microscope” *Opt Lett*. 22(24) (1997)

49. Karadaglić D., and Wilson, T. “Image formation in structured illumination wide-field fluorescence microscopy” *Micron*. 39(7) p808-18 (2008)

50. Sibarita, J. B., “Deconvolution microscopy” *Adv. Biochem. Eng. Biotechnol*. 95 p201-43 (2005)

51. Cai, D., Verhey, K. J., and Meyhöfer, E., “Tracking single Kinesin molecules in the cytoplasm of mammalian cells” *Biophys J.* 92(12) p4137-44 (2007)

52. Mashanov, G. I., Nenasheva, T. A., Peckham, M., and Molloy, J. E., “Cell biochemistry studied by single-molecule imaging” *Biochem. Soc. Trans.* 34(5) p983-8 (2006)

53. Miyawaki, A., Sawano, A., and Kogure, T., “Lighting up cells: labelling proteins with fluorophores” *Nat Cell Biol*. Suppl:S1-7 (2003)

54. Maruyama, S., Kikuchi, K., Hirano, T., Urano, Y., and Nagano, T., “A novel, cell-permeable, fluorescent probe for ratiometric imaging of zinc ions. *J. Am. Chem. Soc.* 124(36) p10650-1 (2002)

55. Montana, V., Farkas, D. L., and Loew, L. M., “Dual-wavelength ratiometric fluorescence measurements of membrane potential” *Biochemistry* 28(11) p4536-9 (1989)

56. Jin, L., Millard, A. C., Wuskell, J. P., Clark, H. A., and Loew, L. M., “Cholesterol-enriched lipid domains can be visualized by di-4-ANEPPDHQ with linear and nonlinear optics”. *Biophys. J.* 89:L04–L06 (2005)

57. Fux E., and Mazel, C., “Unmixing coral fluorescence emission spectra and predicting new spectra under different excitation conditions” *Appl Opt.* 38(3) p486-94 (1999)

58. Zimmermann, T., “Spectral imaging and linear unmixing in light microscopy” *Adv. Biochem. Eng. Biotechnol*. 95 p245-65 (2005)

59. Tsurui, H., Nishimura, H., Hattori, S., Hirose, S., Okumura, K., and Shirai, T. “Seven-color fluorescence imaging of tissue samples based on Fourier spectroscopy and singular value decomposition” *J Histochem Cytochem.* 48(5) p653-62 (2002)

60. Harris, A. T., "Spectral mapping tools from the earth sciences applied to spectral microscopy data" *Cytometry A*. 69(8) p872-9 (2006)

61. Rosenberg S. A., Quinlan, M. E., Forkey, J.N., Goldman,Y. E., "Rotational motions of macro-molecules by single-molecule fluorescence microscopy" *Acc Chem Res.* 38(7) p583-93 (2005)

62. Piston, D. W., and Rizzo, M. A., "FRET by fluorescence polarization microscopy" *Methods Cell Biol*. 85 p415-30 (2008)

63. O'Connor, D. V. and Phillips, D. "Time Correlated Single Photon Counting" London. Academic Press. (1984)

64. Dowling, K., Dayel, M. J., Lever, M. J., French, P. M., Hares, J. D., and Dymoke-Bradshaw, A. K. "Fluorescence lifetime imaging with picosecond resolution for biomedical applications" *Opt Lett.* 23(10) p810-2 (1998)

65. Agronskaia A. V., Tertoolen, L., and Gerritsen, H.C. "Fast fluorescence lifetime imaging of calcium in living cells," *J Biomed Opt.* 9(6) p1230-7 (2004)

66. Munro, I., McGinty, J., Galletly, N., Requejo-Isidro, J., Lanigan, P. M., Elson, D. S., Dunsby, C., Neil, M.A., Lever, M. J., Stamp, G. W., and French, P. M. "Toward the clinical application of time-domain fluorescence lifetime imaging" *J Biomed Opt*. 10(5) p051403 (2005)

67. Lakowicz, J. R., Szmacinski, H., Nowaczyk, K., and Johnson, M. L, "Fluorescence lifetime imaging of calcium using Quin-2" *Cell Calcium.* 13(3) p131-47 (1992)

68. van Munster, E. B., and Gadella, T. W., "Fluorescence lifetime imaging microscopy (FLIM)" *Adv. Biochem. Eng. Biotechnol.* 95 p143-75 (2005)

69. Jares-Erijman E. A., and Jovin, T. M. "FRET imaging" *Nat Biotechnol.* 21(11) p1387-95 (2003)

70. Clegg, R.M., "Fluorescence Resonance Energy Transfer (FRET)" in Fluorescence Imaging Spectroscopy and Microscopy (eds. Wang, X.F. & Herman, B.) p179-252 John Wiley & Sons, New York

71. Förster, T. "Zwischenmolekulare energiewanderung und fluoreszenz" *Annals. Phys.* 2 p55-75 (1948)

72. Miyawaki, A., Llopis, J., Heim, R., McCaffery, J. M., Adams, J. A., Ikura, M., and Tsien, R. Y., "Fluorescent indicators for Ca2+ based on green fluorescent proteins and calmodulin" *Nature* 388(6645) p882-7 (1997)

73. Cicchetti, G., Biernacki, M., Farquharson, J., and Allen, P. G., "A ratiometric expressible FRET sensor for phosphoinositides displays a signal change in highly dynamic membrane structures in fibroblasts," *Biochemistry* 43(7) p1939-49 (2004)

74. Newman R.H., and Zhang, J. "Visualization of phosphatase activity in living cells with a FRET-based calcineurin activity sensor" *Mol. Biosyst*. 4(6) p496-501 (2008)

75. Salonikidis, P. S., Zeug, A., Kobe. F., Ponimaskin, E., and Richter, D. W. "Quantitative Measurement of cAMP Concentration Using an Epac Based FRET-Sensor" *Biophys J.* (2008)

76. Nezu, A., Tanimura, A., Morita, T., Shitara, A., and Tojyo, Y. “A novel fluorescent method employing the FRET-based biosensor "LIBRA" for the identification of ligands of the inositol 1,4,5-trisphosphate receptors” *Biochim. Biophys. Acta*. 1760(8) p1274-80 (2006)

77. Violin, J.D., Zhang, J., Tsien, R.Y., and Newton, A.C. “A genetically encoded fluorescent reporter reveals oscillatory phosphorylation by protein kinase C” *J. Cell Biol.* 161(5) p899-909 (2003)

78. Ciruela F., “Fluorescence-based methods in the study of protein-protein interactions in living cells” *Curr. Opin. Biotechnol*. (2008)

79. Maurel D., Comps-Agrar, L., Brock, C., Rives, M. L., Bourrier, E., Ayoub, M. A., Bazin, H., Tinel, N., Durroux, T., Prézeau, L., Trinquet, E., and Pin, J. P. “Cell-surface protein-protein interaction analysis with time-resolved FRET and snap-tag technologies: application to GPCR oligomerization” *Nat Methods* 5(6) p561-7 (2008)

80. Wouters, F. S., and Bastiaens, P. I. “Imaging protein-protein interactions by fluorescence resonance energy transfer (FRET) microscopy” *Curr. Protoc. Protein Sci.* 19 (19.5) (2001)

81. Göttle, M., Dove, S., Steindel, P., Shen, Y., Tang, W. J., Geduhn, J., König, B., and Seifert, R. “Molecular analysis of the interaction of Bordetella pertussis adenylyl cyclase with fluorescent nucleotides” *Mol Pharmacol* 72(3) p526-35 (2007)

82. Kleemola, M., Toivonen, M., Mykkänen, J., Simell, O., Huoponen, K., and Heiskanen, K. M. “Heterodimerization of y(+)LAT-1 and 4F2hc visualized by acceptor photobleaching FRET microscopy” *Biochim. Biophys. Acta*. 1768(10) p2345-54 (2007)

83. Gordon, G.W., Berry, G., Liang, X.H., Levine, B. and Herman, B. “Quantitative fluorescence resonance energy transfer measurements using fluorescence microscopy” *Biophys. J.* 74 p2702-2713 (1998)

84. Xia, Z. and Liu, Y. “Reliable & global measurement of fluorescence resonance energy transfer using fluorescence microscopes” *Biophys. J.* 81 p2395-2402 (2001)

85. Zimmerman, T., Rietdorf, J. Girod, A., Georget, V. and Pepperkok, R. “Spectral imaging and linear unmixing enables improved FRET efficiency with a novel GFP2-YFP FRET pair” *FEBS Lett.* 531 p245-249 (2002)

86. Gu, Y., Di, W.L., Kelsell, D.P. and Zicha, D., “Quantative fluorescence resonance energy transfer (FRET) measurement with acceptor photobleaching and spectral unmixing” *J. Microsc*. 215(2) p162-173 (2004)

87. Wouters, F. S., and Bastiaens, P. I. “Fluorescence lifetime imaging of receptor tyrosine kinase activity in cells” *Curr. Biol.* 9(19) p1127-30 (1999)

88. Duncan, R. R., Bergmann, A., Cousin, M. A., Apps, D. K., and Shipston, M. J. “Multi-dimensional time-correlated single photon counting (TCSPC) fluorescence lifetime imaging microscopy (FLIM) to detect FRET in cells” *J Microsc.* 215(1) p1-12 (2004)

89. Verveer, P. J., Squire, A., and Bastiaens, P. I. “Global analysis of fluorescence lifetime imaging microscopy data” *Biophys J.* 78(4) p2127-37 (2000)

90. Verveer, P. J., Squire, A., and Bastiaens, P. I. “Improved spatial discrimination of protein reaction states in cells by global analysis and deconvolution of fluorescence lifetime imaging microscopy data” *J Microsc.* 202(3) p451-6. (2001)

91. Yudushkin, I. A., Schleifenbaum, A., Kinkhabwala, A., Neel, B. G., Schultz, C., and Bastiaens, P. I., “Live-cell imaging of enzyme-substrate interaction reveals spatial regulation of PTP1B” *Science* 315(5808) p115-9 (2007)

92. Verveer, P. J., Wouters, F. S., Reynolds, A. R., and Bastiaens, P. I., “Quantitative imaging of lateral ErbB1 receptor signal propagation in the plasma membrane” *Science.* 290(5496) p1567-70 (2000)

93. Gautier, I., Tramier, M., Durieux, C., Coppey, J., Pansu, R. B., Nicolas, J. C., Kemnitz, K., and Coppey-Moisan, M. “Homo-FRET microscopy in living cells to measure monomer-dimer transition of GFP-tagged proteins” *Biophys J.* 80(6) p3000-8 (2001)

94. Bader, A. N., Hofman, E. G., van Bergen en Henegouwen, P. M. P., and Gerritsen, H. C., “Imaging of protein cluster sizes by means of confocal time-gated fluorescence anisotropy microscopy” *Opt. Express* 15(11) p6934-6945 (2007)

95. de Souza, E. S., Hirata, I. Y., Juliano, L., and Ito, A. S., “End-to-end distance distribution in bradykinin observed by Förster resonance energy transfer” *Biochim. Biophys. Acta.* 1474(2) p251-61 (2000)

96. Shimozono, S., and Miyawaki, A. “Engineering FRET constructs using CFP and YFP” *Methods Cell Biol.* 85 p381-93 (2008)

97. Adams, S. R., Campbell, R. E., Gross, L. A., Martin, B. R., Walkup, G. K., Yao, Y., Llopis, J., and Tsien, R. Y. “New biarsenical ligands and tetracysteine motifs for protein labeling in vitro and in vivo: synthesis and biological applications” *J. Am. Chem. Soc.* 124(21) p6063-76 (2002)

98. Hoffmann, C., Gaietta, G., Bünemann, M., Adams, S. R., Oberdorff-Maass, S., Behr, B., Vilardaga, J. P., Tsien, R. Y., Ellisman, M. H., Lohse, M. J. “A FlAsH-based FRET approach to determine G protein-coupled receptor activation in living cells” *Nat. Methods* 2(3) p171-6 (2005)

99. Evans, N. J., Walker, J. W. “Endothelin receptor dimers evaluated by FRET, ligand binding, and calcium mobilization” *Biophys J.* 95(1) p483-92 (2008)

100. McGrath N., and Barroso, M. “Quantum dots as fluorescence resonance energy transfer donors in cells” *Biomed. Opt.* 13(3) p031210 (2008)

101. Clapp, A. R., Medintz, I. L., and Mattousi, H. ““Förster resonance energy transfer investigations using quantum-dot fluorophores” *Chemphyschem*. 7(1) p47-57 (2006)

102. Campbell, R. E., Tour, O., Palmer, A. E., Steinbach, P. A., Baird, G. S., Zacharias, D. A., and Tsien, R. Y., “A monomeric red fluorescent protein” *Proc. Natl. Acad. Sci. U.S.A* 99 p7877–7882 (2002)

103. van der Krogt, G. N., Ogink, J., Ponsioen, B., and Jalink, K. “A comparison of donor-acceptor pairs for genetically encoded FRET sensors: application to the Epac cAMP sensor as an example” *PLoS ONE*. 3(4) e1916 (2008)

104. Bayle, V., Nussaume, L., and Bhat, R. A. “Combination of novel GFP mutant TSapphire and DsRed variant mOrange to set up a versatile in planta FRET-FLIM assay” *Plant Physiol*. (2008)

105. Bunney, T. D., Harris, R., Gandarillas, N. L., Josephs, M. B., Roe, S. M., Sorli, S. C., Paterson, H. F., Rodrigues-Lima, F., Esposito. D., Ponting, C. P., Gierschik, P., Pearl, L. H., Driscoll, P. C., and Katan, M. “Structural and mechanistic insights into Ras association domains of phospholipase C epsilon” *Mol. Cell* 21(4) p495-507 (2006)

106. Ruddon, R.W., “Cancer Biology” New York. Oxford University Press. (1995)

107. Takai, Y., Sasaki, T. and Matozaki, T. “Small GTP-Binding Proteins” *Physiol. Rev*. 81 p153-190 (2001)

108. Parada, L.F., Tabin, C.J., Shih, C. & Weinberg, R.A., “Human EJ bladder carcinoma is homologue of Harvey sarcoma virus ras gene” *Nature* 10 p474-478 (1982)

109. Downward, J. “Targeting Ras signaling pathways in cancer therapy” *Nature* 3 p11-21 (2003)

110. Magee T., and Marshall, C. “New insights into the interaction of Ras with the plasma membrane” *Cell* 98(1) p69-80 (1999)

111. Alberts, B., Johnson, A., Lewis, J., Raff, M., Roberts, K. and Walter, P. “Molecular Biology of The Cell” New York. Garland Science (2002)

112. MacDonald, S.G., Crews, C.M., Wu, L., Driller, J., Clark, R., Erikson RL. and McCormick F. “Reconstitution of the Raf-1-MEK-ERK signal transduction pathway in vitro” *Mol. Cell Biol.* 13 p6615-6620 (1993)

113. Yordy, J.S. and Muise-Helmericks R.C., “Signal transduction and the ETS family of transcription factors” *Oncogene* 19 p6503-6513 (2000)

114. Rodriguez-Viciana P., Warne, P. H., Dhand, R., Vanhaesebroeck, B., Gout, I., Fry, M. J., Waterfield, M. D., and Downward J. “Phosphatidylinositol-3-OH kinase as a direct target of Ras” *Nature* 370 p527-532 (1994)

115. Khwaja, A., Rodriguez-Viciana, P., Wennstrom, S., Warne, P.H., and Downward J., “Matrix adhesion and Ras transformation both activate a phosphoiniositide-3-OH kinase and protein kinase B/Akt cellular survival pathway” *EMBO J.* 16 p2783-2793 (1997)

116. Burgering, B. M., and Medema R. H., “Decisions on life and death: FOXO Forkhead transcription factors are in command when PKB/Akt is off duty” *J. Leukoc. Biol.* 73(6) p689-701 (2003)

117. Perez, O. D., Kinoshita, S., Hitoshi, Y., Payan, D. G., Kitamura, T., Nolan, G. P., and Lorens, J. B. “Activation of the PKB/AKT pathway by ICAM-2” *Immunity* 16(1) p51-65 (2002)

118. Uddin, S., Hussain, A. R., Al-Hussein, K. A., Manogaran, P. S., Wickrema, A., Gutierrez, M. I., and Bhatia, K. G. “Inhibition of phosphatidylinositol 3'-kinase/AKT signaling promotes apoptosis of primary effusion lymphoma cells” *Clin. Cancer. Res.* 11(8) p3102-8 (2005)

119. Romashkova, J. A., and Makarov, S. S. “NF-kappaB is a target of AKT in anti-apoptotic PDGF signaling” *Nature.* 401(6748) p86-90 (1999)

120. Spaargaren, M. and Bischoff, J.R., “Identification of the guanine nucleotide dissociation stimulator for Ral as a putative effector molecule of R-Ras, H-Ras, K-Ras and Rap” *Proc. Natl. Acad. Sci U.S.A.* 91 p12609-12613 (1994)

121. De Ruiter, N.D., Burgering B.M., and Bos, J.L., “Regulation of the Forkhead transcription factor AFX by Ral-dependent phosphorylation of threonines 447 and 451” *Mol. Cell Biol.* 21 p8225-8235 (2001)

122. Lim, K.H., Baines, A.T., Fiordalisi, J.J., Shipitsin, M., Feig, L.A., Cox, A.D., Der., C.J. and Counter, C.M. “Activation of RalA is critical for Ras-induced tumorigenesis of human cells” *Cancer Cell* 6 p533-545 (2005)

123. Katan, M “Families of phosphoinositide-specific phospholipase C: Structure and function” *Biochim. Biophys. Acta*. (1-2) p5-17 (1998)

124. Rebecchi, M. J. & Pentyala, S. N. “Structure, function and control of phosphoinositide-specific phospholipase C” *Physiol. Rev.* 80 p1292-1324 (2000)

125. Bunney, T. D. and Katan, M. “Phospholipase C epsilon: linking second messengers and small GTP-ases” *Trends Cell Biol.* 16(12) p640-648 (2006)

126. Song, C., Hu, C. D., Masago, M., Kariya, K., Yamawaki-Kataoka, Y., Shibatohge, M., Wu, D., Satoh, T., and Kataoka, T. “Regulation of a novel human phospholipase C, PLCε, through membrane targeting by Ras” *J. Biol. Chem.* 276 p2752-2757 (2001)

127. Harris, R., Bunney, T. D., Katan, M. and Driscoll, P. C. “Backbone 1H, 13C, and 15N resonance assignments for the two 13 kD Ras associating domains (RA1 and RA2) from phospholipase C epsilon” *J. Biomol. NMR* 33(2) 138 (2005)

128. Sorli, S. C., Bunney, T. D., Sugden, P. H., Paterson, H. F., and Katan, M. “Signaling properties and expression in normal and tumor tissues of two phospholipase C epsilon splice variants” *Oncogene* 24 p90–100 (2005)

129. Apolloni, A., Prior, I. A., Lindsay, M., Parton, R. G., and Hancock, J. F. “H-ras but not K-ras traffics to the plasma membrane through the exocytic pathway” *Mol. Cell Biol.* 20(7) p2475-87 (2000)

130. Wright, L. P., and Philips, M. R., “Lipid posttranslational modifications. CAAX modification and membrane targeting of Ras” *J. Lipid Res.* 47(5) p883-91 (2006)

131. Coleman, W. B., Throneburg, D. B., Grisham, J. W., and Smith, G. J., “Overexpression of c-K-ras, c-N-ras and transforming growth factor beta co-segregate with tumorigenicity in morphologically transformed C3H 10T1/2 cell lines” *Carcinogenesis.* 15(5) p1005-12 (1994)

132. Wohlgemuth, S., Kiel, C., Kramer, A., Serrano, L., Wittinghofer, F., and Herrmann, C. “Recognizing and defining true ras binding domains I: biochemical analysis” *J. Mol. Biol.* 348 p741–758 (2005)

133. Cole, M. J., Siegel, J., Webb, S. E., Jones, R., Dowling, K., Dayel, M. J., Parsons-Karavassilis D., French, P. M., Lever, M. J., Sucharov, L. O., Neil, M. A., Juskaitis R., and Wilson, T., “Time-domain whole-field fluorescence lifetime imaging with optical sectioning” *J. Microsc.* 203(3) p246-57 (2001)

134. Petran, M., Hadravsky, M. Egger, M. D., and Galambos, R. “The Tandem Scanning Reflected Light Microscope” *J.O.S.A.* 58 p661-664 (1968)

135. 43. Kino, G. S., Corle, T. R., and Xiao, G. Q., “Real Time Confocal Scanning Optical Microscope” *Appl. Phys. Lett.* 53 p716-718 (1988)

136. Grant, D. M., Elson, D. S., Schimpf, D., Dunsby, C., Requejo-Isidro, J., Auksorius, E., Munro, I,, Neil, M. A., French , P.M., Nye, E., Stamp, G., and Courtney, P., “Optically sectioned fluorescence lifetime imaging using a Nipkow disk microscope and a tunable ultrafast continuum excitation source” *Opt Lett.* 30(24) p3353-5 (2005)

137. van Munster, E. B., Goedhart, J., Kremers, G. J., Manders, E. M., and Gadella, T. W. Jr. “Combination of a spinning disc confocal unit with frequency-domain fluorescence lifetime imaging microscopy” *Cytometry A.* 71(4) p207-14 (2007)

138. Buranachai, C., Kamiyama, D., Chiba, A., Williams, B. D., and Clegg, R. M., “Rapid Frequency-Domain FLIM Spinning Disk Confocal Microscope: Lifetime Resolution, Image Improvement and Wavelet Analysis” *J Fluoresc.* (2008)

139. Tanaami, T., Otsuki, S., Tomosada, N., Kosugi, Y., Shimizu, M., and Ishida, H., “High-speed 1-frame/ms scanning confocal microscope with a microlens and Nipkow disks” *Appl. Opt.* 41(22) p4704-8 (2002)

140. Ranka, J. K., Windler, R. S., and Stentz, A. J., “Visible continuum generation in air-silica microstructure optical fibers with anomalous dispersion at 800 nm”, *Opt. Lett.* 25 p25-27 (2000)

141. Dudley, J. M., Genty, G., and Coen, S., “Supercontinuum generation in photonic crystal fiber” *Rev. Mod. Phys.* 78 p1135-84 (2006)

142. Cumberland, B. A., Travers, J. C., Kennedy, R. E., Popov, S. V., and Taylor, J. R., “2 W/nm peak-power all-fiber supercontinuum source and its application to the characterization of periodically poled non-linear crystals” *Opt. Comm.* 277 (1) p134-137 (2007)

143. Genty, G., Lehtonen, M., Ludvigsen, H., Broeng, J., and Kaivola, M., “Spectral broadening of femto-second pulses into continuum radiation in microstructured fibers”, *Opt. Express* 10 p1083-1098 (2002)

144. Genty, G., Lehtonen, M., and Ludvigsen, H., “Enhanced bandwidth of supercontinuum generated in microstructuted fibers”, *Opt. Express* 12, p3471-3480 (2004)

145. Knight, J. C., Birks, T. A., Russell, P. St. J., and de Sandro, J. P., "Properties of photonic crystal fiber and the effective index model" *JOSA A*, 15 (3) p748-752 (1998)

146. Birks, T. A., Wadsworth, W. J., and Russell. P., St. J., "Supercontinuum generation in tapered fibres" *Opt. Lett.* 25 (19) p1415-17 (2000)

147. Travers, J. C., Kennedy, R. E., Popov, S. V., Taylor, J. R., Sabert, H., and Mangan, B. "Extended continuous-wave supercontinuum generation in a low-water-loss holey fiber" *Opt. Lett.* 30(15) p1938-1940

148. McConnell, G., "Confocal laser scanning fluorescence microscopy with a visible continuum source" *Opt. Express* 12(13) p2844-2850 (2004)

149. Dunsby, C. Lanigan, P., McGinty, J., Elson, D. S., Requejo-Isidro, J., Munro, I., Galletly, N., McCann, F., Treanor, B., Önfelt, B., Davis, D. M., Neil, M. A. A., and French, P. M. W., "An electronically tunable ultrafast laser source applied to fluorescence imaging and fluorescence lifetime imaging microscopy" *J. Phys. D: Appl. Phys.* 37 p3296-3303 (2004)

150. Auksorius, A., Boruah, B. R., Dunsby, C., Lanigan, P., Kennedy, G., Neil, M. A. A., and French, P. M. W., "Stimulated emission depletion microscopy with a supercontinuum source and fluorescence lifetime imaging" *Opt. Lett.* 33(2) p113-115 (2008)

151. Wang, E., Babbey, C. M., and Dunn, K. W. "Performance comparison between the high-speed Yokogawa spinning disc confocal system and single-point scanning confocal systems" *J Microsc.* 218(2) p148-59 (2005)

152. Rocks, O. Peyker, A., Kahms, M., Verveer, P. J., Koerner, C., Lumbierres, M., Kuhlmann, J., Waldmann, H., Wittinghofer, A., and Bastiaens, P. I., "An acylation cycle regulates localization and activity of palmitoylated Ras isoforms," *Science* 307(5716) p1746-52 (2005)

153. Peyker, A., Rocks, O., and Bastiaens, P. I., "Imaging activation of two Ras isoforms simultaneously in a single cell," *Chembiochem.* 6(1) p78-85 (2005).

154. Esposito, A., Dohm, C. P., Bähr, M., and Wouters, F. S. "Unsupervised fluorescence lifetime imaging microscopy for high content and high throughput screening" *Mol Cell Proteomics.* 6(8) p1446-54 (2007)

155. Elson, D. S. Munro, I., Requejo-Isidro, J., McGinty, J., Dunsby, C., Galletly, N., Stamp, G. W., Neil, M. A. A., Lever, M. J., Kellett, P. A., Dymoke-Bradshaw, A., Hares, J., and French, P. M. W., "Real-time time-domain fluorescence lifetime imaging including single-shot acquisition with a segmented optical image intensifier," *New J. Phys.* 6 p1367-2630 (2004)

156. Ballew, R. M., and Demas, J. N., "An error analysis of the rapid lifetime determination method for the evaluation of single exponential decays," *Anal. Chem.* 61(1) p30-33 (1989)

157. Rosen L. B., Ginty, D. D., Weber, M. J., and Greenberg, M. E. "Membrane depolarization and calcium influx stimulate MEK and MAP kinase via activation of Ras" *Neuron.* 12(6): p1207-21 (1994)

158. Cullen, P. J., and Lockyer, P. J., "Integration of calcium and Ras signaling," *Nat. Rev. Mol. Cell Biol.* 3(5) p339-48 (2002)

159. Walker S., A., Cullen, P. J., Taylor, J. A., and Lockyer, P. J. "Control of Ras cycling by Ca2+" *FEBS Lett.* 546(1) p6-10 (2003)

160. Farnsworth, C. L., Freshney, N. W., Rosen, L. B., Ghosh, A., Greenberg, M. E., and Feig, L. A. "Calcium activation of Ras mediated by neuronal exchange factor Ras-GRF" *Nature* 376(6540) p524-7 (1995)

161. Fam, N. P., Fan, W. T., Wang, Z., Zhang, L. J., Chen, H., and Moran, M. F. "Cloning and characterization of Ras-GRF2, a novel guanine nucleotide exchange factor for Ras" *Mol. Cell Biol*. 17(3) p1396-406 (1997)

162. Tognon, C. E., Kirk, H. E., Passmore, L. A., Whitehead, I. P., Der, C. J. and Kay, R. J. "Regulation of RasGRP via a phorbol ester-responsive C1 domain" *Mol. Cell. Biol.* 18(12) p6995-7008 (1998)

163. Clyde-Smith, J., Silins, G., Gartside, M., Grimmond, S., Etheridge, M., Apolloni, A., Hayward, N., and Hancock, J. F. "Characterization of RasGRP2, a plasma membrane-targeted, dual specificity Ras/Rap exchange factor" *J. Biol. Chem.* 275(41) p32260-7 (2000)

164. Yamashita, S., Mochizuki, N., Ohba, Y., Tobiume, M., Okada, Y., Sawa, H., Nagashima, K., and Matsuda, M. "CalDAG-GEFIII activation of Ras, R-ras, and Rap1" *J. Biol. Chem.* 275(33) p25488-93 (2000)

165. Filvaroff, E., Calautti, E., McCormick, F., and Dotto, G. P. "Specific changes of Ras GTP-ase-activating protein (GAP) and a GAP-associated p62 protein during calcium-induced keratinocyte differentiation" *Mol. Cell. Biol.* 12(12) p5319-28 (1992)

166. Chow, A., Davies, A. J., and Gawler, D. J., "Investigating the role played by protein-lipid and protein-protein interactions in the membrane association of the p120GAP CaLB domain" *Cell Signal.* 11 p442-51 (1999)

167. Davis, A. J., Butt, J. T., Walker, J. H., Moss, S. E., and Gawler, D. J. "The Ca2+-dependent lipid binding domain of P120GAP mediates protein-protein interactions with Ca2+-dependent membrane-binding proteins. Evidence for a direct interaction between annexin VI and P120GAP" *J. Biol. Chem.* 271(40) p24333-6 (1996)

168. Lockyer, P. J., Kupzig, S., and Cullen, P. J. "CAPRI regulates Ca(2+)-dependent inactivation of the Ras-MAPK pathway" *Curr Biol.* 11(12) p981-6 (2001)

169. Cullen, P. J. "Bridging the GAP in inositol 1,3,4,5-tetrakisphosphate signaling" *Biochim. Biophys. Acta*. 1436(1-2) p35-47 (1998)

170. Kelley, G. G., Reks, S. E., Ondrako, J. M., and Smrcka, A. V. "Phospholipase C(epsilon): a novel Ras effector" *EMBO J.* 20(4) p743-54 (2001)

171. Kaestner, L., Tabellion, W., Weiss, E., Bernhardt, I., and Lipp, P. "Calcium imaging of individual erythrocytes: problems and approaches" *Cell Calcium.* 39(1) p13-9 (2005)

172. Bush, D. S., and Jones, R. L., "Measurement of cytoplasmic calcium in aleurone protoplasts using indo-1 and fura-2" *Cell Calcium* 8(6) p455-72 (1987)

173. Prasher, D., McCann, R. O., and Cormier, M. J. "Cloning and expression of the cDNA coding for aequorin, a bioluminescent calcium-binding protein" *Biochem. Biophys. Res. Commun.* 126(3) p1259-68 (1985)

174. Baird, G. S., Zacharias, D. A., and Tsien, R. Y. "Circular permutation and receptor insertion within green fluorescent proteins" *Proc. Natl. Acad. Sci. U. S. A.* 96(20) p11241-6 (1999)

175. Yu, D., Baird, G. S., Tsien, R. Y., and Davis, R. L. "Detection of calcium transients in Drosophila mushroom body neurons with camgaroo reporters" *J. Neurosci.* 23(1) p64-72 (2003)

176. Nagai, T., Sawano, A., Park, E. S., Miyawaki, A. "Circularly permuted green fluorescent proteins engineered to sense Ca2+" *Proc. Natl. Acad. Sci. U. S. A.* 98(6) p3197-202 (2001)

177. Ohkura, M., Matsuzaki, M., Kasai, H., Imoto, K., and Nakai, J., "Genetically encoded bright Ca2+ probe applicable for dynamic Ca2+ imaging of dendritic spines" *Anal. Chem.* 77(18) p5861-9 (2005)

178. Nagai, T., Yamada, S., Tominaga, T., Ichikawa, M., and Miyawaki, A., "Expanded dynamic range of fluorescent indicators for Ca2+ by circularly permuted yellow fluorescent proteins" *Proc. Natl. Acad. Sci. U. S. A.* 101 p10554-10559 (2004)

179. Palmer, A. E., and Tsien, R. Y., "Measuring calcium signaling using genetically targetable fluorescent indicators" *Nat. Protoc.* 1(3) p1057-65 (2006)

180. Varadi, A., and Rutter, G. A., "Green fluorescent protein: applications and protocols" *Methods in Molecular Biology* 183 p255-264 (2002)

181. Mochizuki, N., Yamashita, S., Kurokawa, K., Ohba, Y., Nagai, T., Miyawaki, A., and Matsuda, M. "Spatio-temporal images of growth-factor-induced activation of Ras and Rap1" *Nature.* 411(6841) p1065-8 (2001)

182. Wang, L., Tsien, R. Y. "Evolving proteins in mammalian cells using somatic hypermutation" *Nat. Protoc*. 1(3) p1346-50 (2006)

183. Karasawa, S., Araki, T., Nagai, T., Mizuno, H., and Miyawaki, A., "Cyan-emitting and orange-emitting fluorescent proteins as a donor/acceptor pair for fluorescence resonance energy transfer" *Biochem. J.* 381(Pt 1) p307-12 (2004)

184. Goedhart, J., Vermeer, J. E., Adjobo-Hermans, M. J., van Weeren, L., and Gadella, T. W. Jr. "Sensitive detection of p65 homodimers using red-shifted and fluorescent protein-based FRET couples" *PLoS ONE* 2(10) e1011 (2007)

185. Lessard, G. A., Habuchi, S., Werner, J. H., Goodwin, P. M., De Schryver, F., Hofkens, J., and Cotlet, M., "Probing dimerization and intraprotein fluorescence resonance energy transfer in a far-red fluorescent protein from the sea anemone Heteractis crispa" *J. Biomed. Opt.* 13(3) p031212 (2008)

186. Merzlyak, E. M., Goedhart, J., Shcherbo, D., Bulina, M. E., Shcheglov, A. S., Fradkov, A. F., Gaintzeva, A., Lukyanov, K. A., Lukyanov, S., Gadella, T. W., and

Chudakov, D. M. “Bright monomeric red fluorescent protein with an extended fluorescence lifetime” *Nat. Methods.* 4(7) p555-7 (2007)

187. Piljic A., and Schultz, C. “Simultaneous recording of multiple cellular events by FRET” *ACS Chem. Biol*. 3(3) p156-60 (2008)

188. Mahajan, N. P., Linder, K., Berry, G., Gordon, G. W., Heim, R., and Herman, B. “Bcl-2 and Bax interactions in mitochondria probed with green fluorescent protein and fluorescence resonance energy transfer” *Nat Biotechnol.* 16(6) p547-52. (1998)

189. Shcherbo, D., Merzlyak, E. M., Chepurnykh, T. V., Fradkov, A. F., Ermakova, G. V., Solovieva, E. A., Lukyanov, K. A., Bogdanova, E. A., Zaraisky, A. G., Lukyanov, S., and Chudakov, D. M. “Bright far-red fluorescent protein for whole-body imaging” *Nat. Methods* 4(9) p741-6 (2007)

190. Ai, H. W., Shaner, N. C., Cheng, Z., Tsien, R. Y., and Campbell, R. E., “Exploration of new chromophore structures leads to the identification of improved blue fluorescent proteins” *Biochemistry* 46(20) p5904-10 (2007)

191. Calleja, V., Ameer-Beg, S. M., Vojnovic, B., Woscholski, R., Downward, J., and Larijani, B. “Monitoring conformational changes of proteins in cells by fluorescence lifetime imaging microscopy” *Biochem J.* 372(1) p33-40 (2003)